UNCLASSIFIED

ORNL-1975
Progress

PHYSICS DIVISION

SEMIANNUAL PROGRESS REPORT

FOR PERIOD ENDING SEPTEMBER 10, 1955

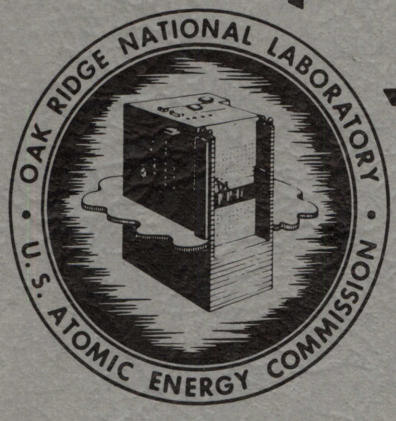

OAK RIDGE NATIONAL LABORATORY
OPERATED BY
UNION CARBIDE NUCLEAR COMPANY
A Division of Union Carbide and Carbon Corporation
UCC
POST OFFICE BOX P · OAK RIDGE, TENNESSEE

UNCLASSIFIED

ORNL-1975

COPY NO. _____

Contract No. W-7405-eng-26

PHYSICS DIVISION

SEMIANNUAL PROGRESS REPORT

for Period Ending September 10, 1955

A. H. Snell, Director

Edited by
J. L. Fowler and E. O. Wollan
Associate Directors

DATE ISSUED

OAK RIDGE NATIONAL LABORATORY
Operated by
UNION CARBIDE NUCLEAR COMPANY
A Division of Union Carbide and Carbon Corporation
Post Office Box P
Oak Ridge, Tennessee

Physics Division progress reports previously issued in this series are as follows:

ORNL-325 Supplement	December, January, and February, 1948-1949
ORNL-366	Period Ending June 15, 1949
ORNL-481	Period Ending September 25, 1949
ORNL-577	Period Ending December 15, 1949
ORNL-694	Period Ending March 15, 1950
ORNL-782	Period Ending June 15, 1950
ORNL-865	Period Ending September 20, 1950
ORNL-940	Period Ending December 20, 1950
ORNL-1005	Period Ending March 20, 1951
ORNL-1092	Period Ending June 20, 1951
ORNL-1164	Period Ending September 20, 1951
ORNL-1278	Period Ending December 20, 1951
ORNL-1289	Period Ending March 20, 1952
ORNL-1365	Period Ending June 20, 1952
ORNL-1415	Period Ending September 20, 1952
ORNL-1496	Period Ending December 20, 1952
ORNL-1620	Period Ending September 10, 1953
ORNL-1705	Period Ending March 10, 1954
ORNL-1798	Period Ending September 10, 1954
ORNL-1879	Period Ending March 20, 1955

ORNL-1975
Progress

INTERNAL DISTRIBUTION

1. C. E. Center
2. Biology Library
3. Health Physics Library
4-6. Central Research Library
7. Reactor Experimental Engineering Library
8-19. Laboratory Records Department
20. Laboratory Records, ORNL R.C.
21. A. M. Weinberg
22. L. B. Emlet (K-25)
23. J. P. Murray (Y-12)
24. J. A. Swartout
25. E. H. Taylor
26. E. D. Shipley
27. E. J. Murphy
28. F. C. VonderLage
29. A. H. Snell
30. A. Hollaender
31. K. Z. Morgan
32. F. L. Culler
33. M. T. Kelley
34. E. M. King
35. E. O. Wollan
36. D. W. Cardwell
37. A. S. Householder
38. L. D. Roberts
39. R. B. Briggs
40. R. N. Lyon
41. W. C. Koehler
42. E. P. Blizard
43. M. E. Rose
44. G. E. Boyd
45. Lewis Nelson
46. R. W. Stoughton
47. C. E. Winters
48. W. H. Jordan
49. E. C. Campbell
50. D. S. Billington
51. M. A. Bredig
52. R. S. Livingston
53. C. P. Keim
54. F. C. Maienchein
55. C. E. Clifford
56. G. H. Clewett
57. C. D. Susano
58. C. J. Borkowski
59. M. J. Skinner
60. M. K. Wilkinson
61. S. Bernstein
62. P. M. Reyling
63. D. D. Cowen
64. W. M. Good
65. G. C. Williams
66. J. L. Fowler
67. R. W. Johnson
68. J. R. McNally, Jr.
69. J. L. Gabbard
70. R. A. Charpie
71. E. P. Wigner (consultant)
72. H. A. Bethe (consultant)
73. K. Lark-Horovitz (consultant)
74. Eugene Guth
75. R. W. Peelle
76. W. M. Breazeale (consultant)
77. E. C. Smith
78. C. G. Shull
79. P. R. Bell
80. G. G. Kelley
81. C. C. Harris
82. H. G. MacPherson (consultant)
83. P. H. Stelson
84. J. E. Sherwood
85. U. H. Bents
86. W. Zobel
87. R. B. Murray
88. H. B. Willard
89. J. Schenck
90. J. H. Neiler
91. E. D. Klema
92. C. F. Barnett
93. N. H. Lazar
94. R. R. Dickison
95. A. Simon
96. ORNL – Y-12 Technical Library, Document Reference Section

EXTERNAL DISTRIBUTION

97. W. G. Pollard, ORINS
98. W. K. H. Panofsky, Stanford University
99. L. C. Biedenharn, Rice Institute
100. R. F. Bacher, California Institute of Technology
101. John Dunning, Columbia University
102. Phillips Petroleum Co., Attn: Librarian
103. R. L. Heath, Phillips Petroleum Company
104. S. DeBenedetti, Carnegie Institute of Technology
105. Massachusetts Institute of Technology, Department of Electrical Engineering
106. A. von Hippel, Laboratory for Insulation Research, MIT
107. M. Goodrich, Louisiana State University
108. Truman S. Grey, Massachusetts Institute of Technology
109. V. C. Wilson, General Electric Co., Schenectady
110. D. S. Hughes, University of Texas
111. E. A. Rollor, ANP Project Office, Fort Worth
112. S. Frankel, Physics Dept., University of Pennsylvania
113. G. Griffith, Westinghouse Research Laboratory, E. Pittsburgh, Pennsylvania
114. F. Allison, Emory and Henry University, Emory, Virginia
115. J. A. Sauer, Physics Dept., Pennsylvania State University
116. J. E. Goldman, Dept. of Physics, Carnegie Institute of Technology
117. R. Stephenson, Dept. of Chemical Engineering, New York University
118. M. Goldhaber, Brookhaven National Laboratory
119. M. N. Saha, c/o Library, Institute of Nuclear Physics, 92 Upper Circular Road, Calcutta, India
120. J. A. Wheeler, Palmer Physical Laboratory, Princeton University
121. R. S. Christy, California Institute of Technology
122. T. J. Turner, Wake Forrest College
123. T. Lauritsen, California Institute of Technology
124. N. F. Ramsey, Harvard University
125. University of Notre Dame (Attention: Library)
126. J. H. Van Vleck, Harvard University
127. A. Glassgold, University of Minnesota
128. P. M. Steir, National Carbon Research Laboratories, P.O. Box 6087, Cleveland, Ohio
129. Boeing Airplane Company
130. Division of Research and Development, AEC, ORO

131-465. Given distribution as shown in TID-4500 under Physics Category

DISTRIBUTION PAGE TO BE REMOVED IF REPORT IS GIVEN PUBLIC DISTRIBUTION

INDEX AND SUMMARY

The theoretical development of relativistic wave mechanics has been essentially completed with the demonstration that both the three-field problem and the closed-loop problem can be brought within its framework. In the latter case, divergent and nongauge invariant results of the conventional quantum field theory are avoided completely. As a result, some real experimental checks in meson theory seem possible.

The theory of the high-energy fixed-frequency cyclotron has been further developed to allow cost and performance calculations to be made. Existing analytical formulas for orbit properties have been compared with more exact Oracle results, and a number of general design questions have been studied.

A simple generalization of the extreme shell model, based upon the kinematics of the collective model, has been proposed for the correlation of nuclear ground-state properties. It has also been applied to the problem of the determination of the matrix elements in the beta decay of mirror nuclei and to the correlation of nuclear magnetic and electric quadrupole moments.

Coulomb excitation of the isotopes of Pb, Cd, Mo, Te, Ru, Re, and Ir has been studied. From gamma-ray yields and angular distributions, new information has been obtained about the positions of the energy levels and about corresponding spins and transition probabilities.

Lifetimes for the first excited states of B^{10}, B^{11}, and Si^{28} have been studied by the technique of observing the Doppler shift of gamma radiation excited by proton inelastic scattering.

To clarify the present controversy over the states of Be^8, the $Li^6(He^3,p)Be^8$ proton spectrum has been rigorously re-examined. Up to 10 Mev there exists, besides the ground state, only the 2.9-Mev state. Evidence is presented for a broad level at 12.3 Mev.

Further studies have been made of the inelastic scattering of protons on Si^{28} which results in the excitation of the first excited state of Si^{28}. New resonances in $Si^{28} + p$ have been observed in this way. The 1.78-Mev gamma-ray angular distribution has been studied at numerous energies.

By using improved gamma-ray spectroscopy, the $Be^9(p,\gamma)B^{10}$ and $Be^9(p,\alpha\gamma)Li^6$ reactions have been re-examined as a function of energy and angle.

PUBLICATIONS

W. C. Koehler and E. O. Wollan, "Neutron Diffraction by Metallic Erbium," *Phys. Rev.* **97,** 1177–1178 (1955).

P. H. Stelson and E. C. Campbell, "Cross Section for Excitation of Pb^{207m} by Inelastic Scattering of Neutrons," *Phys. Rev.* **97,** 1222–1226 (1955).

A. Simon, "Ambipolar Diffusion in a Magnetic Field," *Phys. Rev.* **98,** 317–318 (1955).

H. B. Willard, J. K. Bair, and J. D. Kington, "Elastic Scattering Angular Distributions of Fast Neutrons on Light Nuclei," *Phys. Rev.* **98,** 669–673 (1955).

N. H. Lazar and E. D. Klema, "Decay of Bi^{207}," *Phys. Rev.* **98,** 710–718 (1955).

J. L. Fowler and C. H. Johnson, "Differential Elastic Scattering Cross Section for Neutrons on Nitrogen," *Phys. Rev.* **98,** 728–735 (1955).

J. W. T. Dabbs, L. D. Roberts, and S. Bernstein, "'Brute Force' Polarization of In^{115} Nuclei; Angular Momentum of 1.458-ev Neutron Resonance," *Phys. Rev.* **98,** 1512–1513 (1955).

A. H. Snell, book review ("High-Energy Accelerators by M. S. Livingston, Interscience, New York, 1954), *Physics Today,* **8,** No. 6, 27 (1955).

C. G. Shull, book review ("Neutron Optics," by D. J. Hughes, Interscience, New York, 1954), *Physics Today* **8,** No. 6, 29 (1955).

P. H. Stelson and F. K. McGowan, "Gamma-Ray Yields from Coulomb Excitation," *Phys. Rev.* **99,** 112 (1955).

F. K. McGowan and P. H. Stelson, "Angular Distribution of Gamma Rays from Coulomb Excitation," *Phys. Rev.* **99,** 127 (1955).

R. K. Abele, R. E. Zedler, and L. D. Roberts, "Operation of a Pulse Ion Chamber at 4.2°K," *Rev. Sci. Instr.* **26,** 521 (1955).

P. R. Bell, R. C. Davis, and W. Bernstein, "Pulse-Height Variation in Scintillation Counters," *Rev. Sci. Instr.* **26,** 726 (1955).

E. O. Wollan, book review ("Neutron Optics," by D. J. Hughes, Interscience, New York, 1954), *Am. J. Phys.* **22,** 497 (1954).

J. E. Hill, L. D. Roberts, and T. E. Fitch, "Slowing Down Distribution of U^{235} Fission Neutrons from a Point Source in Light Water," *J. Appl. Phys.* **26,** 1013–1017 (1955).

L. D. Roberts, J. E. Hill, and T. E. Fitch, "Slowing Down Distribution to Indium Resonance of U^{235} Fission Neutrons from a Point Fission Source in Two Aluminum Light Water Mixtures," *J. Appl. Phys.* **26,** 1018–1021 (1955).

J. D. Kington, J. K. Bair, H. O. Cohn, and H. B. Willard, "Proton-Neutron Threshold Measurements," *Phys. Rev.* **99,** 1393 (1955).

D. A. Geffen, "Simple Nonrelativistic Model for Single Meson Production," *Phys. Rev.* **99,** 1534 (1955).

PAPERS PRESENTED AT SCIENTIFIC MEETINGS

American Physical Society, Southeastern Section Meeting, Gainesville, Florida, April 7–9, 1955

A. H. Snell and F. Pleasonton, "Charge Spectrum of Cl^{37} Recoils from Neutrino Emission."

L. D. Roberts and R. B. Murray, "On Crystalline Electric Field Splitting Effects in Antiferromagnetic Transitions."

R. B. Murray and L. D. Roberts, "Extension of Molecular Field Theory to a Hexagonal Lattice."

M. E. Rose, "The Gauge Problem in Internal Conversion."

H. O. Cohn and J. L. Fowler, "Elastic Scattering of Neutrons from Neon."

P. M. Stier and C. F. Barnett, "Electron Capture Cross Section for Protons."
D. V. P. Williams and A. D. Callihan, "Resolving Time of Geiger Mueller Counters."
T. A. Welton, "Fixed Frequency Billion Volt Proton Cyclotron."

American Physical Society Meeting, Washington, D.C., April 28–30, 1955

M. K. Wilkinson, C. G. Shull, and R. E. Rundle, "Ferromagnetic Structure of Uranium Hydride."
P. H. Stelson and F. K. McGowan, "Coulomb Excitation of States in Thallium and Lead."
A. Simon, "Ambipolar Diffusion in a Magnetic Field."
H. Brysk and M. E. Rose, "Theoretical Results on Orbital Capture."
H. O. Cohn, J. K. Bair, J. D. Kington, and H. B. Willard, "The $Si^{28}(p,p'\gamma)Si^{28}$ Reaction."

American Institute of Electrical Engineers (Middle Eastern District Meeting), Columbus, Ohio, May 4–6, 1955

C. C. Harris, "Data Storage Methods for Medical Nuclear Instrumentation."
J. E. Francis and P. R. Bell, "Medical Spectrometer."

American Physical Society Meeting, Toronto, Canada, June 1955

J. W. T. Dabbs, L. D. Roberts, and S. Bernstein, "Direct Polarization of In^{115} Nuclei; J Value for the 1.458 ev Resonance."

Conference on Medium Energy Neutron Phenomena (Argonne National Laboratory), Chicago, Illinois, June 3–4, 1955

H. E. Banta, W. M. Good, J. H. Neiler, and E. C. Smith, "Progress of Time-of-Flight Neutron Energy Measurement."
R. W. Lamphere, "Fission Cross Sections of U^{234} and U^{236} up to 4 Mev."
J. K. Bair, H. O. Cohn, J. L. Fowler, A. Galonsky, C. H. Johnson, J. Judish, J. D. Kington, H. B. Willard, and J. E. Wills, "Summary of ORNL Differential Cross Sections for Elastic Neutron Scattering from Light Elements."
P. H. Stelson and E. C. Campbell, "Cross Sections for Excitation of Metastable States by Inelastic Scattering."

Gordon Research Conference, Meriden, New Hampshire, June 27 – July 1, 1955

A. H. Snell, "Magnetic Spectrometry of the Neutrino Recoils of Argon-37."

International Conference on the Peaceful Uses of Atomic Energy, Geneva, Switzerland, August 8–20, 1955

A. H. Snell, "The Nuclear Reactor in Basic Science."
T. A. Welton, "Kinetics of Stationary Reactor Systems."
G. G. Kelley (paper presented by A. H. Snell), "Methods of Pulse Analysis."
S. Bernstein and E. C. Smith, "The Cross Section of the Fission Product Poison Xe^{135} as a Function of Energy."
R. L. Macklin and H. Pomerance (paper presented by E. P. Wigner), "Resonance Capture Integrals."

Paris Low Temperature Conference, Paris, France, August 31 – September 8, 1955

L. D. Roberts, J. W. T. Dabbs, and S. Bernstein, "Direct Polarization of In^{115} Nuclei; J Value for the 1.458 ev Resonance."
R. B. Murray and L. D. Roberts, "Antiferromagnetism in $MnCl_2$ and UI_3 at Liquid Helium Temperatures."

Institute of Radio Engineers (PGNS) Meeting, Oak Ridge, Tennessee, September 14–16, 1955

J. H. Neiler, H. E. Banta, W. M. Good, and E. C. Smith, "Multichannel Time Interval Analyzer."

C. C. Harris, "The 'Hard-Bottoming' Technique in Nuclear Instrumentation Circuit Design."

P. R. Bell, "Medical Radiation Instrumentation with Scintillation Spectrometers."

G. G. Kelley, "Circuits for Pulse Analysis."

ANNOUNCEMENTS

During this period the Applied Nuclear Physics Division was established, with E. P. Blizard (former Associate Director of the Physics Division) as Director and A. Simon (also from the Physics Division) as Associate Director. Shielding research and critical-experiment research will be included in the program of this new division.

Summer personnel included the following research participants and visitors: M. M. Bretscher (Assistant Professor, Alabama Polytechnic Institute), Short-Lived Isomeric Studies; H. A. Gersch (Assistant Professor, Georgia Institute of Technology), Neutron Diffraction; E. V. Ivash (Assistant Professor, University of Texas), Theoretical Physics; A. V. H. Masket (Associate Professor, University of North Carolina) and V. E. Parker (Professor and Chairman of the Physics Department, Louisiana State University), High Voltage; A. Robeson (Assistant Professor, Emory University), Instrumentation Group; J. R. Stevenson (Assistant Professor, Georgia Institute of Technology), Low-Temperature Group; L. C. Biedenharn (summer visitor, Rice Institute), Theoretical Physics; J. M. Jauch (summer visitor, State University of Iowa), Theoretical Physics; T. J. Turner (summer visitor, Wake Forest College), Theoretical Physics; and J. E. Worsham, Jr. (summer visitor, University of Richmond), Neutron Diffraction.

University students here for the summer included the following: V. E. Barnes, II (Harvard University), Recoil Spectrometry; W. M. Bugg (University of Tennessee), D. P. Hamblen (Tulane University), and G. S. Paulett (University of Richmond), High Voltage; G. R. Burleson (Louisiana State University), Instrumentation Group; D. S. Falk (Harvard University), Theoretical Physics; H. Postma (Duke University), Low-Temperature Physics; and J. M. Winter, Jr. (Massachusetts Institute of Technology), Atomic-Beam Project.

J. W. Cable from Florida State University recently joined the Physics Division staff and will be working with the Neutron Diffraction Group.

S. Bernstein (Nuclear Alignment) is on leave of absence in Haifa, Israel, where he will spend the next year in teaching and research at the Israel Institute of Technology.

Terminations: C. G. Shull (Neutron Diffraction); E. C. Smith and P. E. F. Thurlow (Neutron Velocity Selector); P. M. Stier (Heavy-Ion Physics); A. E. Glassgold (Theoretical Physics); and R. L. Gamble (ORINS fellow, Instrumentation Group).

PHYSICS DIVISION
SEMIANNUAL PROGRESS REPORT

RELATIVISTIC WAVE MECHANICS

T. A. Welton

The name, "relativistic wave mechanics," has been applied to a set of developments, largely described previously, in the formalism of quantum field theory. Basically, this new formalism emphasizes the wave mechanics (*not* second-quantized) of the fermions which exist as real particles. The quantized mesonic or electromagnetic field which acts on the fermions is introduced as an unquantized, random, classical field, obeying no equation of motion. Primarily, in order to gain mathematical simplicity, all problems are set up in a space of four equivalent dimensions (positive definite metric), with an independent proper-time variable introduced to allow the definition of transition probabilities. After solution of the appropriate problem in the hypothetical space, physical results in space-time are obtained by simple analytic continuation in the complex planes of the mass parameter and the fourth component of momentum. In addition, the effect of virtual quanta is obtained by averaging the final result over the random values of the classical field. Previously, it has been shown that all processes *not* involving "closed loops" in quantum electrodynamics can be derived from

$$(1)\quad i\frac{\partial\psi}{\partial t_k} = \gamma_{\mu k}p_{\mu k}\psi + e\gamma_{\mu k}A_\mu(x_k)\,\psi \ ,$$

where

t_k = proper time of kth electron,

$$p_{\mu k} = -i\frac{\partial}{\partial x_{\mu k}} \ ,$$

$$\gamma_{\mu k}\gamma_{\nu k} + \gamma_{\nu k}\gamma_{\mu k} = 2\delta_{\mu\nu} \ ,$$

$$A_\mu(x) = \frac{1}{\sqrt{4\pi^3}}\int\frac{dk}{|k|}\,\mathfrak{a}_\mu(k)\,e^{ikx} \ ,$$

in which

$$|k| = (k_1^2 + k_2^2 + k_3^2 + k_4^2)^{1/2} \ ,$$

$$\langle\mathfrak{a}_\mu(k)\,\mathfrak{a}_\nu(k')\rangle = \delta_{\mu\nu}\delta(k + k') \ .$$

Note that separate four-coordinates as well as proper-time variables *must* be used for each actual particle.

A trivial extension shows that a system of nucleons interacting through the meson field can be described by

$$(2)\quad i\frac{\partial\psi}{\partial t_k} = \gamma_{\mu k}p_{\mu k}\psi + g\gamma_{5k}\tau_{ik}A_i(x_k)\,\psi \ ,$$

where

$$\tau_i\tau_j + \tau_j\tau_i = 2\delta_{ij} \qquad (i = 1, 2, 3) \ ,$$

$$A_i(x) = \frac{1}{\sqrt{4\pi^3}}\int\frac{dk}{\sqrt{k^2 + \mu^2}}\,\mathfrak{a}_i(k)\,e^{ikx} \ ,$$

in which

μ = meson mass,

$$\langle\mathfrak{a}_i(k)\,\mathfrak{a}_j(k')\rangle = \delta_{ij}\delta(k + k') \ .$$

It has now been shown that the three-field problem (still without closed loops) is properly described by writing a set of wave equations, each of which contains both electromagnetic and mesonic interaction, and, in addition, the expression for the meson field variable has been altered to allow for electromagnetic effects on mesons:

$$i\frac{\partial\psi}{\partial t_k} = \gamma_{\mu k}p_{\mu k}\psi + \frac{e}{2}(1 + \tau_{3k})\,\gamma_{\mu k}A_\mu(x_k)\,\psi + g\gamma_{5k}\tau_{ik}A_i(x_k)\,\psi \ ,$$

where $A_\mu(x)$ is given as before, and

$$A_i(x) = \frac{1}{\sqrt{4\pi^3}}\int\frac{dk}{\sqrt{k^2 + \mu^2}}\,\mathfrak{a}_i(k)\,\chi_i(k,x) \ ,$$

in which the $\chi_i(k,x)$ are assumed to approach e^{ikx} as $e \longrightarrow 0$, and are otherwise defined to satisfy the appropriate wave equations for the three real meson field variables in the presence of the electromagnetic field $A_\mu(x)$. Thus, photomeson production and the nucleon magnetic moment agree with calculations by conventional methods.

It has finally been shown that the missing closed-loop diagrams can be brought within the framework of this formalism. The vacuum polarization is calculated in the hypothetical space, assuming the vacuum to contain, with a certain density, particles with a definite mass constant n and completely random four-momentum direction. The resulting expressions bear considerable resemblance to the conventional formulas but can lead only to convergent results. The photon self-energy vanishes identically. The other divergences of the closed-loop type are immediately recognized as being due to an improper use of the Cauchy theorem in performing the required analytic continuation in the n space ($n \longrightarrow im$). When this continuation is properly performed, the charge renormalization, for example, also vanishes. Convergence is obtained in the beta decay of the charged pion, and the conventional diagram for the neutral pion decay cancels identically, there being a chance that better agreement would be obtained between theory and observation in this very important process. Thus the modification of the theory here described gives in meson theory strongly observable effects. These are now under calculation in the hope of obtaining a real check of the new theory as well as a marked improvement in the consistency of the meson theory.

ACCELERATOR DESIGN

T. A. Welton D. S. Falk

During the last six months, a number of survey calculations have been performed in order to help solidify laboratory plans for a high-energy fixed-frequency cyclotron. Detailed field and orbit specifications have been given for a number of possible machines with 4, 6, 8, 12, and 16 poles (sectors). Various amounts and shapes of spiral have been used in the field pattern, with exact results which essentially confirm the approximate results obtained by MURA for their spiral-ridge FFAG machines. In general, use of the spiral pattern can markedly reduce the fractional field variation (field amplitude) required to maintain vertical focusing and thus reduce the required size of the machine.

Simple formulas have been devised for calculating the pole face currents or shapes required to produce the necessary field variation. These have been applied to make a series of rough economic evaluations. The generally important result that emerges is that it will be unfeasible to introduce field variation in the dee insulation space. The cost of the current required to produce field variation in the orbit space only is, in general, a small part of the over-all machine cost. Alternatively, variable-thickness iron plates introduced as part of the dee structure just above and below the orbit plane appear promising. Similar structures applied directly to the pole faces, on the other hand, do not, in general, allow sufficient room for dee insulation and orbit oscillations.

Two formal questions have received some attention. Approximate orbit-stability calculations for such a machine are conveniently done by what the MURA group terms the smooth approximation, with the further assumption of nearly circular orbits. With the previously described Oracle code for exact stability calculations, some detailed checks were made of the approximate formulas. It appears that for qualitative estimates of machine cost and appearance the approximate formulas are adequate, but that for detailed design work the Oracle code will be essential. For this reason the code is being modified to give greater flexibility and precision.

One serious limitation on the performance of a spiral machine seems to be the onset of nonlinear radial-vertical coupling effects in the orbit oscillations. Some analytical investigations of this question were mildly reassuring, but it is planned to make a careful numerical study in the near future.

AN EMPIRICAL KINEMATICAL NUCLEAR MODEL

E. D. Klema R. K. Osborn

A simple generalization of the extreme shell model, based upon the kinematics of the collective model, has been proposed for the correlation of nuclear ground-state properties. It has been shown that if the concept of a rotating core is adjoined to that of the single-particle model, largely in disregard of dynamical considerations, then, by the aid of three simple empirical rules, ground-state wave functions may easily be constructed which correctly express the parities, spins, and magnetic moments of all nuclei for which $A \geq 7$, with the exception of W^{183}.

The choice of a particular set of empirical rules was dictated primarily by the twofold desire to keep the number of rules to a minimum and at the same time to restrict the consequent wave function to but two components; hence considerable oversimplification of the true state of affairs is inevitable. However, the internal consistency of the results does point up strikingly the previously observed, but not explicitly investigated, possibility that the nature of the variable degrees of freedom required for generalization of the single-particle model may differ fundamentally for $j = l + \frac{1}{2}$ in contrast with $j = l - \frac{1}{2}$ single-particle configurations – being predominantly those of the core in the former instance and those of the single particle in the latter.

The model has been applied to the analysis of nuclear electric quadrupole moments. The empirical rules found in the work on magnetic moments have, in general, been confirmed; however, the $d_{3/2}$ nuclei form an exceptional group. A correlation of the moments of these nuclei is, however, possible within the context of the present model and suggests that the description of the properties of $I = \frac{3}{2}$ nuclei may be particularly model-dependent. Shape factors have been obtained for a number of odd-even nuclei. A possible explanation of the anomalous magnetic moment of W^{183} has been found in the course of this work.

The present model has also been applied to the problem of the determination of the Gamow-Teller matrix elements in the beta decay of mirror nuclei. The Fermi integrals for these transitions have been re-evaluated numerically, using recent experimental values for the energies of the transitions, and the ft values have been calculated. Values of the ratio of Gamow-Teller to Fermi coupling constants have been obtained for several nuclear models.

COULOMB EXCITATION

F. K. McGowan P. H. Stelson
M. M. Bretscher

GAMMA-RAY YIELDS

The yields of gamma rays resulting from coulomb excitation have been measured for the isotopes of Pd, Mo, Te, Ru, Re, and Ir. The rather complex spectra of the normal elements have been resolved into the contributions of the different isotopes by the use of isotopically enriched targets. Metallic targets were prepared by sintering metallic powders into thin foils. For the medium-weight elements, 50 to 100 mg of the enriched metal was required for each target. About twice this amount was required for the heavier elements.

Light-element impurities in the isotopically enriched targets often yield gamma rays which interfere with the measurements. A common impurity in many of the isotopes is sodium, which gives rise to an intense gamma ray at 440 kev from the reaction $Na^{23}(p,p'\gamma)$. For an element in which there is no coulomb excitation of nuclear gamma rays, we can detect as little as 5 ppm of sodium as an impurity for 3-Mev protons incident on a thick target. We observed sodium as an impurity in the palladium and molybdenum isotopes to the extent of 0.03% and 0.02 to 0.06%, respectively. However, the spectrographic analysis supplied by the Stable Isotope Research and

Production Division for the enriched isotopes did not indicate sodium present as an impurity. For this reason we have undertaken an investigation of gamma-ray yields from thick targets of the light elements when the targets are bombarded with protons. Measurements have been completed for the elements between lithium and manganese at E_p = 1.5 Mev. Lithium and boron would also give rise to troublesome gamma rays of 478 and 430 kev from the reactions $Li^7(p,p'\gamma)Li^7$ and $B^{10}(p,\alpha)Be^{7*}$, respectively. Lithium was detected in the Ir^{193} sample and was also detected by the spectrographic analysis.

In Table 1 a summary is given of values of the reduced transition probabilities for excitation, $B(E2)_{ex}$, based on the interpretation of the observed gamma-ray yields. The first column lists the nucleus to which the gamma ray given in column 2 is assigned. The observed yields of the gamma rays for different proton energies are given in columns 3 and 4. The transitions per microcoulomb are deduced by using the isotopic abundance (column 5) and the total internal conversion coefficient, α_{total} (column 7). Column 9 gives the evaluation of the integral

$$\int_0^E E_f g_2(\xi) \frac{dE}{dE/d\rho x}$$

in units of kev × mg/cm^2.

The half lives, the electric quadrupole moments derived from the excitation energies, the electric quadrupole moments derived from the reduced transition probabilities, and the ratios of the observed reduced transition probabilities for decay to those expected for single-particle transitions are given in Table 2. In Table 3 we list only the gamma rays observed when the listed isotopes were bombarded by protons. Analysis of the yield measurements is not complete.

ANGULAR DISTRIBUTIONS

We have previously reported experiments[1] undertaken to test the Alder-Winther theory of the angular distribution of gamma rays following coulomb excitation.[2] The experimental results deviated considerably from the Alder-Winther theory. However, recent theoretical investigations of the coulomb excitation process by Biedenharn *et al.*,[3] Goldstein *et al.*,[4] Breit *et al.*,[5] and Benedict[6] have brought the theory into agreement with experiment.

If one measures the angular distribution of the gamma radiation with respect to the incident particles, one obtains an angular distribution which is similar to the angular correlation between two gamma rays in cascade. The distribution function is

$$W(\theta) = 1 + \sum_\nu A_\nu a_\nu P_\nu(\cos\theta) \ .$$

The coefficients A_ν are the gamma-gamma angular-correlation coefficients tabulated by Biedenharn and Rose[7] for the spin sequence $j_1(E2)\,J(L_2)\,j_2$, where the j's are the spins of the target nucleus, the coulomb excited state, and the final state after gamma-ray emission, respectively. The a_ν depend on the coulomb excitation process, and it is the comparison of these coefficients, calculated from theory and measured by experiment, which is of interest.

Alder and Winther have given values of a_2 and a_4 based on a semiclassical treatment of the coulomb excitation process. The disagreement of these a's with experiment pointed to the need for a quantum mechanical treatment of the process. Biedenharn *et al.*[3] have developed the formalism and mathematical techniques of the quantum mechanical treatment. Goldstein *et al.*[4] have calculated a_2 and a_4 for the particular case of Cd^{114} excitation by the use of this theory. The results are shown in Fig. 1, which is taken from a preprint of their paper.

Recently, Breit *et al.*[5] pointed out an error in the Alder-Winther calculation of a_2, and they find that the correct semiclassical calculation of a_2 is in considerably better agreement with experiment. In addition, they have also carried out a quantum mechanical calculation for the case

[1] F. K. McGowan and P. H. Stelson, *Phys. Rev.* **99**, 127 (1955); *Phys. Semiann. Prog. Rep. March 20, 1955*, ORNL-1879, p 12–13.

[2] K. Alder and A. Winther, *Phys. Rev.* **91**, 1578 (1953); **96**, 237 (1954).

[3] L. C. Biedenharn, J. L. McHale, and R. M. Thaler, *Phys. Rev.* (to be published).

[4] M. Goldstein *et al.*, *Phys. Rev.* (to be published).

[5] J. Breit, M. E. Ebel, and F. D. Benedict, *Phys. Rev.* (to be published).

[6] F. D. Benedict, *Phys. Rev.* (to be published).

[7] L. C. Biedenharn and M. E. Rose, *Revs. Mod. Phys.* **25**, 729 (1953).

TABLE 1. SUMMARY OF GAMMA-RAY YIELDS AND INFORMATION NEEDED TO OBTAIN THE REDUCED $E2$ TRANSITION PROBABILITIES FOR EXCITATION

Nucleus	E_γ (kev)	E_p (Mev)	$I\left(\frac{\gamma's}{\text{microcoulomb}}\right)$	Isotopic Abundance (%)	Classification	α_{total}	$\frac{\text{Transitions}}{\text{Microcoulomb}}$	$\int_0^E \frac{E_f g_2(\xi)\, dE}{dE/d\rho x}$	$B(E2)_{ex} \times 10^{48}$ (cm^4)
Pd^{104}	555	2.1	7.34×10^3	63.2	$E2$	0.0047	1.17×10^4	3.92×10^2	0.473
		2.4	2.76×10^4				4.39×10^4	1.54×10^3	0.451
		3.3	3.16×10^5				5.02×10^5	1.64×10^4	0.485
Pd^{106}	513	2.1	1.95×10^4	82.33	$E2$	0.0057	2.38×10^4	6.43×10^2	0.596
		2.4	6.63×10^4				8.09×10^4	2.23×10^3	0.575
		2.7	1.64×10^5				2.01×10^5	5.60×10^3	0.569
		3.0	3.29×10^5				4.03×10^5	1.14×10^4	0.516
		3.3	6.12×10^5				7.47×10^5	2.00×10^4	0.592
Pd^{108}	433	2.1	6.88×10^4	94.19	$E2$	0.0089	7.37×10^4	1.53×10^3	0.763
		2.4	1.61×10^5				1.73×10^5	4.35×10^3	0.629
		2.7	3.64×10^5				3.90×10^5	9.46×10^3	0.654
		3.0	6.70×10^5				7.18×10^5	1.75×10^4	0.651
		3.3	1.11×10^6				1.19×10^6	2.83×10^4	0.662
Pd^{110}	374	2.1	1.09×10^5	91.42	$E2$	0.0143	1.21×10^5	2.73×10^3	0.700
		2.4	2.83×10^5				3.14×10^5	6.80×10^3	0.732
		2.7	5.53×10^5				6.14×10^5	1.36×10^4	0.715
		3.0	9.85×10^5				1.09×10^6	2.32×10^4	0.745
		3.3	1.62×10^6				1.80×10^6	3.62×10^4	0.785
Pd^{105}	440	2.1	9.98×10^3	78.19	$E2$?	0.0089	1.01×10^4	1.42×10^3	0.112
		2.4	2.90×10^4				2.93×10^4	4.10×10^3	0.113
		2.7	6.73×10^4				6.79×10^4	9.00×10^3	0.120
		3.0	1.34×10^5				1.36×10^5	1.69×10^4	0.127
		3.3	2.33×10^5				2.35×10^5	2.75×10^4	0.135
Pd^{105}	322	2.1	2.27×10^3	78.19		0.0244*	2.34×10^3	4.42×10^3	0.00839
		2.4	4.85×10^3				4.97×10^3	9.85×10^3	0.00799
		2.7	1.10×10^4				1.13×10^4	1.81×10^4	0.00989
		3.0	2.31×10^4				2.37×10^4	2.97×10^4	0.0127
		3.3	4.62×10^4				3.73×10^4	4.40×10^4	0.0170

TABLE 1 (continued)

Nucleus	E_γ (kev)	E_p (Mev)	$I\left(\frac{\gamma's}{\text{microcoulomb}}\right)$	Isotopic Abundance (%)	Classification	α_{total}	Transitions / Microcoulomb	$\int_0^E \frac{E_f g_2(\xi)\, dE}{dE/d\rho x}$	$B(E2)_{ex} \times 10^{48}$ (cm^4)
Pd^{105}	280	2.1	3.00×10^3	78.19		0.0388*	3.12×10^3	6.37×10^3	0.00776
		2.4	6.50×10^3				6.76×10^3	1.30×10^4	0.00827
		2.7	1.28×10^4				1.34×10^4	2.26×10^4	0.00941
		3.0	2.15×10^4				2.23×10^4	3.54×10^4	0.00998
		3.3	3.81×10^4				3.97×10^4	5.12×10^4	0.0123
Mo^{100}	540	2.4	1.13×10^4	9.67	$E2$	0.0040	1.17×10^5	2.27×10^3	0.614
		2.7	2.69×10^4				2.80×10^5	5.74×10^3	0.579
		3.0	5.19×10^4				5.39×10^5	1.15×10^4	0.557
Mo^{98}	770	2.4	5.83×10^3	95.00	$E2$	0.0015	6.15×10^3	2.77×10^2	0.264
		2.7	2.01×10^4				2.12×10^4	1.11×10^3	0.227
		3.0	5.17×10^4				5.45×10^4	3.07×10^3	0.211
Mo^{96}	770	2.4	5.16×10^3	85.94	$E2$	0.0015	6.01×10^3	2.77×10^2	0.258
		2.7	2.20×10^4				2.57×10^4	1.11×10^3	0.274
		3.0	5.63×10^4				6.57×10^4	3.07×10^3	0.254
Mo^{94}	874	2.4	1.60×10^3	79.1	$E2$	0.0012	2.03×10^3	8.67×10	0.278
		2.7	8.20×10^3				1.04×10^4	4.64×10^2	0.266
		3.0	2.48×10^4				3.14×10^4	1.56×10^3	0.239
Mo^{97}	No gammas observed	1.8 to 3.0		89.63					
Mo^{95}	203	1.8	1.32×10^4	91.27	$E2 + M1$	0.036	1.50×10^4	5.62×10^3	0.0317
		2.1	2.71×10^4				3.07×10^4	1.18×10^4	0.0309
		2.4	4.85×10^4				5.51×10^4	2.05×10^4	0.0319
		2.7	7.93×10^4				9.00×10^4	3.21×10^4	0.0333
		3.0	1.06×10^5				1.21×10^5	4.64×10^4	0.0309
Te^{130}	850	3.3	1.05×10^4	34.44	$E2$	0.0022	3.05×10^4	2.30×10^3	0.360
Te^{128}	750	3.3	2.18×10^4	31.18	$E2$	0.0029	6.87×10^4	4.39×10^3	0.379
Te^{126}	673	3.3	2.82×10^4	18.69	$E2$	0.0038	1.52×10^5	7.06×10^3	0.519

*The total conversion coefficient corresponds to taking the transition to be predominantly $E2$ radiation.

TABLE 2. SUMMARY OF THE REDUCED TRANSITION PROBABILITIES, HALF LIVES, AND QUADRUPOLE MOMENTS FOR THE EVEN ISOTOPES OF Pd, Mo, AND Te

Nucleus	E (kev)	I	$B(E2)_{ex} \times 10^{48}$	$B(E2)_{d} \times 10^{48}$	$T_{1/2}$ (sec)	$(Q_0)_E \times 10^{24}$	$(Q_0)_{B(E2)} \times 10^{24}$	$\frac{(Q_0)_{B(E2)}}{(Q_0)_E}$	$\frac{B(E2)_d}{B(E2)_{sp}}$
Pd^{104}	555	2	0.470	0.0941	1.14×10^{-11}	5.79	2.17	0.376	15.6
Pd^{106}	513	2	0.579	0.116	1.37×10^{-11}	6.01	2.41	0.401	18.8
Pd^{108}	433	2	0.672	0.134	2.77×10^{-11}	6.51	2.59	0.399	21.3
Pd^{110}	374	2	0.735	0.147	5.26×10^{-11}	6.99	2.72	0.389	22.6
Mo^{100}	540	2	0.583	0.117	1.05×10^{-11}	5.40	2.43	0.45	20.4
Mo^{98}	770	2	0.234	0.0468	4.46×10^{-12}	4.55	1.53	0.34	8.4
Mo^{96}	770	2	0.262	0.0524	3.98×10^{-12}	4.56	1.62	0.36	9.6
Mo^{94}	874	2	0.261	0.0522	2.12×10^{-12}	4.30	1.62	0.38	9.9
Te^{130}	850	2	0.360	0.0720	1.77×10^{-12}	5.10	1.90	0.37	8.9
Te^{128}	750	2	0.379	0.0758	3.15×10^{-12}	5.46	1.95	0.36	9.6
Te^{126}	673	2	0.519	0.104	3.94×10^{-12}	5.74	2.29	0.40	13.3

TABLE 3. GAMMA RAYS OBSERVED WHEN THE LISTED ISOTOPES WERE BOMBARDED BY PROTONS

Nucleus	E_γ (kev)	E_p (Mev)	Nucleus	E_γ (kev)	E_p (Mev)
Ru^{104}	358	1.5 to 3.0	Re^{187}	134	3.0 to 4.0
Ru^{102}	475	1.5 to 3.0		167	3.0 to 4.0
Ru^{100}	540	1.8 to 3.0		301	3.0 to 4.0
Ru^{98}	654	2.1 to 3.0	Re^{185}	128	3.0 to 4.0
Ru^{96}	835	2.1 to 3.0		159	3.0 to 4.0
	1005*	2.1 to 3.0		287	3.0 to 4.0
Ru^{101}	131	1.5 to 3.0	Ir^{193}	140	3.0 to 4.0
	187	1.5 to 3.0		217	3.0 to 4.0
	303	1.5 to 3.0		357	3.0 to 4.0
	545*	2.1 to 3.0	Ir^{191}	114	3.0 to 4.0
	720*	2.1 to 3.0		134	3.0 to 4.0
Ru^{99}	92.5	1.5 to 3.0		200	3.0 to 4.0
	722*	2.1 to 3.0		348	3.0 to 4.0

*The observed gamma ray is possibly from the excitation of a small amount of a light-element impurity.

of the 330-kev gamma ray in Pt^{194}. Figure 2, which is taken from the paper by Benedict,[6] presents these results.

The agreement of experiment and theory increases our confidence in the procedure of taking the empirically determined curves of a_2 and a_4 and assigning spins and $E2/M1$ mixtures for the excitation observed in the odd-mass nuclei. Angular distributions have been measured for the gamma rays excited in Cd^{113}, Cd^{111}, and Pd^{105}. A summary of the results is given in Table 4. The observed angular distributions lead to unique spin assignments for the excited states of Cd^{113} and Cd^{111}. However, it is not possible to assign a definite spin to the excited state in Pd^{105}. Of the five possible spin values, only the spins $\frac{1}{2}$ and $\frac{9}{2}$ are incompatible with the measured distribution. Angular distributions have been measured for the excited states of Cd^{116}, Cd^{114}, Cd^{112}, Cd^{110}, Pd^{110}, and Pd^{108}. In every case the measurements indicate that the spin of the coulomb excited state is 2.

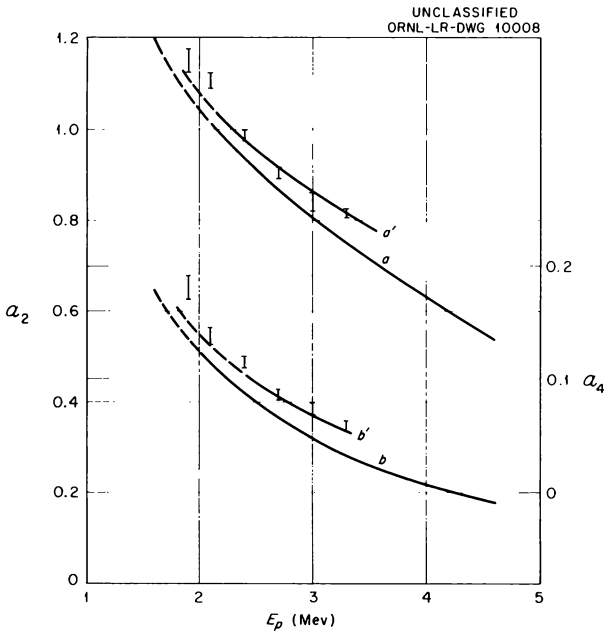

Fig. 1. Cd^{114} Particle Parameters a_2 and a_4 vs Energy of the Incident Proton. The scale for the curves (*a*), representing the parameter a_2, appears on the left; that for the curves (*b*), representing a_4, appears on the right. The data are from McGowan and Stelson and are for thick targets. The unprimed curves are for thin targets; the primed curves include approximate thick-target corrections. The dashed portions of the curves show the region where the present calculations are least reliable.

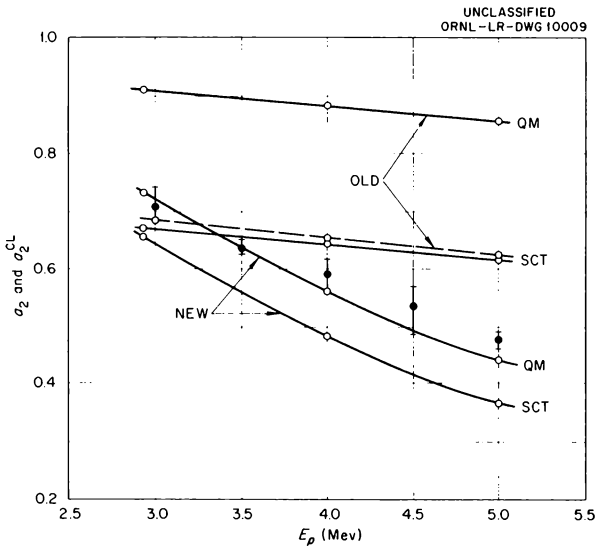

Fig. 2. Values of $a_2(\xi)$ and $a_2^{cl}(\xi)$ Plotted Against Proton Energy E_p for Platinum with Excitation Energy of 330 kev. The open circles are computed from theories, where SCT and QM denote semiclassical and quantum mechanical, respectively. Experimental points are shown as closed circles with vertical spreads. The old and new signs correspond to curves marked accordingly. The dashed curve includes thick target corrections and admixture of Pt^{196} taken from McGowan and Stelson.

TABLE 4. PROTON-GAMMA ANGULAR-DISTRIBUTION COEFFICIENTS OF THE TERMS IN THE EXPANSION OF THE CORRELATION FUNCTION IN LEGENDRE POLYNOMIALS FOR A THICK TARGET

Nucleus	E_γ (kev)	E_p (Mev)	ξ_i	Spin Sequence	$(A_2)_{\gamma\gamma}$	$(a_2A_2)_{exp}$	$(A_2)_{exp}$	$(A_4)_{\gamma\gamma}$	$(a_4A_4)_{exp}$	$(A_4)_{exp}$	δ_γ
Cd^{113}	582	3.3	0.428	$\frac{1}{2}(E2)\,\frac{5}{2}(E2)\,\frac{1}{2}$	0.2857	0.218 ± 0.023	0.266 ± 0.030	0.3809	−(0.036 ± 0.029)	0.579 ± 0.468	
		3.0	0.501	$\frac{1}{2}(E2)\,\frac{5}{2}(E2)\,\frac{1}{2}$	0.2857	0.223 ± 0.033	0.262 ± 0.040	0.3809	−(0.032 ± 0.043)	0.418 ± 0.566	
	300	2.4	0.340	$\frac{1}{2}(E2)\,\frac{3}{2}(E2+M1)\,\frac{1}{2}$		0.012 ± 0.006	0.016 ± 0.008		0.005 ± 0.008	~0	0.285 ± 0.01 or −(3.9 ± 0.1)
		2.1	0.422	$\frac{1}{2}(E2)\,\frac{3}{2}(E2+M1)\,\frac{1}{2}$		0.018 ± 0.006	0.022 ± 0.008		−(0.005 ± 0.008)	~0	0.29 ± 0.01 or −(4.0 ± 0.2)
Cd^{111}	610	3.3	0.452	$\frac{1}{2}(E2)\,\frac{5}{2}(E2)\,\frac{1}{2}$	0.2857	0.225 ± 0.022	0.269 ± 0.030	0.3809	−(0.066 ± 0.028)	1.00 ± 0.42	
		3.0	0.532	$\frac{1}{2}(E2)\,\frac{5}{2}(E2)\,\frac{1}{2}$	0.2857	0.172 ± 0.019	0.19 ± 0.03	0.3809	−(0.031 ± 0.025)	0.39 ± 0.31	
	342	2.4	0.395	$\frac{1}{2}(E2)\,\frac{3}{2}(E2+M1)\,\frac{1}{2}$		0.077 ± 0.004	0.096 ± 0.005		−(0.016 ± 0.006)	~0	0.37 ± 0.01 or −(6.1 ± 0.3)
		2.1	0.490	$\frac{1}{2}(E2)\,\frac{3}{2}(E2+M1)\,\frac{1}{2}$		0.099 ± 0.005	0.115 ± 0.006		−(0.011 ± 0.007)	~0	0.40 ± 0.01 or −(6.9 ± 0.2)
Pd^{105}	440	2.7, 3.0, 3.3		$\frac{5}{2}(E2)\,\frac{5}{2}(E2+M1)\,\frac{5}{2}$			−(0.079 ± 0.015)			~0	1.7 ± 0.1
		2.7, 3.0, 3.3		$\frac{5}{2}(E2)\,\frac{3}{2}(E2+M1)\,\frac{5}{2}$			−(0.079 ± 0.015)			~0	−(0.32 ± 0.05) or −(1.8 ± 0.2)
		2.7, 3.0, 3.3		$\frac{5}{2}(E2)\,\frac{7}{2}(E2+M1)\,\frac{5}{2}$			−(0.079 ± 0.015)			~0	−(0.52 ± 0.20) or −(1.2 ± 0.6)

NUCLEAR LIFETIME MEASUREMENTS

H. B. Willard
J. K. Bair
H. O. Cohn
J. D. Kington

Gamma-ray transitions between excited states in light nuclei are usually too fast to be measured by direct electronic methods. Estimates of lifetimes can sometimes be obtained by making use of the recoil motion of the residual nucleus. Devons *et al.*[1] have written a comprehensive discussion of the various methods available in such measurements. They are of two types: (1) the direct measurement of the distance traveled by the recoil nucleus before de-excitation, (2) observation of the Doppler shift in the gamma-ray energy. Method 1 has a limit of about 10^{-11} sec, whereas method 2 covers the range 10^{-8} to 10^{-14} sec. Only method 2 has been used in the present work.

It can be shown, by making a Lorentz transformation, that the gamma-ray energy dependence with respect to the angle, θ, it makes with the direction of the recoiling nucleus in vacuum is given by

$$E = E_0\left(1 + \frac{v}{c}\cos\theta\right) ,$$

where E_0 is the radiation energy for a nucleus at rest, v is the velocity of the recoil, and c is the velocity of light. A maximum shift,

$$\frac{\Delta E}{E_0} = \frac{2v}{c} ,$$

is obtained by observation of the gamma-ray energies at $\theta = 0$ and $\theta = \pi$. If the recoil is slowed down and stopped in a backing material, the maximum shift is reduced to

$$\frac{\Delta E}{E_0} = \frac{2v}{c}\left(\frac{\lambda\alpha}{1 + \lambda\alpha}\right) ,$$

where $\lambda = 1/\tau$, in which τ is the mean life for the transition, and $\alpha = R/v$, in which R is the range of the recoil in the stopping material. In this equation we assume that the range is proportional to the velocity.

In exothermic nuclear reactions, recoils are produced in all directions, and coincidences between the recoils and the gamma rays must be taken in order to measure the Doppler shift. However, endothermic reactions which produce recoil nuclei within a small forward cone can be used to measure energy shifts without resort to coincidence techniques. It was therefore decided to limit this preliminary investigation to levels excited by inelastic scattering of protons.

Targets backed by tantalum were bombarded by 450-Mev protons, and the gamma rays produced by inelastic scattering from the first excited states of B^{10}, B^{11}, and Si^{28} were detected by a 3 × 3 in. NaI crystal located 60 cm from the targets. The energy shift for $\theta = 0$ to $\theta = 160$ deg was measured in alternation for several cycles. Instrumental shifts were checked by locating a ThC″ source at the target. These tests, as shown in Fig. 1, indicated that shifts greater than 0.5% could be detected. Improvements in the technique should reduce this limit to about 0.1%.

Boron-10 has a ground state of 3^+ and a first excited state of 1^+ at 720 kev. Measurements[2]

[1] S. Devons, G. Manning, and D. St. P. Bunbury, *Proc. Phys. Soc. (London)* **68A**, 18 (1955).

[2] J. Thirion and V. L. Telegdi, *Phys. Rev.* **92**, 1253 (1953).

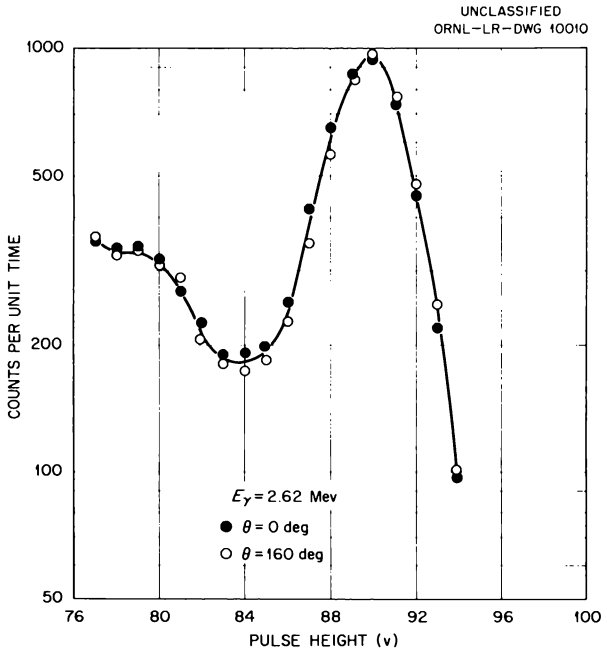

Fig. 1. Instrumental Check at $\theta = 0$ deg and $\theta = 160$ deg for Doppler Shift Measurements Using a ThC″ Source (2.62-Mev Gamma Ray).

[method 1 on the $Be^9(d,n)B^{10}$ reaction] give a lifetime of $(7 \pm 2) \times 10^{-10}$ sec, consistent with an $E2$ transition. No energy shift was observed in the $B^{10}(p,p'\gamma)B^{10}$ reaction (Fig. 2) when targets thick for recoils were used. This gives the limit $\tau > 10^{-12}$ sec. Thin targets, such that the recoils were stopped in the tantalum backing, were also used, with no observable shift ($\tau > 10^{-13}$ sec).

The ground state of B^{11} is $\frac{3}{2}^-$, and the first excited state[3] at 2.14 Mev is either $\frac{1}{2}$ or $\frac{3}{2}$. An observed energy shift of 1.7% (Fig. 3) was obtained with a target whose stopping power was 50 kev for 3-Mev protons (thick for the recoil B^{11} nuclei). A shift of about 1.3% was obtained for a target one-tenth as thick, where the recoils were stopped in the tantalum backing. These results give a mean life of $\tau < 10^{-13}$ sec. More accuracy is required before one can conclude whether the state is $\frac{1}{2}$ or $\frac{3}{2}$.

Silicon-28 has a ground state of 0^+ and an excited state of 2^+ at a 1.78-Mev excitation. No energy shift (Fig. 4) was observed by using a target thick for recoils, indicating a mean lifetime of $\tau > 10^{-13}$ sec. This is consistent with the Weisskopf estimate of 5×10^{-12} sec for an $E2$ transition.

[3] J. K. Bair, J. D. Kington, and H. B. Willard, *Phys. Rev.* (to be published).

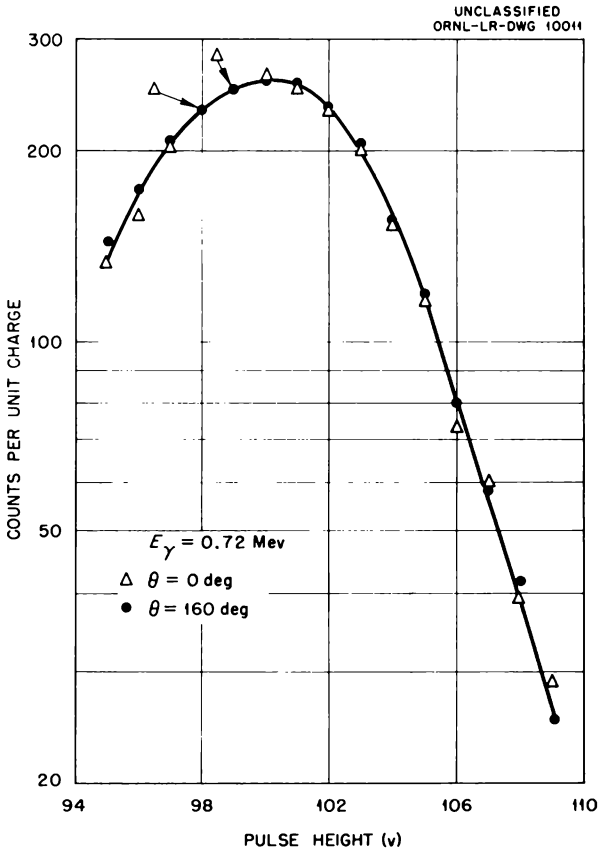

Fig. 2. Spectra Obtained at θ = 0 deg and θ = 160 deg for the 0.72-Mev Gamma Ray from Inelastic Proton Scattering on B^{10}.

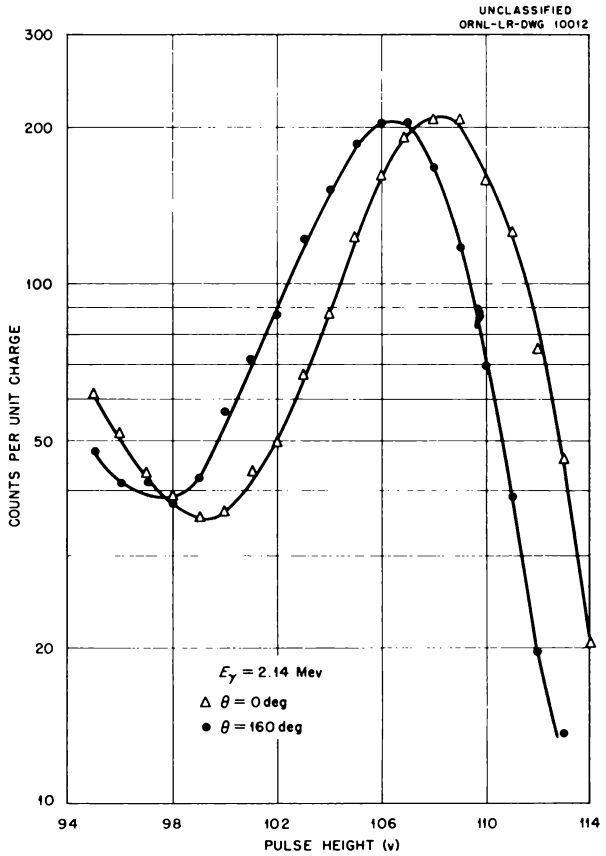

Fig. 3. Spectra Obtained at θ = 0 deg and θ = 160 deg for the 2.14-Mev Gamma Ray from Inelastic Proton Scattering on B^{11}.

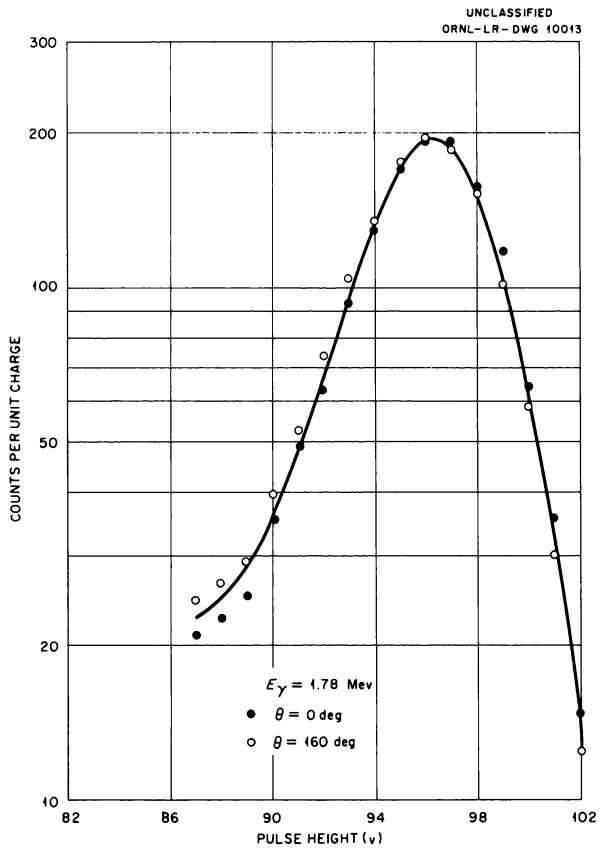

Fig. 4. Spectra Obtained at $\theta = 0$ deg and $\theta = 160$ deg for the 1.78-Mev Gamma Ray from Inelastic Proton Scattering on Si^{28}.

ENERGY LEVELS OF Be^8

C. D. Moak W. R. Wisseman

In spite of the fact that Be^8 was one of the first nuclei to be studied with high-voltage accelerator techniques, there is still some considerable doubt about the identities and positions of certain levels reported for this relatively simple nucleus.[1] The reaction $Li^6 + He^3 \longrightarrow Be^8 + H^1$ has been studied carefully with an NaI crystal spectrometer in an attempt to find not only the well-established levels of Be^8 but also any weak broad lines which might have been missed in other experiments where competing reactions might produce a masking effect.

Many reactions have been used in the study of Be^8. Experiments with rather poor statistics have been reported[2-8] for the following reactions: $B^{11}(\gamma,t)Be^8$, $B^{10}(\gamma,d)Be^8$, $Li^7(d,n)Be^8$, and $Li^7(p,\gamma\alpha)He^4$. Titterton has reviewed several of these papers in discussing the evidence for levels in Be^8 at 4, 5.3, and 7.5 Mev, in addition to the well-established level at 2.9 Mev. Steigert and Sampson[9] have recently reported alpha-alpha scattering data which indicate a level at 7.5 Mev. Jentschke[10] has recently reported on some new alpha-alpha scattering data which indicate the presence of a level at approximately 12.5 Mev. Trail and Johnson have reported a careful reexamination of the $Li^7(d,n)Be^8$ reaction with a multichannel neutron telescope and have obtained very good statistics; they found only the 2.9-Mev level up to about 10 Mev in Be^8, in contradiction with earlier conclusions.[11] Treacy has studied the alpha particles from the $B^{10}(d,\alpha)Be^8$ reaction and has found only the 2.9-Mev level up to 7 or 8 Mev in Be^8, where the background of three-body-breakup alpha particles begins to obscure the spectrum.[12] Malm and Inglis[13] have studied the alpha particles from the $B^{11}(p,\alpha)Be^8$ reaction at several angles and at several bombarding energies and have obtained very good statistics; they have found only the 2.9-Mev level up to 7 or 8 Mev in Be^8.

The $Li^6(He^3,p)Be^8$ reaction has several advantages in a search for weak levels in Be^8. Unlike the $Li^7(d,n)Be^8$ reaction, the outgoing particles are charged, and corrections and normalizations of the data are less important. Unlike the $B^{10}(d,\alpha)Be^8$ and the $B^{11}(p,\alpha)Be^8$ reactions, the outgoing particle, being a proton, can be distinguished from the alpha particles following Be^8 breakup. Finally, the rather high Q value for the $Li^6(He^3,p)Be^8$ reaction makes a greater range of Be^8 excitation available for study. The disadvantage is that the Li^6 target must be fairly free of Li^7, or confusion may arise from the competing reaction $Li^7(He^3,p)Be^9$. Preliminary runs in which 92% Li^6 and 8% Li^7 were used indicated that targets would need to be better than 98% Li^6 to avoid the possibility that a spurious level of Be^9 might obscure a weak Be^8 level underneath.

Doubly-charged He^3 ions of 1.25 Mev from the 625-kv cascade accelerator were used to bombard a target which assayed 99.96% Li^6 and which was obtained from the Stable Isotope Research and Production Division. The target was mounted in the NaI charged-particle spectrometer shown in Fig. 1. The spectrometer is fitted with a selection of absorbers and may be moved through the angular range from 45 to 135 deg with respect to the incident beam. Pulses were analyzed with a 120-channel serial-memory quartz delay line type of analyzer.

Preliminary runs were made at several angles, and sufficiently good statistics were obtained to establish that, at least up to 10 Mev in Be^8, no level appeared with greater than 1% of the ground-state intensity, other than the 2.9-Mev level.

[1] F. Ajzenberg and T. Lauritsen, *Revs. Mod. Phys.* **27**, 77 (1955).

[2] M. E. Calcraft and E. W. Titterton, *Phil. Mag.* **42**, 666 (1951).

[3] M. J. Brinkworth and E. W. Titterton, *Phil. Mag.* **42**, 952 (1951).

[4] H. T. Richards, *Phys. Rev.* **59**, 796 (1941).

[5] L. L. Green and W. M. Gibson, *Proc. Phys. Soc. (London)* **62A**, 407 (1949).

[6] B. Trumpy, T. Grotdal, and A. Graue, *Nature* **170**, 1118 (1952).

[7] J. Catala, J. Aguilor, and F. Busquets, *Anales real soc. espan. fis. y quim. (Madrid)* **49A**, 131 (1953).

[8] E. K. Inall and A. J. F. Boyle, *Phil. Mag.* **44**, 1081 (1953).

[9] F. E. Steigert and M. B. Sampson, *Phys. Rev.* **92**, 660 (1953).

[10] W. K. Jentschke, private communication.

[11] C. C. Trail and C. H. Johnson, *Phys. Rev.* **95**, 1363 (1954).

[12] P. B. Treacy, *Phil. Mag.* **44**, 325 (1953).

[13] R. Malm and D. R. Inglis, *Phys. Rev.* **92**, 1326 (1953).

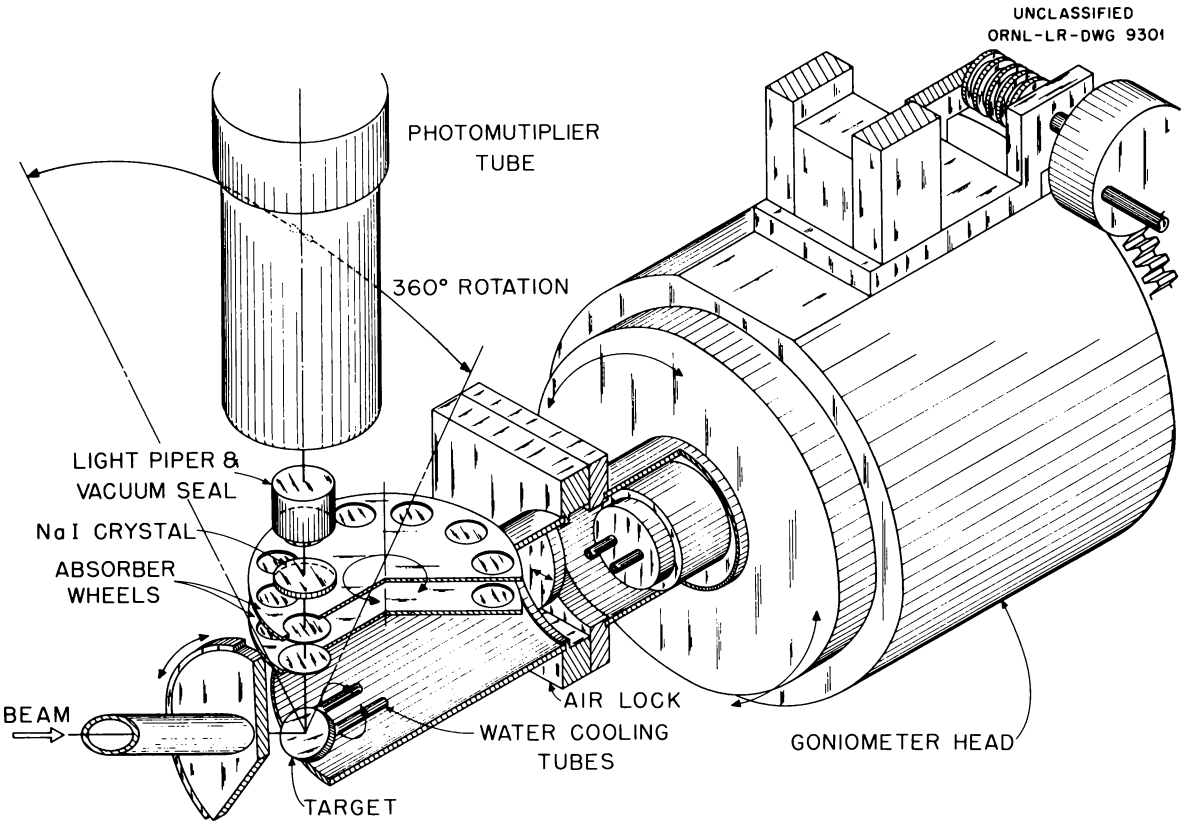

Fig. 1. NaI Charged-Particle Spectrometer.

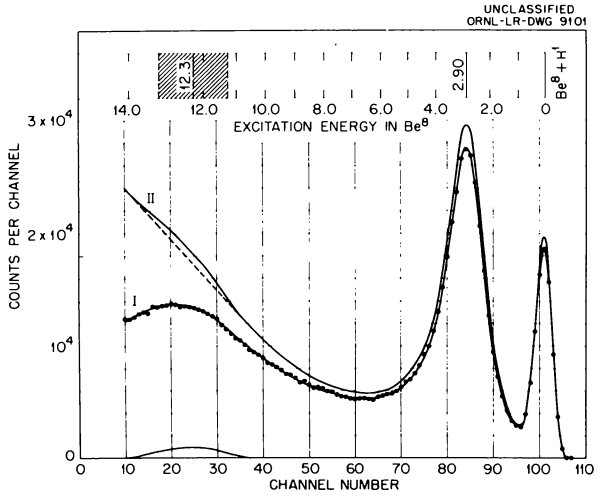

Fig. 2. (I) Pulse-Height Spectrum in NaI for the Reaction $Li^6 + He^3 \rightarrow Be^8 + H^1$ Taken at 45 deg with Respect to the Incident Beam. Bombarding energy, 1.25 Mev; aluminum absorber, 22.14 mg/cm^2. **(II) Data Normalized to Unit Energy Interval Instead of Unit Pulse-Height Interval and Plotted to Arbitrary Scale.**

At 45 deg, the center-of-mass motion increases the energy available, and several extra runs were made at this angle. An aluminum absorber was selected which would screen out the most energetic alpha particles arising in the reaction. The data for 45 deg are shown in Fig. 2, along with the curve derived by normalization to unit energy interval rather than unit pulse-height interval. In addition to the monotonic rise toward low pulse height attributable to $Li^6(He^3,p\alpha)\alpha$, there is some indication of a broad peak in the curve in this region. The broad level which appears to exist at 12.3 Mev in Be^8 may be removed by constructing a fictitious range-energy relation for aluminum which would straighten out the upper curve in this region. This was done and it was found that the new normalization curve would indicate errors in the dE/dx values for aluminum in excess of 20%. Since these values are believed to be known far more accurately than this, it is concluded that the data give tentative evidence for a broad level in Be^8 at 12.3 Mev. Recent work on alpha-alpha

scattering by Jentschke[10] at the University of Illinois has indicated a level in Be^8 at 12.5 Mev.

The $Li^6(He^3,p)Be^8$ reaction has been carefully examined for levels in the range 0 to 14 Mev. The ground state, the 2.9-Mev state, and, tentatively, a 12.3-Mev state have been found. No other levels were observed, and it is believed that a sharp level 1% as intense as the ground-state transition would have been observed had such a level existed.

THE $Si^{28}(p,p'\gamma)Si^{28}$ REACTION

J. K. Bair J. D. Kington
H. O. Cohn H. B. Willard

Inelastic scattering of protons by Si^{28} has been studied by detection of the 1.78-Mev gamma ray emitted from the first excited state.[1] Figure 1 shows the relative yield of this gamma ray obtained from a 3- to 5-Mev bombarding proton energy. The gamma ray was detected with a 3 × 3 in. NaI crystal located at 0 deg and 20 cm with respect to the beam striking a SiO_2 target 2 kev thick at 3 Mev. A later run, with points spaced less than 1 kev apart, revealed four additional, very narrow low-intensity resonances at 3.88, 3.93, 3.97, and 4.93 Mev. No resonances were observed in the region of 1.8 to 3.0 Mev (20-kev steps).

[1] H. B. Willard *et al.*, *Phys. Semiann. Prog. Rep. March 20, 1955*, ORNL-1879, p 15.

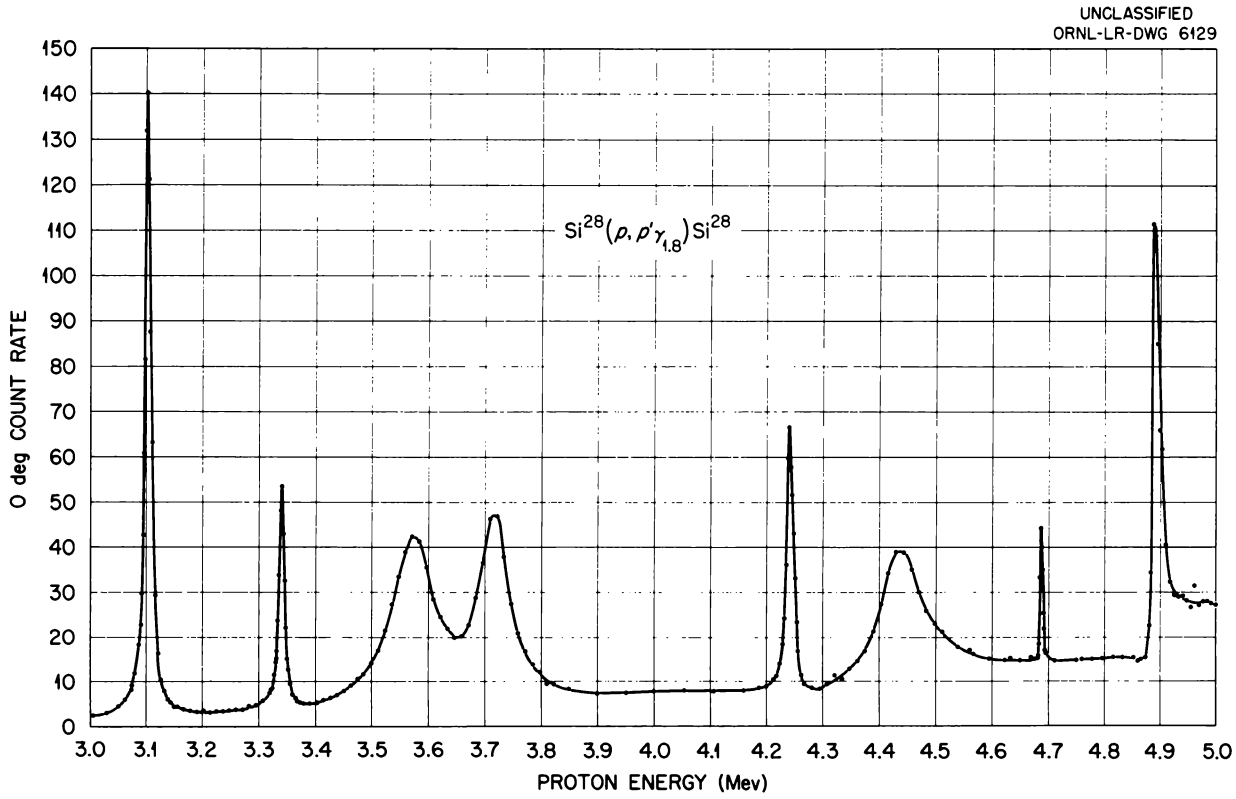

Fig. 1. Relative Yield at $\theta = 0$ deg of the 1.78-Mev Gamma Ray Emitted in the Inelastic Scattering of Protons on Si^{28} from a 3- to 5-Mev Bombarding Energy.

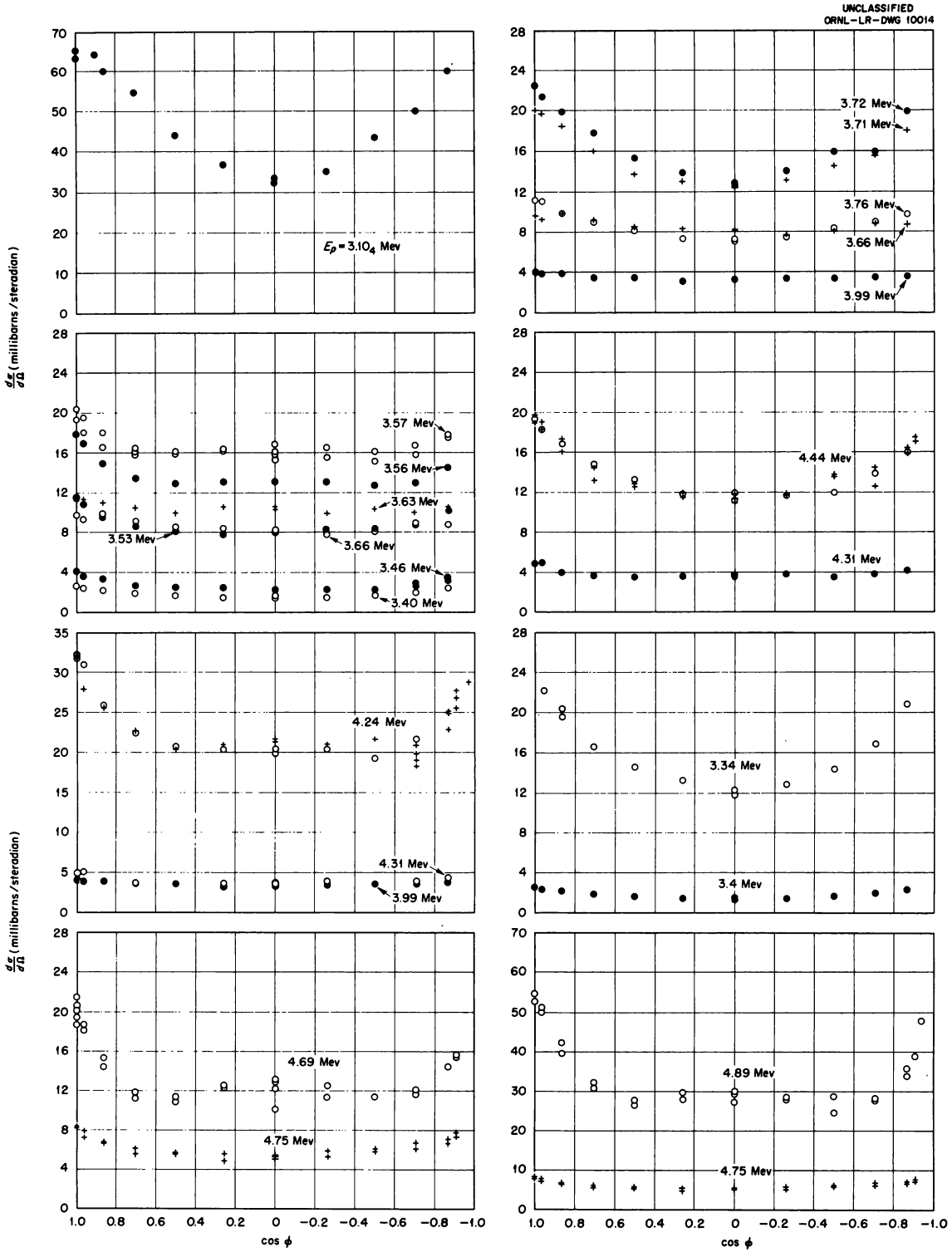

Fig. 2. Angular Correlations with Respect to the Incoming Proton of the 1.78-Mev Gamma Ray Emitted in the $Si^{28}(p,p'\gamma)Si^{28}$ Reaction at Selected Bombarding Energies.

Two different methods were used to determine the absolute zero degree differential cross section of this reaction at the peak of the 3.10-Mev resonance. The thickness of a thin target was measured by weighing before and after the evaporation of silicon metal. The value of 20 $\mu g/cm^2$ was checked by comparison of the yield relative to a thick silicon-metal target:

$$\frac{Y_{max}(\Delta E)}{Y_{max}(\infty)} = \frac{2}{\pi} \tan^{-1} \frac{\Delta E}{\Gamma} .$$

The thick-target yield can also be related to the cross section by using known values of the stopping cross section. An average value obtained was $\sigma_{pp'}$ (0 deg, 3.10 Mev) = 64 ± 12 millibarns/steradian.

Angular distributions of the gamma rays were measured at and in between all eight main resonances, with the crystal located about 50 cm from the target. Results are shown in Fig. 2, normalized to the 0 deg cross section at 3.10 Mev.

PROTON BOMBARDMENT OF Be^9

J. D. Kington
J. K. Bair
H. O. Cohn
H. B. Willard

Proton capture gamma rays, from a Be^9 target 7 kev thick at 1 Mev, were detected with a 3 × 3 in. NaI crystal located at 90 deg with respect to the beam and 2 in. (front face) from the target. Pulses were amplified and recorded by a 20-channel pulse-height analyzer.[1] The sum of all gamma-ray pulses of energy greater than 1.5 Mev is plotted in the lower part of Fig. 1. Known levels[2] at E_p = 0.998 and 1.087 Mev were observed, but, with the exception of a possible broad level tailing off from 1.15 to 1.55 Mev, no new levels were found[3] up to 2.058 Mev, the $Be^9(p,n)B^9$ reaction threshold. Measurements were not extended above this energy in order to prevent neutron activation in the crystal. A similar run at 0 deg displayed the same features.

Gamma rays of 3.57 Mev from the $Be^9(p,\alpha\gamma)Li^6$ reaction were detected with a 1½ × 2 in. NaI crystal biased to count all the gamma-ray pulses with energies between 1.9 and 3.9 Mev. The crystal was mounted at 90°deg and 12 in. (front face) from the target. As shown in the upper part of Fig. 1, only the previously observed resonance[4] at E_p = 2.57 Mev and Γ = 40 kev appears between the 1.6- and 2.8-Mev bombarding energy.

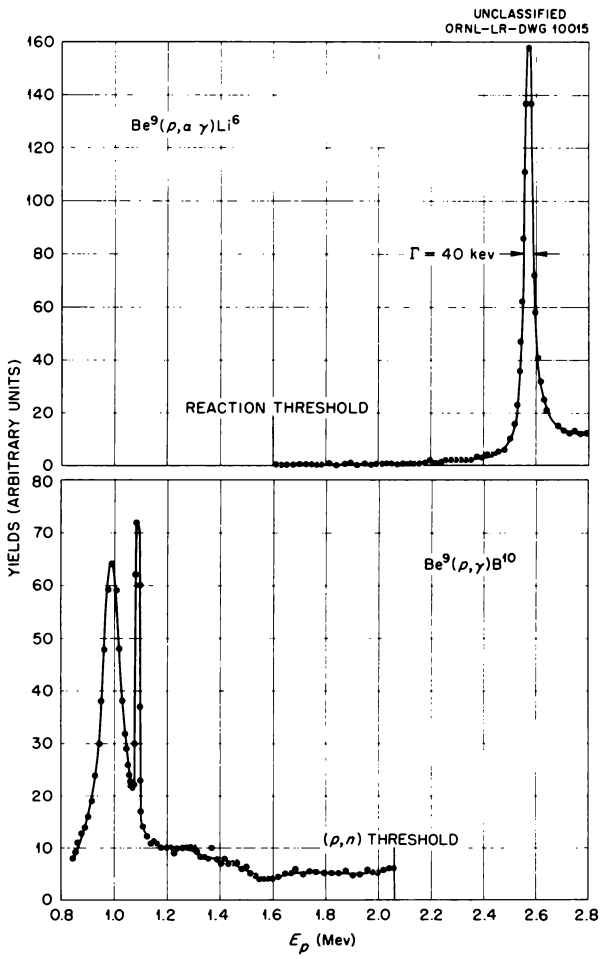

Fig. 1. The $Be^9(p,\gamma)B^{10}$ Yield at θ = 90 deg (Lower Curve) and the $Be^9(p,\alpha\gamma)Li^6$ Yield of 3.57-Mev Gamma Rays at θ = 90 deg (Upper Curve).

[1] G. G. Kelley, P. R. Bell, and C. G. Goss, *Phys. Quar. Prog. Rep. Dec. 20, 1951*, ORNL-1278, p 27.

[2] F. Ajzenberg and T. Lauritsen, *Revs. Mod. Phys.* **27**, 77 (1955).

[3] H. T. Richards, R. V. Smith, and C. P. Browne, *Phys. Rev.* **80**, 524 (1950).

[4] T. M. Hahn *et al.*, *Phys. Rev.* **85**, 934 (1952).

PROTON ENERGY RESOLUTION OF THE ORNL 2.5-Mv VAN DE GRAAFF

J. H. Gibbons

The energy resolution of protons from the ORNL 2.5-Mv Van de Graaff has been investigated by a study of the gamma-ray yield at the 993.3-kev resonance in the reaction $Al^{27}(p,\gamma)Si^{28}$. Proton-beam control slits were 3 ft from the 90-deg deflection magnet, and the target was 15 ft from the control slits. The control-slit opening used was 0.050 in. A $\frac{1}{2} \times \frac{1}{2}$ in. slit was placed about 3 ft from the target to ensure proper current integration.

Van de Graaff energies were monitered and controlled by a proton resonance fluxmeter, calibrated with an $Li^7(p,n)Be^7$ threshold measurement. Proton current on the target was about 25 μa.

The observed yield curve is shown in Fig. 1. The energy difference between one-fourth and three-fourths of the increase in yield due to the resonance is 240 ev. Since the true resonance width[1] is about 100 ev and the Doppler effect (due to thermal motion of target atoms) is 140 ev, the value of 240 ev represents only an upper limit to the proton energy spread. If one assumes the observed width to be the square root of the sum of the squares of the various contributing effects, one obtains a value of 170 ev for the proton spread.

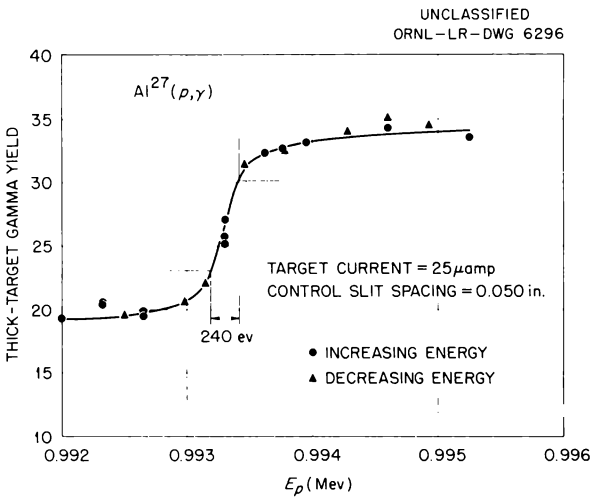

Fig. 1. $Al^{27}(p,\gamma)$ Yield from a Thick Target.

[1] R. S. Bender *et al.*, *Phys. Rev.* **76**, 273 (1949).

CROSS SECTION FOR THE $H^3(d,n)He^4$ REACTION FROM 1 TO 5 Mev

A. Galonsky C. H. Johnson

Monoenergetic deuterons from the 5.5-Mv Van de Graaff accelerator were used to bombard a tritium-filled gas cell, and neutrons produced in the $H^3(d,n)He^4$ reaction were detected with a telescope-type neutron spectrometer.[1]

The incident beam was collimated so that the number of deuterons could be accurately measured with a current integrator. A sample of tritium was obtained for mass analysis[2] when the cell was filled so that the number of tritium atoms per square centimeter could be determined from the length and pressure in the gas cell. A well-defined group of monoenergetic neutrons was observed with the neutron spectrometer. The absolute neutron flux was found from the number of counts, the detecting geometry, the number of hydrogen atoms in the radiator, and the n-p scattering cross section[3] near 0 deg.

With both a target thickness and deuteron energy increment of 50 to 100 kev, the cross section near 0 deg was measured from 1 to 5 Mev. Figure 1 shows the measurements in the center-of-mass system. Smooth curves are drawn for both the center-of-mass and the laboratory systems.

At 2.20 Mev, the differential cross section was measured at 15-deg intervals from 0 to 150 deg and was compared with the alpha-particle detection

[1] C. C. Trail and C. H. Johnson, *Phys. Semiann. Prog. Rep. Sept. 10, 1954*, ORNL-1798, p 8.

[2] Mass spectroscopic analysis was made by C. E. Melton of the Stable Isotope Research and Production Division.

[3] J. L. Fowler and J. E. Brolley, Jr., *Revs. Mod. Phys.* (to be published).

measurements of Stratton and Freier.[4] The agreement is within experimental error, although the present cross sections are about 7% lower than those of Stratton and Freier.

In the early stages of the experiment, angular distributions were also obtained at E_d = 1.53, 2.20, 3.05, 3.97, 4.98, and 5.79 Mev, but because of faulty current integration there was an error in the cross sections, which increased from 15% at 1.53 Mev to 33% at 4.98 Mev. These measurements were normalized at 6 deg to the absolute cross section from Fig. 1 and are presented as open symbols in Fig. 2. Since the maximum energy attained for the absolute measurement was only 5 Mev, the correct cross section at 5.79 Mev was obtained from the data with faulty current integration by extrapolating the error to 41%. The absolute measurements at 2.20 Mev are presented as solid circles.

Figure 3 presents smoothed curves of these distributions in the laboratory system. The integrated total cross sections at these six energies

[4] T. F. Stratton and G. D. Freier, *Phys. Rev.* **88**, 261 (1952).

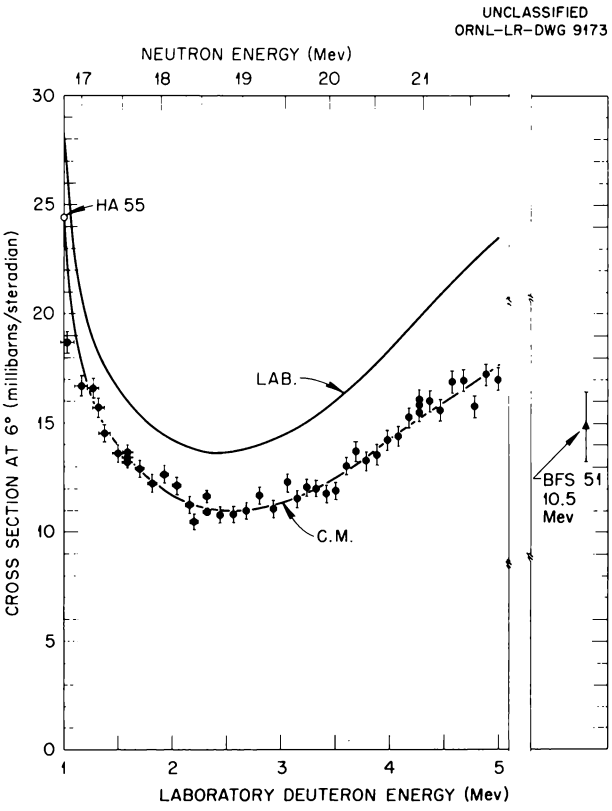

Fig. 1. Energy Dependence of the $H^3(d,n)He^4$ Differential Cross Section at 6 deg. The point at 10.5 Mev is taken from ref. 5 and the one at 1.0 Mev from A. Hemmendinger and H. V. Argon, *Phys. Rev.* **98**, 70 (1955). On the solid circles, which are the data of this experiment, only the statistical uncertainty in the cross section and the total thickness of the tritium target are indicated. The curve for the laboratory cross section was obtained by transformation of the curve drawn through the center-of-mass cross-section points.

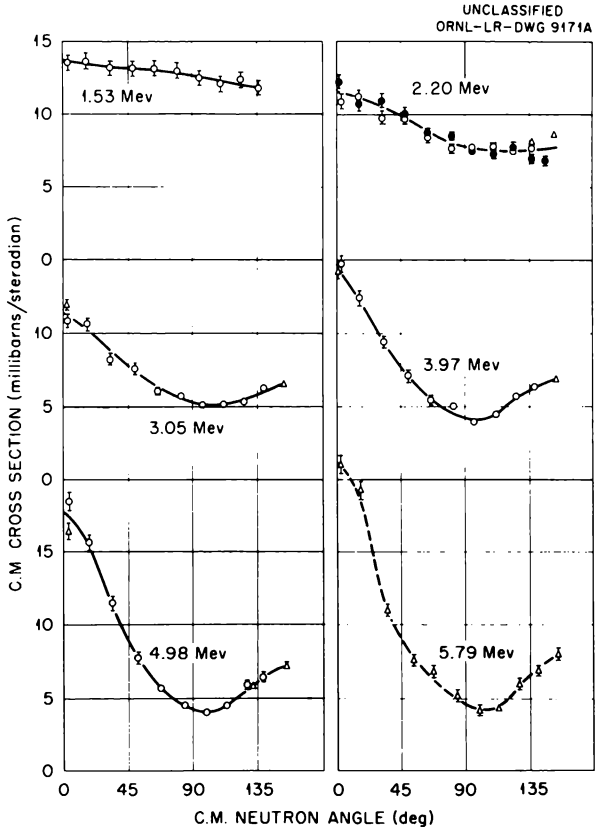

Fig. 2. $H^3(d,n)He^4$ Angular Distributions in the Center-of-Mass System. Energies indicated are the laboratory deuteron energies. For each point only the statistical uncertainty is indicated. The distance from the tritium target to the $(CH_2)_n$ radiator was 7.0 cm for the open circles, 9.4 cm for the open triangles, and 9.7 cm for the solid circles. The solid circles were obtained three months after the other points, with an improved tritium gas target. The absolute value of the cross section at 5.79 Mev is less certain than at the other energies.

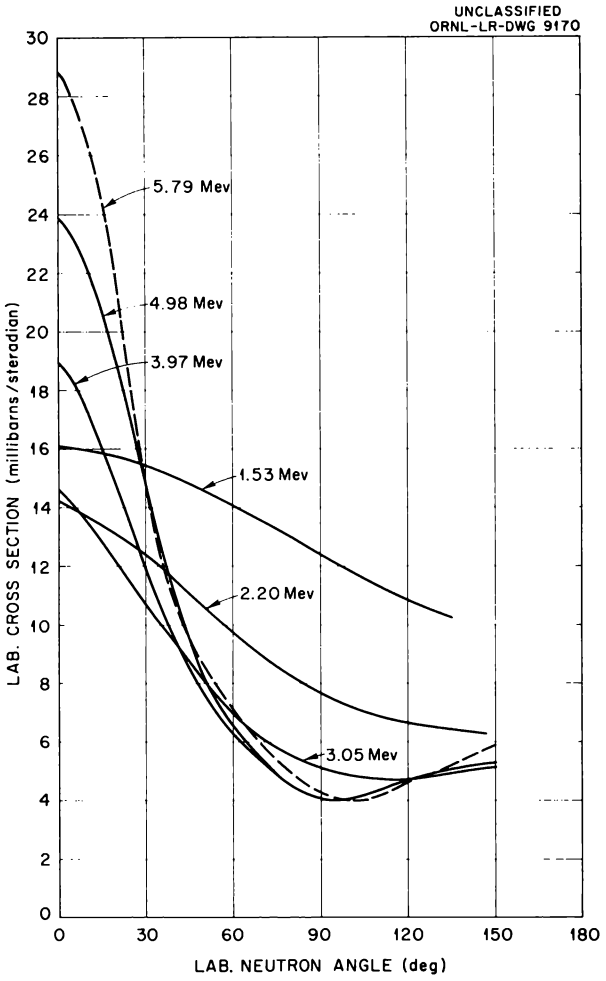

Fig. 3. $H^3(d,n)He^4$ Angular Distributions in the Laboratory System. Energies indicated are the laboratory deuteron energies. The curves were obtained by transformation of the center-of-mass curves of Fig. 2. The absolute value of the cross section at 5.79 Mev is less certain that at the other energies.

are shown in Fig. 4. The cross section decreases from the well-known resonance at 107 kev to a minimum at 3.5 Mev and increases slightly beyond 3.5 Mev. Since it decreases[5] to 48 millibarns at 10.5 Mev, these measurements may indicate a resonance between 5 and 10 Mev or an interesting energy dependence of stripping.

[5] J. E. Brolley, Jr., J. L. Fowler, and E. J. Stovall, Jr., *Phys. Rev.* **82**, 502 (1951).

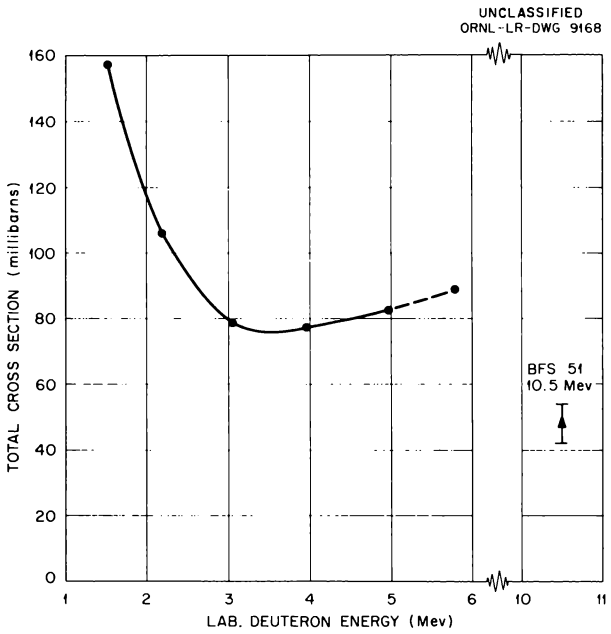

Fig. 4. Energy Dependence of the $H^3(d,n)He^4$ Total Cross Section. The point at 5.79 Mev is less accurate than the points from 1.53 to 4.98 Mev. The point at 10.5 Mev is taken from ref. 5.

A STUDY OF THE $V^{51}(p,n)Cr^{51}$ REACTION

J. H. Gibbons R. L. Macklin
H. W. Schmitt

Studies of neutrons from the reaction $V^{51}(p,n)Cr^{51}$ have been made by using protons from the ORNL 2.5-Mv Van de Graaff. The neutron detector used in relative yield measurements was a set of three paraffin-moderated BF_3 counters grouped in a hemispherical array about the vanadium target. Assuming the $Li^7(p,n)Be^7$ threshold to be 1.8816 Mev, the $V^{51}(p,n)Cr^{51}$ threshold was found to be 1.5656 ± 0.0015 Mev, in agreement with earlier work.[1,2]

Many resonances were observed (Fig. 1) at neutron energies up to 120 kev above threshold. The observed average level spacing in this region is less than 2 kev. The Cr^{52} exitation energy was about 12.4 Mev. Observed level widths represent, in all cases, the estimated instrumental width due to target thickness (~1 kev) and proton energy spread (~250 ev). Yields at some of the more intense peaks were 100 to 500 neutrons per steradian per microcoulomb.

[1] P. H. Stelson, W. M. Preston, and C. Goodman, *Phys. Rev.* **80**, 287 (1950).

[2] R. V. Smith and H. T. Richards, *Phys. Rev.* **74**, 1257 (1948).

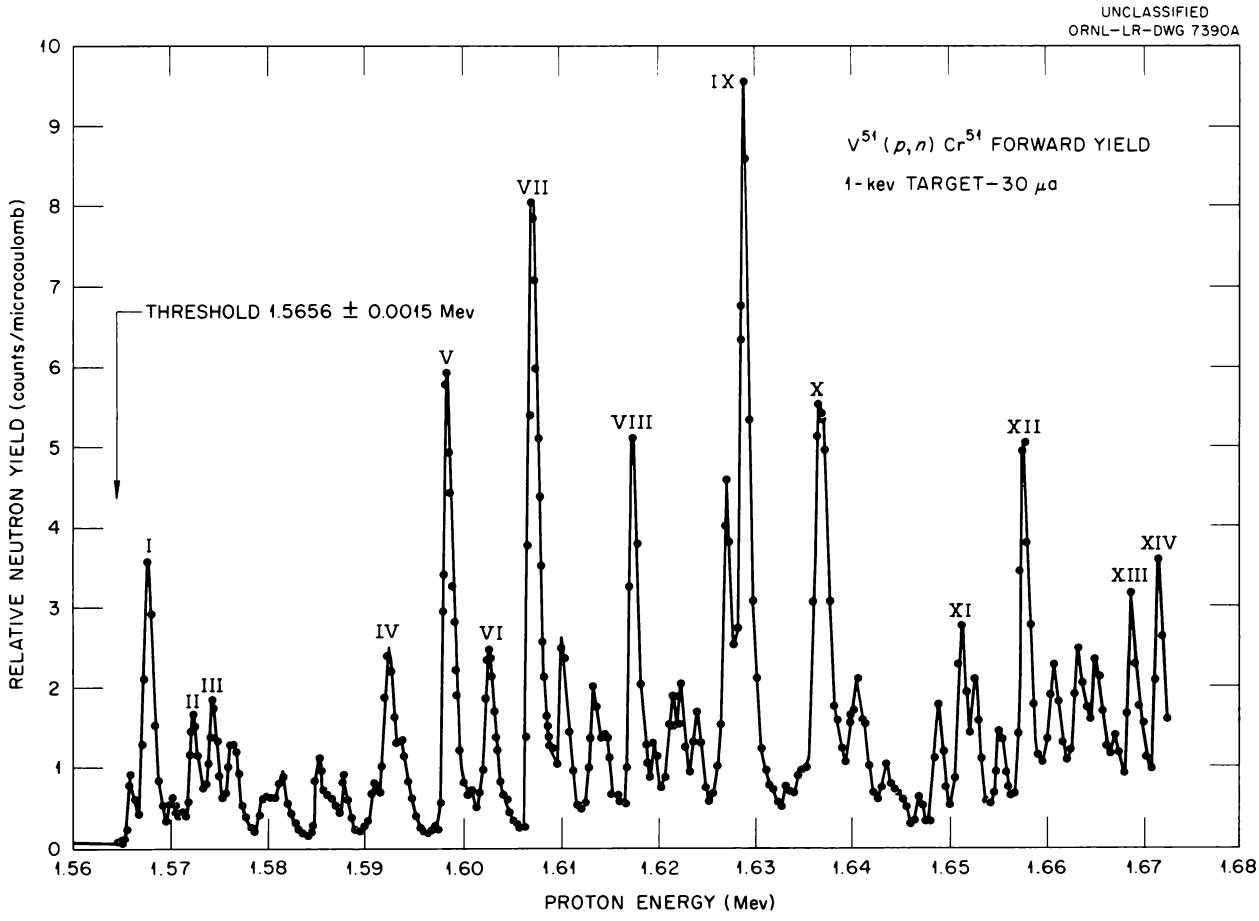

Fig. 1. Relative Neutron Yield vs Proton Energy in the Reaction $V^{51}(p,n)Cr^{51}$.

Neutron angular distributions at 11 of the more intense peaks were measured in the forward hemisphere with a small high-pressure BF_3 counter. Two showed significant departure from center-of-mass isotropy. The two anisotropic distributions (Fig. 2) are consistent with $J = 4$ levels in the compound nucleus Cr^{52}, with $l = 1$ for both the proton and the neutron.

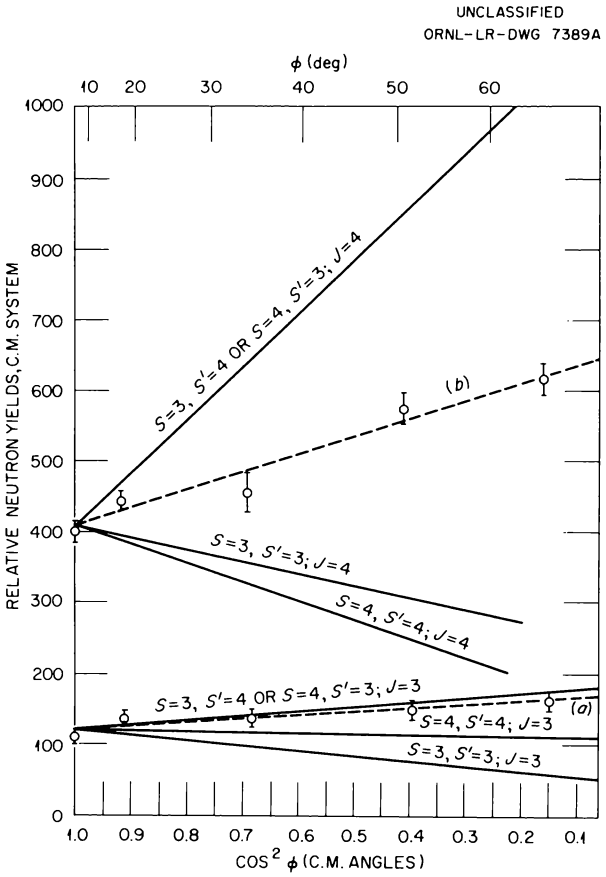

Fig. 2. Neutron Angular Distributions. Solid lines are calculated from channel spin formalism. Curve *a* corresponds to peak IV in Fig. 1 and curve *b* to peak V.

FISSION CROSS SECTION OF U^{233} FROM 4 TO 150 kev

R. W. Lamphere

The fission cross section of U^{233} has been measured relative to U^{235} over the energy range 3.4 to 150 kev by use of neutrons produced by bombarding a 5-kev thick target of vanadium with a 70-μa beam of protons from the ORNL 2-Mv Van de Graaff. Data are listed in Table 1.

The figures in the last column were obtained by using the U^{235} fission cross section found by Yeater *et al.*[1] for energies up to 40 kev. The last seven values were found by using the U^{235} cross-section curve given in BNL-250.[2] The accuracy of the U^{233} cross section is determined principally by the accuracy to which the U^{235} is known. The probable error of the ratios, $\sigma_f(23)/\sigma_f(25)$, depends only on this experiment and is estimated to be within 5%. The last point tallies with results obtained several months ago at this Laboratory, when the ratio of the fission cross section was measured from 150 kev to 4.0 Mev by using neutrons from the Li(p,n) and $H^3(p,n)$ reactions. All errors are standard deviations. Those given in column 4 are counting errors only but do include the uncertainties arising from the background correction.

TABLE 1. FISSION CROSS SECTION OF U^{233} RELATIVE TO U^{235}

E_n	$\frac{\sigma_f(23)}{\sigma_f(25)}$	ΔE_n	Statistical Counting Error	$\sigma_f(23)$
3.44	1.40	3.2	1.6	7.8
12.8	1.41	5.5	2.2	4.9
26.0	1.38	3.8	3.1	3.3
33.3	1.43	4.3	2.7	3.1
39.6	1.36	3.3	3.0	3.0
49.1	1.39	3.5	2.9	2.9
60.0	1.37	6.1	2.9	2.8
71.8	1.42	4.6	2.3	2.7
96.0	1.36	6.2	2.8	2.4
114.5	1.40	5.3	3.0	2.4
128.5	1.45	5.6	2.2	2.4
151.9	1.50	6.2	3.0	2.4

The third column gives the estimated total energy spread in the neutron beam incident on the foils. This spread results from two causes: variation of neutron energy with angle, and peaks in the $V^{51}(p,n)Cr^{51}$ neutron yield. This yield curve has been carefully measured by Macklin, Gibbons, and Schmitt, of this Laboratory, by use of a 1-kev-thick vanadium target and is to be published soon in *The Physical Review.* Since the levels are quite sharp, neutron energy spread from this source will depend on how many levels are bridged by the target thickness. This was determined by use of the data taken by Macklin and co-workers, who loaned the author a preprint of their results.

The precision uranium foils were prepared by R. E. Greene, of the K-25 Plant.

[1] M. L. Yeater *et al.*, *A High-Resolution Measurement of the Fission Cross Section of U^{235} in the Energy Range 1 to 40 kev Using the GE Betatron Velocity Selector*, KAPL-1109 (June 4, 1954).

[2] M. D. Goldberg *et al.*, *Neutron Cross Sections*, BNL-250 (Aug. 1, 1954).

NEUTRON ABSORPTION CROSS SECTIONS OF U^{235} AND Pu^{239} IN THE 5- TO 50-kev ENERGY RANGE

R. L. Macklin H. W. Schmitt J. H. Gibbons

The spherical-shell transmission method has been used many years for measurements of the inelastic cross section with fast neutrons.[1-3] The inelastic cross section measured is the sum of the absorption cross section and part of the inelastic cross section, where the latter depends on the energy threshold of the neutron detector used. With a flat-response detector, only the absorption cross section is measured.

In a measurement of the neutron absorption cross section for fissionable materials in the 5- to 50-kev energy range, a detector of high response to these neutrons and of zero or very low response to fission neutrons is required. The $I^{127}(n,\gamma)I^{128}$ reaction is an approach to such a detector. Since the sodium cross section is low compared with the iodine cross section in the entire energy range of interest (5 kev to several Mev) and since the sodium activity is long-lived compared with the iodine activity, a sodium iodide crystal was used, and the 25-min β^- activity of I^{128} was measured after an irradiation. Irradiations were made with a U^{235} shell, a Pu^{239} shell, and a U^{238} shell surrounding the crystal.

The neutron yield from the $V^{51}(p,n)Cr^{51}$ reaction used as the neutron source was quite low, hence close spacing of the experimental components was required (see Fig. 1). Because of appreciable scattering of source neutrons from the shell into the paraffin-moderated BF_3 monitor counters, standard shell-on, shell-off measurements could not be used, and all transmissions were measured relative to U^{238}, thus minimizing this effect.

At each of the six energies used in these measurements, the transmission of the U^{238} shell was computed from known total and absorption cross sections. By use of these results, the transmissions of the U^{235} and Pu^{239} shells at corresponding energies were determined. An analysis similar to that used by Beyster and Carter[4] was carried out to determine the absorption cross sections. These results are summarized in Table 1.

TABLE 1. ABSORPTION CROSS SECTIONS OF U^{235} AND Pu^{239}

E_n	σ_a(U-235)	σ_a(Pu-239)
4.4 ± 0.4	5.5 ± 0.5	4.4 ± 0.6
11.8 ± 0.5	4.1 ± 0.4	3.2 ± 0.5
33.1 ± 0.4	2.7 ± 0.4	1.7 ± 0.5
39.6 ± 0.5	3.0 ± 0.4	2.2 ± 0.5
44.0 ± 0.5	2.7 ± 0.4	2.4 ± 0.5
48.8 ± 0.5	2.9 ± 0.4	2.5 ± 0.5

The rather large uncertainties in these values arise from the following considerations:

1. The close juxtaposition of the experimental components and the use of a cylindrical crystal that is large compared with the inside cavity of the shell give rise to appreciable obliquity and geometric corrections which can only be approximated.
2. The ratio of the $I^{127}(n,\gamma)$ cross section for fission neutrons to that for the source neutrons enters directly in a correction term, and, since the ratio is experimentally not well known, a corresponding uncertainty is introduced in the results.
3. Uncertainties in the U^{235} and Pu^{239} fission cross sections enter in the same manner as the uncertainty in iodine sensitivity discussed in (2).
4. In the analysis it is assumed that the total cross section of the fissionable material is known, but, since it is known to within 5% at best, a corresponding uncertainty is introduced in the present results.
5. The uncertainties in the experimental measurements themselves, as judged from the consistency and reproducibility of the data, amount to about 2% of the transmission, and this is included in the uncertainty of the final result.

[1] D. D. Phillips, *Inelastic Collision Cross Sections of Various Elements for 14 Mev Neutrons*, AECU-404 (April 1, 1949).

[2] J. R. Beyster, Second Pittsburgh Conference on Medium Energy Nuclear Physics (unpublished).

[3] H. A. Bethe, Second Pittsburgh Conference on Medium Energy Nuclear Physics (unpublished).

[4] J. R. Beyster and R. E. Carter, LA-1429 (unpublished).

UNCLASSIFIED
ORNL-LR-DWG 5678A

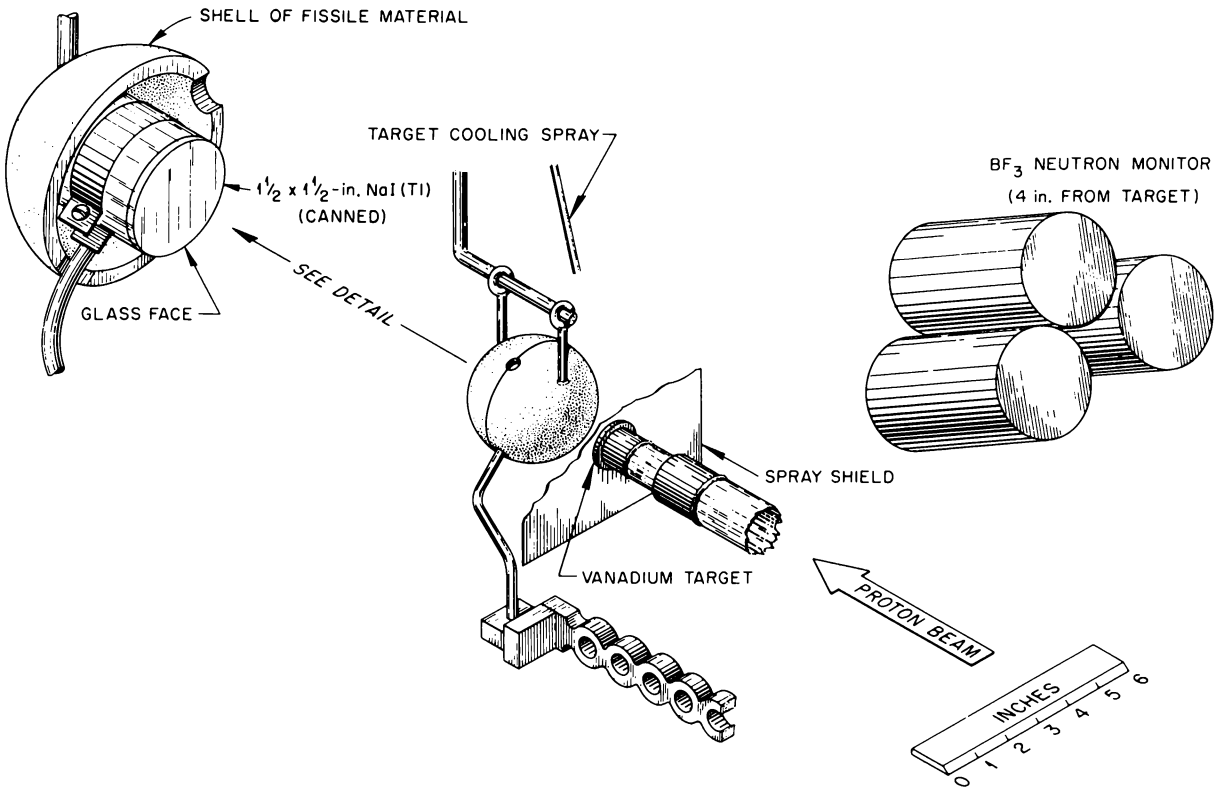

Fig. 1. Experimental Arrangement for Determining Neutron Absorption Cross Sections in the 5- to 50-kev Energy Range.

CYLINDER ACTIVATION AND SOLID ANGLE

A. V. H. Masket H. W. Schmitt R. L. Macklin

In the course of the analysis of the spherical-shell transmission work reported in the previous paper, the activation of the cylindrical NaI(Tl) detectors used was desired. This consists of finding the activation A from an external point source of strength Q (neutrons per second), neglecting self-absorption. The general formula is

$$(1) \qquad A = \frac{Q\Sigma}{4\pi}\int\frac{dV}{R^2},$$

where Σ is the macroscopic absorption cross section, dV a volume element, and R the distance from Q to the volume element. In cylindrical coordinates (ρ, θ, Z) with the origin at the center of the base of the cylinder and with Z along its axis,

$$(2) \quad A = \frac{Q\Sigma}{4\pi}\int_0^L\int_0^{2\pi}\int_0^a \frac{\rho\, d\rho\, d\theta\, dZ}{Z^2+\rho^2+D^2-2\rho D\cos\theta},$$

where a and L are respectively the radius and height of the cylinder, and D is the distance of the source from the origin. Equation 2 can be

integrated over ρ and θ to give the single integral

$$(3) \qquad A = \frac{Q\Sigma}{4} \int_0^L dZ \ln \frac{a^2 + Z^2 - D^2 + \sqrt{(a^2 + Z^2 - D^2)^2 + 2Z^2D^2}}{2Z^2} .$$

This integral was evaluated on the Oracle as a function of D and L. The activation of any cylinder from any point can be obtained by the addition or subtraction of values computed from Eq. 3

The solid angle subtended by the cylinder from an external point has been obtained as a special case of a new and quite powerful method of computing solid angles. The use of a line integral representation avoids the traditional expansion in spherical harmonics, with attendant limitations on geometry and questions of convergence. The general formula derived is

$$(4) \quad \Omega_C = - \oint_{C'} \cos\theta \, d\phi = - \oint_{C'} \phi \sin\theta \, d\theta \ ,$$

where C' is a deformation which is made so that the outline C does not touch or encircle the polar axis over the path of integration.

In the case of a circular disk of unit radius viewed from a point Z units from the plane of the disk and ρ units from the axis,

$$(5) \quad \begin{cases} \Omega = 2\pi - 2Z \int_0^{\pi} (Z^2 + S_1^2)^{-1/2} \, d\phi, & \rho < 1, \\ \Omega = \pi - 2Z \int_0^{\pi/2} (Z^2 + S^2)^{-1/2} \, d\phi, & \rho = 1, \\ \Omega = 2Z \int_0^{\arcsin(1/\rho)} [|(Z^2 + S_2^2)^{-1/2}| - |(Z^2 + S_1^2)^{-1/2}|] \, d\phi, & \rho > 1, \end{cases}$$

where

$$S = 2\cos\phi \ ,$$
$$S_1 = \rho\cos\phi + |(1 - \rho^2 \sin^2\phi)^{1/2}| \ ,$$
$$S_2 = \rho\cos\phi - |(1 - \rho^2 \sin^2\phi)^{1/2}| \ .$$

For the lateral surface of a right circular cylinder of unit radius and height H viewed from a point in the base plane ρ units ($\rho > 1$) from the cylinder axis,

$$(6) \quad \Omega = 2H \int_0^{\arcsin(1/\rho)} (H^2 + S_2^2)^{-1/2} \, d\phi \ .$$

From values computed from Eqs. 5 and 6 one can readily find by addition and subtraction the solid angle subtended by any right circular cylinder at any point.

ANGULAR DISTRIBUTION OF NEUTRONS ELASTICALLY SCATTERED FROM FLUORINE AT 0.66, 1.05, 1.45, 2.15, AND 2.92 Mev

J. E. Wills, Jr.

Angular distributions of neutrons elastically scattered from F^{19} have been measured in an attempt to determine potential scattering phase shifts in the $F^{19}(n,n)F^{19}$ reaction. The neutron energies chosen for the study were between resonances in the neutron total cross section. Unfortunately, due to the close spacing of the levels in F^{20}, the angular distributions may not be free from interference from nearby resonances.

Neutrons were scattered from cylindrical samples of Teflon (C_nF_{2n}) and carbon, in an experimental arrangement similar to one previously described.[1] They were detected by means of a propane-filled gas counter, which was rotated about an axis perpendicular to the direction of the neutron beam.

[1] H. B. Willard, J. K. Bair, and J. D. Kington, *Phys. Rev.* **98**, 669 (1955).

The neutron source was an $H^3(p,n)He^3$ reaction. The gas target thickness was about 20 kev at the highest energy and about 45 kev at the lowest energy. Protons for the reaction were supplied by the ORNL 5.5-Mv Van de Graaff generator.

Corrections for the attenuation of the neutrons in the sample were made in the differential cross sections for both Teflon and carbon. A rough calculation of the multiple scattering in the samples showed the scattering to be small in all cases. This correction was not made in the curves shown. The differential cross section of fluorine was obtained by subtracting the cross section of carbon from that of Teflon.

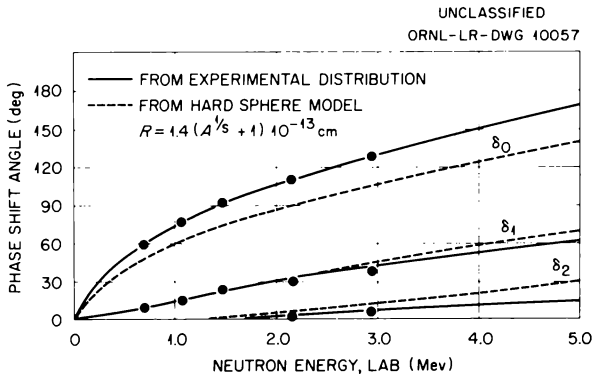

Fig. 1. Potential Scattering Phase Shifts for Neutrons Scattered from Fluorine.

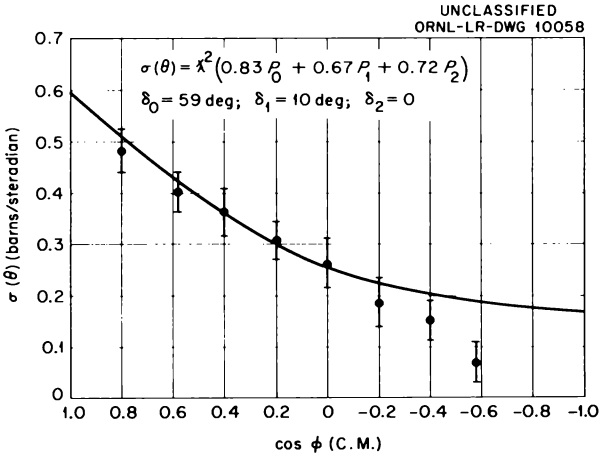

Fig. 2. Angular Distribution of Fluorine at 0.66 Mev.

The angular distributions were fitted by assuming all the scattering to be potential. Phase shifts were assumed which would give the curves shown in the figures. The *s*-wave scattering phase shifts required were in all cases larger than those expected from the scattering of a hard sphere of reasonable radius [$R = 1.4(A^{1/3} + 1)\ 10^{-13}$ cm]. The *p*-wave phase shifts were roughly the same as those from the hard sphere, while the *d*-wave phase shifts were somewhat smaller, as shown in Fig. 1. The distributions are shown in Figs. 2 through 6; the indicated errors are statistical.

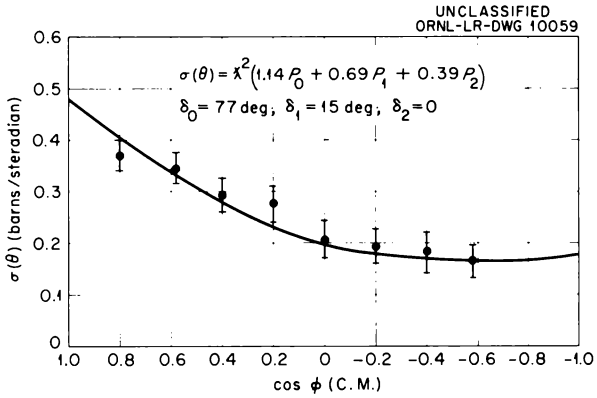

Fig. 3. Angular Distribution of Fluorine at 1.05 Mev.

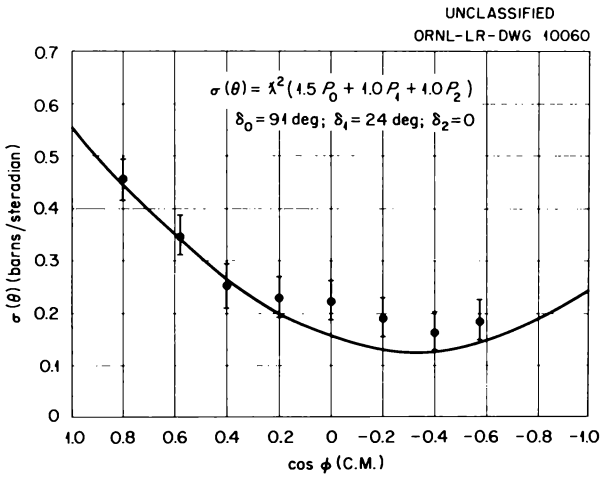

Fig. 4. Angular Distribution of Fluorine at 1.45 Mev.

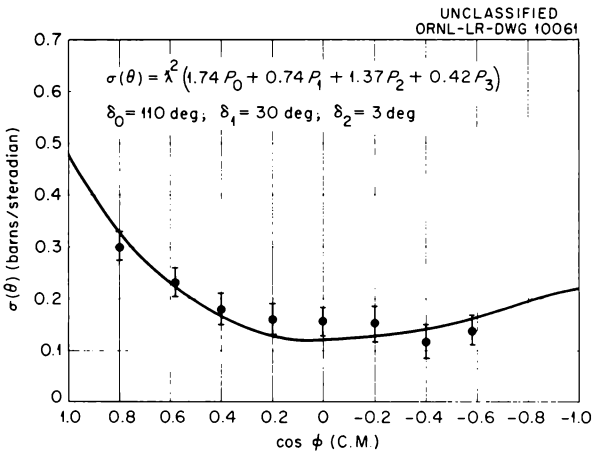

Fig. 5. Angular Distribution of Fluorine at 2.15 Mev.

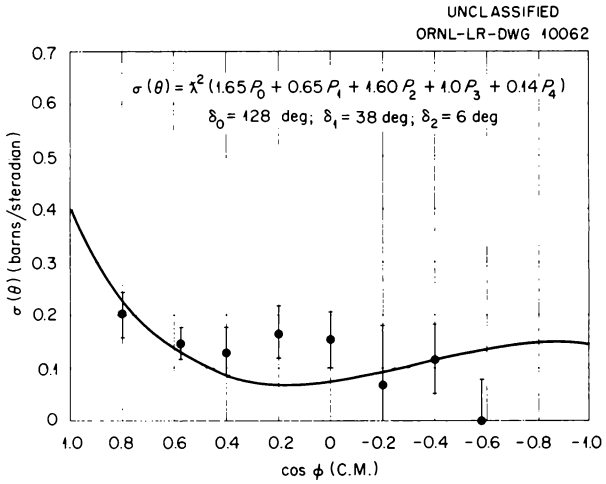

Fig. 6. Angular Distribution of Fluorine at 2.92 Mev.

DIFFERENTIAL ELASTIC SCATTERING OF NEUTRONS FROM NEON

H. O. Cohn J. L. Fowler

A method has been developed for determining the absolute differential elastic cross section for scattering of neutrons from nuclei in a gaseous form. The gas was contained in a proportional counter (Fig. 1) upon which neutrons were incident, and scattered neutrons were detected by an anthracene crystal together with a photomultiplier. Real coincidence between proton recoils in the anthracene crystal and nuclei recoils in the proportional counter gave a measure of the scattering cross section. The direct neutrons from the region of the anthracene crystal were removed with LiF-impregnated paraffin shields. Coincidences due to gamma rays produced a background (by the Compton effect and possibly by pair production) which must be evaluated and subtracted.

The method has been used for preliminary measurements of the differential cross section of neon as a function of angle for 1.56- and 1.78-Mev neutron energies. The neutron source was the $H^3(p,n)$ reaction produced by protons from the 5.5-Mv Van de Graaff machine. Neon gas of natural abundance was contained in a proportional counter[1-3] at about 2 atm pressure. To decrease ion collection time, CO_2 gas to the extent of 2% was added. The primary neutrons incident upon the crystal gave a pulse-height distribution similar to that shown in Fig. 2 for the case of 1.56-Mev neutrons. The window of a single-channel analyzer was adjusted to accept pulses between the limits indicated in Fig. 2, and the output gated a 2-μsec-long pulse in the coincidence circuit. The pulse from the integral bias discriminator of the neon-counter amplifier furnished a gate for the other channel of the coincidence circuit.

In setting up the experiment, the coincidence rate was measured as a function of the delay of one channel relative to the other. The curve obtained indicated that the width of the coincidence gates was adequate for the collection time of the neon counter. With a sufficiently long delay (4.7 μsec) in one channel, the accidental-coincidence resolving time was found to be 2.6 μsec. The beam current was adjusted during most

[1] J. L. Fowler and C. H. Johnson, *Phys. Rev.* **98**, 728 (1955).

[2] H. O. Cohn and J. L. Fowler, *Phys. Rev.* **99**, 1625 (1955).

[3] H. O. Cohn and J. L. Fowler, *Phys. Semiann. Prog. Rep. March 20, 1955*, ORNL-1879, p 6–7.

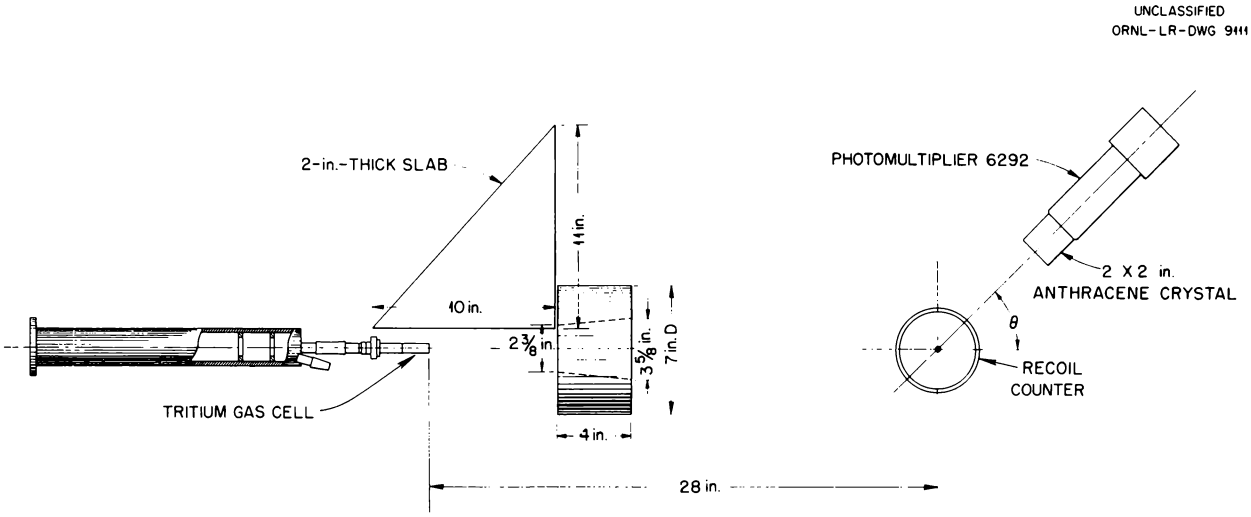

Fig. 1. Experimental Apparatus for Measuring the Differential Scattering Cross Section of Nuclei in a Gaseous Form.

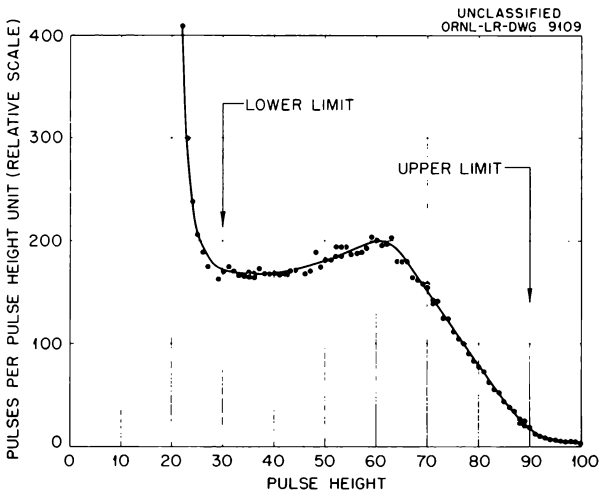

Fig. 2. Proton Recoil Spectrum in an Anthracene Crystal for 1.56-Mev Incident Neutrons.

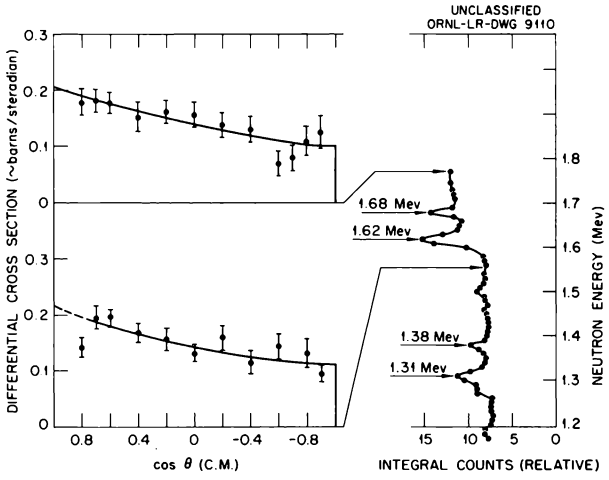

Fig. 3. Neutron Differential Elastic Scattering Cross Section of Neon at 1.56 and 1.78 Mev.

of the subsequent runs to give an accidental rate the order of one-half the real coincidence rates. Bias curves for the neon counter were obtained by measuring the coincidence rate as a function of the integral bias of the neon amplifiers. For each angular setting of the differential cross-section measurements, the integral bias was set well on the plateaus of these bias curves.

The evaluation of the gamma-ray background, which amounted to about 30%, was accomplished by removing the direct neutrons with a $4\frac{1}{2}$-in.-thick plug in the LiF-impregnated shielding. A check of this background measurement was made by extrapolating the curve of coincidence rate vs crystal bias from the region above the neutron pulses (Fig. 2) into the region of operation of the crystal biases for the neutron detection experiments.

Figure 3 shows preliminary results for the differential elastic scattering of neutrons from neon. By measuring the direct neutron flux with the same crystal which is used to detect the scattered

flux, the method can be made absolute in the same way that absolute differential cross-section measurements are made for solid samples.[1,4] The energy scale for the data in Fig. 3 is indicated on the right side. Plotted here are previous measurements[2,3] of integral counts of the neon counter as a function of neutron energy. This quantity gives the position of the resonances in the total neutron cross section of neon. The neutrons for the differential curves are at nonresonance energies. Errors shown are statistical. The absolute cross-section scale must be considered tentative until one has used the method to check a measured cross section. Nevertheless, the magnitude of the differential cross section found is reasonable for this region of the periodic table and for these neutron energies.

[4]H. B. Willard, J. K. Bair, and J. D. Kington, *Phys. Rev.* **98**, 669 (1955).

ELASTIC NEUTRON SCATTERING BY Li^7 AS A POLARIZATION ANALYZER

H. B. Willard J. K. Bair H. O. Cohn J. D. Kington

Resonant p-wave neutrons are elastically scattered by a $J = 3^+$ level in Li^8 at a 2.28-Mev excitation. The interference with the s-wave potential scattering background should give rise to strong polarizations. Angular distributions of the elastically scattered neutrons indicate that the channel spin mixture of the s-wave scattering is nearly statistical.[1] Accordingly, the polarization at 90 deg (c.m.) has been calculated as a function of incident neutron energy, as shown in Fig. 1.

This reaction has been used as an analyzer of the neutrons emitted from the $Li^7(p,n)Be^7$ reaction at $\bar{E}_{p,lab} = 2.296$ Mev, $\theta_{1,lab} = 85°$, $\bar{E}_{n,lab} = 280$ kev, $\theta_{2,lab} = \pm 90°$. The technique used was similar to that previously described.[2] In this case the lithium target thickness was 8 kev, and the lithium scattering sample was 1 in. in diameter and 4 in. in height. The measured product polarization $P_1(85°_{lab})\ P_2(90°_{lab}) = -0.17 \pm 0.04$, hence from Fig. 1, $P_1(85°) = +0.46 \pm 0.11$, in good agreement with the value measured[2] at $\theta_{1,lab} = 42°$ and the expected angular and energy dependence of the primary polarization.[3] Note that the positive value of P_1 comes from the definition of the unit

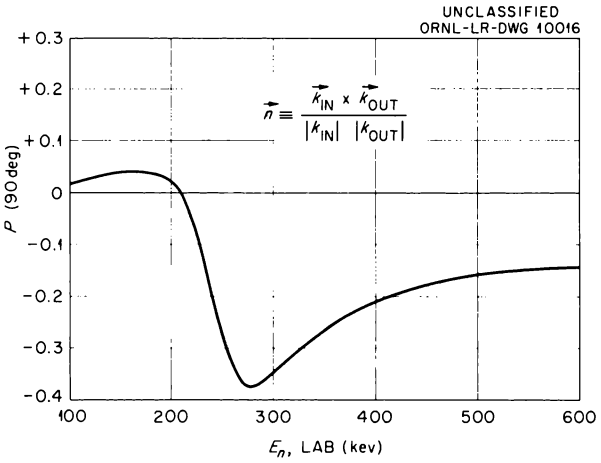

Fig. 1. Calculated Polarization at $\phi_{c.m.} = 90$ deg Resulting from Elastic Neutron Scattering by Li^7 as a Function of Incident Neutron Energy (Laboratory System).

normal to the reaction plane:

$$\vec{n} = \frac{\vec{k}_{in} \times \vec{k}_{out}}{|k_{in}|\ |k_{out}|} .$$

Corrections have not been made for multiple neutron scattering in the sample, which would raise the above value.

[1]H. B. Willard *et al.*, *Phys. Semiann. Prog. Rep. March 20, 1955*, ORNL-1879, p 5–6.

[2]H. B. Willard, J. K. Bair, and J. D. Kington, *Phys. Rev.* **95**, 1359 (1954).

[3]R. K. Adair, *Phys. Rev.* **96**, 709 (1954).

THE $Be^9(n,\alpha)He^6$ CROSS SECTION

E. C. Campbell P. H. Stelson

The cross section for the reaction $Be^9(n,\alpha)He^6$ has been measured from threshold (0.70 Mev) to a 4.4-Mev neutron energy. Monoenergetic neutrons were produced by the use of the $Li(p,n)$ and $H^3(p,n)$ reactions. The residual nucleus, He^6, decays to Li^6 by negatron emission, with an 0.8-sec half life. An electronic timer and an electrostatic proton-beam deflector provided a repetitive cycle for short neutron bombardment and beta-ray counting of the beryllium sample. Further details of the method have previously been given.[1] It is judged that the absolute cross section has been determined to ±20%. The cross-section curve is given in Fig. 1. We have also plotted the cross-section values given by Allen *et al.*[2]

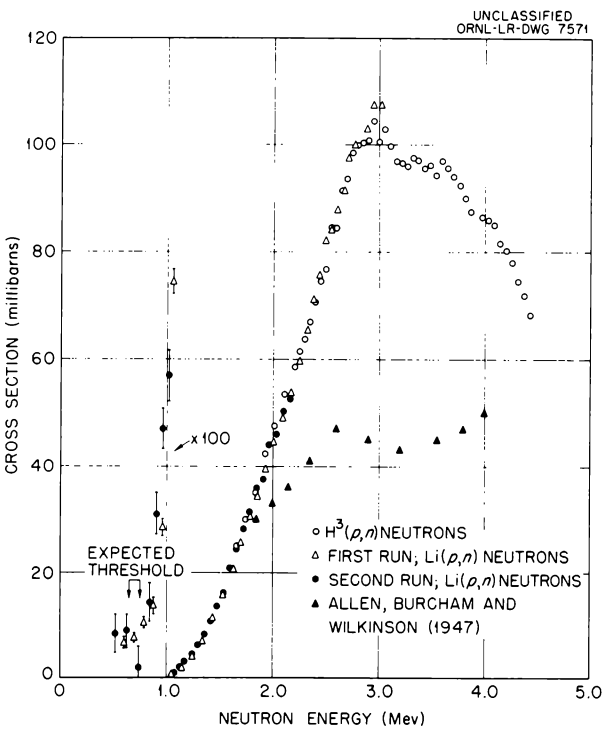

Fig. 1. Cross Section for the $Be^9(n,\alpha)He^6$ Reaction.

[1] E. C. Campbell and P. H. Stelson, *Phys. Semiann. Prog. Rep. March 20, 1955*, ORNL-1879, p 9.

[2] K. W. Allen, W. E. Burcham, and D. H. Wilkinson, *Proc. Roy. Soc. (London)* **192A**, 114 (1947).

THERMAL ABSORPTION CROSS SECTION OF Tc^{99}

H. Pomerance

Because of an alpha contamination (Am^{241}), the graphite parts and ionization chamber of the pile oscillator used in measuring the thermal absorption cross section of Tc^{99} were replaced. The new chamber yields as much current as the old, but the signal seems more sensitive to the placement of the sample than with the old setup.

G. W. Parker of the Chemistry Division prepared a sample of fission-product Tc^{99} as 1.1 g of $KTcO_4$. The same sample was previously measured in transmission with the fast chopper at the LITR. The pile oscillator value for the thermal-neutron capture cross section of Tc^{99} is 19 ± 2 barns, relative to 98 barns for gold. When the technetium is reduced to metal, the measurement will be repeated.

The pile oscillator value is nearly the arithmetical average of 2 barns from an MTR burnout irradiation (performed by G. W. Parker and W. J. Martin) and 44 barns from the fast-chopper measurement (made by E. C. Smith and P. F. Thurlow). All three measurements are subject to criticism. The pile oscillator value may be in error by 20% if the sample is not uniformly spread out but is entirely clumped at one end of the container; it is hoped that this effect was less than 5% for the technetium sample, which was fairly well spread out during preparation. The burnout measurement

was not monitored for neutron flux but depended on a value furnished by the operations group of the MTR; the extent of the error can only be guessed. The fast-chopper work was not reproducible enough in the near-thermal range to allow for a breakdown into a constant scattering cross section and a $1/v$ capture cross section; hence the reliability of the 42-barn value is unknown. Analysis of the lowest resonance was better; it gives a thermal contribution from that one resonance of about 15 barns.

MILLIMICROSECOND TIME-OF-FLIGHT NEUTRON SPECTROMETRY

J. H. Neiler W. M. Good J. H. Gibbons H. E. Banta E. C. Smith

Development of time-of-flight neutron spectrometry has been under way at Oak Ridge National Laboratory for some time.[1] Within the last year, significant progress has been made in technique, notably in the development of a multichannel time analyzer (see paper entitled "Time Interval–Pulse Amplitude Converter") and improvement in the zero-time pulse. Application of the time-of-flight spectrometer in its present form to the measurement of neutrons in the energy range of 1 to 6 Mev has been gratifyingly successful in observing the neutron groups from the $Be^9(d,n)B^{10}$ reaction. Because work in this energy range has been so preliminary, nothing more will be said at this time about the application of the time-of-flight spectrometer to (d,n) reactions and inelastic scattering.

A new technique appropriately described as a cross between chopper and Van de Graaff has been developed around the time-of-flight neutron spectrometer. In essence, the technique consists in using the Van de Graaff to produce pulses of neutrons in a well-defined energy range and in determining the time-of-flight of these neutrons. The $Li^7(p,n)Be^7$ reaction as the neutron source for such a scheme has many attractive features. Because all radiation associated with the proton beam is prompt, scintillator detectors can be used. At the same time, millimicrosecond beam bursts can be produced. The result is a millimicrosecond time scale permitting flight paths of 5 m or less. The kinetics of the reaction are such that at threshold all neutrons have the same energy of about 30 kv and are directed forward. As the energy of the bombarding proton is raised, the neutrons are emitted into a laboratory angle which increases as the proton energy is raised above neutron threshold. At the same time, these neutrons at 0 deg possess two discrete energies, the lower energy tending toward zero and the higher energy steadily increasing as the proton energy is raised above neutron threshold. Thus, in the laboratory system at 0 deg to the proton beam and with a moderately thin target, the number of neutrons per solid angle increases with neutron energy as neutrons are produced in the energy range of 2 to 30 kev. In this way, longer flight paths can be used as correspondingly higher neutron energies are being measured in this energy range. A final useful property of the lithium target is the fact that the $Li^7(p,p'\gamma)Li^{7*}$ reaction gives a gamma ray whose prompt arrival at the fast detector gives a convenient zero time determination on the scale of the time analyzer.

Aside from the mechanics of the $Li^7(p,n)Be^7$ reaction, other features of the scheme are attractive. The short distances and the absence of collimators and moderators make the system extremely flexible, so that it is possible instantly to change resolution to obtain higher counting rates.

The repetition rate is at ones disposal and hence the optimum rate can be chosen, namely, so that the fast neutrons of a given burst cannot overtake the slow neutrons of the preceding burst. Finally, radiation levels are low.

Elsewhere in this report (see paper entitled "Time Interval–Pulse Amplitude Converter") description is given to the neutron detectors and the means employed to produce 10-mμsec neutron bursts. The detector is $B^{10}(n,\alpha\gamma)Li^{7*}$, with the 0.44-Mev gamma ray being detected to the exclusion of other gamma rays by means of an NaI spectrometer. It should be noted that the gamma ray used to detect neutrons is identical with the $Li^7(p,p'\gamma)Li^{7*}$ gamma ray used to obtain "zero time" on the multichannel time scale. This fact is important, since it would seem to imply a very well-known "zero time."

[1] C. W. Snyder and V. E. Parker, *Phys. Rev.* **95**, 635 (1954).

The present performance of the technique can be judged from Figs. 1 and 2. For these measurements, sample thicknesses were chosen which gave about 90% transmission for potential scattering. This transmission figure magnifies statistical uncertainties for low cross sections but enhances the change in transmission caused by a resonance.

A narrow resonance in aluminum is shown in Fig. 2. Its natural width has been estimated[2] to be about 100 ev, due to the $l = 1$ neutrons, so the curve is approximately the resolution function.

The cross section of bismuth is presented in Fig. 1. The relatively high cross section in the 3- to 6-kev range and the pronounced dip at 14 kev are not well understood, especially when compared with other data.[3] Data in the 10- to 16-kev range were taken with a single proton energy setting and neutron flight path. The spectrum was covered completely, both for sample "in" and sample

[2]R. H. Rohrer, H. W. Newson, and J. H. Gibbons, *Phys. Rev.* **95**, 302 (1954).

[3]D. J. Hughes and J. A. Harvey, *Neutron Cross Sections*, BNL-325 (July 1, 1953).

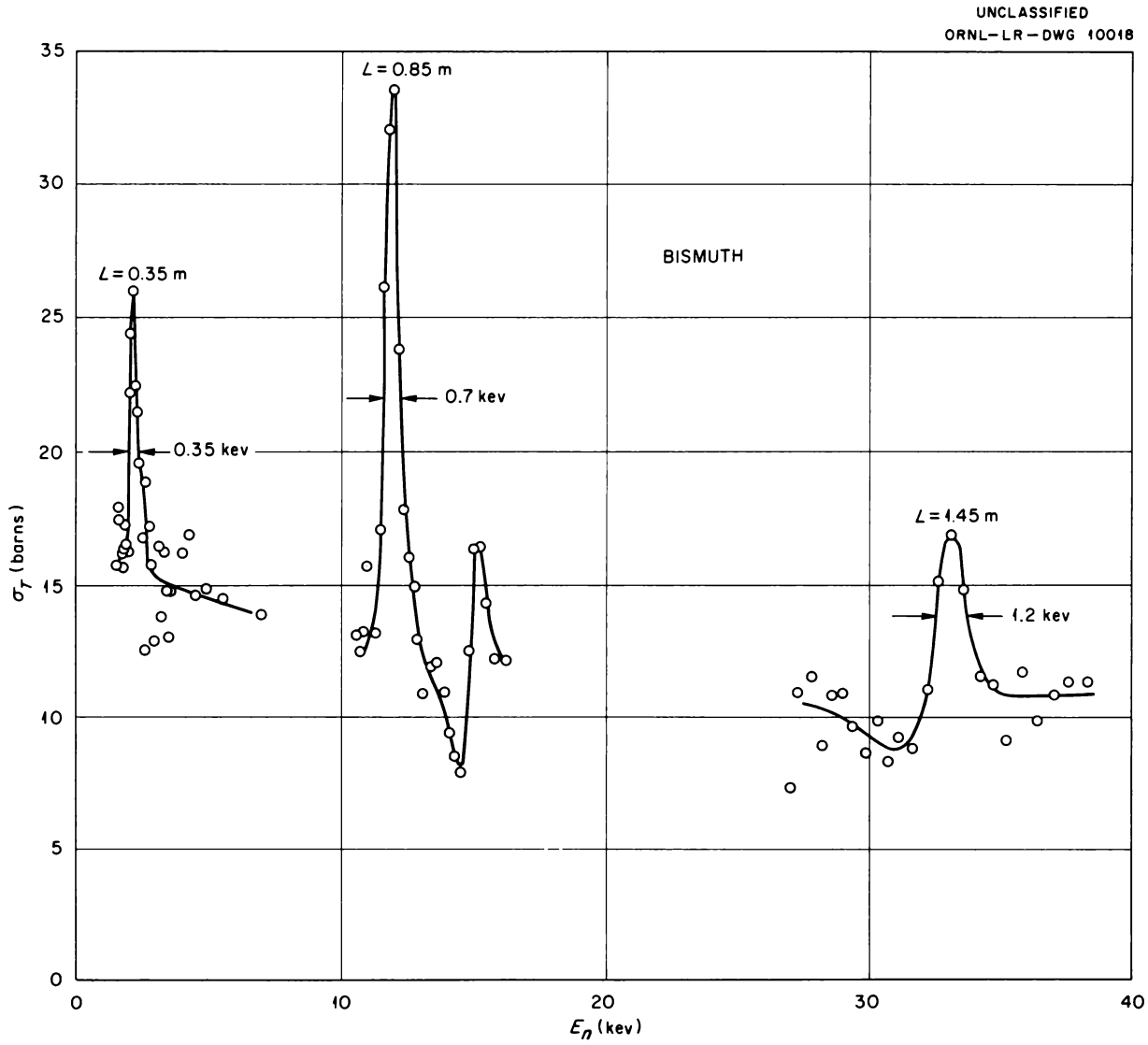

Fig. 1. Selected Resonances in σ_T(Bi).

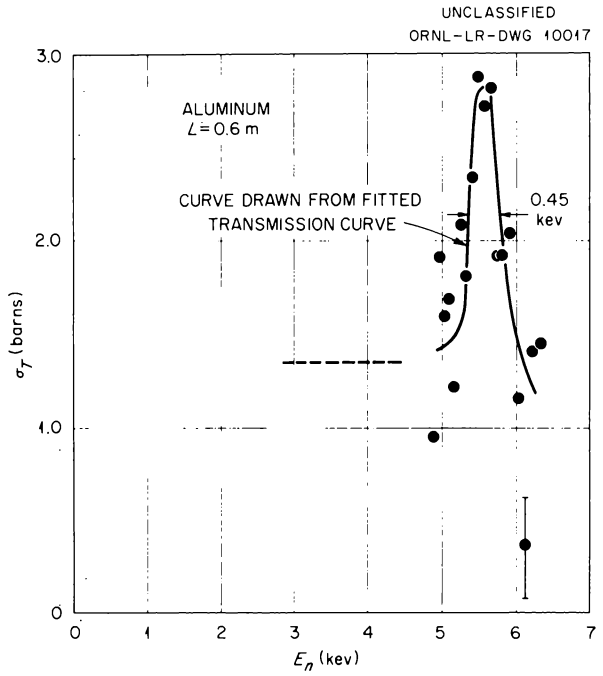

Fig. 2. Narrow Resonance in σ_T(Al).

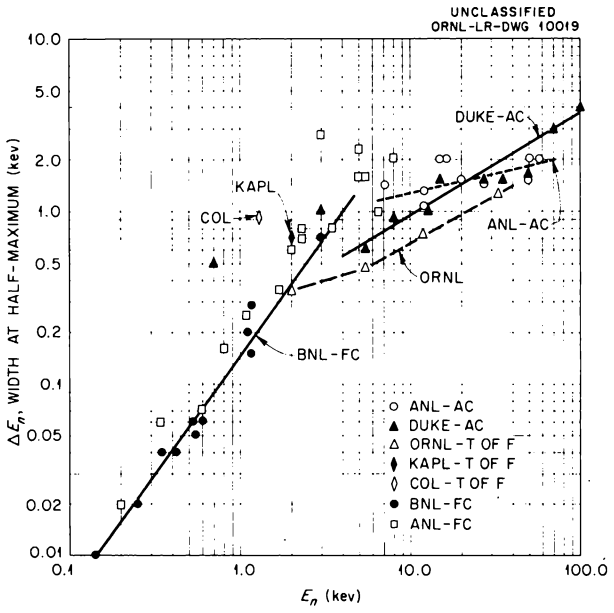

Fig. 3. Comparison of Estimated Resolutions for Various Techniques in Use.

"out." This process was repeated several times, and results were added to give better counting statistics. Cross-section points were calculated from data in corresponding channels. The time required to cover the 10- to 16-kev region was about 3 hr for 2% counting statistics. This time, for instance, could have been roughly halved if 40 rather than 20 channels had been available. Backgrounds were about 20%.

Experience with the instrument, as used in obtaining Figs. 1 and 2, reveals backgrounds as one of the major problems. The background can be resolved into four components:

1. background (Van de Graaff off) due to cosmic rays, etc.;
2. background (Van de Graaff on, beam stop in) due to terminal x rays, etc.;
3. background (Van de Graaff on, beam on target, paraffin cone in) due to air- and floor-scattered neutrons;
4. background due to beta and gamma rays from I^{128} radioactivity in the detector induced by $Li^7(p,n)Be^7$ neutrons.

The relative magnitudes of the various backgrounds are approximately (1) = 14, (2) = 4, (3) = 2, and (4) = 16. It is hoped that detector shielding with Li^6, as well as with cadmium, will appreciably reduce effect (4).

Results to date with the technique just described permit comparisons with other existing techniques for doing the same job. Such a comparison is shown in Fig. 3. The whole time-of-flight technique is expected to get an impetus from the development of pulsing at the terminal described elsewhere in this report (see paper entitled "An Ion-Source Pulsing System"). The dividends are expected to be increased beam currents, with greatly reduced backgrounds.

DISINTEGRATION OF Mg^{27}

W. S. Lyon[1] N. H. Lazar

The disintegration scheme of 9.45-min Mg^{27} has been determined from gamma-ray spectrometer measurements and gamma-ray counting. Magnesium oxide was bombarded in the ORNL Graphite Reactor for 10 min and was then dissolved in HNO_3; iron carrier was added, and $Fe(OH)_3$ was precipitated by addition of ammonia to remove Mn^{56} and other impurities. The solution was then acidified, and magnesium was precipitated by addition of NaOH. Cylindrical NaI crystals, 3 × 3 in., were used in the scintillation spectrometer in conjunction with a multichannel analyzer.[2] The sources were placed on the axis of the cylinder, 9.3 cm from the top face of the crystal. Two prominent gamma rays at 0.834 and 1.015 were found with relative intensities of 0.70 and 0.30 (Fig. 1).

By means of a beta-gamma coincidence experiment, in which the beta rays were detected in a proportional counter and in which a 3 × 3 in. NaI crystal was used as a gamma-ray detector, the absolute source intensity of an aliquot of a solution containing $Mg(OH)_2$ was determined. The absolute gamma-ray intensity was determined with a separate scintillation spectrometer. The sum of the intensities of the gamma rays agreed within 5% with the source disintegration rate. Thus, there appear to be two beta-ray groups separated in energy by approximately 0.180 Mev, with essentially no beta-ray transitions to the ground state directly.

From simple shell-model considerations, the first three states in Al^{27} should be expected to be $d_{5/2}$, $d_{3/2}$, and $s_{1/2}$ (not necessarily in that order). The ground-state spin is measured[3] as $\frac{5}{2}$. Because of the high intensity of the 0.862-Mev gamma ray, $s_{1/2}$ is the most likely assignment for the first excited state. On this basis, the expected intensity of the 0.180-Mev cascade gamma ray may be computed to be about 1% of the 1.015-Mev transition. Unfortunately, this region of the gamma-ray spectrum is distorted by gamma rays Compton-scattered from the surrounding lead shield. To remove the back-scatter peak, the source was placed at the apex of a conical hole cut into a table made of 2-in. lead bricks. The crystal was placed under the table in a lead shield so that it could "see" only into the surroundings of the source through the conical collimator. The pulse-height spectrum obtained in this way with a source of Zn^{65} is shown in Fig. 2. A run obtained with an Mg^{27} sample is shown in Fig. 3. The intensity of the gamma ray at 0.175 ± 0.015 Mev is 2.2% of the 1.015-Mev gamma ray. The decay scheme shown in Fig. 4 is consistent with these considerations.

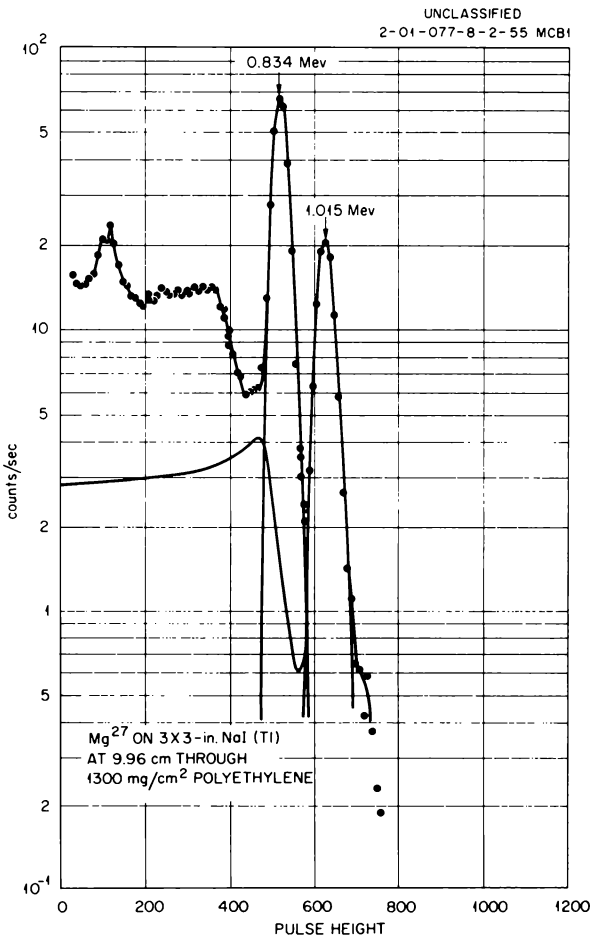

Fig. 1. Gamma-Ray Spectrum from Mg^{27}.

[1] Analytical Chemistry Division.

[2] G. G. Kelley, P. R. Bell, and C. G. Goss, *Phys. Quar. Prog. Rep. Dec. 20, 1951*, ORNL-1278, p 27.

[3] J. M. Hollander, I. Perlman, and G. T. Seaborg, *Revs. Mod. Phys.* **25**, 469 (1953).

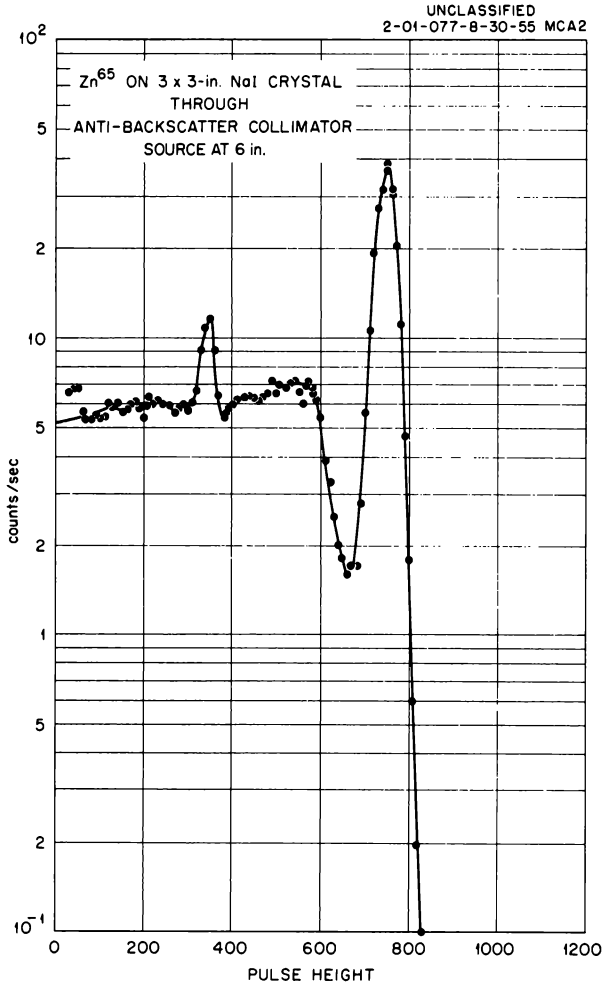

Fig. 2. Spectrum of 1.114-Mev Gamma Ray from Zn^{65} Obtained by Using the Anti-Back-Scattering Collimator.

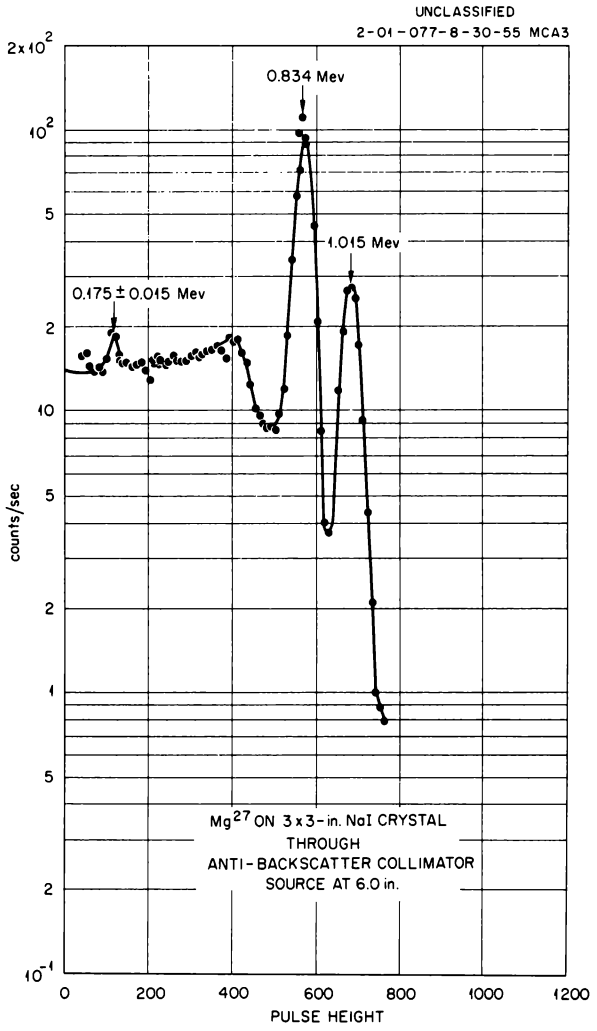

Fig. 3. Gamma-Ray Spectrum from Mg^{27} Obtained by Using the Anti-Back-Scattering Collimator.

UNCLASSIFIED
2-01-077-DS

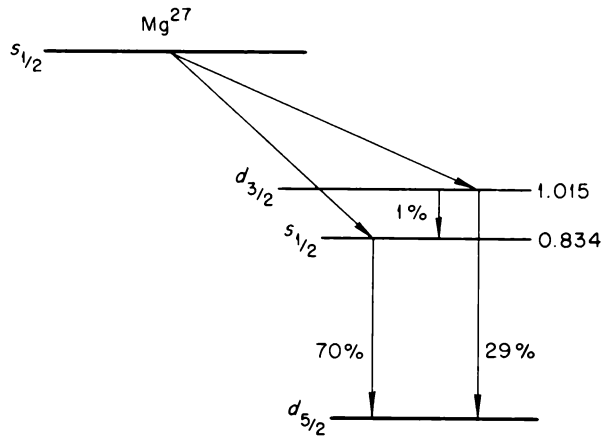

Fig. 4. Decay Scheme of Mg^{27}.

DECAY OF Ca^{49} AND Sc^{49}

N. H. Lazar G. D. O'Kelley E. Eichler

The decays of 8.6-min Ca^{49} and its 57-min daughter, Sc^{49}, have been studied with gamma-ray scintillation spectrometers and beta-ray detectors. Both natural calcium and calcium enriched to 51.4% in Ca^{48} were bombarded in the ORNL Graphite Reactor, and the samples were in position to be counted usually within 5 min. A typical gamma-ray spectrum which followed the decay of Ca^{49} and which was obtained with a 3 × 3 in. NaI scintillation spectrometer used in conjunction with the multichannel analyzer is shown in Fig. 1. Gamma rays of 3.10, 4.05, and 4.68 Mev were observed with relative intensities of 1.0, 0.094 ± 0.015, and 0.0031 ± 0.0005. Samples were counted for several half lives, and no other prominent peaks were observed. In the region below 1.5 Mev, the spectrum became progressively distorted due to the buildup of bremsstrahlung from the decay of the Sc^{49} daughter, and possible peaks became more difficult to observe; thus only an upper limit of about 5% of the 3.10-Mev gamma ray could be placed on the intensity of possible cascade gamma rays in that region.

The anthracene well counter, ½ in. thick by 1 in. in diameter, was used to obtain the beta-ray spectrum from a sample of Ca^{49} obtained from a bombardment of enriched calcium. The gamma-ray contribution was determined by absorbing the beta rays with copper and correcting for the decay. The end point was determined from a Fermi plot of the data, Fig. 2, as 1.95 ± 0.05 Mev. A second beta-ray group, with an end point of 0.89 ± 0.15 Mev and a relative intensity of 0.14, was determined after the subtraction of the highest energy group, which was assumed to have the statistical shape.

The intensity of the beta-ray transitions to the ground state was determined from a comparison of the intensity of the 3.10-Mev gamma ray of Ca^{49} (prepared from enriched calcium) measured with a scintillation spectrometer with the total number of beta rays measured in a 4π beta counter.[1] The ratio of beta rays to gamma-ray intensity was

[1] The authors are indebted to A. R. Brosi for permission to use his 4π counter.

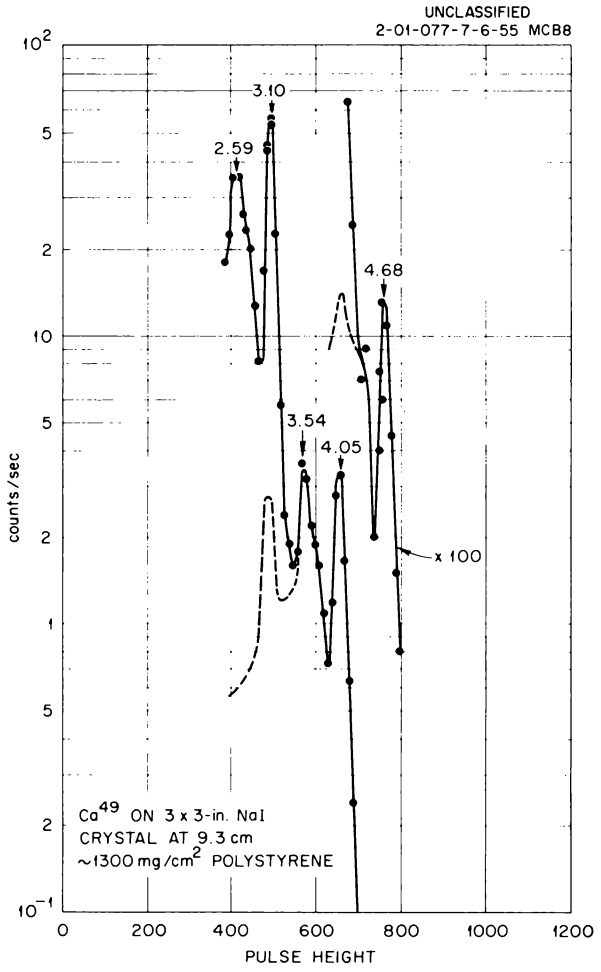

Fig. 1. Gamma-Ray Spectrum from Ca^{49}-Sc^{49} Obtained with 3 × 3 in. NaI Spectrometer.

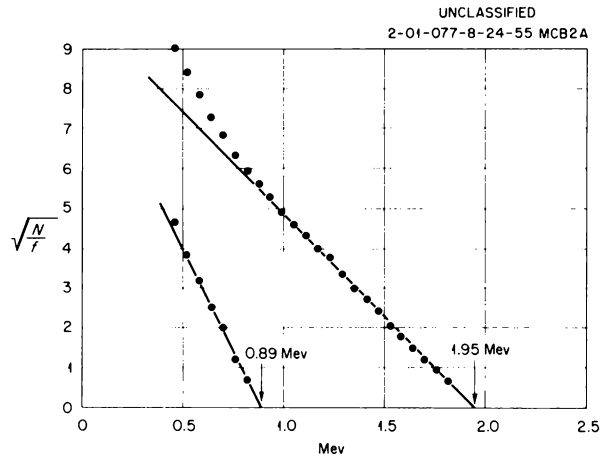

Fig. 2. Fermi Plot of Beta Rays from Ca^{49} Obtained with Anthracene Crystal Spectrometer.

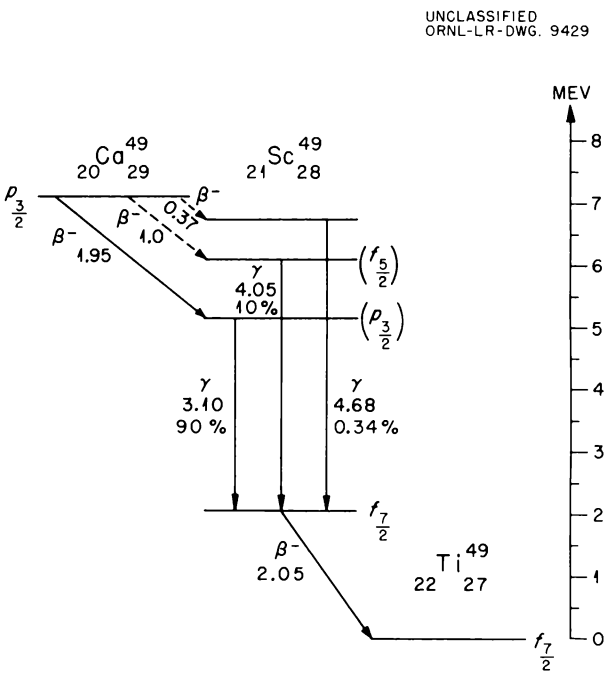

Fig. 3. Decay Scheme for Ca^{49}-Sc^{49}.

$N_\beta/N_\gamma = 0.985 \pm 0.050$, when the intensities of the 4.05- and 4.68-Mev gamma rays were taken into account. Thus, within experimental error, all beta-ray transitions decay to excited states.

A Fermi plot of the beta rays obtained from a somewhat thicker Sc^{49} sample was also made, and the end point was determined as 2.05 ± 0.05 Mev.

The decay scheme shown in Fig. 3 is consistent with all these experiments. The spin assignments are based on shell-model considerations and comparison with similar nuclei. The $f_{7/2}$ ground-state assignment of Sc^{49} is established on the basis of the fact that almost all nuclei with the number of odd particles falling in the region between 20 and 27 have $f_{7/2}$ spin; this is particularly true of those with 21 particles.[2] The $p_{3/2}$ ground-state assignment for Ca^{49} is also fairly certain, since all known nuclei with 29 particles have $p_{3/2}$ spin in their ground state.[2] Thus, the ground-state beta transition from Ca^{49} to Sc^{49} would be second

[2] R. H. Nussbaum, thesis, University of Amsterdam, 1955.

forbidden, and one would not expect to find it occurring with appreciable probability. The spin of the ground state of Ti^{49} has been measured[3] as $\frac{7}{2}$, and the assignment $f_{7/2}$ is therefore made. The first excited state in Ti^{49} is at 1.35 Mev, but a gamma ray of this energy is not seen. The probable assignment[4] for this state is $p_{3/2}$, and thus the beta-ray transition to this state would be second forbidden. The second excited state is at 1.70 Mev, and an angular distribution from the stripping reaction on Ti^{48} indicates that this is also a p state.[4] Thus the pure beta emission observed for Sc^{49} is consistent with the known facts about Ti^{49}.

The assignment of $p_{3/2}$ to the first excited state of Sc^{49} instead of to the second state is also based on a comparison with similar nuclei. Calcium-41 with 21 odd particles shows the familiar $f_{7/2}$ ground state and the $p_{3/2}$ state as the first excited state[5] at 1.9 Mev. In addition, in the ground states of nuclei with 29 particles, as mentioned above, the $p_{3/2}$ level appears to be lower than the $f_{5/2}$ level. The comparative half life for the beta transitions from Ca^{49} classifies these two excited states as odd parity, and the only question is the order of the $p_{3/2}$ and $f_{5/2}$. One final bit of evidence confirms our assignment, namely, the relative intensity of the 4.05-Mev transition to the possible cascade through the 3.10-Mev state. If the upper level were $p_{3/2}$, the crossover transition would have to be $E2$, and the relative probabilities of the 4.10- to the 0.95-Mev gamma ray would be 1 to 40 based on

$$\tau \sim \left(\frac{197}{E}\right)^{2l+1} .$$

The proposed assignments predict this ratio to be 64 to 1, and the fact that this transition could not be observed implies that the latter ratio is probably correct.

One bit of information remains somewhat puzzling. The energy of the first excited state of Sc^{49} is 3.10 Mev, and the state, if the single-particle model applies, is due to the excitation of the twenty-first proton, there being a "closed" shell of 28 neutrons in the nucleus. The only similar nucleus known is Ca^{41}, with 20 protons and 21 neutrons. Here the first excited state,[5] also $p_{3/2}$, is at only 1.90 Mev. If one attempts to correlate nuclei with different configurations in this region, for example, with three odd nucleons, two extra nucleons, etc., past the doubly magic cores at 20-20, 20-28, and 28-28, one finds remarkably good agreement in the energy of the first excited states. It seems extremely desirable to us to attempt a theoretical approach to the nuclei in this region, possibly along the same lines suggested by Ford and Levinson[6] for Ca^{43}, to determine if these trends can be reasonably explained.

[3] C. D. Jeffries, *Phys. Rev.* **92**, 1096 (1953).

[4] M. M. Bretscher *et al.*, *Phys. Rev.* **96**, 103 (1954); F. B. Shull and M. M. Bretscher, *Phys. Rev.* **96**, 826 (1954).

[5] J. R. Holt and T. N. Marsham, *Proc. Phys. Soc. (London)* **66A**, 565 (1953).

[6] C. Levinson and K. W. Ford, *Phys. Rev.* **99**, 792 (1955), and private communication.

NUCLEAR LEVELS IN Sr^{88} FROM THE DISINTEGRATION OF Y^{88} AND Rb^{88}

N. H. Lazar E. Eichler[1] G. D. O'Kelley[1]

Levels in Sr^{88} excited by the decay of 17.8-min Rb^{88} and 104-day Y^{88} were studied by means of gamma-ray scintillation spectroscopy. Both single-crystal and coincidence spectroscopy experiments were performed by using 3 × 3 in. cylindrical NaI(Tl) crystals as scintillators, recording the pulse-height spectra on a 20-channel analyzer.

Figure 1 shows the gamma-ray spectrum obtained from a Y^{88} source placed 9.3 cm from the top face of a 3 × 3 in. NaI(Tl) crystal whose upper edge had been beveled at an angle of 45 deg to the axis of the cylinder to increase the photopeak detection efficiency. The area of the peak at 2.76 Mev, when corrected for coincident summing of the 0.908- and 1.85-Mev gamma rays,[2] indicated that the intensity of the 2.76-Mev crossover gamma ray is $(5 \pm 3) \times 10^{-3}$ times that of the 1.85-Mev transition. The relative intensities of the 0.908- and 1.85-Mev gamma rays were also determined. Correcting the intensities for coincident summing, the ratio $I(1.85)/I(0.908)$ was found to be 1.09 ± 0.05, where the error quoted is primarily an estimate of the uncertainty in the detection efficiencies involved.

[1]Chemistry Division.

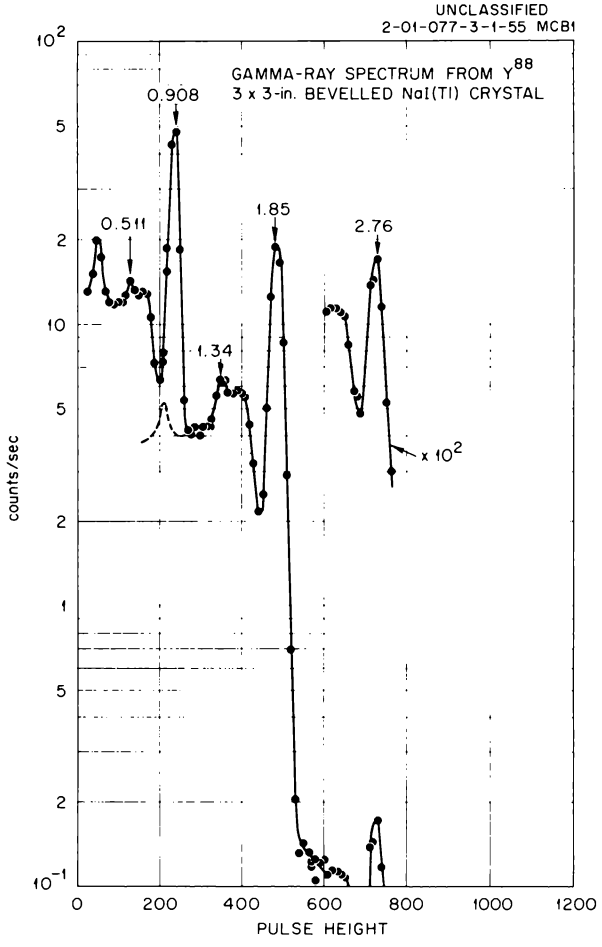

Fig. 1. Gamma-Ray Spectrum of Y^{88}.

The Rb^{88} gamma-ray spectrum obtained with the beveled crystal spectrometer is shown in Figs. 2 and 3. The analysis up to 2.8 Mev employed as guides the spectral shapes obtained in the same spectrometer from sources of Y^{88} and Na^{24}. Above 2.8 Mev the spectrum from the 4.44-Mev gamma ray from the $N^{15}(p,\alpha\gamma)C^{12}$ reaction was used for estimating the relative height of the full-energy and pair peaks.[3]

The peak at a pulse height of 120 was caused by annihilation radiation, largely due to pairs produced in the lead detector shield. A bulge at the 280 pulse height was seen to decay with a much longer half life than that of Rb^{88} and was attributed to the 1.076-Mev gamma ray in the decay of 19-day Rb^{86}. No other impurities were found after following the decay of some samples as long as five half lives of Rb^{88}.

With the previously used small NaI(Tl) crystals,[4] the peak at 1.39 Mev would have been difficult to detect because of the pair peak at 1.34 Mev from the 1.85-Mev gamma ray. Besides the gamma rays at 0.908 and 1.85 Mev discussed in the decay of Y^{88}, peaks due to gamma rays at 2.11 and 2.68 Mev are seen in Fig. 2, and gamma rays at 3.01, 3.24, 3.52, 3.65, and 4.87 Mev are resolvable in Fig. 3. The relative intensities of these gamma rays are given in Table 1.

Spectra were obtained in coincidence with the gamma rays at 0.908, 1.85, 2.11, and 2.68 Mev.

[2]N. H. Lazar and E. D. Klema, *Phys. Rev.* **98**, 710 (1955).

[3]The authors wish to acknowledge the assistance of H. B. Willard, J. K. Bair, and H. O. Cohn in performing the Van de Graaff experiment.

[4]S. Thulin, *Arkiv Fysik* **9**, 111–196 (1955).

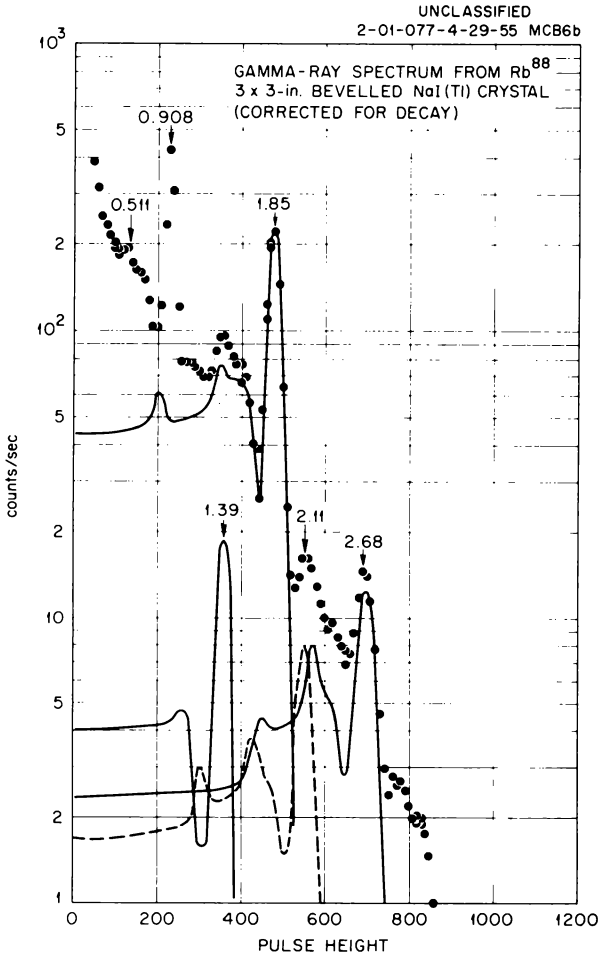

Fig. 2. Gamma-Ray Spectrum of Rb^{88} – Low-Energy Region.

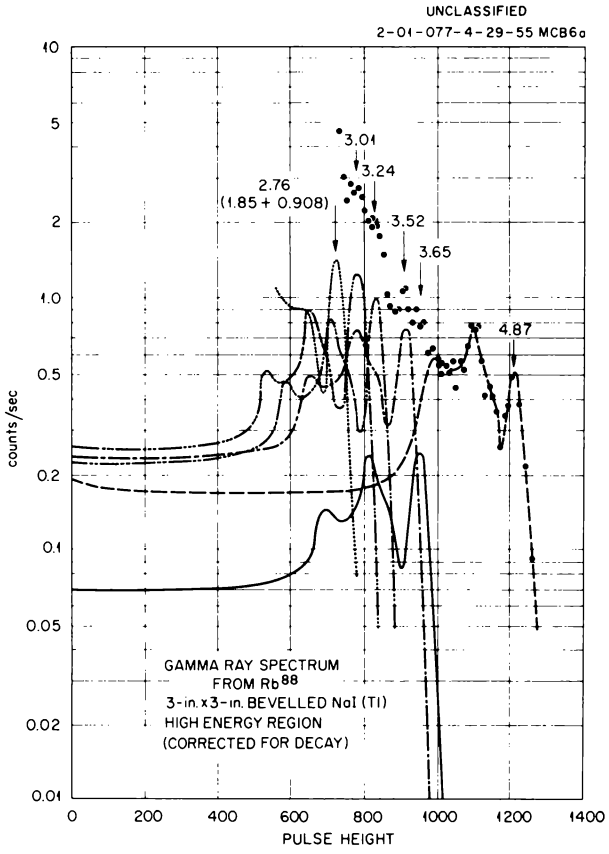

Fig. 3. Gamma-Ray Spectrum of Rb^{88} – High-Energy Region.

Calculations of the expected coincidence peak intensities, based on the intensities obtained from the single-crystal data, were found to agree with the experimental measurements.

The gamma-gamma coincidence and gamma-ray intensity data are consistent with the decay scheme shown in Fig. 4. From the gamma-ray intensities it is apparent that less than 1% of the gamma-ray transitions bypass the 1.85-Mev state. Thus it is possible to measure the intensity of the ground-state beta transition by an absolute measurement of the number of 1.85-Mev gamma rays and beta rays emitted from a sample of Rb^{88}. From such an experiment the ground-state beta transition was found to occur in 75.9 ± 5.0% of the total beta transitions.

TABLE 1. ENERGIES AND INTENSITIES OF GAMMA RAYS FROM Rb^{88}

Energy (Mev)	Intensity Relative to 1.85-Mev Gamma Ray
1.850 ± 0.008	1.000
0.908 ± 0.005	0.631 ± 0.050
1.39 ± 0.03	0.062 ± 0.015
2.11 ± 0.03	0.045 ± 0.007
2.68 ± 0.05	0.107 ± 0.010
3.01 ± 0.05	0.014 ± 0.005
3.24 ± 0.03	0.014 ± 0.002
3.52 ± 0.05	0.011 ± 0.002
3.62 ± 0.05	0.004 ± 0.002
4.87 ± 0.05	0.014 ± 0.003

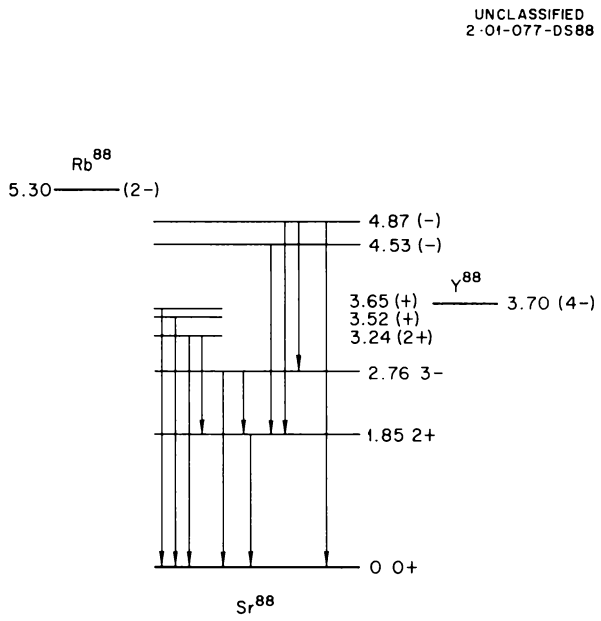

Fig. 4. Proposed Decay Scheme for the Levels of Sr^{88}.

Comparative half lives for all the beta transitions from Rb^{88} were calculated from the gamma-ray intensities, on the assumption that 76% of all beta transitions are to the ground state of Sr^{88}; the results are listed in Table 2. The log *ft* value of 7.9 for the beta-ray group to the first excited state is in good agreement with the proposed 2+ spin, but the transition to the 2.76-Mev level is slower than was expected for an allowed decay. Odd parity was assigned to the 4.87- and 4.54-Mev states, since the comparative half lives of the beta transitions to these levels correspond to those expected for allowed transitions.

Even parity is assigned to the states at 3.25, 3.52, and 3.68 Mev, again using as a guide the comparative half lives of the beta transitions feeding them. A spin of 2+ can be assigned to the 3.25-Mev level, from the intensities of the 3.25- and 1.39-Mev gamma rays.

An attempt was made to identify the first few excited states of $_{38}Sr^{88}_{50}$, with proton configurations predicted from the single-particle model. The single-particle states available for the twenty-ninth through the fiftieth protons are $f_{5/2}$, $p_{3/2}$, $p_{1/2}$, and $g_{9/2}$; $_{40}Zr^{90}_{50}$, with two more protons, appears to fill the $p_{1/2}$ shell,[5] and so a reasonable assignment for the last ten protons in the ground state of Sr^{88} is $(f_{5/2})^6 (p_{3/2})^4$. If one of the $p_{3/2}$ protons is excited into the $p_{1/2}$ orbital, the resulting coupling would very likely yield a 2+ state. If the proton is excited to the $g_{9/2}$ orbital, it might couple to the resulting hole to yield the 3– excited state. The pertinent configurations might be $(p_{3/2})^{-1} (p_{1/2})_{2+}$ and $(p_{3/2})^{-1} (g_{9/2})_{3-}$. Since the neighboring nucleus $_{39}Y^{89}_{50}$ is known to have a $g_{9/2}$–$p_{1/2}$ isomeric transition with an energy of 0.913 Mev, it is tempting to try to explain the slowness of the 0.908-Mev transition, compared with the single-particle estimates, on the basis of the $g_{9/2}$–$p_{1/2}$ proton orbital change between the initial and final states.

TABLE 2. INTENSITIES AND COMPARATIVE HALF LIVES OF THE BETA-RAY TRANSITIONS COMPUTED FROM THE GAMMA-RAY INTENSITIES (TRANSITIONS LABELED BY FINAL STATES)

Beta-Ray Groups	Intensity	Logarithm of Comparative Half life
β_0	0.759	7.5
$\beta_{1.85}$	0.043	7.9
$\beta_{2.76}$	0.136	6.7
$\beta_{3.24}$	0.017	7.3
$\beta_{3.32}$	0.0025	7.9
$\beta_{3.68}$	0.00083	8.1
$\beta_{4.53}$	0.025	5.2
$\beta_{4.87}$	0.017	5.0

[5] K. Ford, private communication.

DETERMINATION OF THE HALF LIFE OF Th^{232}

N. H. Lazar F. E. Senftle[1] T. Farley[1]

The geologic ages of rocks and minerals calculated from the Pb^{208}/Th^{232} ratio are consistently lower, by about 11%, than the ages computed from the Pb^{206}/U^{238} and Pb^{207}/U^{235} ratios. Thus a redetermination of the half life of Th^{232}, currently accepted[2] as 1.39×10^{10} years, was undertaken. The method used was a determination of the absolute gamma-ray disintegration rate of ThC″(Tl^{208}) in equilibrium with the parent Th^{232}. Correction for the branching ratio of ThC(Bi^{212}) gives the disintegration rate of the parent from which the half life could be calculated.

The thorium series is in equilibrium to better than 99% in 35 years. The samples used were all sufficiently old that a correction for nonequilibrium was not necessary. A spectroscopic analysis of the samples showed no impurities to greater than 0.05% in the three samples used for the determination. The average thorium content of the nitrate samples was determined by ignition to thorium oxide and also by precipitation of thorium hydroxide from solutions of the salts, followed by ignition to the oxide. The average analysis for thorium of samples 2a, 4a, and 5a are 41.78 ± 0.09%, 41.42 ± 0.23%, and 41.81 ± 0.06%, respectively.

Since this method depends in a critical way on the branching ratio, $\alpha/(\alpha + \beta)$, of ThC, this ratio was determined in the following manner. A piece of platinum sheet was suspended over about 600 g of shelf thorium nitrate for about 12 hr. The active deposit on the platinum was used as the source. This was placed in a 2π alpha-proportional counter large enough so that the entire path length of the highest energy particles was within the counting volume. The alpha particles were collimated with a $\frac{1}{32}$-in. brass plate drilled with a large number of holes 0.06 in. in diameter. The chamber had a 0.003-in.-dia center electrode operated at approximately 1500 v and was filled with a 10% methane-argon counting gas. The output, after amplification, was fed into the multichannel analyzer,[3] suitably adjusted for long-pulse operation. The ratio of the intensity of the two alpha groups from ThC and ThC′(Po^{212}) was determined as 0.366, somewhat higher than the figure obtained by Kovarik and Adams,[2] 0.337, by means of an absorption measurement.

The pulse-height spectrum obtained with a 3 × 3 in. NaI crystal from the gamma rays from an equilibrium sample of Th^{232} and its daughters is shown in Fig. 1. The 2.62-Mev gamma ray was used to determine the disintegration rate of ThC″, since no transitions bypass that level. The samples were made up into cylindrical capsules about 1 cm in diameter and 1.3 cm tall and were

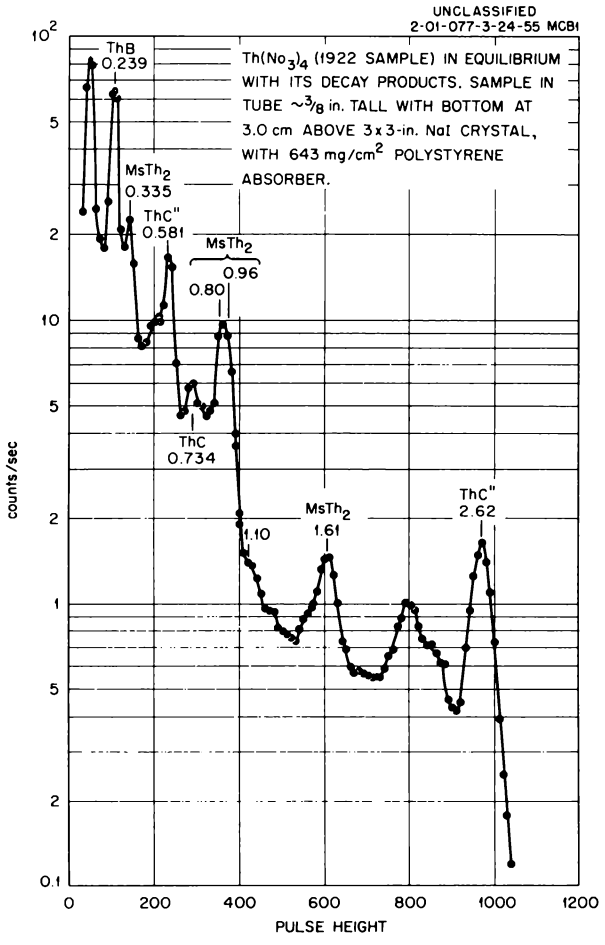

Fig. 1. Gamma-Ray Spectrum from Natural Thorium in Equilibrium with Its Daughters.

[1] U.S. Geologic Survey, Washington, D. C.

[2] A. F. Kovarik and N. I. Adams, *Phys. Rev.* 54, 413 (1938).

[3] G. G. Kelley, P. R. Bell, and C. G. Goss, *Phys. Quar. Prog. Rep. Dec. 20, 1951*, ORNL-1278, p 27.

sealed and stored for several weeks to ensure complete equilibrium. The geometry was defined by assuming that the source was concentrated at the center of the capsule. The expression used for calculating the intensity of the gamma ray from the measured peak area, $P(2.62)$, was

$$(1) \qquad I(2.62) = \frac{P(2.62)}{T\epsilon_p(2.62)\,\Omega[1 - \epsilon_T(0.580)\,\Omega f_{0.580} - \epsilon_T(0.510)\,\Omega f_{0.510} - \epsilon_T(0.820)\,\Omega f_{0.820}]},$$

where ϵ_p and ϵ_T are the intrinsic peak and total efficiencies which have been determined for the 3 × 3 in. NaI crystals for the particular solid angle, $\Omega = \omega/4\pi$, subtended by the crystal at the source. The expression in the brackets in the denominator of Eq. 1 takes into account coincident summing which occurs with cascade gamma rays. The factor f_γ is defined as the ratio of the intensity of gamma rays with energy E_γ to the 2.62-Mev gamma-ray intensity, and the values used are those given by Elliot *et al.*[4] The factor T is inserted to take into account absorption of the gamma rays with the polystyrene beta-ray absorbers and any self-absorption in the source. This factor was less than 5% for all sources.

The three samples were placed on the axis of the crystals at a height of about 9 cm from the top face. Both unbeveled cylinders and cylinders whose upper edge had been beveled at 45 deg to the axis to a diameter of 2 in. were used. The results obtained with the beveled crystal agree among themselves and within 6% with the unbeveled-crystal results (Table 1); however, they are systematically higher than the latter. It is felt that the efficiency of the unbeveled crystal is known with the higher accuracy, and these values are given below. Using the new value for the branching ratio of ThC and averaging the three values for $I(2.62)$ obtained with the unbeveled crystal, we obtain $\lambda = 1.46 \times 10^{-18}$ sec^{-1} or $t_{1/2} = 1.40 \times 10^{10}$ years, with an expected uncertainty of 5%.

[4] L. G. Elliot, R. L. Graham, J. Walker, and J. L. Wolfson, *Phys. Rev.* 93, 356 (1954).

TABLE 1. INTENSITY OF 2.615-Mev GAMMA RAY FROM ThC″ AND DECAY CONSTANT OF Th^{232} DETERMINED WITH BEVELED AND UNBEVELED CRYSTALS FOR VARIOUS SAMPLES OF $Th(NO_3)_4$

Sample	Thorium Content (g)	Beveled Crystal		Unbeveled Crystal	
		I_γ	$\lambda(\times 10^{-18}\ \text{sec}^{-1})$	I_γ	$\lambda(\times 10^{-18}\ \text{sec}^{-1})$
2a	1.099	1693	1.65	1610	1.57
4a	1.062	1613	1.63	1545	1.56
5a	0.445	679.1	1.63	646	1.55
					Av 1.56 ± 0.06

ALPHA-PARTICLE EMISSION FROM ORIENTED Np^{237} NUCLEI AND THE SPHEROIDAL SHAPE OF THE Np^{237} NUCLEUS

L. D. Roberts J. W. T. Dabbs H. Postma G. W. Parker R. D. Ellison

Recently there has been much success in explaining many nuclear phenomena on the basis of a spheroidal nuclear model, and the large quadrupole moments observed for many of the heavy nuclei indicate that the deviation from a spherical shape may be quite large. Hill and Wheeler[1] have suggested that this spheroidal shape should have a marked effect on the alpha-particle emission of heavy nuclei. For example, they note that, for a positive quadrupole moment, the barrier against alpha emission will be thinner at the nuclear poles than at the nuclear equator and that a strong preferential alpha emission through the nuclear poles might then be expected. They also note that this preferential emission should be observable from a system of aligned nuclei. We have oriented Np^{237} and have observed an anisotropy of alpha-particle emission.

Bleaney *et al.*[2] have recently made a microwave study of the energy levels of the NpO_2^{++} ion in the hexagonal crystal $NpO_2Rb(NO_3)_3$, in which all the linear NpO_2^{++} groups are equivalent and lie parallel to the crystalline c axis. They give the effective spin Hamiltonian in the absence of an external magnetic field as

$$\mathcal{H} = P[I_z^2 - \tfrac{1}{3}I(I+1)] + AS_zI_z + B(S_xI_x + S_yI_y) \quad ,$$

where

$$A = 0.166 \pm 0.002 \text{ cm}^{-1} \quad ,$$
$$|B| = 0.02 \pm 0.02 \text{ cm}^{-1} \quad ,$$
$$P = -0.030 \pm 0.002 \text{ cm}^{-1} \quad .$$

The z direction is taken along the c axis.

Neglecting the B term, the energy levels (in °K) obtained from the above $\mathcal{H}$ are shown in Fig. 1. It is observed that the over-all splitting is very large. The microwave experiments give the relative signs of A and P but do not give their absolute values. The absolute signs quoted[2,3] are those suggested by present theoretical ideas concerning the electronic structure of the NpO_2^{++} ion, assuming positive nuclear magnetic and quadrupole moments.

Since $\mathcal{H}$ contains a magnetic hyperfine structure coupling term, the nuclear spin-lattice relaxation time may be expected to be quite short; and upon cooling a single crystal of $NpO_2Rb(NO_3)_3$, a substantial nuclear alignment relative to the crystalline c axis should be obtained at 1°K. Observation of the ratio $R_{\parallel}/R_{\perp}$ of the intensities of alpha-particle emission parallel and perpendicular to the c axis as a function of temperature should then reveal any dependence of the alpha emission on the spatial orientation of the nuclei.

An experiment of this type has been done, and the apparatus used for these observations is shown in Fig. 2. By turning the small hand wheel at the top of the vacuum chamber, the orientation of the crystal located at the lower end may be changed so that the ZnS scintillation counter will view the crystal precisely either along or perpendicular to the crystalline c axis. A thin aluminum window (0.35 mg/cm^2 thick) which would transmit the alpha particles but which would prevent room-temperature radiation from falling on the crystal was placed just above the crystal. Further, to

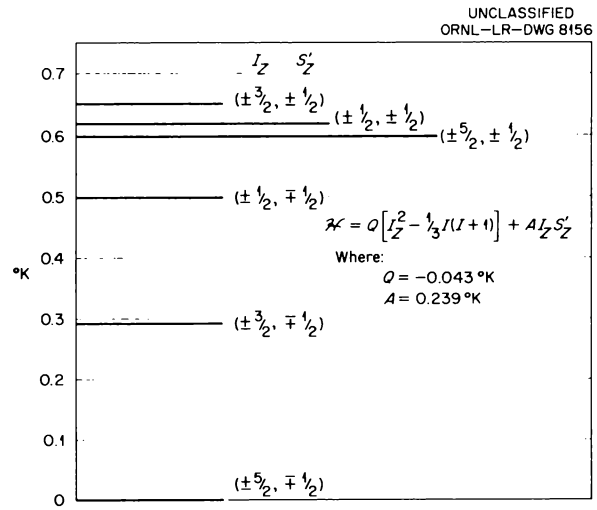

Fig. 1. Energy Levels of $NpO_2Rb(NO_3)_3$ (in °K) at Low Temperatures.

[1] D. L. Hill and J. A. Wheeler, *Phys. Rev.* **89**, 1102 (1953).

[2] B. Bleaney *et al.*, *Phil. Mag.* **45**, 992 (1954).

[3] J. C. Eisenstein and M. H. L. Pryce, *Proc. Roy. Soc. (London)* **229A**, 20 (1955).

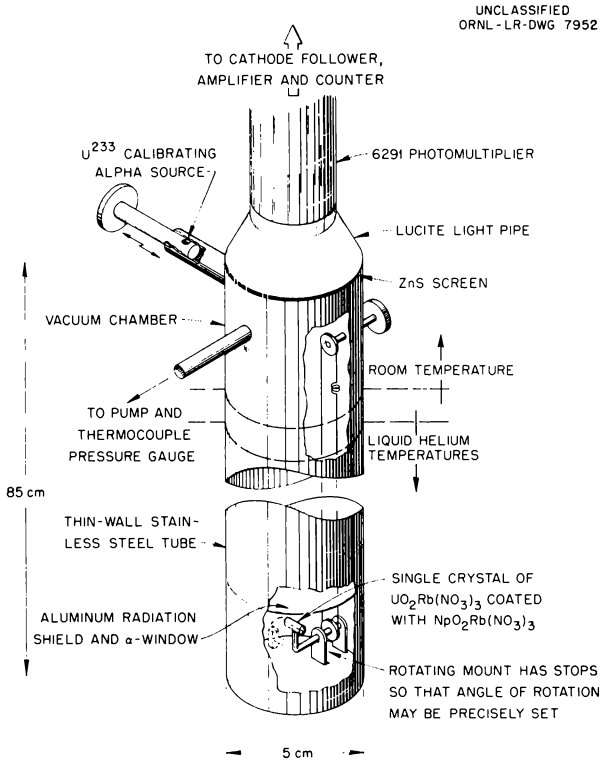

Fig. 2. Apparatus for Observing Anisotropic Alpha-Particle Emission.

maintain the crystal at the temperature of the surrounding liquid helium or nitrogen bath, a small pressure of helium heat-exchange gas (0.01 to 0.1 mm Hg) was maintained in the vacuum chamber. The bath temperature was obtained from the measured liquid helium or nitrogen vapor pressures. The heating of the sample due to the alpha particles was negligible. The sample was prepared by growing a single crystal of $UO_2Rb(NO_3)_3$ and then growing a layer consisting of one part of $NpO_2Rb(NO_3)_3$ to two parts of $UO_2Rb(NO_3)_3$ on the outside of this crystal. This layer contained approximately 0.040 g of neptunium and was about 0.03 cm thick. It was thus a thick alpha source. An x-ray examination of the layer at eight points revealed in each case the same structure as in the substrate uranyl salt. The over-all dimensions of the crystal were 8 mm in diameter by 1 cm along the *c* axis. The data were taken by making alternate 10- to 15-min counts parallel and perpendicular to the *c* axis. The counting rate was about 75 counts/min and the background was about 5 counts/min; the data presented, Fig. 3, represent some 40 days of counting. To keep a check on the constancy of performance of the counting equipment, a calibrating alpha source was located at the top of the vacuum chamber. This source was inserted for 10 min every hour (giving ~50,000 counts in this period), and the sensitivity of the equipment was invariably found to be uniform within a few tenths of a per cent. The calibrating source was, of course, retracted while the sample counts were being made.

Figure 3 displays a plot of the observed ratio $R_{\parallel}/R_{\perp}$ as a function of reciprocal temperature normalized to unity at the zero of $1/T$. A roughly linear decrease in this ratio of about 9% was found to occur as the temperature was lowered from 77 to 1.16°K. In order to demonstrate that this decrease was not due to some mechanical change of the equipment with temperature, the crystal was turned 90 deg in its mounting. Thus the positions which previously had yielded the counting rates $R_{\parallel}$ and $R_{\perp}$ now gave $R_{\perp}$ and $R'_{\perp}$. The ratio $R_{\perp}/R'_{\perp}$, which should be independent of temperature, was then measured at 77°K, with 1 atm pressure over the bath, and at 1.16°K, with 0.47 mm pressure over the bath, and was found to be the same, within 1%, at the two temperatures. This behavior of two ratios, $R_{\parallel}/R_{\perp}$ and $R_{\perp}/R'_{\perp}$, with temperature demonstrates that the development of an anisotropy in alpha emission at low temperatures, Fig. 3, is a property of the $NpO_2Rb(NO_3)_3$ crystal. In view of the above discussion, it is reasonable to associate this observed anisotropy with spatial orientation of the Np^{237} nuclei. *Assuming the*

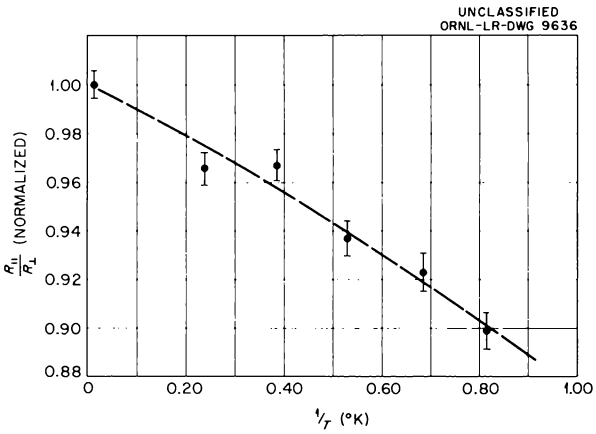

Fig. 3. Observed Ratio of Counting Rates Parallel and Perpendicular to Crystalline *c* Axis as a Function of Temperature.

correctness of the signs given by Bleaney *et al.*[2] and by Eisenstein and Pryce[3] for A, P, and the nuclear moments, the Np^{237} nuclei tend to orient in the $\pm\frac{5}{2}$ state as the temperature is lowered (see Fig. 1). Our result then indicates preferential emission of the alpha particles at the major nuclear axis of Np^{237}. If the quadrupole moment of Np^{237} is indeed positive, as assumed above, our result would indicate that barrier effects in alpha emission in Np^{237} due to the spheroidal nuclear shape are weaker than the combined effects of the variation of preformation probability over the nuclear surface, and the restrictions on the alpha-particle angular distribution imposed by the angular momentum states available in the daughter nucleus and by possible parity changes.

CROSS SECTIONS FOR ELECTRON CAPTURE BY PROTONS AND ELECTRON DETACHMENT BY NEGATIVE HYDROGEN IONS

P. M. Stier C. F. Barnett W. A. Bugg[1]

Previous reports of this series[2] have included descriptions and results of a number of experiments in which were investigated the electron capture and loss cross sections by fast hydrogen atoms and ions passing through gases. The particle energy region studied was from 3 to 200 kev. The target gases were hydrogen, helium, nitrogen, oxygen, neon, and argon. The present results include measurements made of the cross sections for electron capture by a proton and for electron loss by a negative hydrogen ion for energies from 3 to 30 kev.

The apparatus used for the electron-capture measurements is shown schematically in Fig. 1. The proton beam from the 3- to 30-kev accelerator was deflected within the differentially pumped gas cell by a radial electrostatic field. To avoid attenuation of the ion beam due to small-angle elastic scattering and to maintain the advantages of differentially pumping the detector region, the ion beam was moved across the exit slit by a linear electrostatic sweep superimposed on the deflection voltage, and the emergent beam was integrated. A proton which captured an electron moved tangentially off the orbit and did not reach the detector. The cross section is directly obtained from the exponential dependence of the attenuation on the pressure.

The cross sections for detachment of an electron from H^- ions were measured by the same techniques. The H^- ions were selected by electrostatic analysis of the beam emergent from a gas cell placed between the accelerator and the apparatus depicted in Fig. 1.

The energy dependence of the electron capture cross sections is shown in Figs. 2–5. Good agreement is seen between the present results and the recent measurements in hydrogen gas by Whittier[3] and in helium by Stedeford and Hasted.[4]

[1]Summer employee.

[2]P. M. Stier *et al.*, *Phys. Semiann. Prog. Rep. Sept. 10, 1954*, ORNL-1798, p 64; also, P. M. Stier and C. F. Barnett, *Phys. Semiann. Prog. Rep. March 20, 1955*, ORNL-1879, p 39.

[3]A. C. Whittier, *Can. J. Phys.* **32**, 275 (1954).

[4]J. B. H. Stedeford and J. B. Hasted, *Proc. Roy. Soc. (London)* **227A**, 466 (1955).

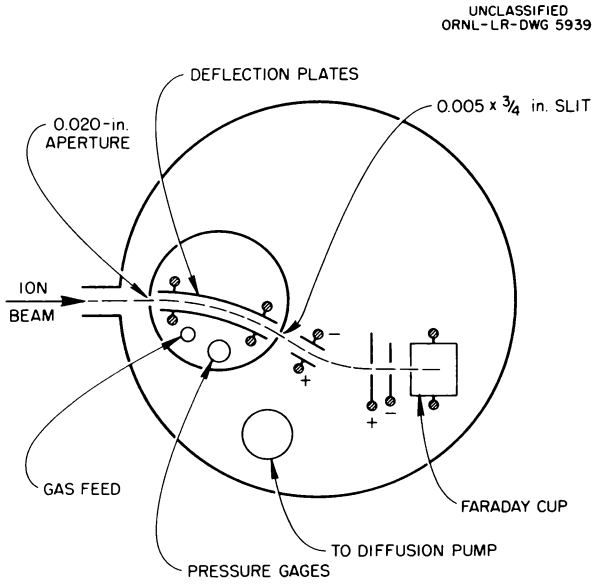

Fig. 1. Schematic Drawing of Apparatus Used in Low-Energy Electron-Capture Experiment.

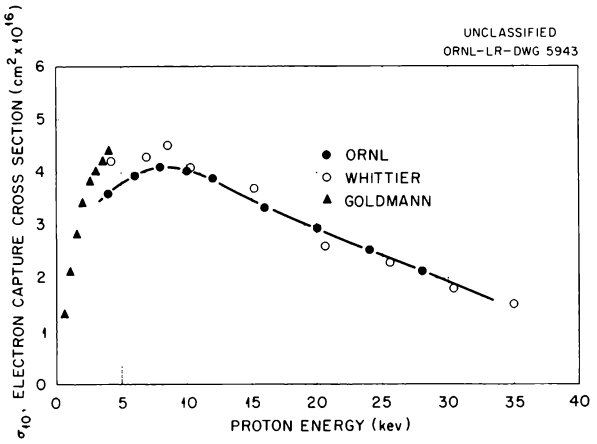

Fig. 2. Electron Capture Cross Section σ_{10} for Protons in Hydrogen.

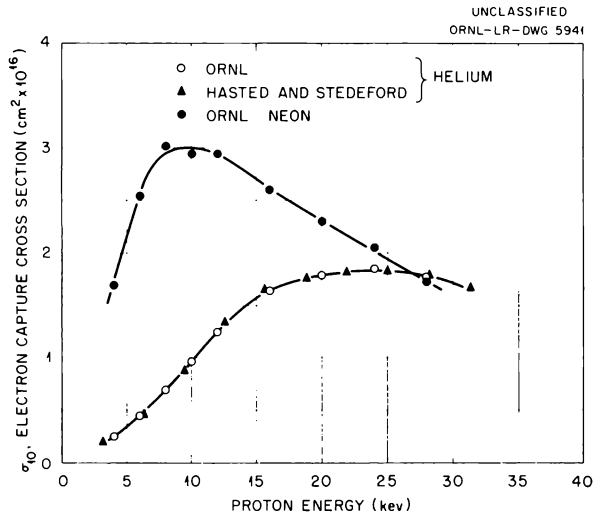

Fig. 3. Electron Capture Cross Section σ_{10} for Protons in Helium and Neon.

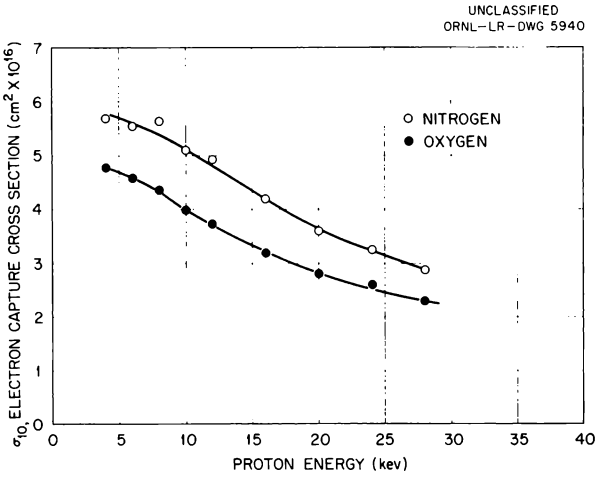

Fig. 4. Electron Capture Cross Section σ_{10} for Protons in Nitrogen and Oxygen.

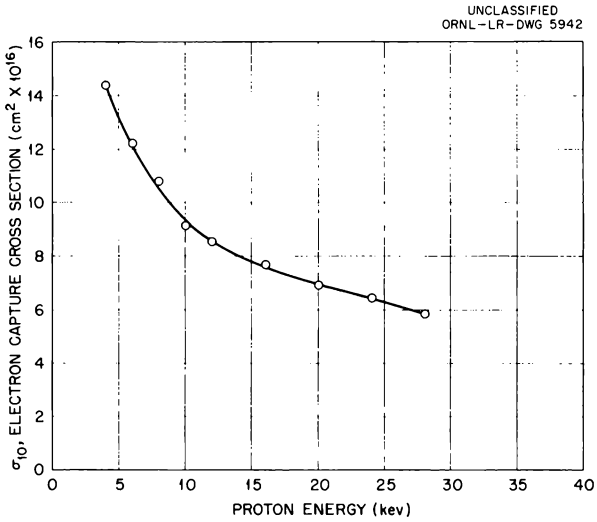

Fig. 5. Electron Capture Cross Section σ_{10} for Protons in Argon.

The most prominent difference between the behavior of the protons in the various gases is that the capture cross section in helium gas decreases much more rapidly toward zero as the energy is reduced. This behavior is as expected from the previously reported observation[2] that for energies below 10 kev the average charge of a hydrogen beam passing through helium is nearly +1. The large average charge in helium is to be compared with the average charge of nearly zero in the more easily ionized gases, for example, argon and nitrogen. Figure 4 shows that at 4 kev the capture cross section appears to be near its maximum value for nitrogen and oxygen, whereas this cross section is seen to be rising rapidly in argon (Fig. 5).

The cross sections for detachment of an electron, from the negative hydrogen ion are shown in Fig. 6. These cross sections are relatively independent of energy and, except for argon, vary only slightly from gas to gas. Electron detachment cross sections have been reported by Whittier[3] for hydrogen gas and by Stedeford and

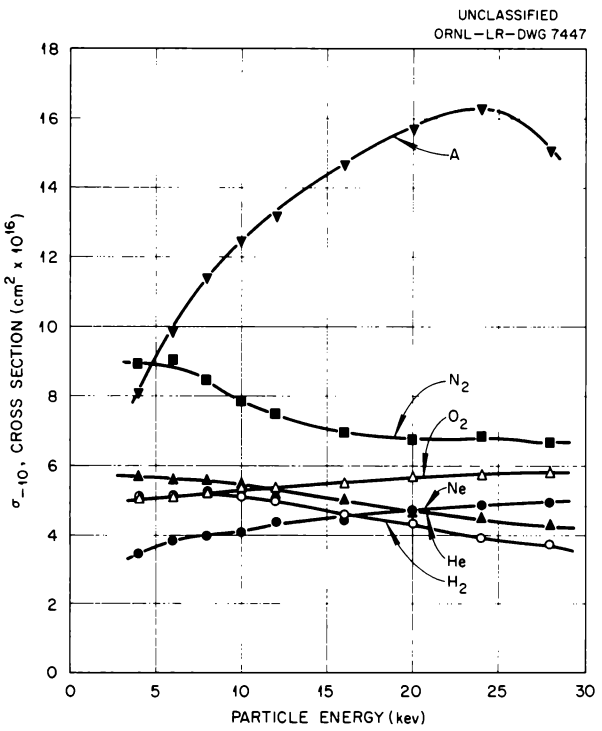

Fig. 6. Electron Detachment Cross Section, σ_{-10}, from H^- in Various Gases.

Hasted[4] for hydrogen, helium, neon, and argon. Whittier's results are from 10 to 20% higher than the present data, although they show the same energy dependence. The results of Stedeford and Hasted were higher by a somewhat larger amount. Each of the experiments is much less precise than the corresponding electron capture work because of the smallness of the H^- beams available. In view of this, the state of the agreement may be considered satisfactory.

These results conclude the study of electron capture and loss by fast hydrogens in the energy range from 3 to 200 kev. A composite report of the several experiments is being prepared for publication.

ELECTRON LOSS CROSS SECTION FOR FAST HELIUM ATOMS

P. M. Stier C. F. Barnett

As a continuation of the study of electron capture and loss, the cross section for loss of an electron by fast helium atoms has been studied. The energy range was from 30 to 200 kev. The target gases were hydrogen, helium, nitrogen, oxygen, neon, and argon.

Measurements were made in the apparatus[1] used to determine the electron loss cross sections for hydrogen atoms. The schematic diagram of the target chambers is reproduced in Fig. 1. Briefly, the procedure was as follows: With helium atoms incident on the cross-section chamber, voltage was applied to successive pairs of electrostatic plates. Ions formed by electron loss within the field were deflected from the initial path. The cross section was determined from the attenuation observed as the potential was applied. In preliminary experiments it was found that the data were nonreproducible. The cross section was a function of the chamber pressure and also of the particular electrostatic plate used in the determination. To eliminate the effects of elastic scattering, the lower aperture of the cross-section chamber was replaced by a movable 0.005-in. slit. This slit was moved linearly across the beam, and the emergent flux of particles was integrated. The cross sections determined by this integration method were found to vary in the same manner as the data obtained with the aperture, indicating that elastic scattering played little or no role in the measurement of the cross sections. These variations in cross sections were traced to differences in the pressure established in the neutralizer.

[1] P. M. Stier, C. F. Barnett, and G. E. Evans, *Phys. Semiann. Prog. Rep. March 10, 1954*, ORNL-1705, p 43.

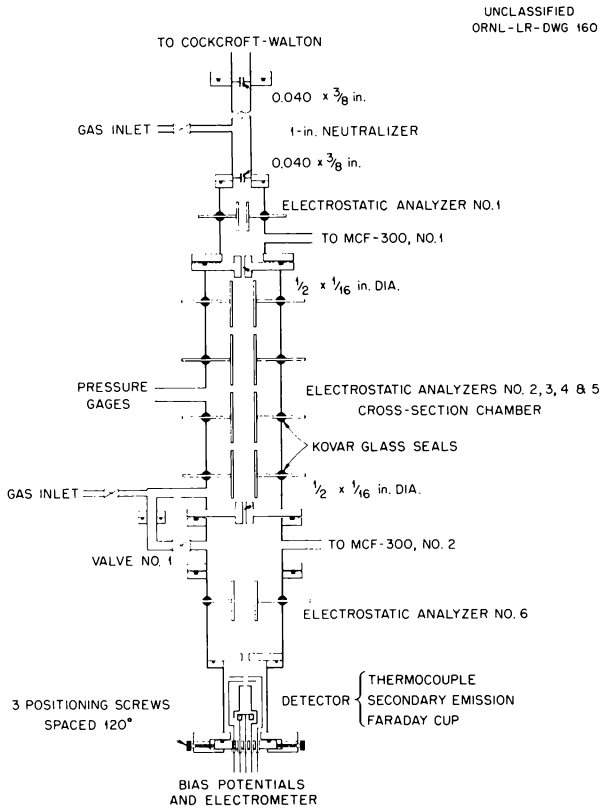

Fig. 1. Schematic Drawing of Electron-Loss Apparatus.

Figure 2 shows the dependence of the cross section on the neutralizer pressure for a 100-kev He^0 beam in hydrogen. Since only neutral helium atoms are incident on the charge-exchange chamber, it must be concluded that the character of the neutral beam was dependent on the amount of gas in the neutralizer. The conclusion drawn from the observations was that an appreciable number of electron capture collisions in the neutralizer leave the fast helium atom in the metastable state. For low neutralizer pressures, when the mean free path is comparable to the dimensions, there is a high probability of the fast helium atoms emerging in the metastable state. As the pressure is increased, the small-angle elastic collisions subsequent to the capture collision may de-excite the helium atoms.

This explanation is supported by the curves (Fig. 2) for the fast H, N, and Ne atoms. The measured cross section depends on the neutralizer pressure for Ne and He but not for H and N. This

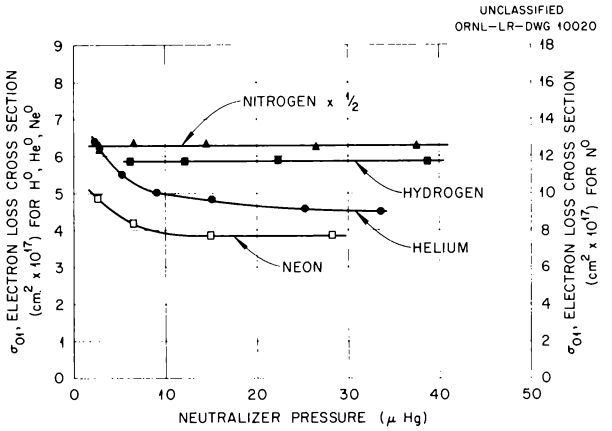

Fig. 2. Variation of the Measured Cross Section σ_{01} with Neutralizer Pressure for Fast H^0, He^0, N^0, and Ne^0 in Hydrogen. Energy, 100 kev; pressure in charge-exchange chamber, ~2 μ Hg.

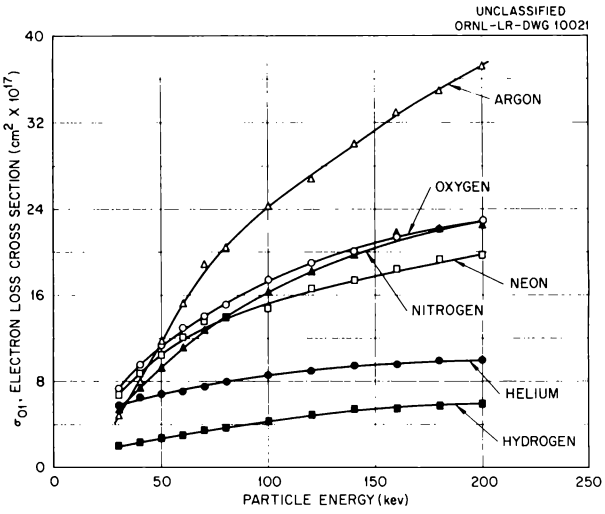

Fig. 3. Electron Loss Cross Section σ_{01} for He^0 in Various Gases.

corresponds to the existence of strong metastable states for He and Ne atoms but no highly populated metastable states in H and N.

At higher pressures, equilibrium is established between the flux of ions, atoms in the ground state, and atoms in the metastable state. The cross sections reported are for electron loss by this equilibrium distribution of metastable-state and ground-state atoms. The energy dependence

of the electron loss cross sections determined in these experiments is shown in Fig. 3. The much more rapid variation of the cross section with energy is conspicuous for the heavier stopping gases.

The data from the present experiment also allow calculation of the fraction, F_0, of the helium beam which is neutral after passage through a "thick" gas target. The values obtained agree well with the previously reported measurements.[1]

RECOIL SPECTROMETRY

A. H. Snell F. Pleasonton

MAGNETIC SPECTROMETRY OF THE NEUTRINO RECOILS OF A^{37}

The work on recoil measurements in A^{37} has been completed and will appear in the December 1 issue of *The Physical Review*. What has been accomplished can be described by quoting the abstract of the paper: "The ions that recoil from neutrino emission in the electron capture decay of A^{37} have been subjected to magnetic spectrometry with a resolution amounting to 2.8% in energy. They are found to have an energy of 9.63 ± 0.06 ev, which is in agreement with the value 9.65 ± 0.05 ev to be expected on the basis of a two-body breakup, the neutrino having an energy of 815 ± 2 kev as determined by others from the threshold of the $Cl^{37}(p,n)A^{37}$ reaction. The momentum balance sets an upper limit of about 5 kev for the rest mass of the neutrino. Auger electron emission following the orbital electron capture leaves the recoils mostly multiply charged, the percentage abundances in charge states 1 to 7 being 6.2 ± 0.1, 15.7 ± 0.4, 39.2 ± 0.5, 26.7 ± 0.4, 10.0 ± 0.2, 1.8 ± 0.1 and 0.4 ± 0.1, respectively. Neutrals were not measured. The natural width at half-intensity of the singly-charged recoil line is 1.7 ev, which is fully accounted for by the thermal motion of the argon atoms. The natural width of the triply-charged recoil line is 2.5 ev, which is mostly but not entirely accounted for by thermal motion plus recoil from the emission of one 2300-ev *K* Auger electron. The singly-charged recoils are thought to result from *L*-capture and from *K*-capture followed by *K* x-ray emission, neither of these processes involving recoil from the 2300-ev Auger electron."

FUTURE PLANS

Because of the success with A^{37} in measuring the charge spectrum of the ions that result from the Auger processes following the creation of a vacancy in one of the inner shells of the chlorine atom, and because this is information of new and unique character, of interest in our knowledge of the Auger effect, an attempt will be made to measure like charge distributions for other elements. Xenon-131*m* appears to be a possible candidate for investigation. It results from a weak branch in the beta decay of I^{131} and will possess electronic shell vacancies as the result of the internal conversion of the gamma ray of de-excitation from the metastable level. The radioactivity will be quite weak, and we have modified our instrument to take this into account.

An electrostatic collecting system, called a "howitzer," has been built in such a way as to provide a conical region pervaded by a radial electric field that converges at the apex of the cone, which is at the object position for the magnetic spectrometer. Application of a small field in this region will throw most of the ions toward the spectrometer, and there should be a large increase in collection efficiency, as compared with the A^{37} experiment in which no collecting field was used. Upon arrival near the object position of the spectrometer, all ions will again be accelerated, this time by several hundred volts applied across a gap, and this acceleration will be so large compared with the voltage drop across the howitzer that point-of-origin effects in the howitzer will lead to only a small percentage spread in the final energy. Thus the whole line corresponding to each charge will be accepted by the spectrometer. The collecting voltage across the howitzer will be made inversely proportional to the charge of the ions being investigated, so that even though the ions have a small recoil energy (~1 ev) the efficiency of collection will be the same for all charges.

The apparatus has been assembled for this experiment, and we are at present working to get a sufficiently good vacuum without the use of refrigerants (liquid nitrogen would condense the xenon). The Operations Division is cooperating in the extraction and purification of the Xe^{131}.

ATOMIC-BEAM SPECTROSCOPY

J. E. Sherwood

The objective of this work is the measurement of moments of radioactive nuclei by observation of atomic-beam spectra. To this end, an atomic-beam magnetic-resonance apparatus has been constructed and is nearly ready for use. This machine operates in the conventional Rabi fashion,[1] except for the details to be described. A schematic diagram is shown in Fig. 1. Unlike conventional atomic-beam machines, this apparatus permits a direct and unique determination of the sign of the nuclear magnetic moment.

The deflecting magnets are a new design and are such that, in the absence of transitions, only states having a negative (total) magnetic moment reach the detector. Thus, for normal potassium

[1] J. B. M. Kellogg and S. Millman, *Revs. Mod. Phys.* 18, 323 (1946).

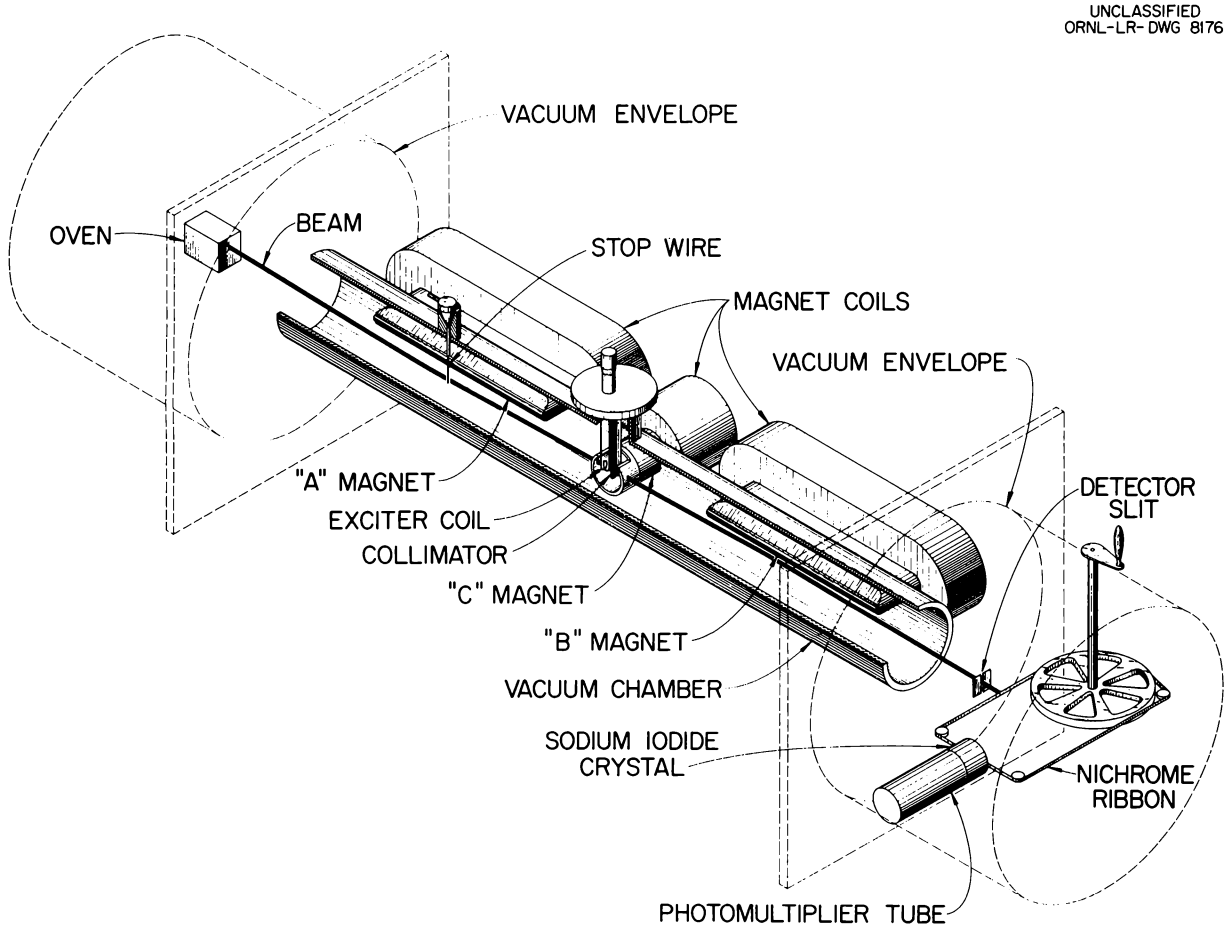

Fig. 1. Schematic Diagram of Atomic-Beam Apparatus.

($j = \frac{1}{2}$, $i = \frac{3}{2}$, $\mu_i > 0$), only the states (f, m) = (2, 2), (2, 1), (2, 0), (2, −1) are observed. This gives rise to eight high-frequency lines characterized by $\Delta f = 1$, $\Delta m = 0, \pm 1$. If the nuclear moment were negative, the states (2, −2), (1, −1), (1, 0), (1, 1) would be present, and nine lines could be seen. The present machine has been used to observe the high-frequency, weak-field spectrum of normal potassium. All lines were readily found except the (2, −2) → (1, −1) line. This indicates that the nuclear magnetic moment is positive, as is known to be the case.

These magnets also provide a "focusing" action, somewhat similar to that of the Princeton atomic-beam machine.[2] In the final form, this focusing action should result in considerably higher beam intensity than is possible with the conventional field arrangement.

Work at the present time is directed mainly toward perfecting the radioactivity detector. This consists, as indicated in the figure, of a metal tape on which the beam is allowed to deposit at one spot. This spot is then transferred to a scintillation counter where the activity is measured.

[2] A. Lemonick and F. M. Pipkin, *Phys. Rev.* **95**, 1356 (1954).

INTERPRETATION OF THE SMALL-ANGLE MAGNETIC SCATTERING FROM IRON

H. A. Gersch[1] C. G. Shull M. K. Wilkinson

Previous neutron-diffraction studies[2] on iron have shown the occurrence of extensive small-angle scattering at temperatures near the Curie temperature of 770°C. This report is concerned with the interpretation of those experimental results.

Van Hove has recently shown[3] how the Born approximation scattering of neutrons by ferromagnetic crystals can be expressed as a four-dimensional Fourier transform of a pair correlation function between spins which depends on a space vector and a time variable. His work includes a general treatment of the long-range part of the correlation which is present for temperatures close to the Curie temperature and which is a consequence of the large spontaneous fluctuations in magnetic moment in the vicinity of the Curie point. These fluctuations, which extend over distances much larger than interatomic distances and which decay over times much greater than microscopic relaxation times, give rise to greatly increased small-angle scattering of neutrons. The situation here is entirely analogous to the abnormally large scattering which occurs for a gas near the critical point. For the gas, the spontaneous density fluctuations increase indefinitely as critical conditions are approached, and result in greatly increased small-angle scattering of both neutrons and electromagnetic waves. For light waves, the phenomenon is called critical opalescence. By analogy, the scattering of neutrons by a ferromagnetic crystal near the Curie point is called critical magnetic scattering. It is this phenomenon which has been experimentally observed and analyzed by following Van Hove's ideas.

Theoretical treatment of the pair correlation function is, in general, a very difficult problem in statistical mechanics. However, near the Curie point, where the behavior of the correlation over macroscopic distances is important, the use of macroscopic methods introduced by Ornstein and Zernike[4] make possible a rather complete discussion. Application of these methods by Van Hove resulted in the following expression for the differential cross section per unit outgoing neutron energy interval $d\epsilon$:

$$\frac{d^2\sigma}{d\Omega\, d\epsilon} = \left(\frac{\gamma e^2}{m_0 c^2}\right)^2 \frac{2N}{3\pi\hbar} S_0(S_0+1)\frac{k}{k_0}|F(K)|^2 \frac{\Lambda_1 |\vec{K}|^2}{r_1^2(|\vec{K}|^2 + K_1^2)(\Lambda_1^2|\vec{K}|^4 + \omega^2)},$$

[1] Summer participant, Georgia Institute of Technology.

[2] M. K. Wilkinson and C. G. Shull, *Phys. Semiann. Prog. Rep. March 10, 1954*, ORNL-1705, p 31.

[3] L. Van Hove, *Phys. Rev.* **95**, 1374 (1954).

[4] L. S. Ornstein and F. Zernike, *K. Akad. Amsterdam. Proc.* **17**, 793 (1914); *Physik. Z.* **19**, 134 (1918).

where γ is the magnetic moment of the neutron in nuclear magnetons, N is the number of scattering atoms, each with spin S_0, $\vec{k}$ and $\vec{k_0}$ are final and initial neutron wave vectors, $\vec{K} = \vec{k_0} - \vec{k}$, $F(K)$ is the form factor for the magnetic electrons, and $\omega = \hbar(k_0^2 - k^2)/2m_n$.

The parameters r_1, K_1, Λ_1 describe the space and time dependence of the pair correlation between two spins, for distances large compared with interatomic distances and over times that are long compared with microscopic relaxation times. The description is of this form. The instantaneous correlation between a spin at the origin with one at a distance R is determined by the method of Ornstein and Zernike to be

$$\langle S_0(0)\, S_R(0)\rangle \cong (4\pi r_1^2 R)^{-1}\, S_0(S_0+1)\exp(-K_1 R),$$

valid for $K_1 v_0^{1/3} \ll 1$, where v_0 is the volume per spin. The parameter Λ_1^{-1} measures the decay time of a plane wave fluctuation of the magnetic moment. Further details of the time dependence are not necessary in the present case because calculations show that, in the range of experimental conditions we consider, the neutron energy transfers are negligible, compared with the incident neutron energy (the time the neutron spends in a scattering length is small compared with a relaxation time), and only the instantaneous correlation is necessary. The parameter K_1, which essentially measures the range of this correlation, is related to the length r_1 through

$$(K_1 r_1)^2 = \frac{\chi_1}{\chi},$$

where χ_1 is the susceptibility if exchange interactions were absent ($\chi_1 = C/T$, with C the Curie constant), and χ is the observed susceptibility. Detailed considerations show that r_1 varies smoothly as the temperature T passes through the Curie temperature T_c, so that, since χ approaches infinity as T_c is approached, K_1 tends toward zero. For $T \gg T_c$, $\chi_1/\chi \to 1$ and $K_1 \to 1/r_1$, so r_1 is a microscopic length of the order of interatomic separations.

To compare with the measured cross sections, $d^2\sigma/d\Omega\, d\epsilon$ has to be integrated over final neutron energy ϵ. Performing this operation for the case of negligible energy transfers, valid for our experimental conditions, results in

$$\frac{1}{N}\frac{d\sigma}{d\Omega} = \frac{2}{3}\left(\frac{\gamma e^2}{m_e c^2}\right)^2 \frac{S_0(S_0+1)}{r_1^2}\,\frac{1}{(k_0\theta)^2 + K_1^2},$$

where θ is the scattering angle, assumed to be small. This expression describes the special scattering which occurs in the temperature interval defined by $K_1 v_0^{1/3} \ll 1$ and in the small angular region defined by $(k_0\theta) \ll v_0^{-1/3}$.

Figure 1 is a typical measured differential cross section for neutrons of wavelength 0.9 Å scattered from iron at a fixed scattering angle of 0.9 deg for several temperatures. In drawing the smooth curve through these points we have been guided by data taken over much smaller temperature intervals than those shown, for which the necessary slit corrections have not yet been made. Calculation shows that the effect of possible variations in the shape of the curve on the final results are rather slight.

In fitting the above expression to this curve, r_1 is determined from the differential cross section at $T = T_c$, and K_1 is chosen to fit the shape of the curve, assuming r_1 to be fixed. This assumption is supported by a detailed calculation of the long-range correlation function for a specific statistical model, the spherical model of a ferromagnet. These calculations show that r_1 varies by a negligible amount over the temperature range considered. The value for r_1 obtained from Fig. 1 is 1.1 Å.

Figure 2 shows the temperature dependence of K_1 obtained in this way. The result may be checked by calculating K_1 from the relation $(K_1 r_1)^2 = \chi_1/\chi$ by using the value for r_1 obtained above and the experimental values for the susceptibility. The values for K_1 so determined are also indicated in Fig. 2.

Almost identical results for r_1 and K_1 are obtained from experimental cross sections taken at several other small angles.

The theory is strictly valid for temperatures such that the range K_1^{-1} is much larger than interatomic distances; in the present case, this implies an upper limit of some 25° from the Curie temperature. However, the agreement between the two methods of determining K_1 appears satisfactory over a larger temperature range, in view of the rather large uncertainties in experimental susceptibilities (~30%) near T_c and of the precision of the necessary slit corrections applied to the experimental data.

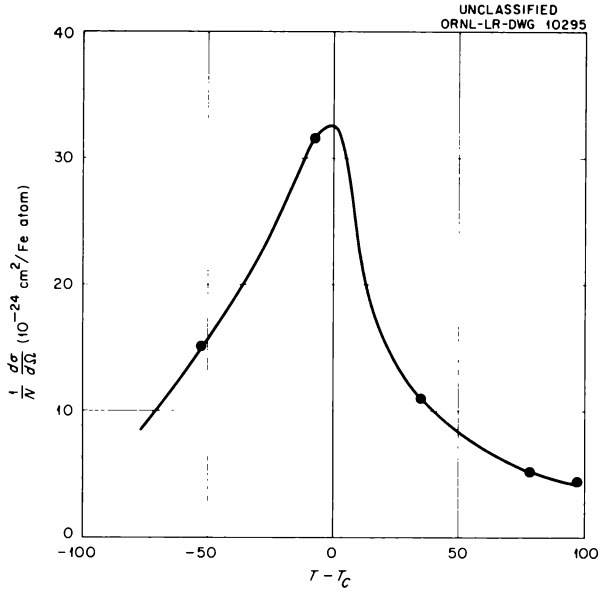

Fig. 1. Magnetic-Scattering Cross Section for Iron at 0.9 deg.

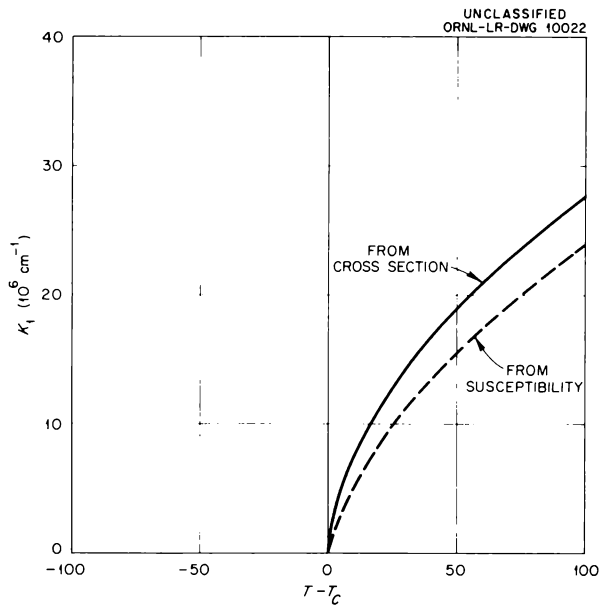

Fig. 2. Inverse Correlation Range.

ANTIFERROMAGNETIC STRUCTURES IN $MnBr_2$ AND $FeBr_2$

W. C. Koehler E. O. Wollan

Neutron-diffraction data have been obtained at temperatures down to 1.5°K for $MnBr_2$ and $FeBr_2$ in a search for evidence of long-range magnetic ordering of the ionic moments in these compounds. The bromides of iron and manganese have been reported to crystallize in the layer structure characteristic of CdI_2 – for example, a nearly hexagonal close-packed stacking of bromine ions, with the small cations located between alternate layers of bromine. This CdI_2 structure is one of the simplest of the known layer-type structures, and the investigations of magnetic structures of this layer type should lead to a better understanding of magnetic interactions in general and of layer structures in particular.

Stout[1] has observed a sharp anomaly in the specific heat of $MnBr_2$ at about 2.18°K which indicates a cooperative phenomenon. The diffraction data show (1) that below this temperature the compound is antiferromagnetic, with manganese ion moments aligned ferromagnetically within each hexagonal layer, (2) that moments in adjacent layers are aligned antiferromagnetically, and (3) that the orientation of the moments is normal to the hexagonal axis of the crystal.

The magnetic unit cell required to index the antiferromagnetic intensity maxima in the diffraction pattern is one with a c axis equal to twice the c axis of the chemical cell. The (001) reflection of the magnetic cell has been studied in detail as a function of temperature down to 1.5°K and shows a tendency to follow a Brillouin type of curve below about 2.2°K. At 1.5°K the moments have a value which is 0.7 of that at temperature saturation. Above 2.2°K the (001) intensity falls off slowly with increasing temperature, and the intensity fall-off is accompanied by appreciable line broadening. These effects may be attributed to short-range ordering phenomena and are being investigated more fully.

The magnetic and nuclear intensities also furnish evidence that, for this preparation of $MnBr_2$, the

[1] J. W. Stout, personal communication.

manganese ions are disordered from layer to layer with respect to the particular set of interstices between the layers of bromine ions which they occupy. Such ordering faults are quite common in hexagonal layer structures and have been observed, for example, in cobalt and in $NiBr_2$.

Work is now in progress to extend the range of temperatures to 1.2°K, at which the moments are expected to be 90% saturated. The increased magnetic intensities in the pattern should permit a more precise magnetic-structure determination.

Neutron-diffraction data at 4.2°K for $FeBr_2$ show that the same type of sheet structure as that found for $MnBr_2$ exists for $FeBr_2$, except that in this case the moments are directed parallel to the hexagonal axis. At 4.2°K the moments are essentially saturated, and there is evidence that the orbital moment of Fe^{++} in $FeBr_2$ is incompletely quenched.

MAGNETIC STRUCTURE OF Mn_2Sb

M. K. Wilkinson C. G. Shull H. A. Gersch[1]

A neutron-diffraction study of the magnetic structure of Mn_2Sb has been in progress for a considerable time, and much of the experimental data has been presented in an earlier report.[2] It is perhaps desirable to summarize briefly the previous results.

This compound has a tetragonal unit cell containing two molecules and has a ferromagnetic Curie temperature, T_c, of 277°C. The saturation atomic magnetic moment, as measured by Guillaud,[3] was found to be 0.936 Bohr magneton per manganese atom. In order to interpret some of the macroscopic magnetic measurements, Guillaud suggested that the compound actually was *ferrimagnetic*, with the two manganese atoms possessing different atomic magnetic moments coupled antiparallel. Since the two types of manganese atoms are located in crystallographically different sites, Guillaud postulated that they were $3d^5$ ions and $3d^7$ ions with spin atomic magnetic moments of 5 Bohr magnetons and 3 Bohr magnetons. The variation of the measured value of the saturation moment from unity was apparently due to a slight contribution from orbital magnetic moments. Using these values for the magnetic moments, Néel[4] successfully applied the molecular field method to explain the somewhat unusual temperature variation of the inverse magnetic susceptibility and spontaneous magnetization.

The first neutron-diffraction investigations were made with powdered samples, and data were taken at temperatures through T_c. The results were found to agree, in general, with the suggested model, but both the paramagnetic diffuse scattering above T_c and the coherent magnetic scattering below T_c indicated that the suggested magnetic-moment values were too high. Since the complexity of the powder patterns did not permit a straightforward determination of the magnetic scattering amplitudes and the corresponding magnetic moments, it was necessary to perform investigations on single crystals of the material. The magnetic contributions to the observed intensities of several single-crystal reflections were measured by the application of an external magnetic field to vary the direction of the atomic magnetic moments with respect to the scattering vector. These data, which were taken at room temperature, were normalized by a comparison of the magnetic-scattering amplitudes to the nuclear-scattering amplitudes of the same reflection, together with the known nuclear scattering data of manganese and antimony. Before a solution could be obtained for the magnetic-scattering amplitudes, $f_{Mn(I)}$ and $f_{Mn(II)}$, for the two types of manganese atoms, it was necessary to refer the magnetic-scattering amplitudes for the various reflections to zero scattering angle by the magnetic form factor. Since the magnetic form factor was also in doubt, an iterative process was required. For the first approximation, the magnetic form factor suggested by Erickson[5]

[1] Research participant, Georgia Institute of Technology.

[2] M. K. Wilkinson and C. G. Shull, *Phys. Semiann. Prog. Rep. Sept. 10, 1954*, ORNL-1798, p 49.

[3] C. Guillaud, thesis, Strasbourg, 1943.

[4] L. Néel, *Ann. phys.* 3, Serie 12, 137 (1948).

[5] R. A. Erickson, *Phys. Rev.* 90, 779 (1953).

for the divalent manganese ion was used, and only those magnetic reflections were considered which were in a range of sin θ/λ, where the various experimental and theoretical form factors were in reasonable agreement. The values of $f_{Mn(I)}$ and $f_{Mn(II)}$ obtained were then used to calculate the form factor required for each of the magnetic reflections of Mn_2Sb that was measured. A smooth curve through these form-factor values then represented a new average form factor from which new values of $f_{Mn(I)}$ and $f_{Mn(II)}$ could be determined by using all the reflections. This procedure was repeated until the values converged, and this convergence was found to be quite rapid.

Figure 1 is a graphical representation showing the final expressions for the magnetic-scattering amplitude of each of the reflections which was measured, while the final form-factor curve obtained from the magnetic scattering from Mn_2Sb is shown in Fig. 2. This form factor is essentially identical with that suggested by Erickson at values of sin θ/λ up to 2.6; at larger values, the two do not agree. The data shown in these two figures are representative of many sample specimens cut in the shape of pillars from two single crystals which were grown from separate melts. The results were checked with several pillars of different cross-sectional areas, and they were found to be quite reproducible. The values of the magnetic-scattering amplitudes at room temperature were determined to be 0.485×10^{-12} and -0.780×10^{-12} cm. These values disagree slightly with those which would be expected on the basis of magnetic measurements[6] of the net atomic moment made on one of our crystal specimens. The results of the magnetic measurements are represented by the dashed line, and the values determined by neutron diffraction would be expected to fall on this line.

In order to determine the saturation atomic magnetic moments, it was necessary to know the degree of magnetic saturation at room temperature for our samples. Furthermore, according to the Néel theory of ferrimagnetism, the degree of saturation would be different for the two magnetic sublattices of the material. Because of a change in direction of the atomic magnetic moments at 240°K, it was very easy to make these measurements by neutron diffraction. Between 240°K and T_c, the moments are directed along the c axis of the tetragonal unit cell, while below 240°K, the moments become located in the base plane of the cell. Hence, measurements taken on the (001) and (002) reflections at room temperature would be representative of only the nuclear contributions to the reflections, whereas data at 78°K would include also the magnetic contributions at that temperature. Since the magnetic contributions to the reflections at room temperature had already been measured in an external magnetic field, these additional measurements gave the ratio of the magnetization at 295°K to that at 78°K, and a slight extrapolation could be made to absolute zero. It was found that the degree of magnetic saturation at room temperature for the (001) and (002) reflections was slightly but significantly different. Since these two reflections have structure factors which depend differently on the magnetic-scattering amplitudes, $f_{Mn(I)}$ and $f_{Mn(II)}$, this difference was a definite indication of Néel's prediction that the two magnetic sublattices do not have the same temperature dependence of spontaneous magnetization. Furthermore, the degree of magnetic saturation of each sublattice at room temperature could be determined from the experimental data. With this information, the values of the saturation magnetic moments of the manganese atoms, with estimated limits of error, were found to be 2.10 ± 0.15 and -3.95 ± 0.30 Bohr magnetons. While these values are different from those predicted by Guillaud, they do, of course, agree satisfactorily with his experimental value for the net saturation moment. Furthermore, both the paramagnetic diffuse scattering and the coherent magnetic scattering which were obtained in the previous neutron powder-pattern measurements agree satisfactorily with these values.

Since the molecular field calculations of Néel had so successfully accounted for the temperature variation of the inverse susceptibility and spontaneous magnetization by use of 3 and –5 Bohr magnetons for the atomic moments, it was of interest to repeat these calculations for values of 2 and –4 Bohr magnetons. The results are shown in Figs. 3 and 4, together with calculated curves where Guillaud's values and the experimental data were used. It is apparent that both sets of values fit the experimental measurements equally well.

[6]We are indebted to B. Coles and J. E. Goldman, Carnegie Institute of Technology, Pittsburgh, Pa., for making these measurements.

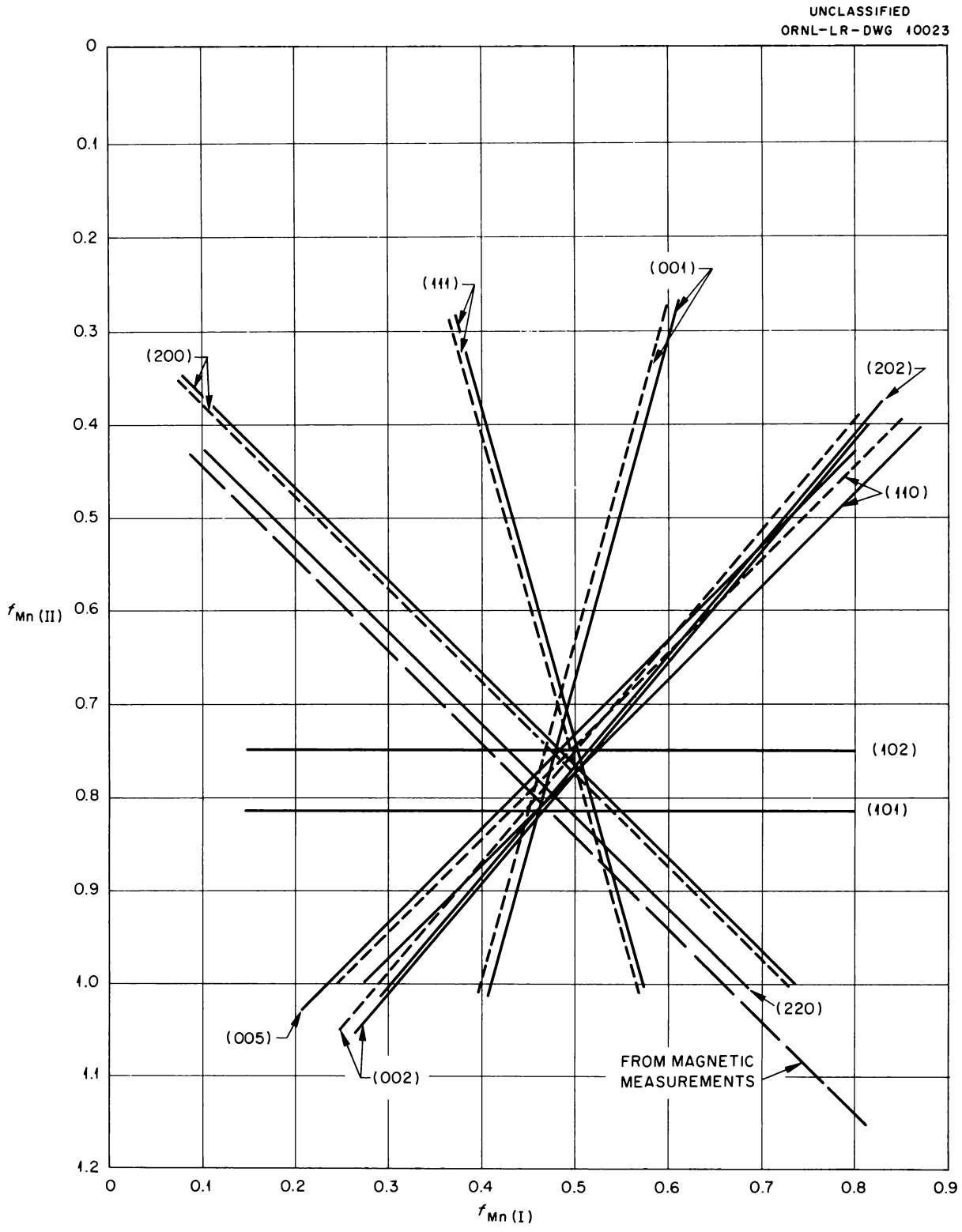

Fig. 1. Magnetic-Scattering Amplitudes of the Magnetic Reflections from Mn_2Sb Plotted as a Function of the Individual Magnetic-Scattering Amplitudes of the Two Manganese Atoms. Solid lines represent data on specimens cut from a crystal grown by Horizons, Inc., and dotted lines represent data on specimens cut from a crystal grown at the University of Missouri.

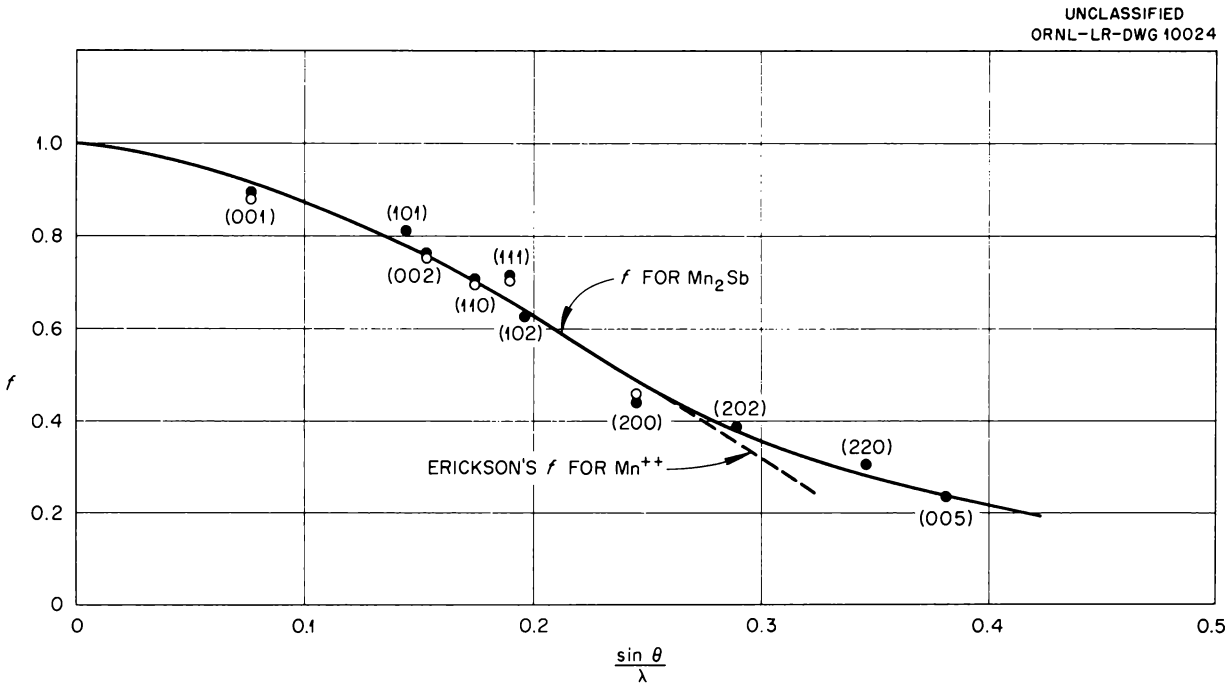

Fig. 2. Magnetic Amplitude Form Factor for Manganese Atoms in Mn_2Sb. The solid points represent data on specimens cut from a crystal grown by Horizons, Inc., and open circles represent data on specimens cut from a crystal grown at the University of Missouri.

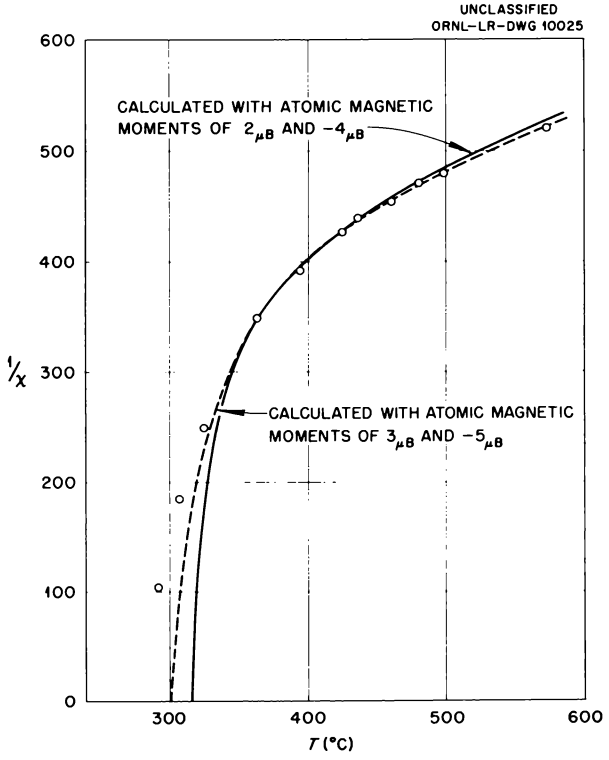

Fig. 3. Temperature Variation of Inverse Susceptibility of Mn_2Sb.

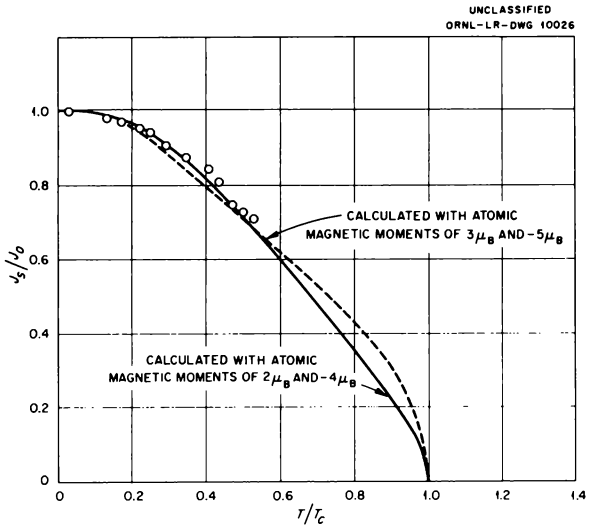

Fig. 4. Temperature Variation of Spontaneous Magnetization of Mn_2Sb.

NEUTRON-DIFFRACTION STUDY OF SYSTEMS OF PEROVSKITE-TYPE COMPOUNDS $La(Mn,Cr)O_3$ AND $(La,Sr)FeO_3$

U. H. Bents W. C. Koehler E. O. Wollan

The study of the mixed oxides of the perovskite system $(La,Ca)MnO_3$ which was previously reported[1,2] is extended to the systems $La(Mn,Cr)O_3$ and $(La,Sr)FeO_3$. It was of interest to compare the $La(Mn,Cr)O_3$ system to the $(La,Ca)MnO_3$ system, since the ends of both series had been found to have the same magnetic structure; they differ in that the sites of the trivalent and tetravalent ions were interchangeable by the simple exchange of electrons in the $(La,Ca)MnO_3$ system, whereas in the $La(Mn,Cr)O_3$ system, the trivalent ion, which has the same electronic configuration and net spin as tetravalent manganese, is not mobile in the crystal lattice. The primary interest in the $(La,Sr)FeO_3$ system was due to the large net spin of the iron ions and the general features of iron-iron interaction.

The samples were prepared by the previously used ceramic techniques outlined by Jonker and Van Santen.[3] All samples for the $La(Mn,Cr)O_3$ series, except the pure $LaCrO_3$, were fired in an atmosphere of pure nitrogen to prevent the production of tetravalent manganese. Controlled mixtures of oxygen and inert gases were used for the $(La,Sr)FeO_3$ series. A fair degree of success was achieved for the production of samples with desired composition. A sample of $LaMnO_3$ with only 2% Mn^{4+} was produced, and a sample of $SrFeO_3$ with 99% Fe^{4+} was finally obtained.

The present studies show the general trends of the antiferromagnetic structure transitions, but some of the structures for the mixed system appear to be complicated and as yet have not been completely determined. In the $La(Mn,Cr)O_3$ system it is found that the *G*-type structure, that is, antiferromagnetic coupling of a metallic ion with its six nearest neighbors, although diluted, persists over the large range of 0 to 70% manganese. The layer-type *A* structure of the pure $LaMnO_3$, where the manganese ions are ferromagnetically coupled in sheets and where adjacent layers are antiferromagnetically coupled, disappears at about 10% chromium content. In the range of 70 to 90% manganese, a diffraction pattern calling for a larger magnetic cell was found. For this range of composition no magnetic structure which gives satisfactory intensity ratios has as yet been devised. In the $(La,Sr)FeO_3$ system, the *G*-type structure characteristic of $LaFeO_3$ also persists over a large range of composition. In the region of 50% Fe^{+++}, a complex magnetic structure not previously encountered was observed. The samples with high concentration of Fe^{4+} were found to be paramagnetic down to 4.2°K, the lowest temperature at which patterns were taken. The results will be reported in more detail after some additional data have been obtained.

[1] E. O. Wollan and W. C. Koehler, *Phys. Semiann. Prog. Rep. March 10, 1954*, ORNL-1705, p 34.

[2] W. C. Koehler and E. O. Wollan, *Phys. Semiann. Prog. Rep. Sept. 10, 1954*, ORNL-1798, p 41; *Phys. Rev.* **100**, 545 (1955).

[3] G. H. Jonker and J. H. Van Santen, *Physica* **16**, 337 (1950); **19**, 120 (1953).

NEUTRON-DIFFRACTION INVESTIGATIONS ON THE PALLADIUM-HYDROGEN SYSTEM

J. E. Worsham, Jr.[1] C. G. Shull M. K. Wilkinson

Neutron-diffraction experiments have been started in an attempt to determine the positions of the hydrogen atoms in the palladium-hydrogen system. X-ray diffraction measurements have shown that as hydrogen is absorbed by the face-centered cubic lattice of palladium, two phases can be formed, depending on the hydrogen concentration. While both phases are face-centered cubic, the lattice constants are 3.88 Å for the unexpanded alpha phase of low hydrogen content and 4.02 Å for the beta phase of high hydrogen content. From an extensive review of the early experiments on this system, Smith[2] has concluded that the hydrogen is present in an extensive "rift network" in the metal. Recent diffusion experiments by Davis[3] on the alpha phase, however, indicate that the hydrogen occupies tetrahedral sites in the lattice.

Preliminary neutron-diffraction measurements have been obtained on powdered samples sealed in an aluminum cell. While attempts have been made to study both the palladium-hydrogen and palladium-deuterium systems for different concentrations of hydrogen and deuterium, inhomogeneities in the sample have prevented analyses on samples of low and intermediate concentrations. For the concentrated beta phase, the samples were more homogeneous, and a determination of the positions of the hydrogen and deuterium atoms can be made from the preliminary data. In this series of experiments, data were first obtained from pure palladium, after which hydrogen gas was absorbed at room temperature to a ratio of H/Pd = 0.63, at which composition only the beta phase exists. Upon completion of the experiments with hydrogen, the hydrogen was removed by heating the sample to about 100°C in a vacuum. Deuterium was then absorbed in the palladium to a ratio of D/Pd = 0.62, in the same manner as the hydrogen. This order of experiments is necessary, since the palladium lattice must first be opened by hydrogen before deterium can be absorbed. The diffraction patterns are shown in Fig. 1, and an analysis of the data shows that, in the beta phase, both hydrogen and deuterium occupy the octahedral sites of the face-centered cubic palladium lattice.

Attempts were made to absorb hydrogen gas in a crystal of palladium of square cross section $\frac{1}{16}$ in. on an edge and $\frac{3}{4}$ in. long. The apparatus permitted variation of the sample temperature between room temperature and 200°C, and the pressure of the hydrogen gas was variable up to $1\frac{1}{2}$ atm. No appreciable hydrogen was absorbed under any of the conditions accessible. The failure of the single crystal to absorb hydrogen was probably due to the large decrease in surface area from that present in the powder and also to the absence of deformations which would be a free passage for hydrogen into the interior of the crystal.

Attempts were also made to charge a single crystal of palladium with hydrogen electrolytically. However, the neutron scattering data indicated no appreciable hydrogen in the crystal. X-ray examination of the crystal surface showed the presence of the expanded lattice characteristic of the beta phase, but the surface had become somewhat polycrystalline, with a preferred orientation which was the same as the orientation of the uncharged surface.

[1] Summer visitor, University of Richmond.

[2] D. P. Smith, *Hydrogen in Metals*, University of Chicago Press, Chicago, 1948.

[3] W. D. Davis, *Diffusion of Gases Through Metals. I. Diffusion of Hydrogen Through Palladium*, KAPL-1227 (Oct. 1, 1954).

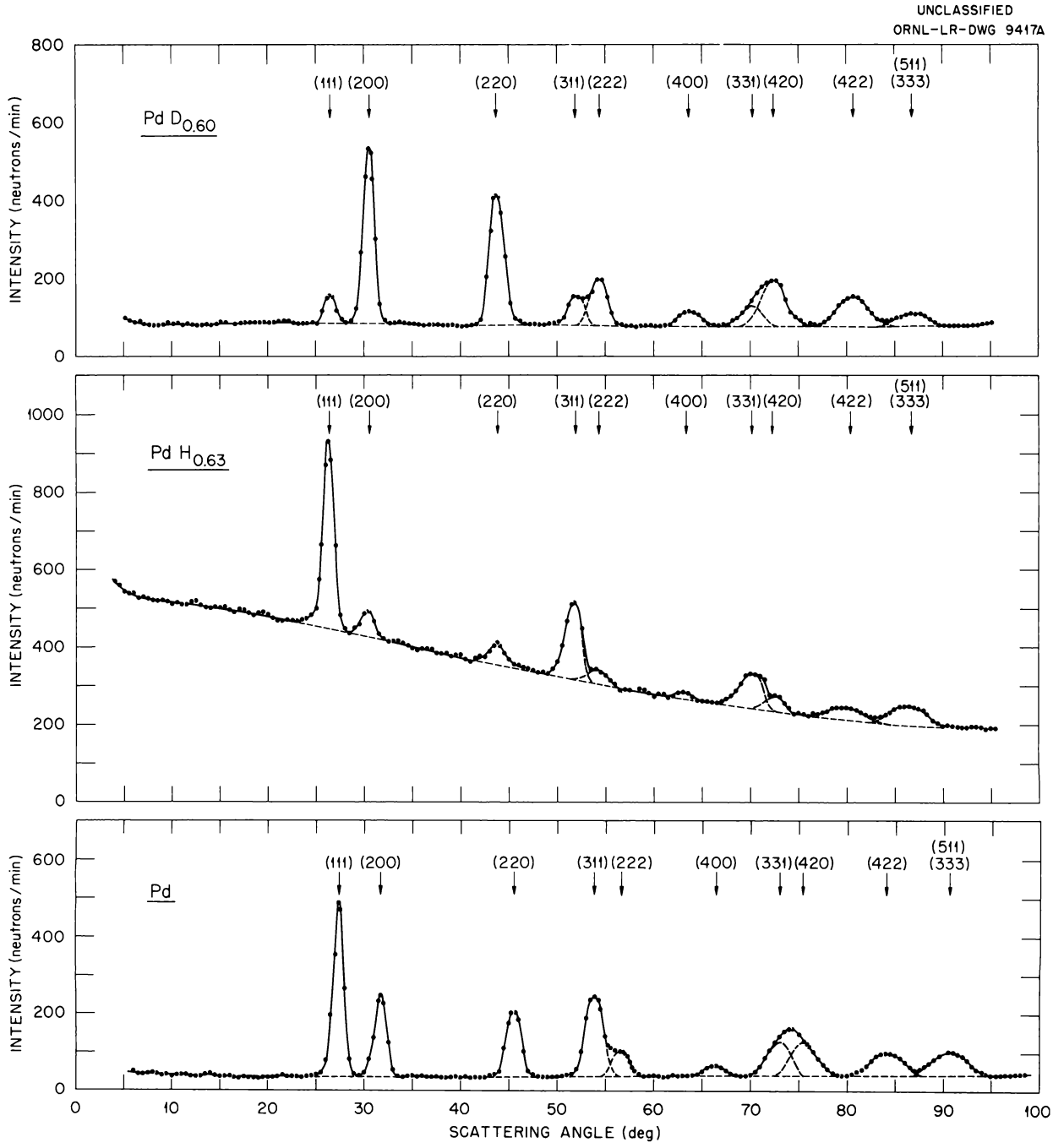

Fig. 1. Neutron-Diffraction Patterns of Pd, $PdH_{0.63}$, and $PdD_{0.60}$.

THE CASCADE ACCELERATOR

R. F. King W. M. Good
C. D. Moak H. E. Banta
A. W. Prichard

In April of this year the first of two accelerator tubes was put into operation in the 625-kv cascade accelerator installation. The tube is located on the floor below the high-voltage generator, and connection is made by means of a vacuum high-voltage feed-through insulator. An over-all view of the generator, the accelerator tube, the feed-through insulator, and the second accelerator tube now under construction is shown in Fig. 1.

The high-voltage supply is a G-E unit consisting of five 125-kv sections stacked in a vertical column. Each section contains a set of transformers, rectifiers, and filter condensers mounted in oil. In addition to the plate and filament transformers and the transformer windings used to drive the section above, each section is provided with a 115-v isolation transformer which passes power for the ion source up through the column to the top of the machine. The current capacity of the supply at 625 kv is 25 ma, well in excess of any anticipated target currents.

The feed-through insulator consists of an upper and a lower ceramic column with a conductor running along the axis for the entire length of the two sections. The interior is evacuated by oil diffusion pumps placed at the mid-point.

During initial tests on the feed-through insulator, internal sparking and field emission currents were observed. At a given voltage setting, the sparking gradually diminished, and voltage could be advanced to a higher value. Over a period of two weeks, the insulator was gradually conditioned to withstand the full 625 kv available; however, it was found that after standing for several days, the insulator required a small amount of reconditioning.

A marked improvement in the stability of the insulator was observed when a small amount of argon was introduced into the vacuum system to quench field emission at the metal surfaces. The pressure was gradually increased to approximately 1 μ Hg; above this point the vacuum pumps did not work well. Up to an argon pressure of 1 μ, the performance of the insulator continued to improve, electron emission from the metal surfaces essentially disappeared, and internal sparking stopped. After several months of routine operation at 0.8 μ Hg argon pressure, gradual improvement in performance has been observed. The insulator is reconditioned under vacuum each day for approximately 5 min. The argon pressure is then raised to 0.8 μ and left there during accelerator runs. After extended runs at top voltage, no reconditioning seems to be necessary.

The accelerator tube, located at the foot of the feed-through insulator, is equipped to handle protons, deuterons, tritons, He^3 ions, and alpha particles with ion currents up to 1 ma. The lens system delivers a well-focused beam of approximately 3 mm in diameter over the voltage range of the machine. The accelerator has been used principally for He^3-ion bombardments in some studies of light-element charged-particle reactions. A component of doubly charged He^3 ions in the beam has been used to push the bombardment energy up to 1.25 Mev.

The second accelerator tube being constructed in a large open space on the upper floor will be used principally as a high-flux neutron generator.

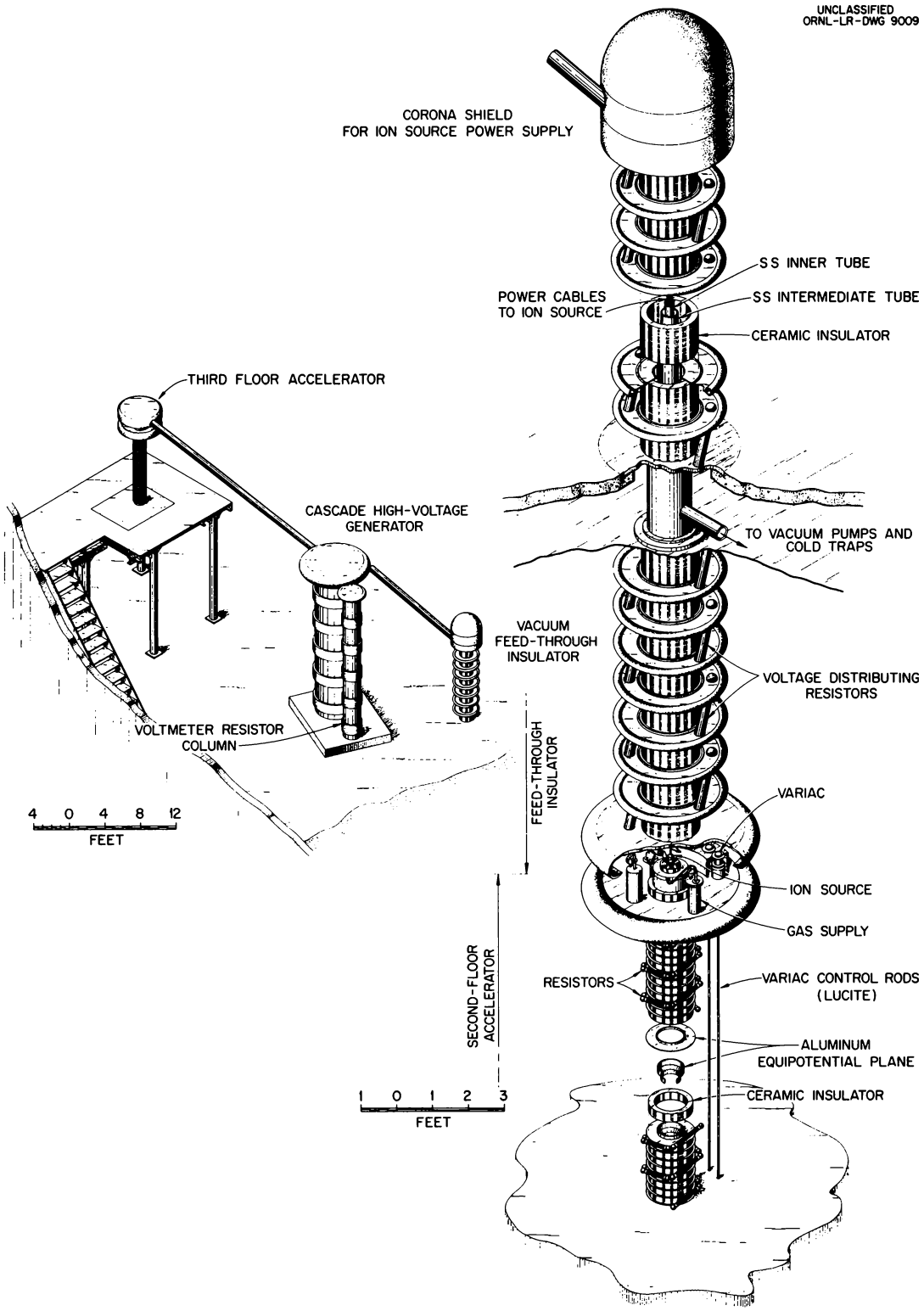

Fig. 1. Cascade Accelerator Installation.

AN ION-SOURCE PULSING SYSTEM

R. F. King V. E. Parker

Certain neutron time-of-flight techniques are being developed at the Laboratory. Short bursts of ions from a high-voltage accelerator are used to generate neutrons and trigger the timing circuits. In the past, short bursts of ions have been made by deflecting the accelerated beam back and forth across an aperture. A serious neutron background arose when the deflected beam was off the target. By pulsing the ion beam before it enters the accelerator, one can reduce this background and at the same time increase the average beam current without excessively loading the accelerator tube.

A beam pulser was designed to fit between the ion source and an aperture placed at the entrance to the accelerator tube. A unipotential lens was placed midway between the source and the aperture to bring the ions back into focus with unit magnification. The apparatus is shown in Fig. 1. Radio-frequency voltage applied to the deflector plates was used to sweep the focused beam first to one side then the other, permitting it to pass through the aperture and enter the accelerator tube only for a short time at and near the zero axis of the sweep voltage. The 0.5-Mc sweep voltage used was large enough to sweep the beam across the aperture in 0.01 cycle.

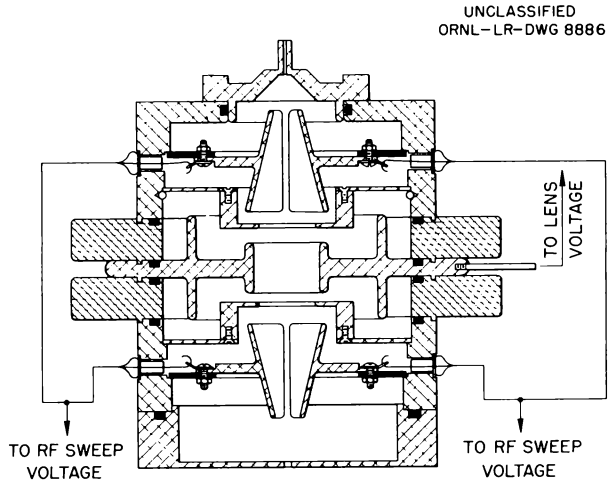

Fig. 1. Beam-Pulser Assembly.

After test-bench experiments, the pulser was installed on the 625-kv cascade accelerator, with a fixed aperture 150 mils in diameter. As on the test bench, the best method of tuning was to set a desired value of extraction voltage and coil current, then adjust the accelerator lens voltage, the unipotential lens voltage, and the sweep voltage for the most uniform pulse height and desired length, as displayed on a Tektronix model 517 oscilloscope. All three of these adjustments interacted with one another somewhat. The focused but unswept proton beam on the target was 150 to 200 μa and appeared circular in cross section and well-focused to a diameter of 100 mils. When the sweep voltage was turned on, the 100-mil spot would change to a line 100 mils wide and $\frac{3}{4}$ in. long.

The duration of these short pulses could not be accurately measured with the oscilloscope. The time spread of the gamma rays produced by bombarding a lithium target with the pulsed proton beam at an energy of 500 kev was measured by a multichannel time analyzer built by J. H. Neiler and known to have a resolving time of less than 7 mμsec. Pulses were produced that had steep sides and quite short tails and which were 16 mμsec wide at half maximum. Average current on the target was about 1.5 μa or about 1% of the unpulsed beam current.

TIME INTERVAL–PULSE AMPLITUDE CONVERTER

J. H. Neiler G. G. Kelley P. R. Bell H. E. Banta

A time interval–pulse amplitude converter has been constructed which will permit use of the standard ORNL multichannel analyzers for time-interval analysis. The useful range of the instrument is approximately 10^{-9} to 10^{-6} sec, with a time resolution of less than 10^{-9} sec for fast pulses from a mercury-relay pulser and approximately 5×10^{-9} sec for annihilation radiation pulses in a pair of scintillation counters. The circuit diagram of the converter is given in Fig. 1, and a block diagram of the converter and the associated circuitry for use with a pulsed neutron source is given in Fig. 2. The dashed box encloses those blocks which comprise the converter itself. The arrangement for use with two scintillation counters or a pulser is quite similar.

The wide-band amplifiers and inverters ahead of the converter provide input signals of the required amplitude and fast rise time. One of these input signals must be negative at the input of the converter. It should have an average repetition rate not greater than about 20,000 pulses/sec in order to prevent pile-up in the A-1D amplifier driving the multichannel. Usually, two Hewlett Packard wide-band amplifiers are used for this signal, with the second amplifier driven to about four times overload by the signal which is being timed. This signal cuts off V_1, providing pulses which rise rapidly to about 3 v above B+ as the shorted delay line discharges. The length of the pulse at the plate of V_1 is about 30×10^{-9} sec. The diode lengthener thus applies a fast-rising lengthened pulse to the grid of V_3 and the plate of V_2, which are both normally biased off; V_3 is turned on by this pulse and draws a constant current of about 0.5 ma as long as it is on. This current is integrated at the plate by the input capacitance of a standard ORNL A-1D linear amplifier. The result will be an output voltage from the amplifier proportional to the conduction time of the constant current for times up to the clipping time of the amplifier tube. Termination of the conduction interval occurs when the second input signal arrives. This signal turns on V_2 and thus rapidly returns the plate to B+ and the grid of V_3 to the normal biased off condition. The second input signal must be

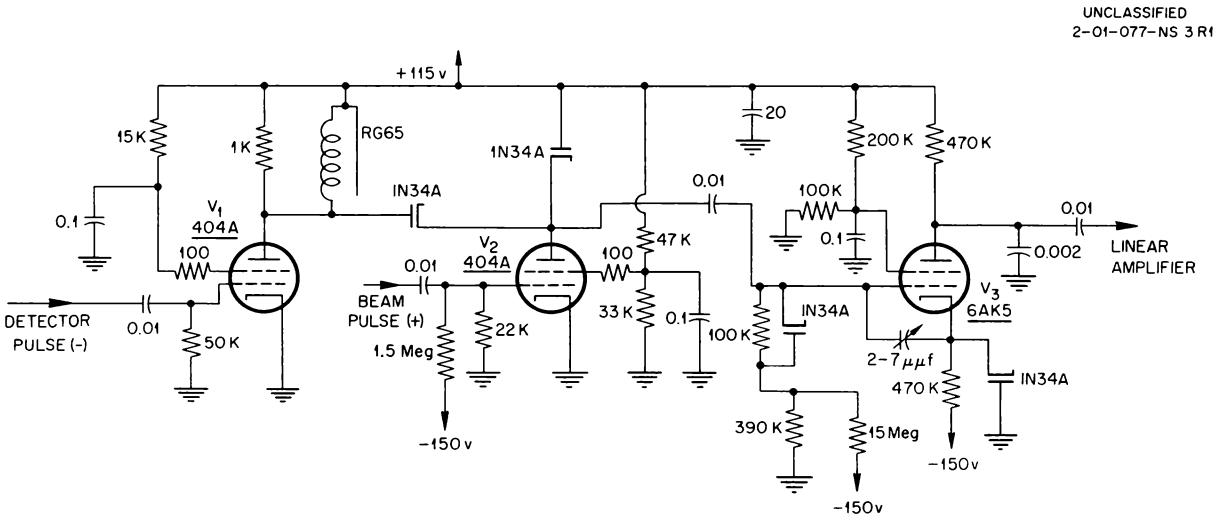

Fig. 1. Circuit Diagram of the Time Interval–Pulse Amplitude Converter.

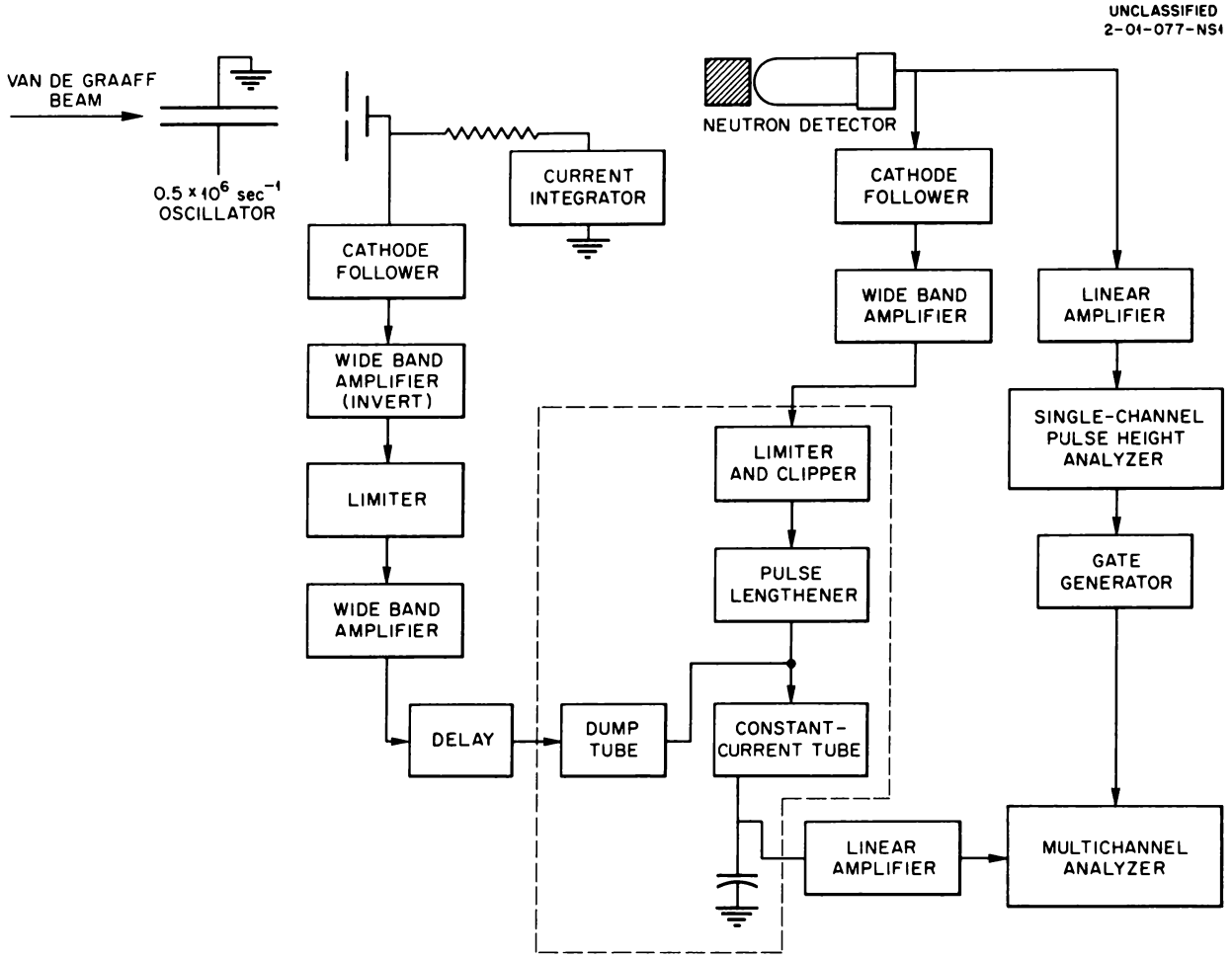

Fig. 2. Block Diagram of Multichannel Neutron Time-of-Flight Spectrometer.

positive, of about a 4-v amplitude, and should be essentially the same shape as the plate signal of V_1. In order to provide this shape, a limiter stage is provided ahead of the converter, and the limited signal goes through one stage of wide-band amplification. After this final amplification, the signal is delayed to provide the proper time relationship between it and the detector pulse. This delay should be greater than the sum of the longest time interval to be measured plus the clipping time in the plate of V_1.

The arrangement shown in Fig. 2 is being used for velocity selection of intermediate-energy neutrons (2 to 40 kev) and spectrometry of fast neutrons (1 to 10 Mev). (See paper in this semi-annual, entitled "Millimicrosecond Time-of-Flight Neutron Spectrometry.") In both cases a pulsed beam from the 2.5-Mev Van de Graaff is produced by deflecting the beam past a slit so that bursts of charged particles strike the target twice per cycle of beam deflection. The oscillator frequency ordinarily used is 500 kc, although both lower and higher values are possible by changes of capacitance and inductance. The present repetition rate of 10^6 beam pulses/sec may be near the upper limit, since there is a need for recovery time in the converter circuitry. The deflector plates are 4-ft tantalum sheet channels spaced to just avoid intercepting the undeflected beam. The slits which intercept the beam are at a distance of approximately 18 ft from the center of the deflector plates. In order to prevent excessive beam loss due to beam divergence, a strong-focus lens is used, centered 4 ft from the deflector center, to bring the beam back to a focus at the slits.

The target assembly was designed for minimum capacitance and scattering in the forward angles, while allowing for electrical shielding of the target and cathode-follower input.

For intermediate energies, the $Li^7(p,n)Be^7$ reaction is used. The higher-energy work is presently concerned with (d,n) stripping measurements on light nuclei but is directed toward inelastic neutron scattering studies. The operation of the time analysis system is the same in either case. The charge pulses on the target are amplified, delayed, and limited to provide the time reference signal indicating the starting time of the neutron burst. The neutron detector is placed to allow flight times of the order of several hundred millimicroseconds, and the delay of the beam pulse is chosen accordingly. The pulse amplitudes recorded by the multichannel are thus proportional to the difference between the neutron flight time and the fixed delay of the beam pulse.

Detection of the intermediate-energy neutrons is accomplished by an NaI(Tl) crystal which observes the 478-kev gamma ray from the $B^{10}(n,\alpha\gamma)Li^7$ reaction in a slab of enriched B^{10} placed between the crystal and the neutron source. In addition to the fast signal from the NaI, treated as described above, a slower, linear signal is used to provide a gate signal to the multichannel analyzer only when the detector pulse appears in the single-channel window set over the 478-kev gamma photopeak. This reduces background in the timer and eliminates time jitter which would arise if a spread of amplitudes of detector signal were allowed to operate the timer and multichannel. Figure 3 is a typical time–pulse-height spectrum obtained while performing transmission measurements in the 5- to 15-kev region. The peak at 455 pulse-height units is due to the detection of $Li^7(p,p\gamma)Li^7$ gammas from the target; this peak provides a reference time and is used to calibrate the flight time corresponding to other pulse-height settings by varying by known amounts the beam pulse delay. The peak at 390 pulse-height units (phu) is the high-energy group of neutrons from the $Li^7(p,n)Be^7$ reaction, and the broad peak from 150 to 275 phu corresponds to the low-energy group of neutrons between 5 and 15 kev produced in the relatively thin target. The sharp break at 120 phu marks the top of a pedestal produced by the grid cathode capacitance of V_3.

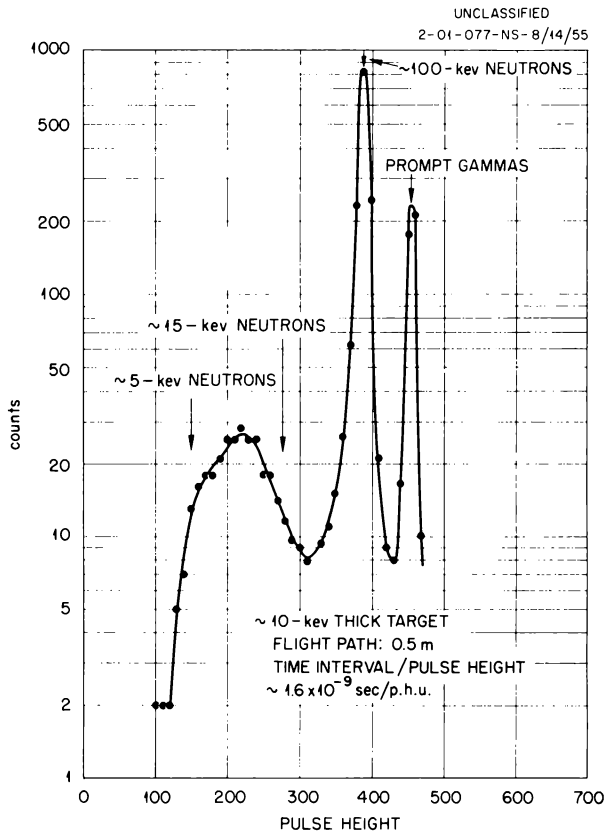

Fig. 3. Pulse-Time Spectrum of Neutrons from $Li^7(p,n)Be^7$.

A measure of the over-all time resolution of the system is provided by the width of the gamma-ray peak. When the delay is reduced and the multichannel gain increased in order to provide sufficient channels for good resolution of this peak, the full width of the peak at half maximum can be made as narrow as 6×10^{-9} sec by sufficiently increasing the beam deflection. It is believed that the major part of this limiting resolving time arises in the electronics – specifically, jitter in the constant-current tube conduction interval.

Neutrons in the energy range 1 to 10 Mev have been detected by observing the proton recoils in organic phosphors. In this case the single-channel window is set rather wide or an integral bias is used, since the much faster decay time of the organic phosphors results in less time jitter from pulse amplitude variations. Over-all time resolutions are comparable to those obtained with the NaI(Tl) detector.

ENERGY RESPONSE OF CsI TO PROTONS

A. Galonsky C. H. Johnson C. D. Moak

Protons accelerated by the 5.5-Mv electrostatic generator were scattered by a thin nickel foil into a 2-mm-thick CsI(Tl) crystal placed at 90 deg with respect to the beam axis. A peak in the spectrum corresponding to elastic scattering of protons by nickel was observed, and the pulse height of the peak was measured with a precision pulser. Proton energies incident on the crystal were corrected for losses of energy in the nickel foil (0.56 mg/cm^2), in an aluminum reflector on the CsI crystal (0.20 mg/cm^2), and to the recoiling nickel atoms. The data obtained in this manner for eight proton energies between 0.88 and 4.33 Mev are represented by the crosses in Fig. 1. The least-squares-adjusted straight line is drawn through the crosses. The line extrapolates to 0.07 ± 0.02 Mev at zero pulse height.

These measurements on CsI may be compared with similar observations on NaI by Brolley and Ribe.[1] They find that pulse height vs proton energy is linear above 2 Mev but that the curve extrapolates to 0.28 Mev. When the greater light output and shorter decay time of NaI are not essential, the nonhygroscopic character of CsI makes it preferable to NaI as a scintillation detector for protons. Francis,[2] however, has observed a phosphorescent decay time of about 200 sec in CsI.

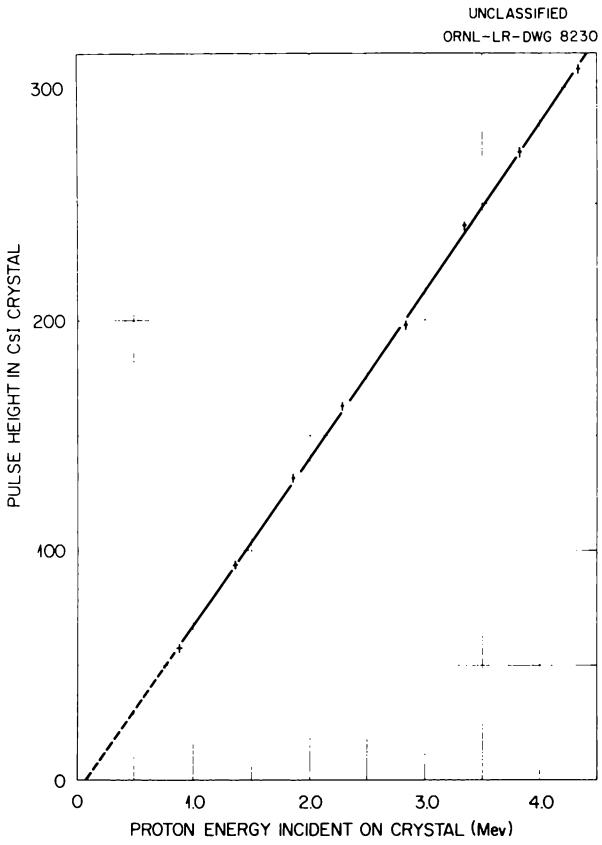

Fig. 1. Pulse Height for Scintillations Produced by Protons on CsI(Tl) vs Proton Energy.

[1] J. E. Brolley, Jr., and F. L. Ribe, *Phys. Rev.* **98**, 1112 (1955).

[2] J. E. Francis, private communication.

PHOSPHORESCENCE IN CsI(Tl)

J. E. Francis P. R. Bell

Cesium iodide (thallium activated) has been proposed and has been used as a scintillation phosphor. The main advantage of CsI(Tl) is that it is not deliquescent. Its use should proceed with caution because of a long-lived phosphoresce that has been observed.

Preliminary measurements indicate that the decay time of the phosphorescence is approximately 220 sec. The decay time was determined by measuring the d-c current from the anode of a photomultiplier tube on which was mounted a CsI(Tl) crystal after the crystal was exposed to ordinary room light and also after exposure to a large source of Co^{60} for 10 min.

The phosphorescence was so intense from ordinary room light that the voltage divider potentials were seriously disturbed. Pulses from a source were observed on an oscilloscope, and with the previous settings of the high voltage on the photomultiplier the pulses showed a reversed polarity. A number of minutes were required for the pulses to have the proper sign, and it was several hours before the noise level subsided to nearly normal.

RESOLUTION OF SCINTILLATION SPECTROMETERS

G. G. Kelley P. R. Bell R. C. Davis N. H. Lazar J. H. Neiler

An investigation is in progress to attempt to determine the factors involved in crystal resolution. It was believed (with some doubt) until recently that these factors were understood and consisted of (1) statistics of photoelectron production and collection at the photocathode and first dynode of the photomultiplier, (2) crystal nonuniformity, (3) amplifier noise, and (4) statistics of photon emission, the factors being listed in the usual order of importance, with the first factor of much greater importance than the others. The results of tests using a pulsed light source at the Savannah River Laboratory,[1] which indicated considerably better resolution than we have been able to obtain with scintillation crystals, led us to experiment with a light source of our own. Using this source, a pulsed electron beam on a P15 phosphor, we have obtained resolutions of better than 4% at an output pulse height equivalent to a 661-kev gamma ray on a good NaI(Tl) scintillation crystal. The best crystal resolution measured by us at this energy is 6.4%. This figure was obtained several times during the course of one day in 1952 and has not been approached since. The best resolution that can be obtained consistently is about 6.8%. Attempts to associate this difference with one of the smearing factors have failed.

The pulser which we use is a special RCA cathode-ray tube about 4 in. long by 1 in. in diameter mounted in the top end of a standard light shield. Below the face of the tube may be placed attenuators and filters on a copper-gauze electrostatic shield. Pulse lengths from 0.02 to 1.0 μsec have been used, with no appreciable change in line width.

The results are the same with the light collimated by distance as they are with the light diffused by a polyethylene diffuser or a ground Lucite diffuser, when light-pulse intensity is adjusted for the same voltage pulse.

The possibility that multiple-process pulses could give differing amounts of light, depending on the details of each interaction, has been refuted by an experiment in which a crystal was cut down into successively smaller pieces. When results were corrected for electron escape, the resolution remained unchanged at about 7.3%, with the crystal as small as $1 \times 1 \times 0.5$ mm. With such a small crystal, multiple processes are very unlikely. This same experiment made it appear that crystal nonuniformity of a gross nature could not be responsible. It also eliminated crystal self-absorption as the explanation.

[1] F. E. Kinard and J. S. Stutheit, *A Light Source for Testing Photomultiplier Tubes*, DP-42 (March 1954).

When the fraction of the light which is allowed to strike the photocathode from a scintillation crystal is reduced, resolution becomes worse but not according to the square root of the output, as would be expected if statistics in the photomultiplier were the principal factor (see Table 1). The light collection was varied by use of a light piper, as indicated in the table. It may be seen that the effect is the same as that which would be produced if the crystal had an intrinsic resolution of about 6%.

Such an effect would be produced if the light were emitted only in groups of about 40 photons/group, or if the interactions of an energetic electron with the lattice were such that a small number of possibilities control the amount of light energy produced. A grouping of the photons would cause the fluctuations of current during a pulse to be greater than those obtained from the pulser. Single trace photographs were taken of the pulse current in the two cases, with no apparent difference in noisiness at equal currents.

To test the possibility that the nonrandomness of the pulses from the pulse generator was responsible for the better resolution obtained with it, the pulser was used simultaneously with a source and a crystal. Its output was increased to such an extent that the light which got into the photomultiplier around the crystal produced a line just above the 661-kev line from the source. The pulser resolution was 4.4%, with an integral counting rate from the source of 2200 counts/sec, as it had been at the same pulse height with no crystal.

One further factor which has not been considered until very recently is the statistical fluctuation in the spectrum of the photons from pulse to pulse. Its influence depends in an involved way upon the emission spectrum of the phosphor and the shape of the response curve of the photomultiplier in the emission region. Attempts to assign the extra smearing observed to this effect are not conclusive at present, although indications are that it is too small to be seen. Further tests will be made by using pulses from different phosphors.

Other experiments will include an extension of those mentioned, as well as a measurement of resolution vs energy with a crystal and with the pulser over a wide range of energy.

TABLE 1. VARIATION IN RESOLUTION OF A SCINTILLATION COUNTER WITH VARIATION IN THE EFFICIENCY OF LIGHT COLLECTION

	Pulse Height	Crystal Resolution A	Pulser Resolution B	$\sqrt{A^2 - B^2}$
Piper + black tape	650	8.65	5.9	6.4
Piper alone	950	8.0	4.9	6.4
Piper + Al foil	1150	7.4	4.4	6.0
No piper	1400	7.3	4.0	6.1

EFFICIENCY OF NaI CRYSTALS

P. R. Bell R. C. Davis N. H. Lazar

In order to determine the intensity of gamma rays from a measured peak in a pulse-height spectrum, it is necessary to know the peak efficiency of the crystal, defined as the probability that a gamma ray will give a pulse proportional to its full energy if it strikes the crystal. The peak efficiency, ϵ_p, has been determined for $1\frac{1}{2} \times 1$ in. and 3×3 in. cylindrical NaI crystals and also for 3×3 in. cylindrical crystals beveled at 45 deg to the axis of the cylinder so that the top surface is 2 in. in diameter. Two methods were used for such a determination, and the general principles of the measurements will be described briefly below. In the first method, one uses the calculated total efficiency for NaI and measures the ratio of peak area to total area for sources which emit monochromatic gamma radiation. The total efficiency, defined as the probability that a gamma ray will interact with the crystal if it strikes the crystal, is a function only of the absorption coefficient of NaI and the position of the source along the axis of the cylinder, and has been computed by the Mathematics Panel for sources placed at various heights above $1\frac{1}{2} \times 1$, $1\frac{1}{2} \times 1\frac{1}{2}$, 3×3, and 3×3 in. cylindrical crystals beveled as described above. The product of R, the ratio of peak area to total area, with ϵ_T, the total efficiency of the crystal, is just ϵ_p.

To determine R vs energy, sources of Cr^{51} (0.320 Mev), Be^{7} (0.479 Mev), Sr^{85} (0.513 Mev), Cs^{137} (0.661 Mev), Nb^{95} (0.759 Mev), Mn^{54} (0.820 Mev), Zn^{65} (1.114 Mev), Na^{22} (1.275 and 0.511 Mev), Y^{88} (1.85 and 0.908 Mev), and Na^{24} (2.76 and 1.38 Mev) were used. The crystal and phototube were suspended by strings in the center of an empty room shielded on all sides by 2 ft of concrete. The nearest walls and the floor were at least 5 ft from the crystal. In this way, distortion of the Compton distribution due to scattering of gamma rays into the crystal was minimized. The sources were all placed on thin polyethylene foils, and only polystyrene absorbers were used when it was necessary to remove beta rays emitted from the sample. This reduced, as much as possible, bremsstrahlung and such gamma-ray scattering effects as would necessarily occur with these absorbers.

The second approach to determine ϵ_p was to measure the ratio of the disintegration rate in the source to the number of gamma rays detected which give pulse size proportional to their full energy, when all disintegrations are followed by gamma rays. The source disintegration rate was determined by a coincidence method, so that the efficiency of the beta detector, in this case a $\frac{1}{4} \times \frac{1}{4} \times \frac{1}{8}$ in. anthracene split crystal scintillation counter, does not appear in the calculations. In particular, the number of gamma rays detected by an NaI crystal was determined in coincidence with the beta rays detected in the anthracene crystal. The ratio of the observed peak area in the NaI to the number of beta rays, counted with a separate scaler at the same time, gives the desired peak efficiency times the solid angle, which can be determined very accurately. Corrections were made to the beta-ray counting rate to take account of gamma rays which interact with the anthracene and which then could not yield full-energy gamma-ray pulses in the NaI. Due to the small beta detector used, these corrections amounted to less than 5% in all cases.

Determinations of ϵ_p were made at source distances of 3.0 and 9.3 cm from 3×3 in. crystals, both beveled and unbeveled, and at distances of 2.5 and 7.0 cm from $1\frac{1}{2} \times 1$ in. crystals by both methods. Where the energies of the gamma rays were the same, the efficiencies calculated in both ways agreed within 2%. All the data for all crystals fell on smooth curves for the various distances. The estimated uncertainty of the values of ϵ_p for the 3×3 in. crystals is less than 3% for energies to 1 Mev and certainly better than 5% to 2.76 Mev.

Figure 1 shows the peak efficiencies obtained in these experiments. The $4\frac{3}{4}$-in. crystal data were obtained by calibrating source intensity with the 3×3 in. crystal and then measuring the full energy-peak area obtained with the larger crystal.

It may be noticed that the beveled 3×3 in. crystals have higher peak efficiencies than do the unbeveled ones. The cause of this may be traced, mostly, to the higher value of ϵ_T for the beveled crystals because of the greater distance traversed in the crystal, on the average, by gamma rays striking the beveled rather than the unbeveled ones. There is also a slight improvement found in

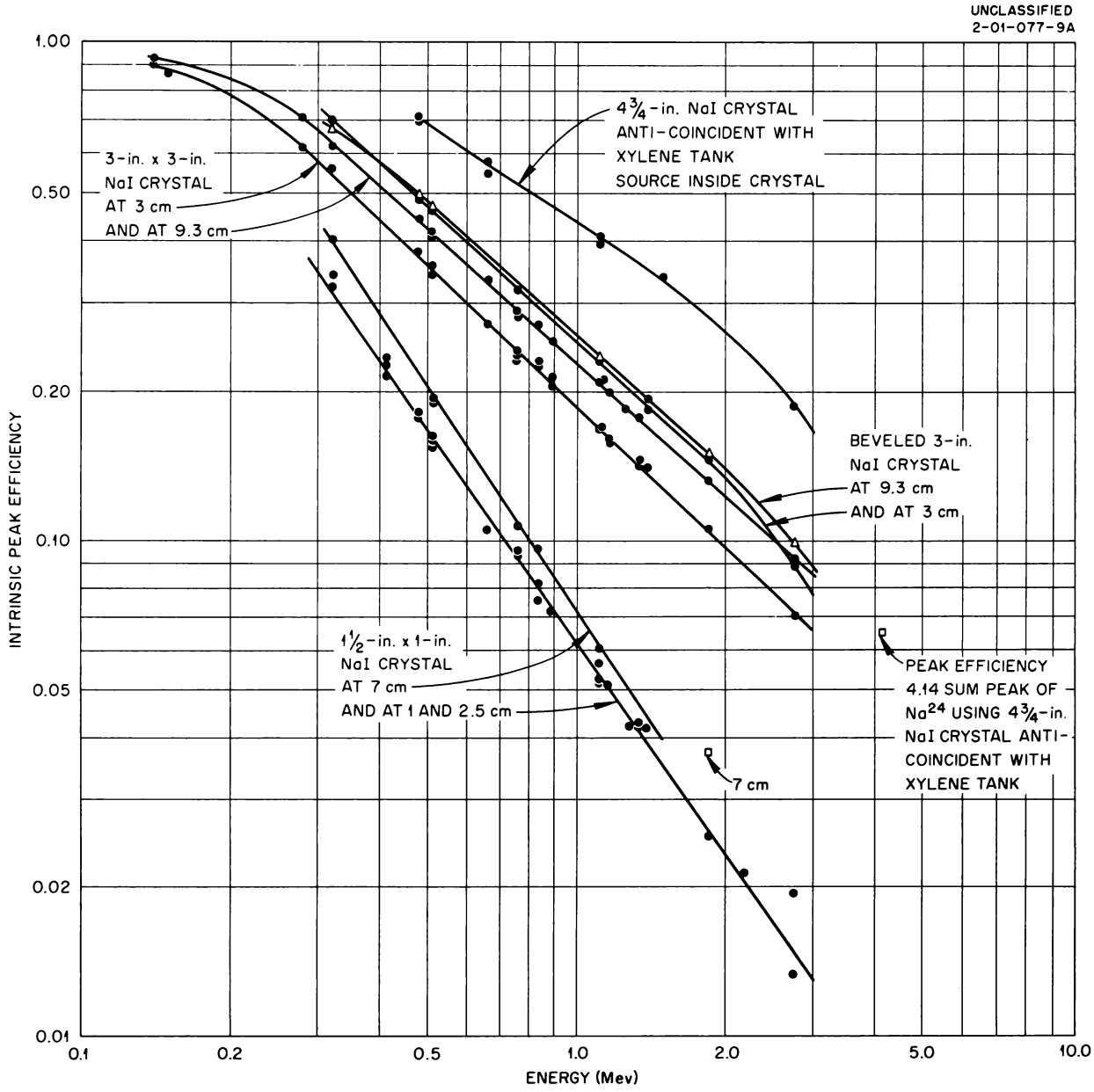

Fig. 1. Peak Efficiency vs Energy for Various NaI(Tl) Crystals.

R, especially at distances less than 5 cm, due to the removal of corners where gamma rays, after interacting, would then very probably scatter out of the crystal. In addition, the value of ϵ_p in the beveled crystals is less sensitive to source distance, and so the interpolation for source distances between 3 and 10 cm is more accurately obtained. An important mechanical advantage of the beveled crystals is obtained in performing coincidence experiments where 90-deg geometry is often necessary. In this case, the crystals may be placed closer to the source without being interfered with by lead shields,[1] and thus a lower source strength is required to obtain the same data, thereby improving the true-to-chance counting rate.

[1] P. R. Bell, *β and γ-Ray Spectroscopy*, K. Siegbahn, ed., p 161, North-Holland, Amsterdam, 1955.

LiI(Eu) MANUFACTURE

F. J. Muckenthaler J. Schenck

A limited crystal-growing program has been maintained in order to find a more dependable technique for making single crystals of europium-activated lithium iodide. These scintillators are used for neutron detection and are of interest as a possible neutron spectrometer. They are grown from the melt in a Vycor crucible under continuous evacuation. After the charge has melted, the crucible is slowly lowered out of the hot zone of a constant-temperature furnace.

There has been considerable difficulty with the cracking of the crucible and the crystal upon cooling them to room temperature. It is believed that this is caused by an acceleration by the melt of the devitrification of the Vycor, which so weakens the crucible that it is easily cracked by the slight contraction of the cooling lithium iodide. The difficulty has been overcome by using crucibles into which has been blown a thin lining of Vycor (Fig. 1). The lining is formed so that it is in close contact with the inside of the crucible, but not fused to it. By this method the crucible is protected against the weakening effect of the hot melt. Furthermore, the liner adheres to the crystal as the crystal contracts upon cooling, and pulls free of the crucible wall without cracking either the crucible or the crystal.

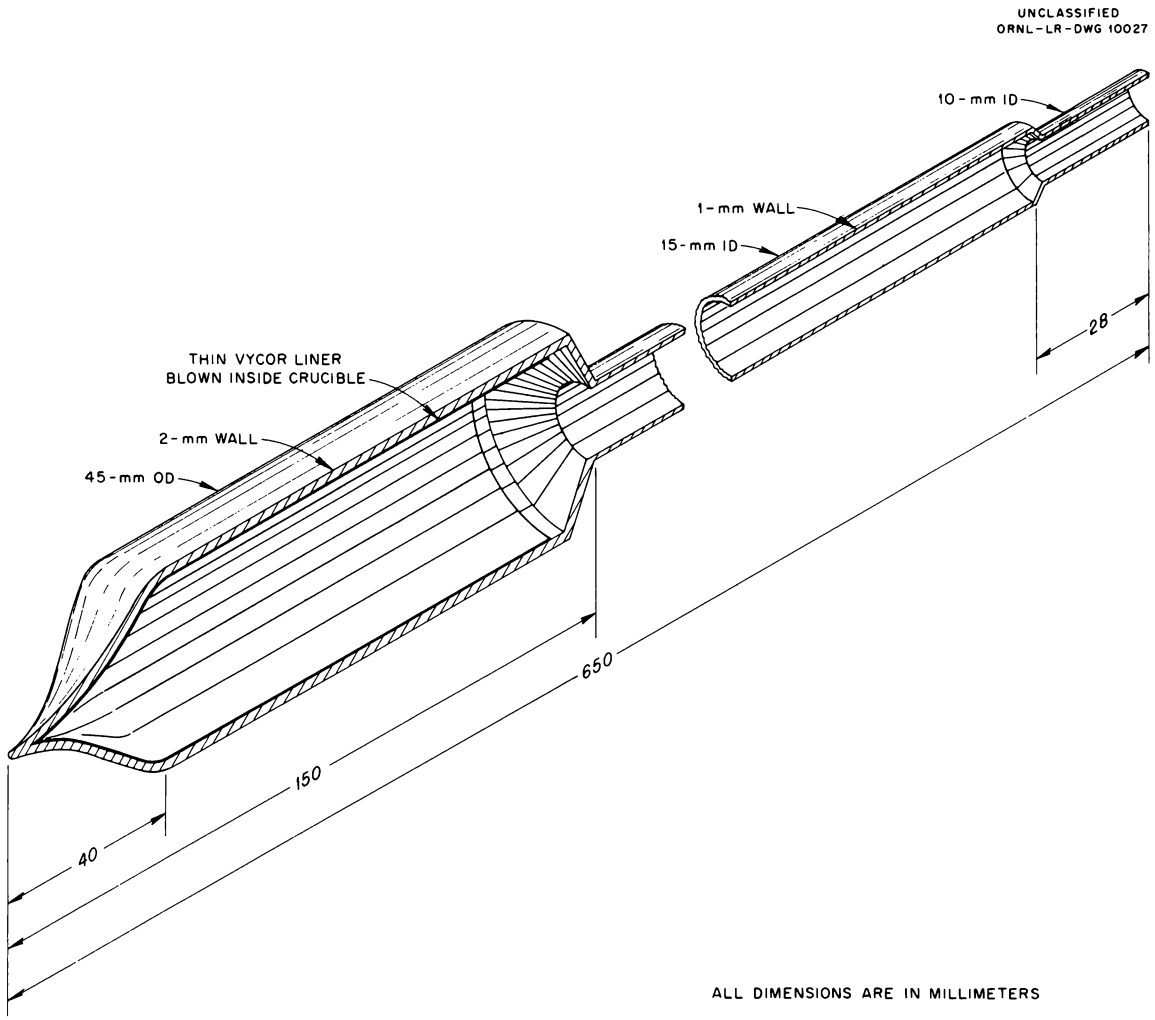

Fig. 1. New Crucible Used in LiI(Eu) Manufacture.

LIQUID SCINTILLATORS

R. C. Davis

Further investigation of liquid scintillators has been made. Three liquids, xylene, trimetatolylphosphate, and phenylcyclohexane, were tested by using *p*-terphenyl as a scintillator and by using various fluor converters. Bubbling hydrogen through the liquids to remove oxygen improved the pulse height tremendously in the cases of xylene and phenylcyclohexane; however, there was no improvement in the case of trimetatolylphosphate. The tests were made by using a 20-ml beaker with approximately 10 ml of solution optically connected with Dow Corning 200 silicon oil to a Dumont 6292 photomultiplier. The radiation used for pulse-height comparison consisted of the 624-kev conversion electrons from Cs^{137}.

The results of this investigation are given in Table 1. It was also found that BBO in quantities near 20 mg/liter could be added to our present liquid scintillator in the anticoincidence tank (containing xylene, *p*-terphenyl, and αnpo) and would increase its pulse height to that of xylene, *p*-terphenyl, and BBO. A 1¼-in. column of tank solution with BBO added was compared with a column of tank solution alone, with the source at 1, 6, and 9 in. from the photomultiplier tube. The edge of the Compton distribution from the Cs^{137} 661-kev gamma line was used for pulse-height comparison. At 9 in. there seemed to be very little improvement when BBO was added, but at 6 in. there was a 7% increase in pulse height, and at 1 in. there was approximately a 14% increase.

TABLE 1. PULSE-HEIGHT COMPARISON OF LIQUID SCINTILLATORS*

p-Terphenyl (~5 mg/ml) is used in each test

Liquid	Fluor Converter	Pulse Height (%**)
TMTP	PBD	11.4
TMTP	POPOP	17.2
TMTP	2,5-Diphenyloxazole	11.8
TMTP	MBBO	14.6
TMTP	Diphenylhexatriene	16.9
TMTP	BBO	18.8
TMTP	αnpo	13.9
Xylene	αnpo	40.3
Xylene	BBO	49.2
Xylene	POPOP	43.8
PCH	αnpo	46.1
PCH	BBO	53.1
PCH	POPOP	53.9
PCH	MBBO	31.6
PCH	Diphenylhexatriene	43.4
PCH	PBD	48.0
PCH	Tetraphenylbutadiene	11.7
PCH	2,5-Diphenyloxazole	41.0
PCH	Tetraphenylbutanediol	34.0
PCH (distilled)	POPOP	53.1

*Code of chemicals listed in table:

TMTP – trimetatolyphosphate

PBD – 2-phenyl-5-(4-biphenylyl)-1,3,4-oxadiazole

POPOP – *p*-di-(5-phenyl-2-oxazolyl)-benzene

MBBO – 2,5-di-(4-biphenylyl)-3-methyloxazolium *p*-toluenesulfonate

BBO – 2,5-di-(*p*-biphenylyl)-oxazole

αnpo – 2-(1-naphthyl)-5-phenyloxazole

PCH – phenylcyclohexane

**Value given is relative to the pulse height of anthracene.

NEUTRON COLLIMATOR EXPERIMENTS

A. Robeson G. Burleson P. R. Bell

A neutron collimator was needed to detect a weak source of fast neutrons in the presence of a greater number of neutrons coming from other locations in a test system. The detection efficiency was required to be large and the collimation rather sharp. The experiment was directed toward the construction of a collimator similar to the focusing gamma collimator described elsewhere in this report (see paper entitled "Collimators for the Medical Spectrometer"), since the requirements were rather similar.

DETECTOR SECTION

The detector was chosen to be a group of enriched BF_3 counters immersed in a moderator cell inside the collimator shield. In order to determine the most efficient moderator arrangement, a number of geometries were tried in which a polonium-beryllium neutron source was suspended above a single BF_3 counter at 36 in. The length of the paraffin stack was $11\frac{1}{2}$ in., except where noted, and the stack was placed on a thick concrete slab. Figures 1 through 5 show the effects found. It is obviously necessary to close the moderator over the counter. This is an unexpected result, since it had previously been found[1] that when a Po-Be source and a detector (fission chamber) were placed a fixed distance apart in a paraffin moderator, the counting rate was greatest when no moderator was between the source and the detector. Even a small thickness of paraffin caused a marked decrease of counting rate. The probable cause of the different results is the streaming of thermal neutrons which cannot occur in the totally enclosed case.

Since the proposed collimator has holes that cover only part of the moderator surface, it was necessary to decide how many counters would be required and what their spacing would be.

A long collimator with a 4×4 in. hole was constructed by using limonite-paraffin bricks in a stack 28×28 in. square and 24 in. high. The source was placed 8 in. below the end of the hole, and a single counter was placed in a $9 \times 12 \times 4\frac{1}{2}$ in. moderator (similar to top of Fig. 5 upside down) on top of the collimator stack. The moderator was surrounded with more bricks and was moved about over this hole. Figure 6 shows the counting rate obtained at various positions of the counter-moderator block. From this result it seemed reasonable to place multiple counters 7 in. apart, making each counter extend nearly to the edge of the moderator block. For this arrangement the counting rate should be approximately 80 to 90% of maximum for neutrons incident on the moderator between the counters.

[1] R. G. Gamble, thesis, University of Texas, 1955.

COLLIMATOR MATERIAL

Gross absorption measurements were made on a number of possible materials for use as shielding media. For the measurements with lithiated paraffin, borated paraffin, and limonite-paraffin, one counter was placed vertically in a $4 \times 4 \times 12$ in. paraffin moderator and surrounded by a $20 \times 20 \times 12$ in. shield stack. The test material was then stacked on top in a 20-in.-square layer of various thicknesses. The Po-Be source was kept at a constant distance of 38 in. above the top of the counter-moderator block. For the water and borated-water tests, the counter was placed vertically in a $4\frac{3}{8}$-in.-dia paraffin cylinder 12 in. long, which was placed in the bottom of a 22-in.-dia tank. The tank was filled to the level of the top of the moderator for the "zero" thickness value.

The absorption curves were approximately exponential after an initial transient. Table 1 gives the thickness of material required to reduce the neutron count by a factor of 10.

The limonite-paraffin blocks were quite noticeably better than any of the rest. The material was prepared by crushing Birmingham iron ore to an aggregate containing considerable fine material and filling the molds tightly by hand. The remaining space was then filled by adding molten paraffin. The block density was approximately 2.28 g/cc. Better fabrication methods would probably increase the density, bringing it closer to the limonite density of 3.6 to 4 g/cc. The limonite for these tests was a gift of the U.S. Pipe and Foundry Company and came from their mine at Russelville, Alabama.

A three-slot collimator with slots 12 in. long which tapered from $1\frac{1}{2}$ in. wide at the source end

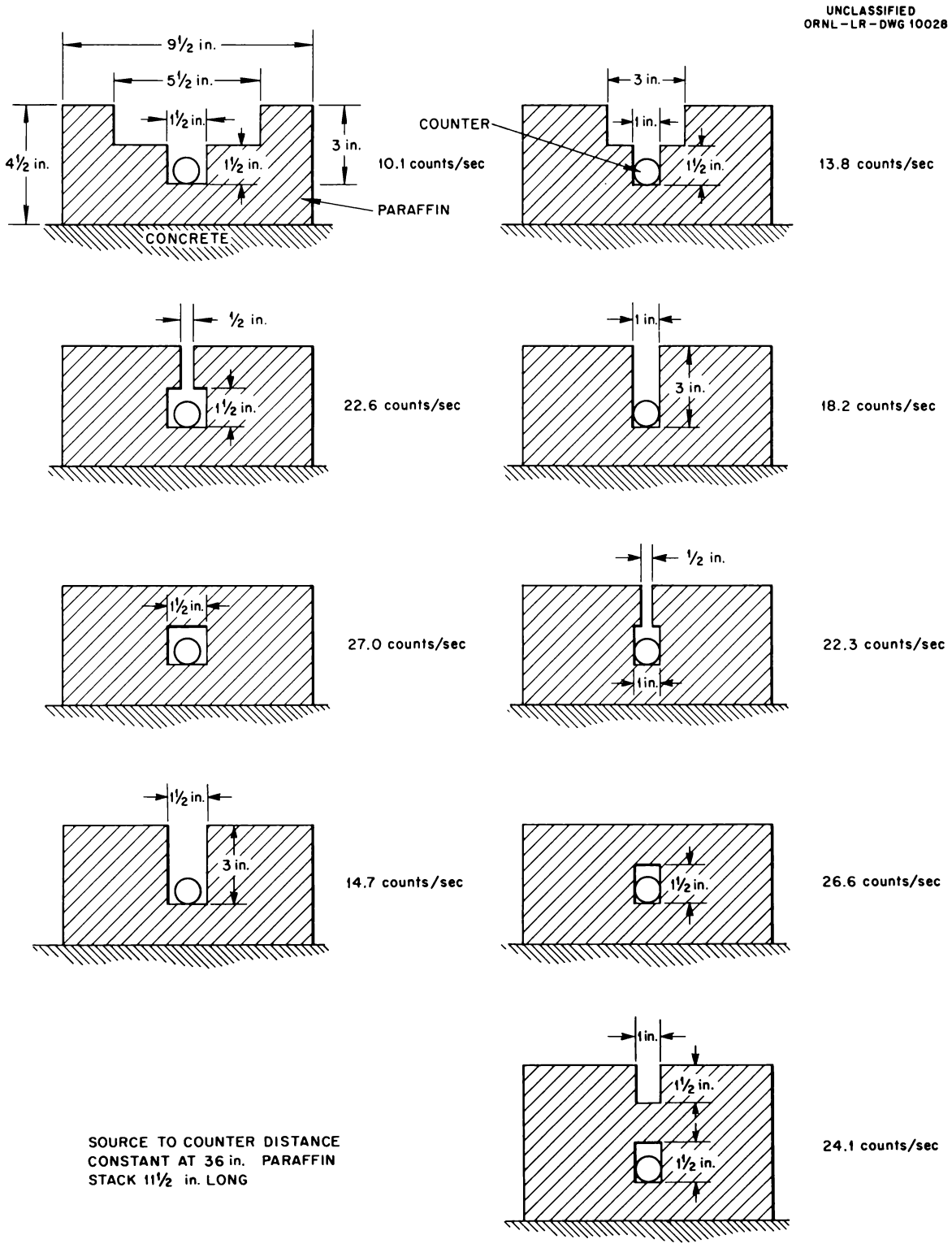

Fig. 1. Effect of Slots in Moderator on Counting Rate in BF_3 Counter.

to 5 in. wide at the detector end was mounted over a 24 × 12 × 4½ in. paraffin moderator block containing three BF_3 counter tubes. The moderator block was surrounded with ⅛-in. cadmium sheet. The outside dimensions of the complete collimator block were 32 in. by 48 in. square. The collimator was 24 in. from the top to the moderator, and an adequate amount of shield was placed around the moderator block on the sides and behind the collimator. Figure 7 shows the response of this collimator to the Po-Be source, as the source was moved above the end of the collimator 0.8 in. from the surface.

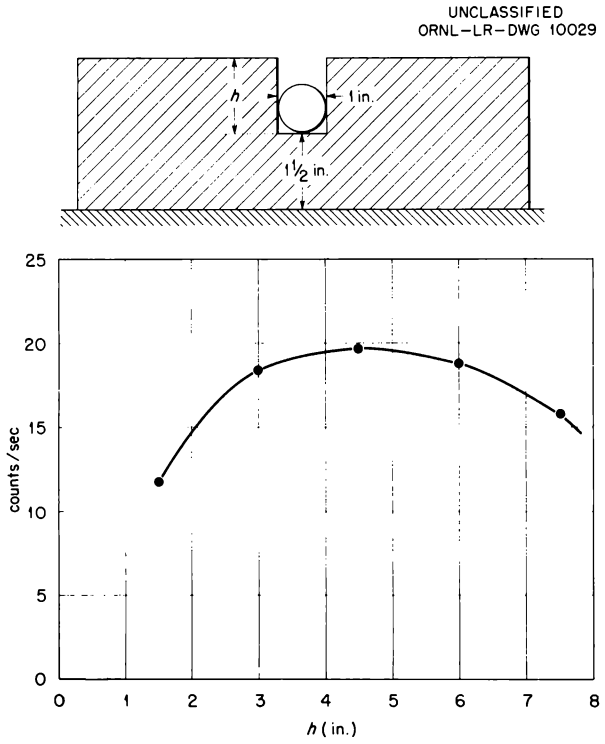

Fig. 2. Effect of Moderator Height with 1-in. Slot.

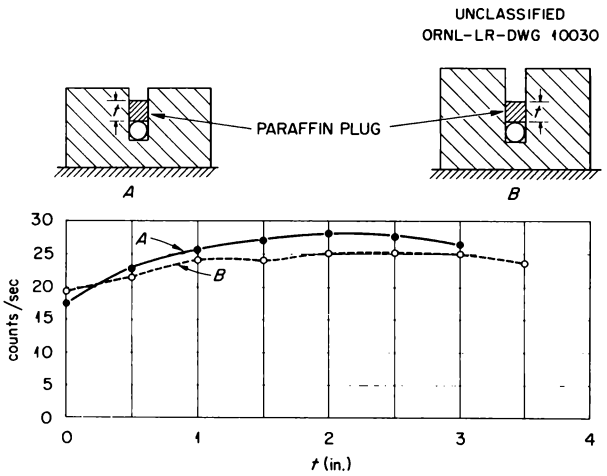

Fig. 3. Effect of Plugs in Moderator Slot.

TABLE 1. THICKNESS OF ABSORBER NECESSARY TO REDUCE NEUTRON COUNT BY A FACTOR OF 10 IN MODERATOR-DETECTOR SYSTEM

Material	Thickness Required for $I/I_0 = 1/10$ (in.)
Water	10
Borated water	10
Borated paraffin	10.6
Lithiated paraffin	9.1
Limonite-paraffin	7.7

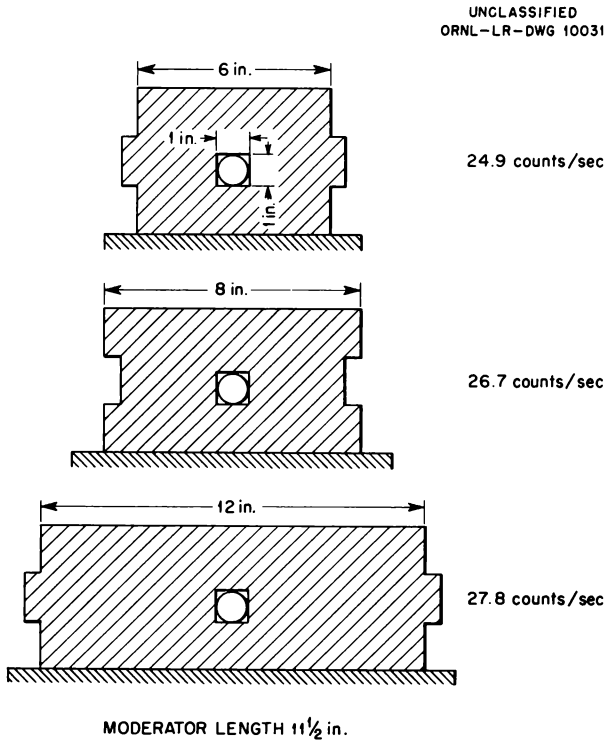

Fig. 4. Effect of Moderator Width.

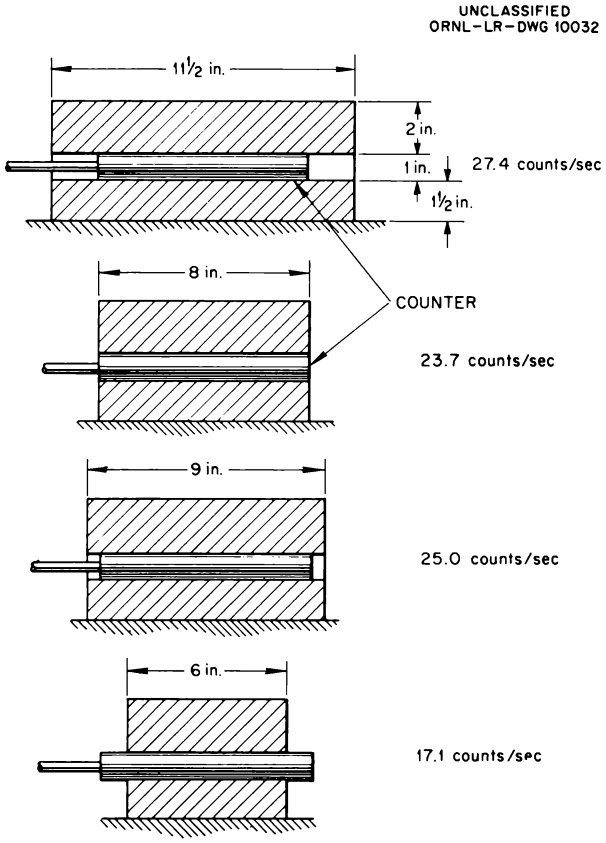

Fig. 5. Effect of Moderator Length.

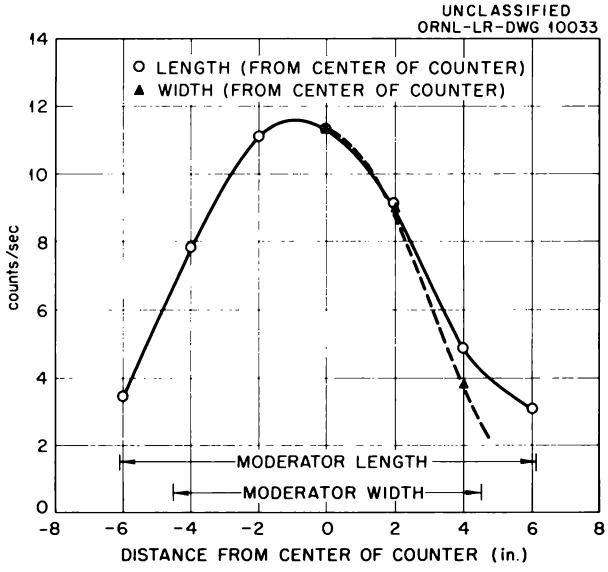

Fig. 6. Counting Rate Obtained as a Function of Position of Moderator-Detector System Relative to Collimated Neutrons.

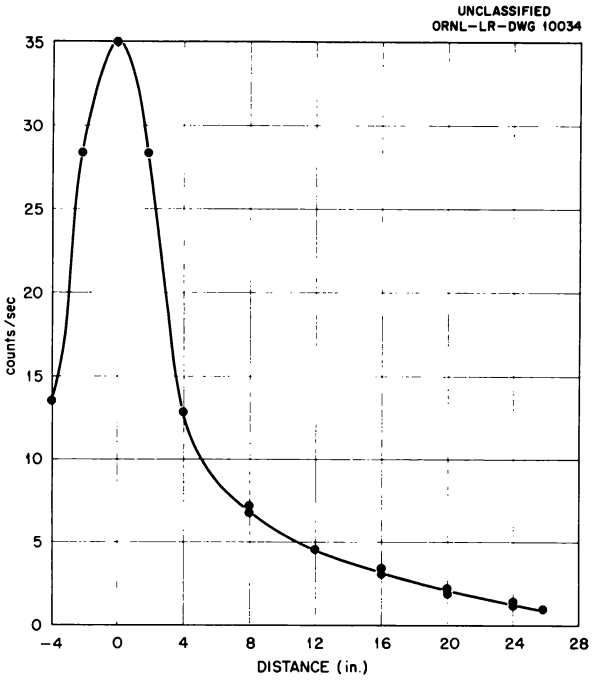

Fig. 7. Response of Three-Slot Neutron Collimator to Po-Be Neutrons.

MEDICAL SCINTILLATION SPECTROMETER

J. E. Francis P. R. Bell C. C. Harris

In the course of several discussions with people engaged in medical applications of radioisotopes, it became evident that the instrumentation necessary in these applications was either inadequate or too expensive. To overcome these shortcomings, the medical spectrometer was designed especially for the medical people. However, the instrument will find many applications in other fields of atomic energy wherever a scintillation spectrometer is required without the need for extreme accuracy of the channel width over the entire range of the instrument.

Scintillation counting of radioiodine and other gamma-emitting substances in biological samples has always been extremely difficult due to the inclusion of scattered radiation in the measurements. This scattered radiation can easily lead to an error of a factor of 2, making precision dosimetry very difficult. The medical spectrometer will provide an accurate measurement of the undegraded primary radiation in the presence of this scattered radiation, thus making precision dosimetry much easier.

The medical spectrometer is a one-chassis unit containing a complete nonoverload linear amplifier, a single-channel analyzer, a count integrator together with a preset timer, and the necessary high-voltage supply for the photomultiplier.

CIRCUIT

Figure 1 is a schematic diagram of the photomultiplier, preamplifier, and linear amplifier. The spectrometer is designed to accept a positive input pulse from the photomultiplier. This is obtained by taking the signal from the last dynode of the photomultiplier. The pulse is fed to the grid of the cathode follower preamplifier (V_1). The signal from the cathode is fed into a 1500-ohm delay line through its characteristic impedance. The delay line is shorted at the far end so that the positive step pulse from the cathode of V_1 is differentiated to obtain a pulse 1 μsec in duration which is placed on the input grid of the first feedback loop (V_2, V_3) of the linear amplifier.

A portion of the signal from the preamplifier is also fed through a network to the cathode of V_2 to compensate for the complex frequency response of the delay line. The signal going through the resistor R_5 to the cathode compensates for the d-c loss in the line. This is adjusted to make the differentiated signal return to the base line at the output of the first group. The signal through R_8 and C_4 is used to compensate for the a-c response of the delay line. These a-c effects occur at relatively short times after the start of the signal. Experience has shown that the input time constant of the preamplifier and the feedback resistor R_9 on the first tube also affect the shape of the signal.

The first feedback loop has a gain of approximately 70. Feedback is accomplished by feeding back a portion of the signal from the plate of V_3 to the cathode of V_2. A step potentiometer provides gain control over a range of 16. Tubes V_4 and V_5 comprise the output group, which has a gain of 120. The output pulses vary from 0 to 100 v.

The pulses from the amplifier are fed into the single-channel analyzer (V_6, V_7, V_8) shown in Fig. 2. The analyzer contains two discriminators (V_6, V_7) whose discrimination level can be continuously varied over a range from a few tenths of a volt to 100 v by means of a multiturn potentiometer labeled E. The two discriminators are biased a fixed amount apart determined by the setting of a second potentiometer labeled ΔE.

An output signal must be greater than a certain amount determined by the setting of E in order to trigger the lower discriminator (V_7) and must be still larger by an amount determined by the setting of E and ΔE to trigger the upper discriminator (V_6). The analyzer is designed to give an output pulse only when the pulse from the amplifier lies in the range between E and $E + \Delta E$.

For a small signal lying below the value determined by E, neither discriminator is triggered and there is no output pulse. When an input signal is large enough to trigger only the lower discriminator, the first plate of V_7 goes negative and charges the 10-$\mu\mu$f coupling condenser to the second grid of V_8 through the 1N67 crystal diode. When the input signal goes down below the trigger level, the first plate of V_7 goes positive, and a positive signal is placed on the second grid of

the anticoincidence tube V_8, which decays with a time constant determined by the 10-$\mu\mu$f condenser and the 47-k grid resistor. This transfers the current from the first half of V_8, which is normally on, to the second half, giving a negative output from the second plate of V_8. If, however, the input signal from the amplifier is large enough to trigger both discriminators, a positive signal is obtained from the second plate of the upper discriminator (V_6) in addition to the signal from the lower discriminator. The signal from the upper discriminator is lengthened by a 1N67 diode and placed on the first grid of V_8. This keeps the first half of V_8 on, so that no output signal is obtained, even when the signal from the lower discriminator appears on the second grid.

It should be noted that the signal from the lower discriminator does not appear on the grid of V_8 until after the input pulse is no longer large enough to trigger the lower discriminator. This is necessary because of the finite rise and fall time of the input pulses. The pulse, when rising, crosses the trigger level of the upper discriminator after it has crossed the trigger level of the lower discriminator and recrosses, when falling, the upper discrimination level before it recrosses the lower discrimination level.

The output pulse from V_8 is fed into a scale-of-two scaler, shown in Fig. 3. Each plate of V_{10} has two stable states and is triggered from one state to another by successive, identical pulses which are fed in through the diode V_9. Thus, the second plate of V_{10} is either at 110 or 210 v. If the second plate is at 110 v and an input signal changes it to 250 v, the coupling condenser V_{11} is charged by drawing current through V_{11A}. Then when a second pulse changes the second plate of V_{10} back to 110 v, this charge is placed on the grid of V_{12A} through V_{11B}, causing the grid of V_{12A} to go negative. So for each two pulses into the scaling circuit, a charge $q = VC$ is placed on the grid of V_{12A}, where V is the difference in voltage of the two stable states of V_{10B}, and C is the coupling capacity.

Tubes V_{12} and V_{13} comprise a two-stage d-c amplifier with a feedback condenser of 1 μf from the plate of V_{13B} to the grid of V_{12A}. When a charge is placed on the grid of V_{12A} by the coupling condenser, the plate of V_{13B} moves up, which pulls the grid of V_{12A} up until equilibrium is reached again. The plate of V_{13B} has to go up 45 v and the plate of V_{13A} down 45 v to obtain 1 ma of current in the cross resistor and meter between the two plates. By using a 100-sec predetermined time, the current in the meter is calibrated in counts per second. The value of the coupling condenser C_c is obtained by the relation

$$q = \frac{N}{2} E_1 C_1 = E_2 C_F ,$$

where E_2 is the change in voltage of C_F, the feedback condenser, E_1 is the voltage change of the scaler plate, and N is the number of counts. The meter can also be used to read count rate by connecting the resistor R_{75}, which allows the charge to leak off continuously.

Figure 4 is the schematic diagram of the power supplies. The positive high-voltage supply is an ordinary shunt-regulated supply, except that the regulated supply of the spectrometer at 270 v is used for the reference voltage.

A multicontact plug is placed at the rear of the chassis to facilitate the use of the spectrometer in special applications. Provision is made for (1) placing the output of the count integrator on a recorder, (2) a special reset input for resetting the count integrator to zero, (3) a scaler output for driving an external scaler, and (4) a scaler output for driving the aural rate indicator.

The aural rate indicator provides a means of adjusting the spectrometer on a gamma-ray peak by ear. Slight changes in counting rate are converted to very noticeable changes in frequency from a speaker. The schematic diagram is shown in Fig. 5, and the operation is covered in a subsequent paper entitled "Surgical Scintillation Probe."

PERFORMANCE

The spectrometer has been tested by using a mercury-relay signal generator to feed signals into the preamplifier. The pulse-height-selector dial E was then adjusted so that the meter was reading one-half the pulse repetition rate in order to eliminate amplifier noise. The dial was adjusted in this way, first to count on the upper edge of the channel and then on the lower edge of the channel. The difference between the two pulse-height settings gave the channel width. The window width is constant within 5% when measured this way for a channel width of 3% of full scale.

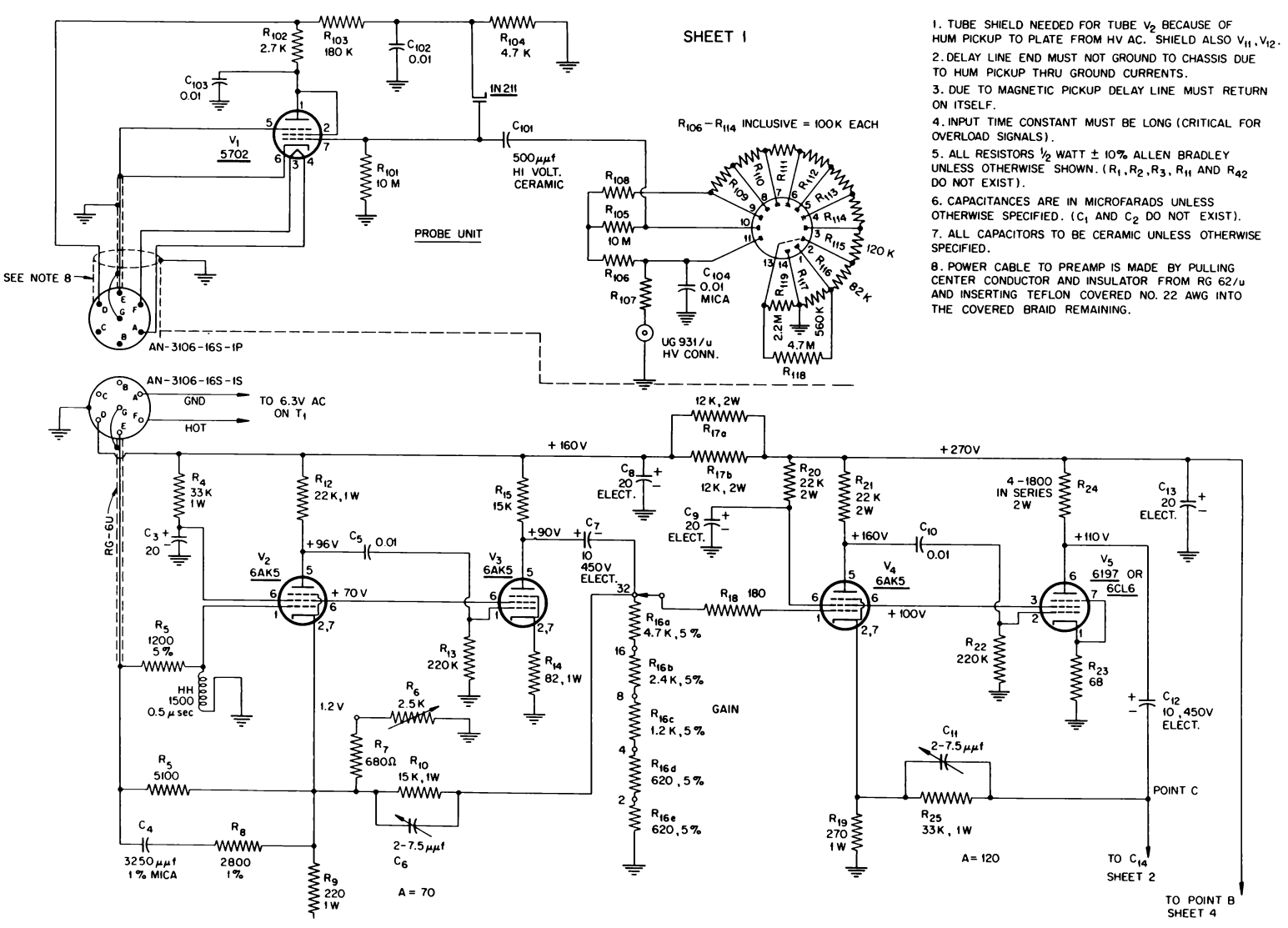

Fig. 1. Schematic Diagram of Photomultiplier, Preamplifier, and Linear Amplifier.

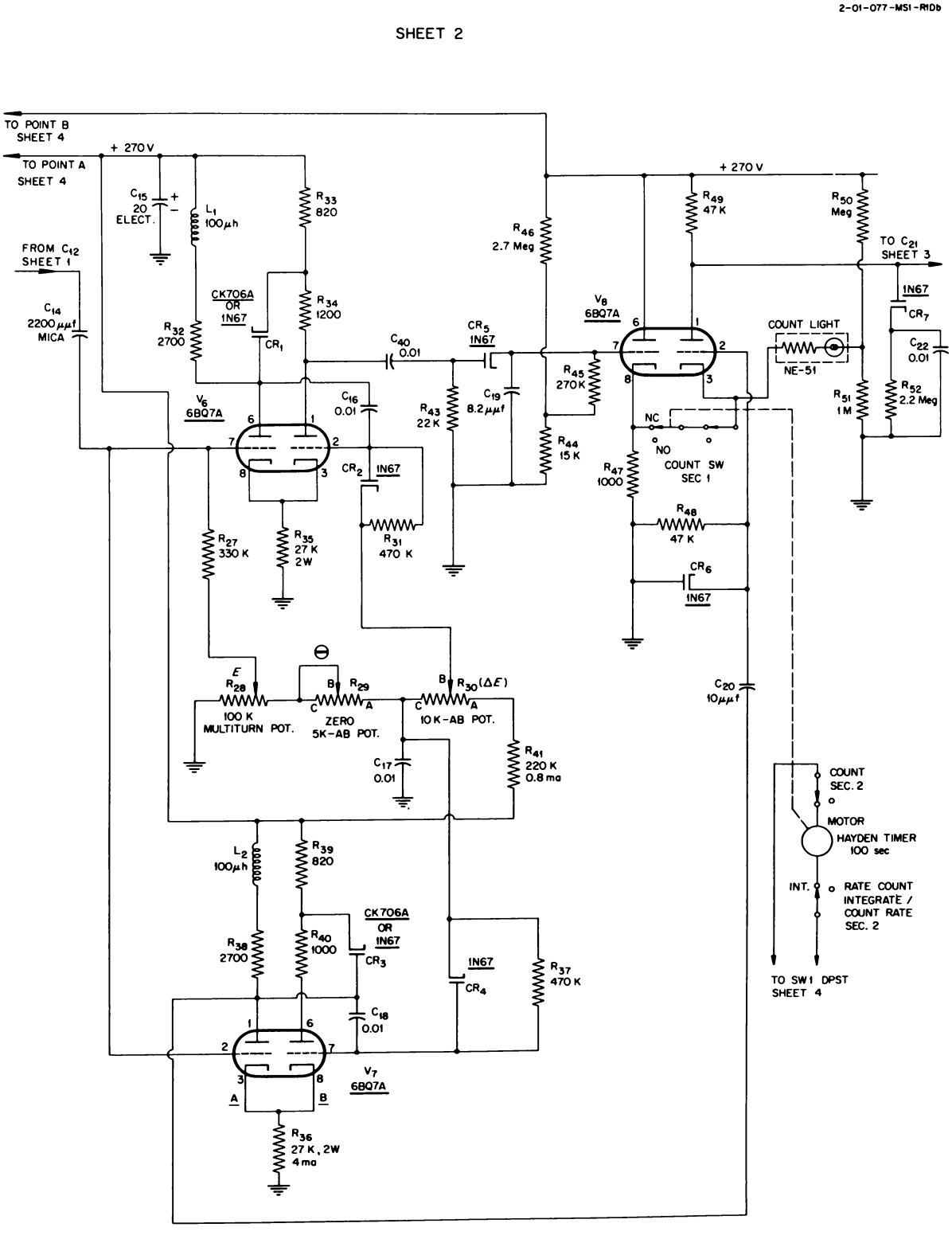

Fig. 2. Schematic Diagram of Single-Channel Analyzer.

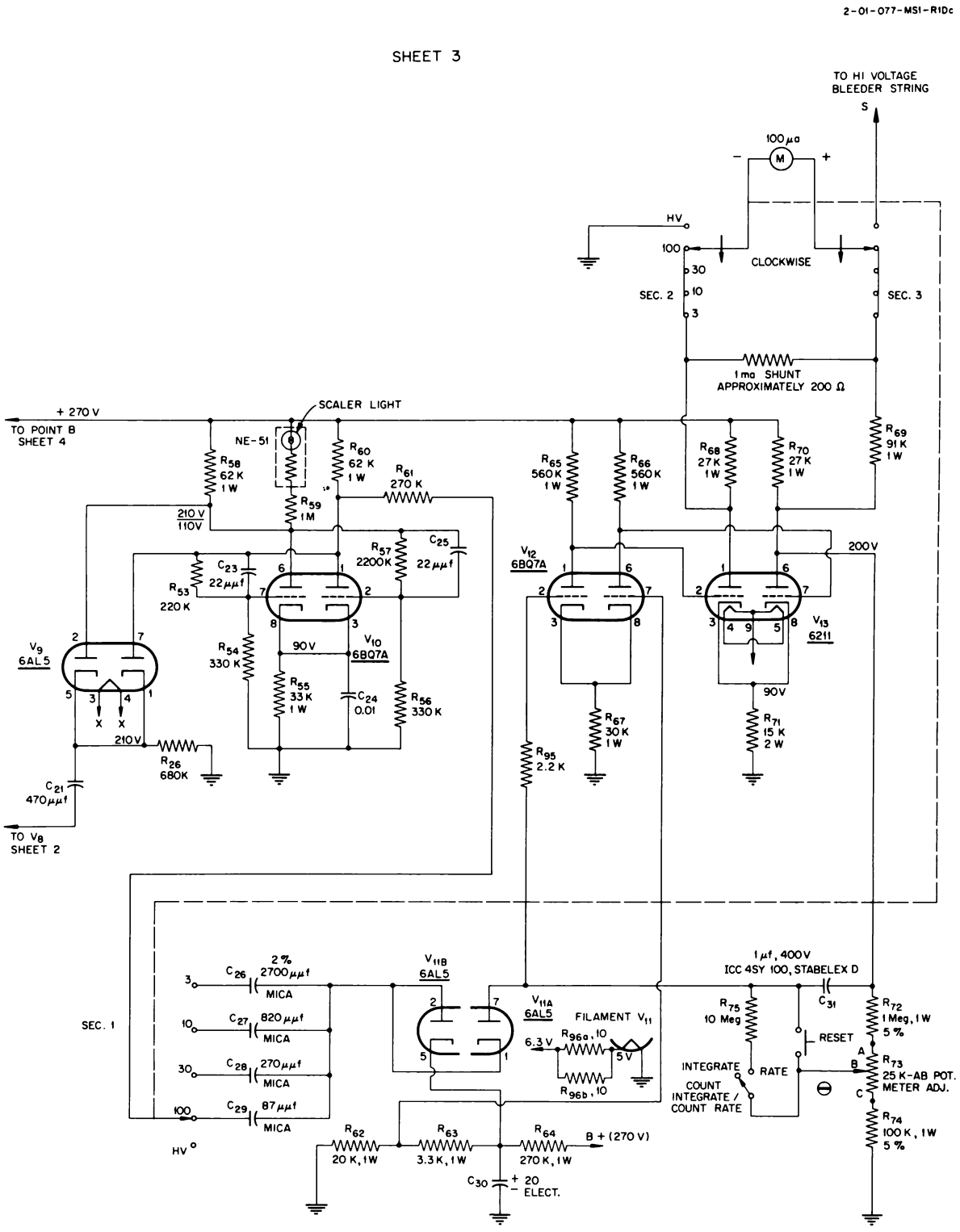

Fig. 3. Schematic Diagram of Data Storage.

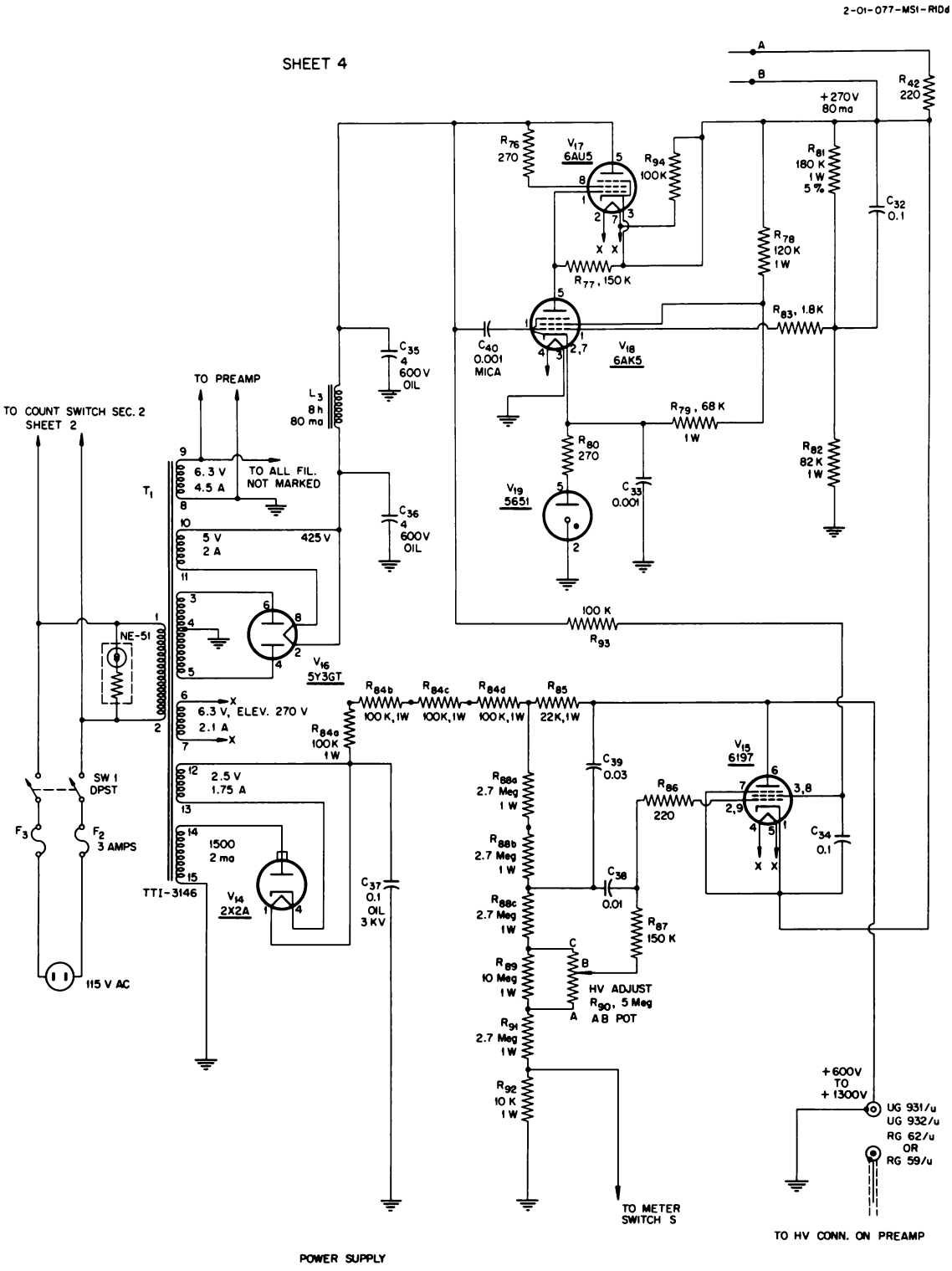

Fig. 4. Schematic Diagram of Power Supplies.

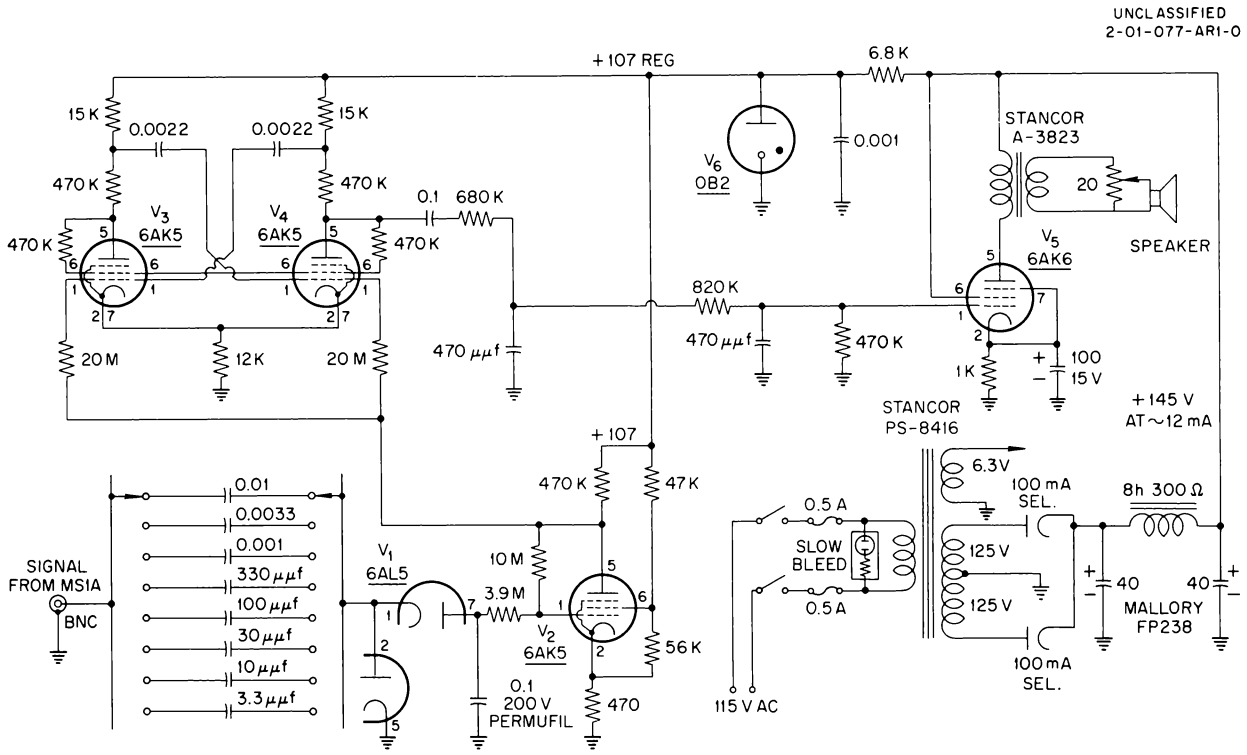

Fig. 5. Schematic Diagram of Aural Rate Indicator.

The spectrometer has also been used to measure the spectra of I^{131}, Cr^{51}, and Cs^{137} in order to check the operation of the spectrometer and also to show the effects of scattered radiation on measurements such as those encountered in medical work.

Figure 6 shows the spectra obtained from Cr^{51}, which has a single gamma ray at 320 kev. The open triangles represent the spectrum obtained with a source with only a small amount of scattering material present. There is a main peak at 780 pulse-height units due to the photoelectric effect. The pulses below 600 pulse-height units are due to Compton scattering within the crystal and the detection of scattered radiation. When water is placed around the source, with very little water between the source and crystal, there is essentially no change in the photoelectric peak, as shown by the curve represented by the closed circles. However, there is a large increase, due to the detection of the scattered radiation, for all pulse heights below this peak. When the source is placed at a greater distance from the crystal and again measured without scattering material, the curve shown by the closed triangles results. It has the same shape, only the intensity is reduced due to the greater distance. Placing water around the source so that the source is in the center of the beaker gives the curve shown by the open circles. Now the main photopeak is reduced due to the absorption by the water. For lower pulse heights there is a large increase in counting rate due to the scattered radiation. When the spectrometer is used for thyroid uptake measurements, where it is necessary to measure the source strengths accurately, the channel width is set to count only the counts in the photoelectric peak, and the scattered radiation does not enter into the measurements.

Figure 7 shows the response of a scintillation counter to Cr^{51} when integral-type counting is used. This is the type of counting that has been in general use. All pulses above a given height are counted, and the counting rate is plotted as a function of the pulse height. The crosses show the response to a bare source. The open circles show the response of the same source when it is immersed in water under the same circumstances

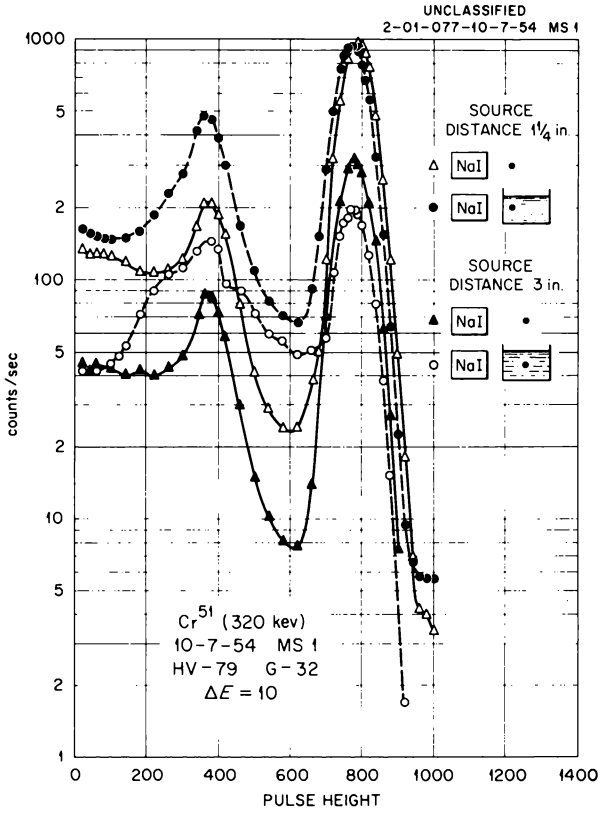

Fig. 6. Pulse-Height Spectrum of Chromium Showing Effects Due to Scattering by Water.

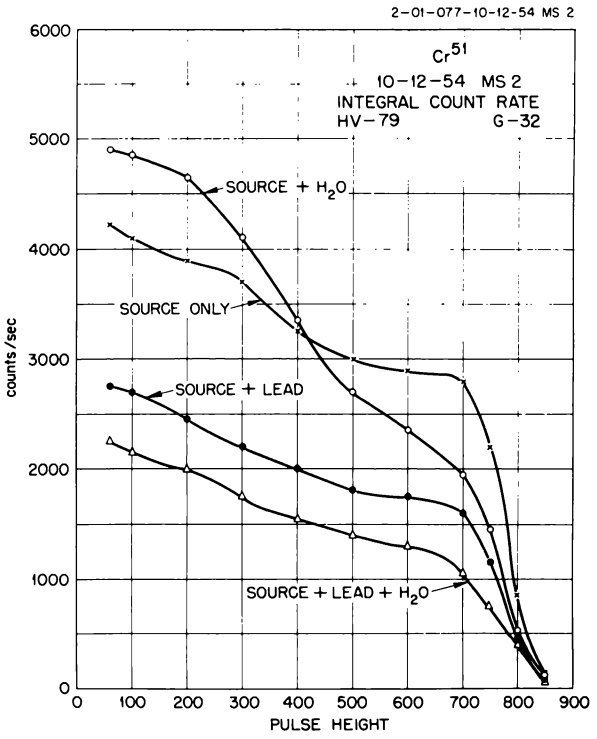

Fig. 7. Integral Pulse-Height Spectrum of Chromium Showing Effects Due to Scattering.

as those shown by the open circles in the preceding curve. For low pulse-height settings (which is where most integral-type counters have been used), the source apparently increases in strength. This is due to the inclusion of the scattered radiation in the measurements. In an effort to minimize the effects of scattered radiation, many counters have been equipped with a thin lead absorber approximately $\frac{1}{16}$ in. thick. This lowers the counting rate for the bare source and does reduce the effects due to scattering, so that the source no longer appears to increase in strength when immersed in water. However, the value for the attenuation of the source is determined by the ratio of the two counting rates at the same pulse height, and the calculated value which would be obtained from the curves depends on which pulse height is chosen for the determination.

Use of the spectrometer reduces the background, since all pulses are eliminated except those which occur in the channel width. This reduction can be as great as a factor of 10 or more.

Measurements have been made on the feasibility of determining the relative amounts of chromium and iodine in the same sample. Figure 8 shows the spectra of chromium and iodine respectively plotted on the same pulse-height scale. Figure 9 shows the spectrum obtained when both sources are measured simultaneously. By matching the 638-kev peak of Fig. 9 with that of Fig. 8 it is possible to obtain the spectrum of chromium by making a point-to-point subtraction.

By using a wide channel width and with proper calibration measurements, it is possible to obtain the relative amounts of chromium and iodine in the same sample. After calibration it is necessary to take counts at only two pulse-height settings to make these measurements. Table 1 shows the calculated counting rate expected for these determinations by using a wide channel width. Table 2 shows the experimental calibration numbers used and the data obtained when a weak source was measured. The source contained 0.718×10^{-3} μc

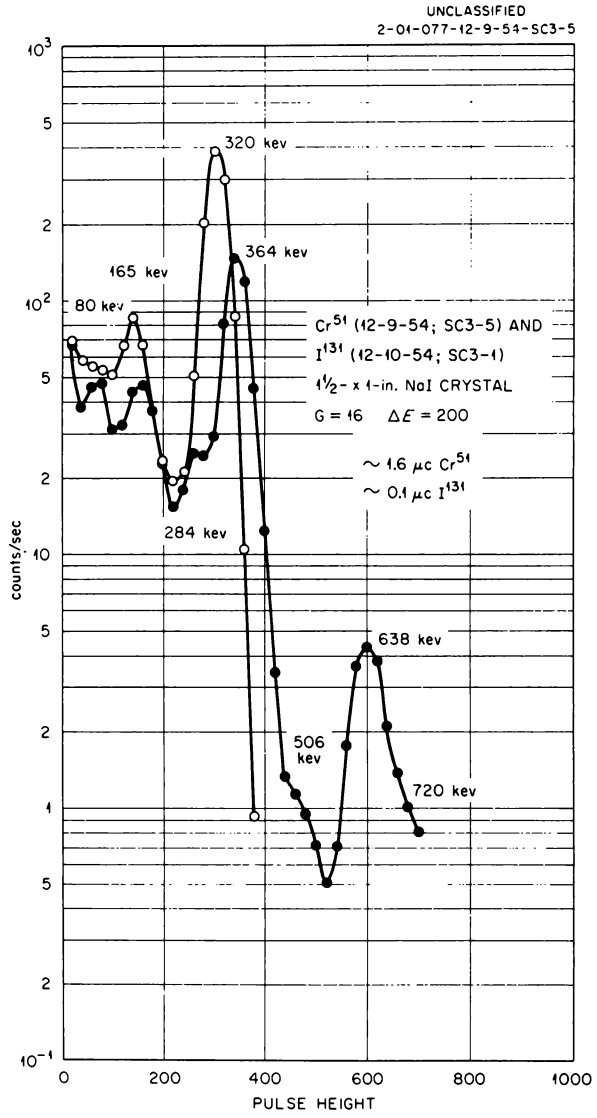

Fig. 8. Spectrum of Iodine and Chromium Under Identical Conditions.

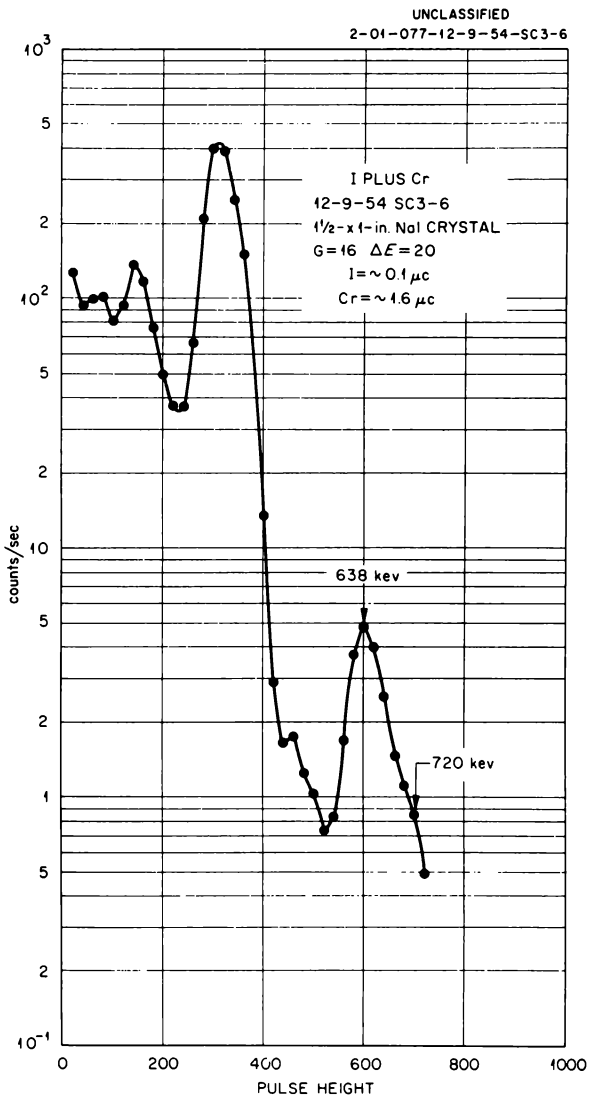

Fig. 9. Spectrum of Mixture of Iodine and Chromium.

of I^{131} and 1.53×10^{-3} μc of Cr^{51}. For the 3 × 3 in. well crystal, the lower limit is approximately 5×10^{-4} μc of I^{131} and 10^{-3} μc of Cr^{51}. Sources containing only iodine can be measured down to 10^{-6} μc without difficulty. The lower limit for iodine and chromium simultaneously can be extended some by going to larger-size crystals, since a larger crystal will increase the detection efficiency of the 638-kev gamma ray of iodine.

Figure 10 shows the intrinsic peak efficiencies for the 3 × 3 in. crystal which were measured as a part of the iodine-chromium experiment. A background measurement using the integral method is also listed for comparison with the differential background.

The spectrometer has been field-tested at the ORINS Medical Division and has proved to be very successful.

TABLE 1. CALCULATED COUNTING RATES PER MICROCURIE

	Disintegration Rate (d/sec)	Efficiency	Gammas per Disintegration	Counting Rate (counts/sec)
		1 × 1½ in. Crystal, Geometry 0.5		
Cr^{51} (320 kev)	3.7×10^4	0.33	0.1	610
I^{131} (364 kev)	3.7×10^4	0.27	0.84	4,190
(638 kev)	3.7×10^4	0.13	0.078	188
		3 × 3 in. Crystal Source in Well, Geometry 1.0		
Cr^{51} (320 kev)	3.7×10^4	0.747	0.1	2,765
I^{131} (364 kev)	3.7×10^4	0.642	0.84	19,950
(638 kev)	3.7×10^4	0.381	0.078	1,110

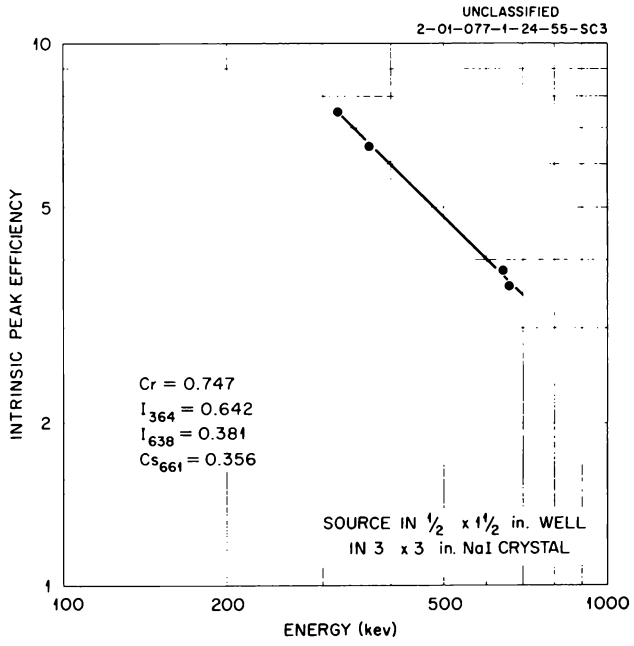

Fig. 10. Intrinsic Peak Efficiency for 3 × 3 in. NaI(Tl) Well Crystal.

TABLE 2. DETERMINING SOURCE STRENGTHS IN A CHROMIUM-IODINE MIXTURE

Calibration Numbers*

Source	Pulse Height	cps per μc
I^{131} (364)	220	16,900
(638)	500	882
Cr^{51} (320)	220	2,300

Weak-Source Determination

Source	Pulse Height	Counts	Time (sec)	cps − bg = true cps
I^{131} alone	220	4096	291	14.05 − 1.915 = 12.13
Cr^{51} alone	220	4096	752	5.44 − 1.915 = 3.52
I^{131} + Cr^{51}	220	4096	238.9	17.15 − 1.915 = 15.23
I^{131} + Cr^{51}	500	4096	3085	1.328 − 0.705 = 0.623
Background	220	2816	1471	1.915
Background	500	512	714 718 738 735	Av 0.705
Integral	40 (60 kev)	4096	230	17.8
background	220 (270 kev)	4096	500	8.2

Source Strength

$$\text{Assay of } Cr^{51} \text{ alone by 320-kev peak} = \frac{3.52}{2300} = 1.53 \times 10^{-3}\ \mu c$$

$$\text{Assay of } I^{131} \text{ alone by 364-kev peak} = \frac{12.13}{16,900} = 0.78 \times 10^{-3}\ \mu c$$

Calculating Cr^{51} and I^{131} from Mixture

$$\text{Assay of } I^{131} \text{ by 638-kev peak} = \frac{0.625}{882} = 0.71 \times 10^{-3}\ \mu c$$

(0.71×10^{-3}) 16,900 = 12 cps calculated counts expected for I^{131} at 220 pulse height from 638-kev measurement.
17.15 − 12 = 5.15 cps due to Cr^{51} and background at 220 pulse height.
5.15 − 1.92 (background) = 3.23 cps due to Cr^{51}.
$\frac{3.23}{2300} = 1.41 \times 10^{-3}$ μc Cr^{51} is the calculated value. This value is to be compared with the assay value of 1.53×10^{-3} μc.

*Assume 3 × 3 in. NaI crystal, source in $\frac{1}{2} \times 1\frac{1}{2}$ in. well, ΔE = 100 pulse-height units.

COLLIMATORS FOR THE MEDICAL SPECTROMETER

P. R. Bell J. E. Francis

Suitable collimators for use with the medical spectrometer had to be developed, since no suitable collimators were known, especially for scanning a patient to determine the distribution of isotopes within the body. Previous collimators used a single cylindrical hole in a lead or tungsten alloy shield block. This hole was usually used with a small cylindrical phosphor of NaI(Tl) or $CaWO_4$ approximately $\frac{1}{4}$ in. in diameter and $\frac{3}{4}$ to 1 in. thick. The efficiency of such a detector and collimator is so low that very large doses were required to obtain indication of the location of the activity. Since spectrometer-type counting equipment was generally not used, the response that was obtained often contained more scattered radiation than primary radiation, which obscured the distribution of the radioisotope in a heavy haze of scattered photons. The response of a scanning system can be greatly improved if a spectrometer-type system is used and if some arrangement is found to use the high sensitivity of large scintillation phosphors.

Figure 1 shows a view of our first multiple-hole focusing collimator designed to permit the use of a 2 × 2 in. NaI(Tl) phosphor. The axes of the 19 tapered hexagonal holes, if prolonged, meet on the central axis 2 in. beyond the end of the shield. A source at this point sees 59% of the face of the detector crystal directly. At a greater or lesser distance, the source can radiate down only part of the holes, so that the response from a point source is less at small or large distances.

Figure 2 shows an isoresponse plot of this collimator taken in a plane containing the axis for 320-kev gamma rays. The point of maximum response is displaced inward to $1\frac{1}{2}$ in. by the inverse-square law. At this point the counting

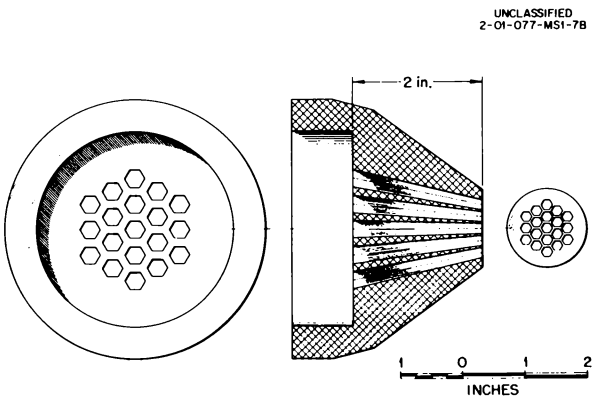

Fig. 1. Focusing Collimator for 2-in. Crystal.

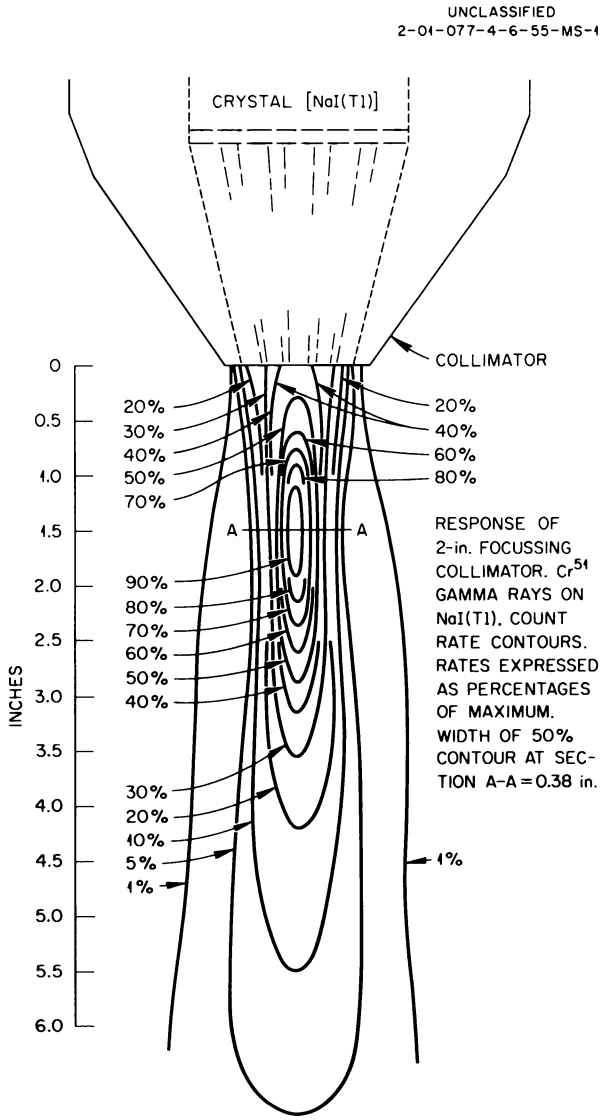

Fig. 2. Contour Map Showing Response of 2-in. Focusing Collimator.

rate for Cr^{51} gamma rays is 52% of that obtained with the collimator removed. In contrast with this behavior, Fig. 3 shows the response of a single-hole collimator giving about the same position resolution. The same source was used, and the response at the distance for maximum response of the 2-in. focusing collimator is only one-twentieth as large. With the 2-in. focusing collimator it was easy to detect a 1-cm-dia activity void in a 4-cm-deep activity layer of large diameter with only 0.07 μc of activity per milliliter. This test demonstrates the ability of the collimator-spectrometer system to reject scattered radiation.

A mock thyroid gland was loaded with 15 μc of I^{131} by the ORINS Medical Division for us to examine. This model had a 0.7-μc hot spot about $\frac{1}{8}$ in. in diameter in one lobe and a $\frac{1}{2}$-cm and a 1-cm polystyrene bead for voids in the other lobe. Figure 4 shows an isometric view of the intensity plot we obtained.

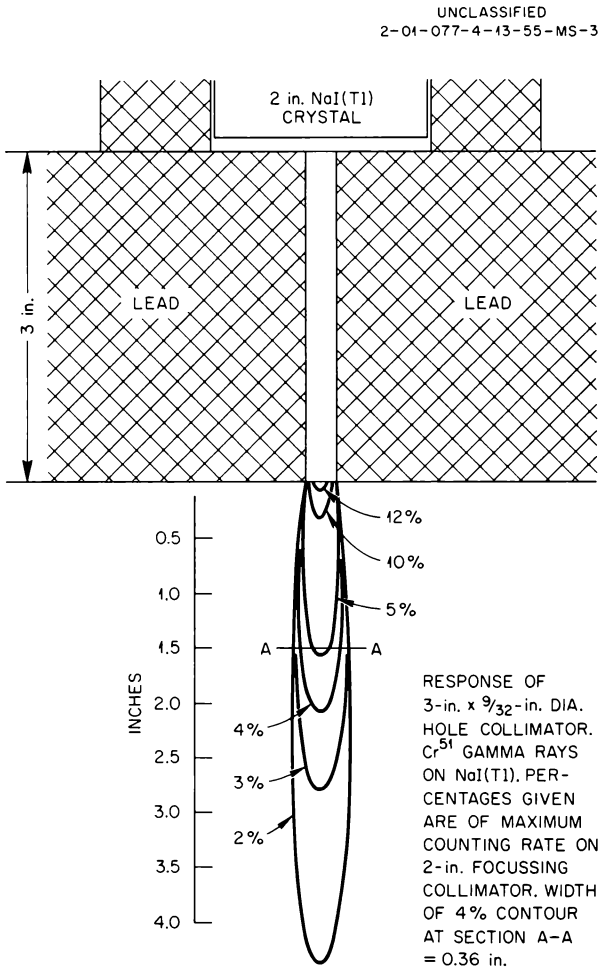

Fig. 3. Contour Map Showing Response of Single-Hole Collimator.

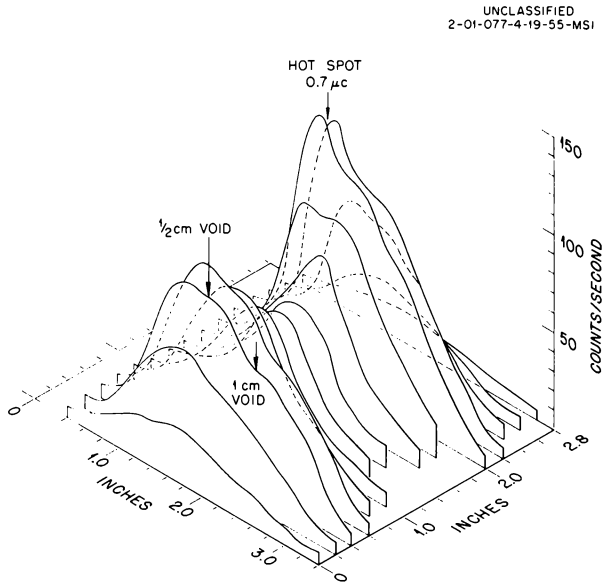

Fig. 4. Isometric Drawing of Distribution of Iodine in Mock Thyroid Obtained by Using Focusing Collimator.

The greater transmission of the focusing collimator allows good outline of a thyroid gland to be obtained in a scanner, with only 5 to 6 μc of I^{131} in the gland. This makes the required dose for scanning (10 to 50 μc) much less than the present customary doses of 200 to 300 μc.

The performance of the 2-in. collimator was so encouraging that a much more ambitious collimator was constructed for a 3-in. working distance. Sixty-one tapered hexagonal holes were required in a lead alloy (94% Pb, 3% Sb, 3% Sn) shield 3 in. thick. The isoresponse plot of this collimator is shown in Fig. 5. The diameter of the 50% contour region is 0.6 cm at $2\frac{5}{8}$ in. from the end of the collimator. The sharpness of the focused region produces good images of activity distributions near the focus, even through obscuring activity closer to the collimator end.

Figure 6 shows the response of the 3-in. collimator to a small dish of I^{131} solution. The one-hole collimators and even the 2-in. focusing

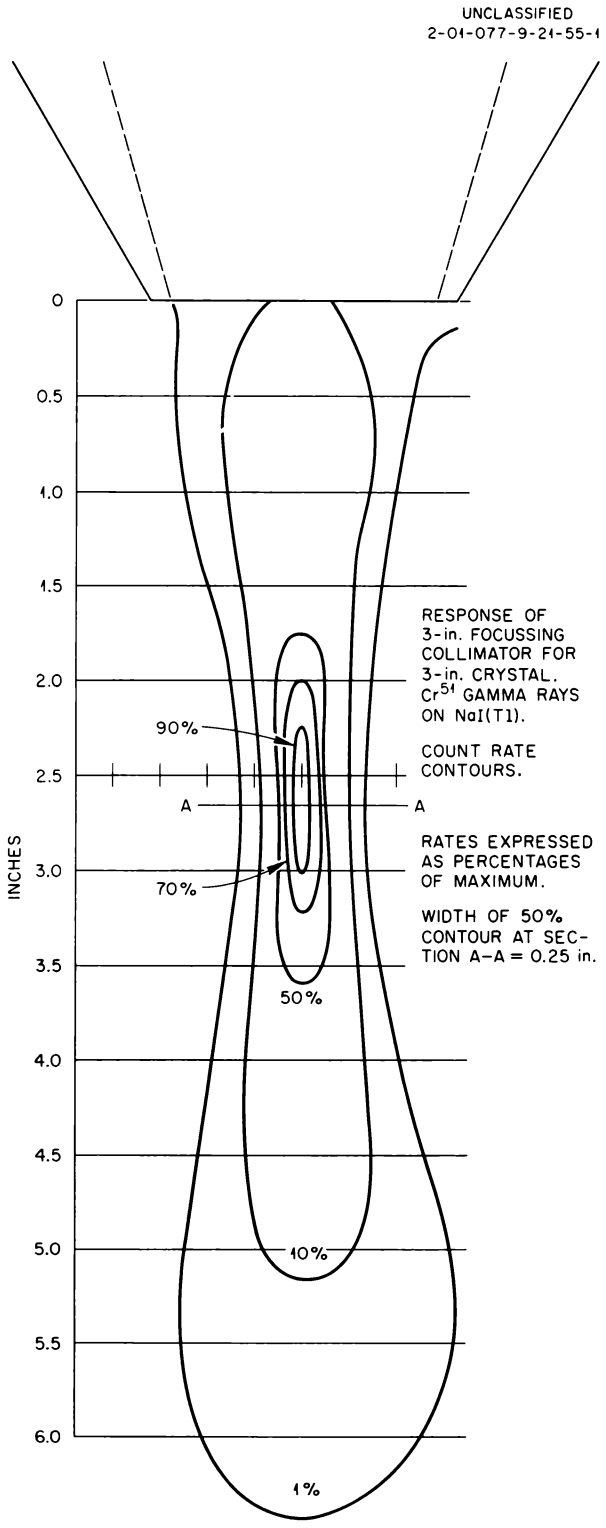

Fig. 5. Contour Map Showing Response of 3-in. Focusing Collimator.

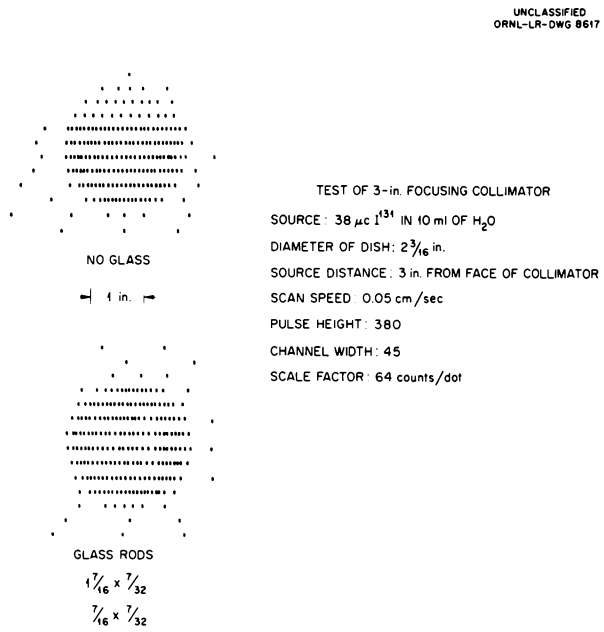

Fig. 6. Test of 3-in. Focusing Collimator.

collimator do not give an image showing a flat level of activity across the center of even as large an object as this, but the upper dot pattern shows a definite flat-topped-disk image. The upper seven lines of the pattern were taken with twice the scale factor of the rest. The lower dot pattern was for the same dish with two small glass-rod segments immersed in the solution, with the axes of these rods in a north-south direction. The wider spacing of the dots where the rods were can be seen. The longer rod was on the right. The 3-in. collimator is in use at the ORINS Medical Division, and one example of its performance on a patient can be seen in Fig. 7. In the upper part of the neck, the two upper parts of the thyroid can be seen. In the lower part, the thyroid can hardly be seen through the large region of iodine-absorbing abnormal tissue extending down into the chest cavity.

Another collimator for use with the 2-in. crystal has been constructed for determining thyroid uptake. This collimator was designed to give a uniform response over an 11-cm-dia region at 25 cm from the crystal surface. The construction of this collimator can be seen in Fig. 8, together with the back shell shield for both this collimator and the 2-in. focusing collimator. The material used was the same very hard lead alloy given

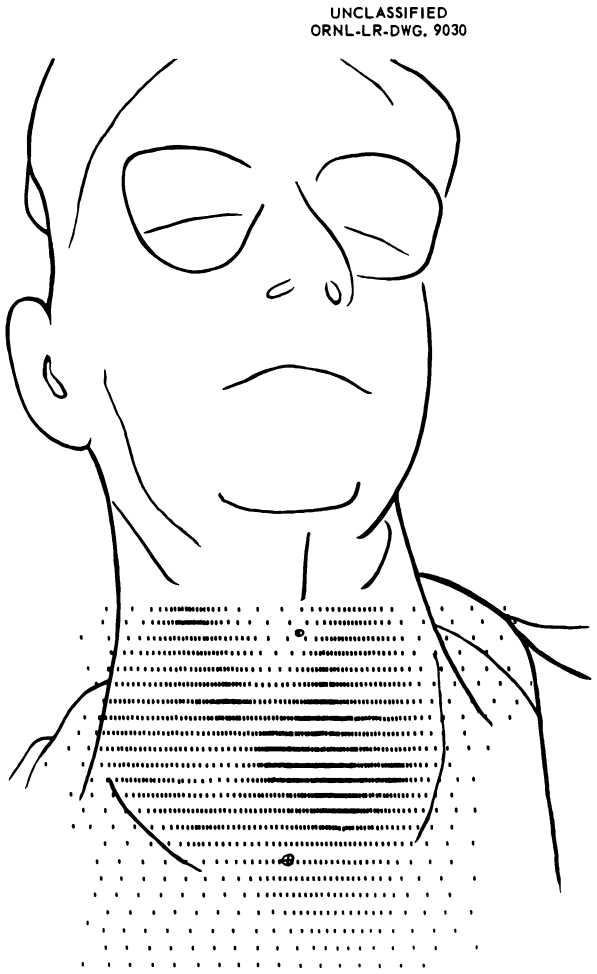

Fig. 7. Number 510574: Female 68 Years. Scan of Large Goiter Two Days After 20 mc of I^{131} by Mouth.

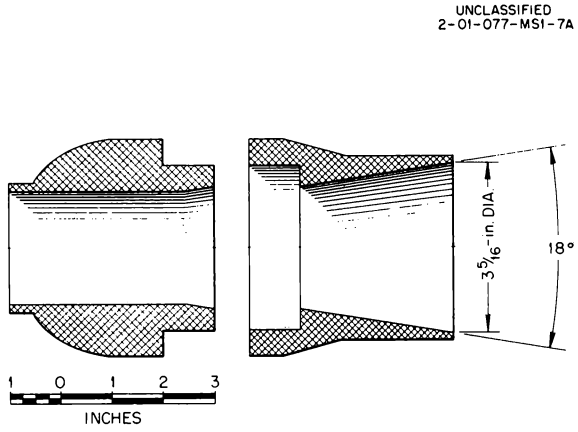

Fig. 8. Assembly of Scintillation Head Showing Flat-Field Collimator.

above. The 2 × 2 in. NaI(Tl) crystal is enclosed in a thin aluminum can, together with a 2 × 2 in. light-piper–shield made of unactivated sodium iodide crystal or a thin pyrex cell containing nearly saturated lead perchlorate solution. Both kinds of light pipers are transparent to shorter wavelengths than the 3250-Å limit of the NaI(Tl) phosphor, and both are good shields against radiation entering from the rear of the shield. The crystal can extends down over the side of the phototube (types 6342, 6655, or 6292) and is sealed by vacuum wax or by a cold-setting rubber compound; α-alumina (Linde "A") is used as a reflector. The 4-in.-long combination of detector crystal and light-piper–shield sits inside the back shell, with the detector nearly flush with the right-hand end. The gap between the shield crystal and the back shell is filled by wrapping the crystal can with 0.01-in.-thick lead foil. The response vs the angle of this collimator to 320-kev gamma rays is shown in Fig. 9, and for 661-kev gamma rays in Fig. 10. The low response in the back direction can be seen. These shields will give low backgrounds, and when used with the medical spectrometer, which discriminates against the scattered radiation and further reduces the background, will allow satisfactory 24-hr thyroid uptake measurements to be made by using a dose of only 1 μc of I^{131}. The counting time required is approximately 100 to 200 sec.

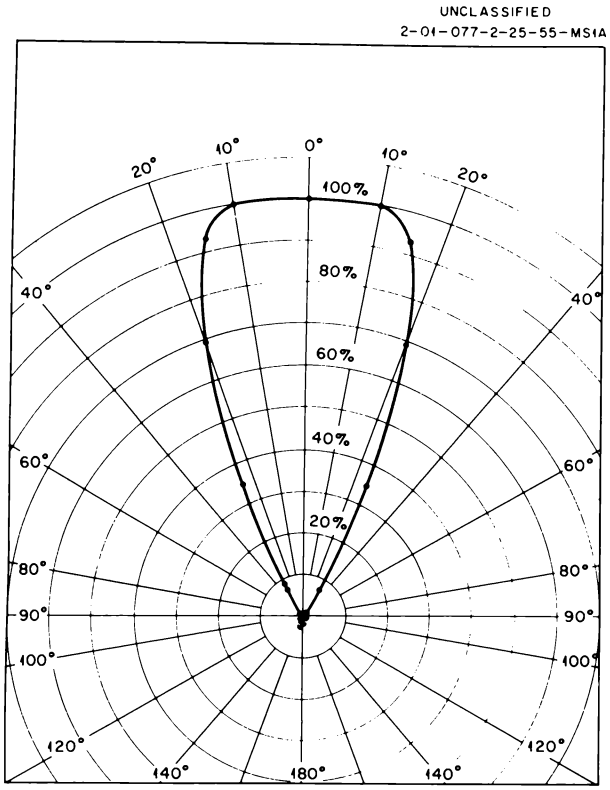

Fig. 9. Polar Diagram Showing Response of Flat-Field Collimator to 320-kev Gamma Ray of Chromium.

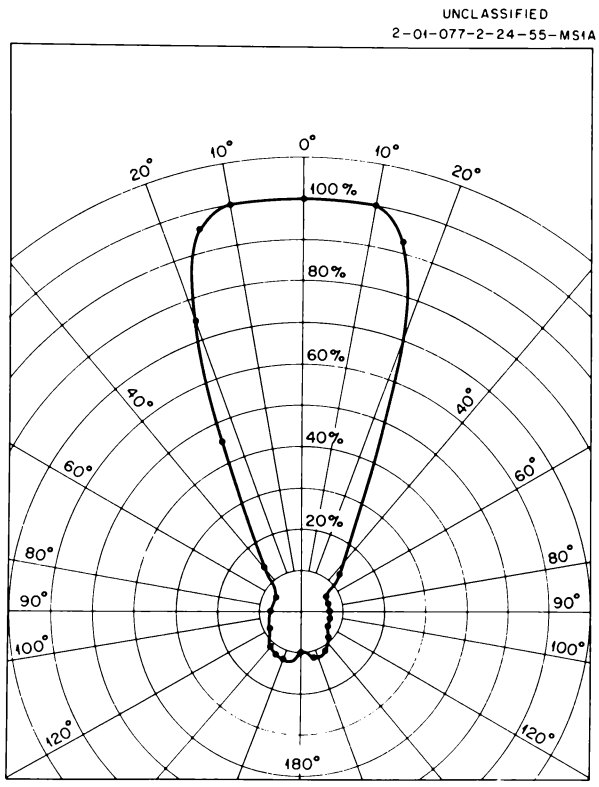

Fig. 10. Polar Diagram Showing Response of Flat-Field Collimator to 661-kev Gamma Ray of Cesium.

SURGICAL SCINTILLATION PROBE

C. C. Harris
J. E. Francis
P. R. Bell
G. G. Kelley

Locating radioactivity-bearing tissue during surgical operations is often extremely difficult without a device which provides sharp localization of the activity. Several counter probes have been devised, but it is felt that the one described here has several new features which make it more satisfactory.

The sensing element is a small cesium iodide crystal mounted on the end of a long, thin, Lucite light-piper. Two such combinations have been constructed. One crystal, 0.220 in. in diameter and $\frac{3}{8}$ in. long, is contained in a nickel tube $\frac{1}{4}$ in. in diameter and $3\frac{3}{16}$ in. long. The other crystal is 0.10 in. in diameter and $\frac{1}{4}$ in. long and is contained in a tube only $\frac{1}{8}$ in. in diameter and $3\frac{1}{2}$ in. long. In the larger tube, the walls around the crystal are 5 mils thick on the side and 2 mils thick on the end. The smaller tube has 12-mil side walls and a 2-mil end. Platinum collimators for closer localization have been constructed with a wall thickness of 0.080 in.

The sensing elements are mounted on a photomultiplier-preamplifier combination that is small enough to be hand-held. The entire probe is hermetically sealed and can be solution-sterilized. Figure 1 shows the probe.

Figure 2 is a schematic diagram of the associated circuitry, which consists of a preamplifier,

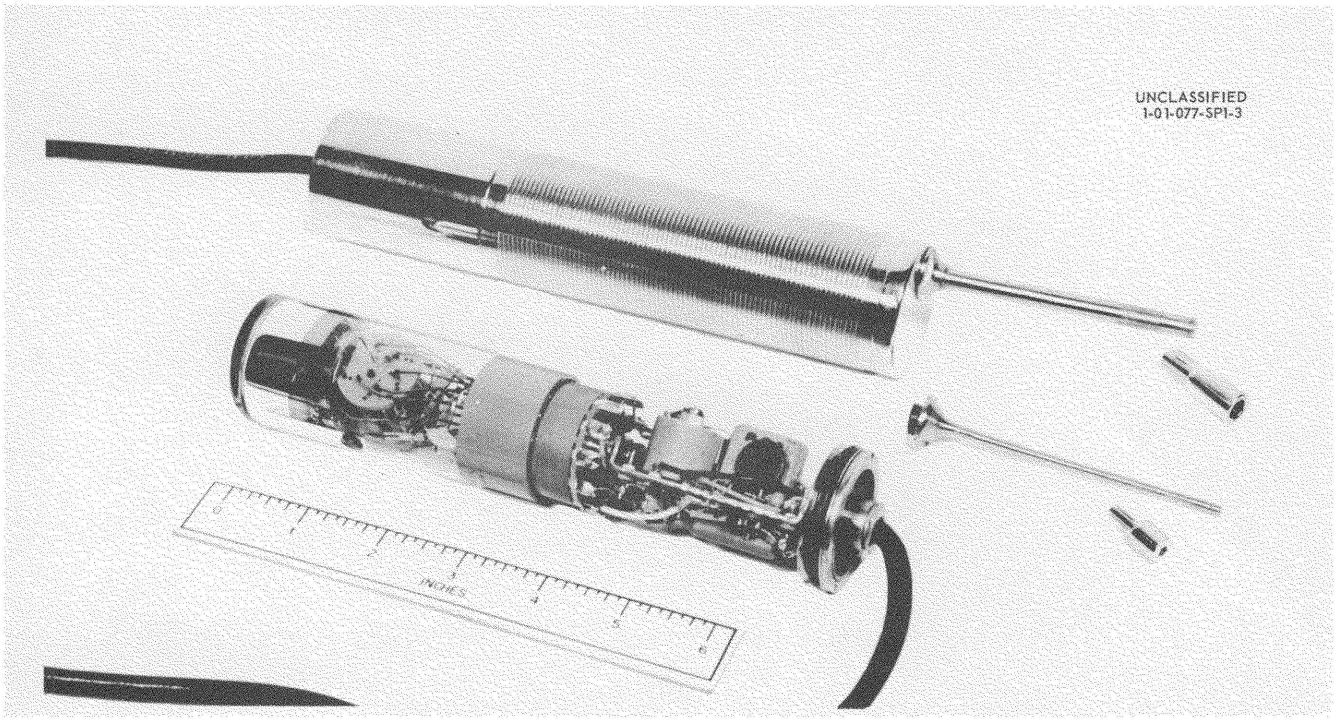

Fig. 1. Photograph of Surgical Probe.

a linear amplifier, a differential discriminator circuit, and an aural count-rate indicator. A positive signal is obtained from the photomultiplier by taking an output from the last dynode. This signal is placed on the grid of the preamplifier, V_1. The preamplifier integrates, amplifies, and inverts the signal and drives the signal cable, placing a signal at the input of the linear amplifier. Gain stabilization and integration are accomplished by plate-to-grid feedback.

The signal from the preamplifier is differentiated by the delay line at the input of the linear amplifier in order to obtain a signal approximately 2 μsec in length. The rest of the linear amplifier consists of two three-tube loops using plate-to-grid feedback with internal plate-to-plate feedback to prevent oscillation. The output pulses from the amplifier are negative in polarity, ranging in size from 0 to about 50 v, and are examined by a differential discriminator circuit. Output pulse height is controlled by a step switch in the high-voltage supply to the photomultiplier.

The discrimination level can be varied from 0 to 50 v. Pulses must exceed a fixed additional level in order to trigger the upper discriminator. This fixed window width is set to be 10% of maximum pulse height. A fixed window width was chosen in the interest of simplicity and was considered proper, since a wholly quantitative answer is not needed. The discriminators consist of biased diodes and vacuum-tube trigger pairs. The trigger circuit for the upper discriminator consists of V_8 and V_9, and the trigger circuit for the lower discriminator is comprised of V_{10} and V_{11}. A pulse which overcomes the bias on a discriminator diode applies a signal to the trigger circuit, causing the trigger circuit to fire. Retriggering is accomplished by a diode which forces a trigger circuit to return to its original state on the fall of the input signal.

Small signals below the discrimination level trigger neither discriminator, and no output is presented to the anticoincidence tube, V_{12}. If a signal triggers the lower discriminator, a differentiated positive signal is placed on the screen grid of V_{12} at the time the input signal recrosses the discrimination level. Tube V_{12} normally operates with its control grid drawing 10 μa and with its screen grid at 0 v, which effectively cuts the plate off. The signal from the lower discriminator drives the screen grid to 6 v, at which point the voltage is diode-limited. This screen signal causes a large plate current to flow, and a negative pulse is sent to the scaler, V_{13} and

UNCLASSIFIED
2-01-077-SP1-0

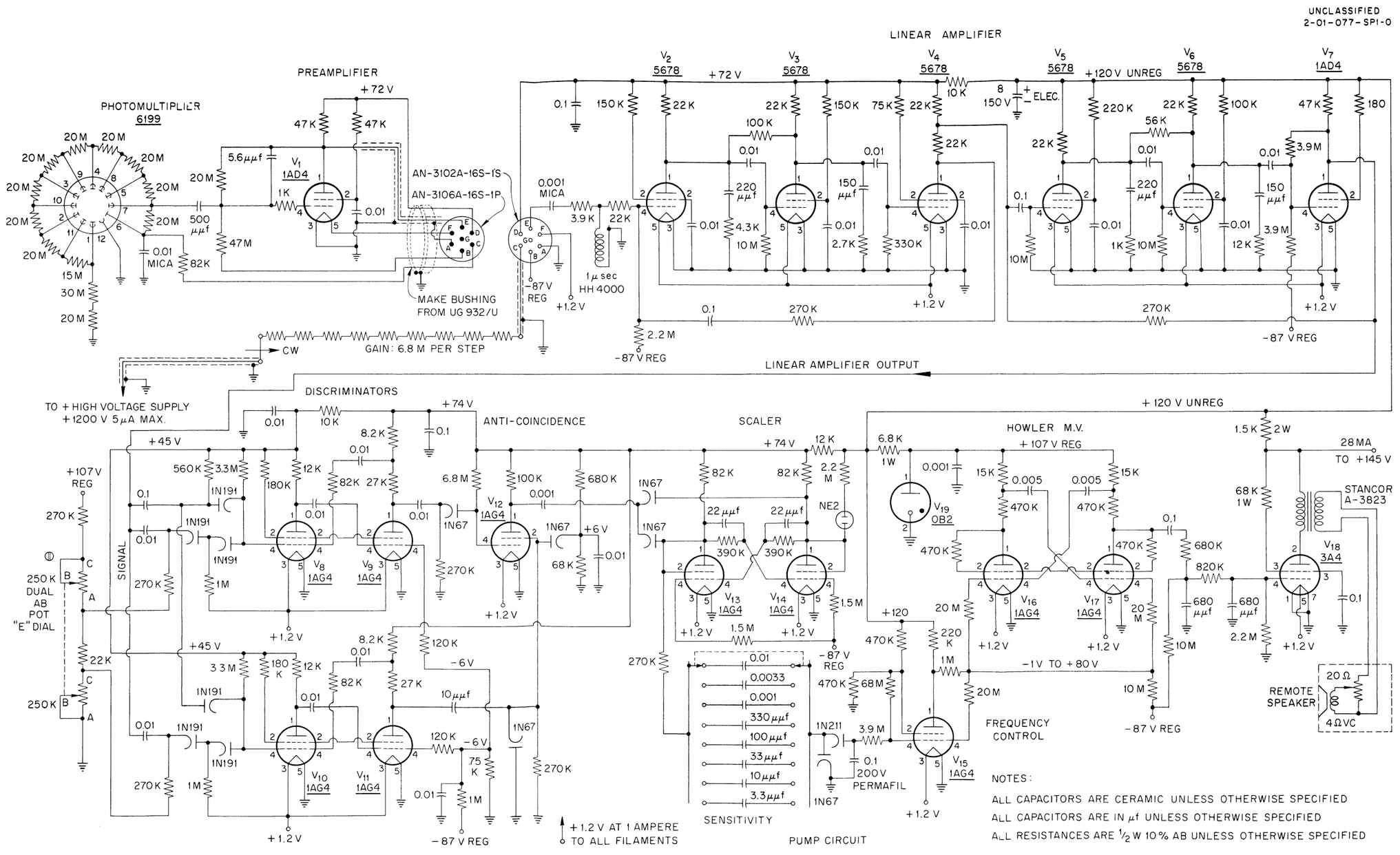

Fig. 2. Schematic Diagram of Surgical Probe.

V_{14}. If, however, the upper discriminator is triggered, a lengthened negative pulse is placed on the control grid of V_{12}, cutting the tube off until after the lower discriminator retriggers. The signal from the upper discriminator is lengthened, since, because of the fall time of the amplifier signal, the discrimination level of the upper discriminator is recrossed before the lower discrimination level is recrossed, at which time the "go" signal is placed on the screen grid of V_{12}. In this manner a drive signal is sent to the scaler only if the lower discriminator alone has been triggered.

The counting rate of the scintillation counter is indicated to the surgeon by an aural count-rate indicator or "howler" that operates in the following manner: For each two pulses into the scaler a charge is placed on the storage capacitor of the pump circuit. The charge on the storage capacitor is allowed to leak into the input of the frequency control circuit at the grid of V_{15}. The plate voltage of V_{15} varies from about −1 to about 80 v as the storage capacitor is charged up to about −26 v, and the variation is linear with the variation on the storage capacitor. Tubes V_{16} and V_{17} comprise a self-starting hard-bottomed multivibrator, the control grids of which are returned to the plate of V_{15}. As the plate voltage of V_{15} varies over its range, the frequency of the multivibrator varies from about 12 to about 1300 cps. The output of the multivibrator is presented to an audio amplifier which drives a remote speaker on which there is a volume control.

An eight-position selector switch at the input of the pump circuit provides a variation of howler sensitivity in steps of about a factor of 3. Full frequency variation can be obtained on about 25 cps at the probe on the most sensitive scale. Because the logarithmic frequency variation of the howler matches the response of the ear (which presents the same percentage frequency change to the ear), regardless of frequency, and because the ear is extremely adept at detecting a very small change in frequency, small changes in count rate are quickly noted. Hence localization of activity is possible with counting rates as low as 5 cps.

The circuit uses mainly filamentary subminiature vacuum tubes, which results in a low-wattage compact design. The entire circuitry, including power supplies, can be enclosed in a hermetically sealed metal box, and, since the input power is only 12 w, a very low temperature rise results.

The probe and the howler were used in a surgical operation at the ORINS Medical Division and met with the approval of the surgeons present. Very sharp localization of activity was obtained, and the aural indicator appeared to be quite useful and satisfactory.

PROGRESS REPORT ON MULTICHANNEL PULSE-HEIGHT ANALYZERS (MC4 AND MC5)

G. G. Kelley P. R. Bell C. C. Harris

The MC4 analyzer (120 channels, 20 at a time), which was reported previously,[1] is in use and is performing as expected. Some circuit changes have been made:

1. A simpler interrogation and inhibit circuit with adjustable constant dead time per pulse has been substituted for the one reported, which had signal-dependent dead time.

2. A cathode follower has been added to the screen of the pulse-lengthener amplifier to keep a constant screen-to-cathode voltage. The standing screen voltage of the tube is reduced to 140 v, permitting the tube to be operated at higher current.

3. A new pulse generator has been developed which produces a double-differentiated type of signal at a sufficient level to operate through the output group of the A-7 linear amplifier. The previous mercury-relay pulse generator operated erratically at the necessary voltage level.

Figure 1 is a circuit diagram of the new interrogation-inhibit circuit. The pulse-height-selector signal from an A-7 linear amplifier is limited to 10 v and passed through two 0.6-μsec sections of delay cable. Diodes at the line input and the

[1] G. G. Kelley, P. R. Bell, and C. C. Harris, *Phys. Semiann. Prog. Rep. Sept. 10, 1953*, ORNL-1620, p 50.

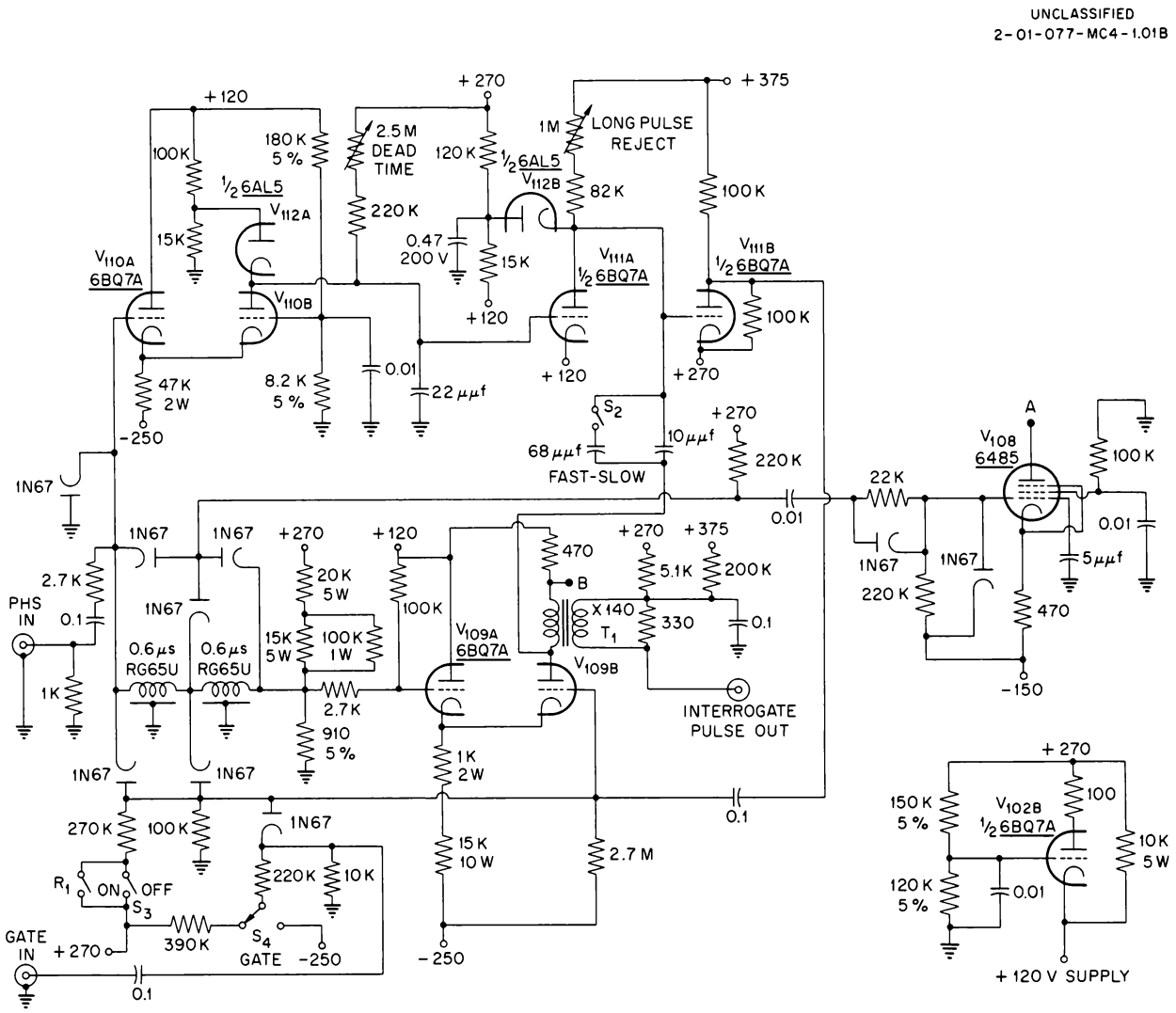

Fig. 1. Circuit Diagram of Interrogation-Inhibit Circuit for MC4 Analyzer Control Unit.

junction between the sections pull down on the normally off side of V_9 (V_{9B}). The grid of the conducting side drops 1.2 μsec later, but the current does not transfer until 0.6 μsec after the end of the pulse-height-selector signal, when the grid of V_{9B} returns to its normal value. This tube conducts for 0.6 μsec at this time, producing an interrogate pulse. This pulse may be interrupted by the arrival of a new signal, or the grid of V_{9B} may be held inoperative by the on-off and gate circuits. If the on-off switch (S_3) is open, the portion of the circuit connected to V_{9B} has a potential slightly below ground. This potential is pulled up to about +10 v when S_3 is closed, permitting normal operation. When the gate switch is in the "normally on" position (to the left in the diagram), the cathode of the associated 1N67 is held up high enough that it does not interfere with circuit operation unless it is pulled down by a 10-v negative "off" gate. When the gate switch is in its other position, the grid of V_{9B} is pulled down through the diode unless a positive 10-v gate pulse is applied.

Interrogation may be inhibited by a negative signal from the plate of V_{111B}. Such a signal is produced if the signal to be interrogated lies in the dead time from a preceding signal or if the pulse-height-selector signal has lasted too

long, indicating pileup. Tube V_{110B} normally is cut off, allowing the potential of its plate and the grid of V_{111A} to be held at +120 v by the grid current in V_{111A}. The presence of a pulse-height-selector signal transfers current from V_{110A} to V_{110B}, whose plate pulls down against the diode V_{112A} at about +15 v, where it remains so long as a pulse-height-selector signal is present. Tube V_{111A} had been conducting, holding the grid of V_{113} at +135 v. When the current is cut off, the voltage rises at a rate depending on the setting of the 1-megohm wide-pulse reject potentiometer and the position of the fast-slow switch. If V_{111B} is brought into conduction before the interrogation time, it prevents interrogation. Interruption of an interrogation which is in progress is prevented by returning the charging condenser to the plate of V_{9B}. The dead-time control delays the return of V_{111A} to its normally conducting state for a time depending on the setting of the 2.5-megohm resistor. Tube V_{111B} will have gone into conduction and will remain conducting until the end of the dead time.

Tube V_{108} is the pulse lengthener hold-down tube. It is cut off from the time of the beginning of a pulse-height-selector signal, until 1.2 μsec after the end of this signal, by diodes from the input, tap, and termination of the delay lines. The tube is turned off slowly by means of a 22-k series resistor in order to prevent a transient difficulty in the lengthener. A diode across the resistor permits the tube to be turned back on speedily.

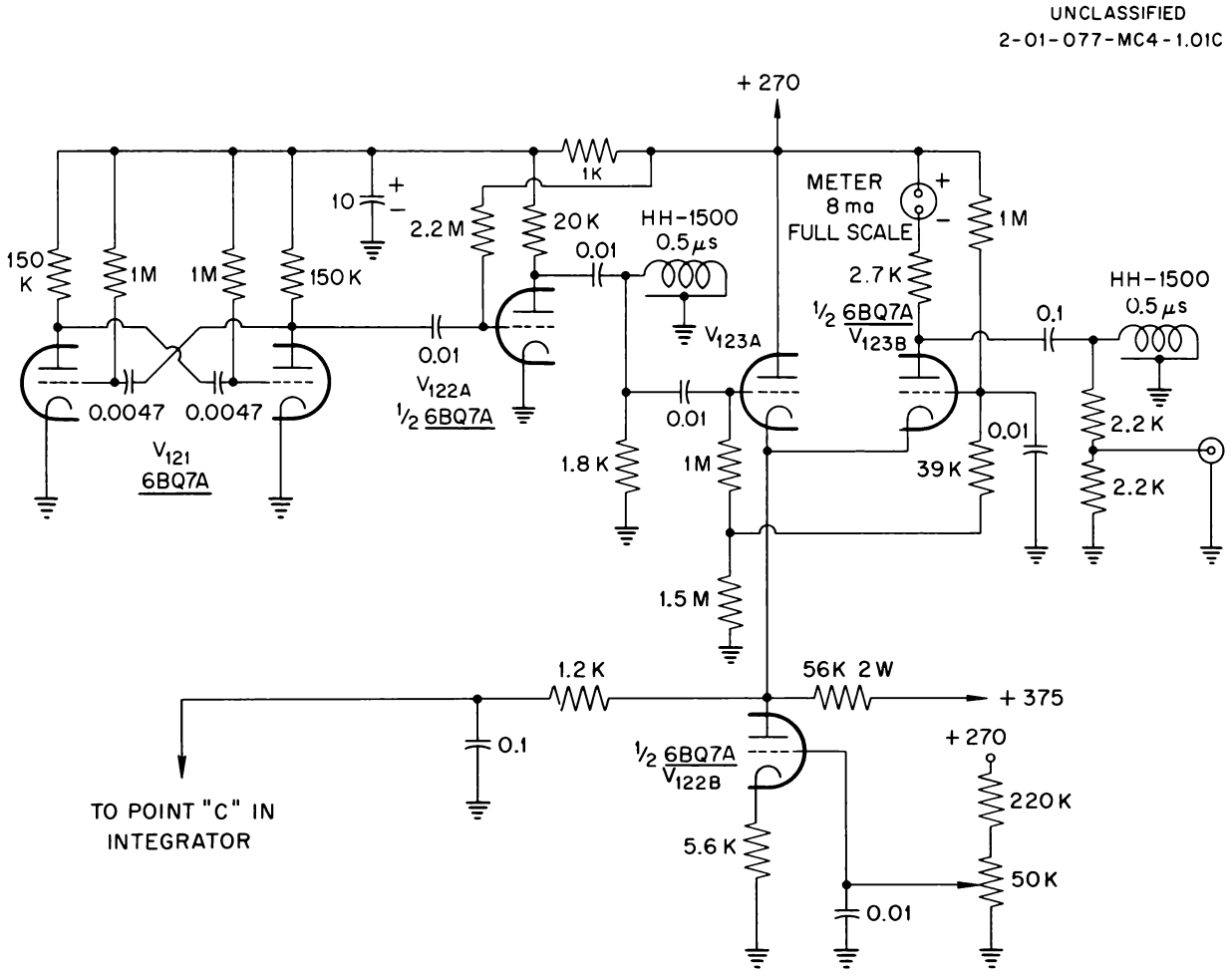

Fig. 2. Test Pulse Generator for MC4 Analyzer Control Unit.

The new pulse generator uses an integrator of essentially the same type as that used in the MC3. It has, however, three current ranges and a multivibrator pick-off circuit which permits its use as an automatic timer. A helipot sets the counting time at 0 to 200 or 0 to 2000 sec. The sweeping pulse is produced by interrupting the plate current of the integrator output tube. Figures 2 and 3 show this part of the device. A hard-bottomed multivibrator, V_{121}, causes V_{122A} to be alternately conducting and cutoff at about a 200-cps rate. At the time of cutoff, a positive 1-μsec pulse is produced by the pulse-forming line. This pulse transfers current from V_{123B} to V_{123A}. This current has three components: (1) the current which is being demanded by the integrator amplifier, (2) the current through V_{122B}, and (3) a biasing current, which permits the output current to be reduced to zero. The current in V_{122B} is adjustable and allows the sweep to be started at any signal height. Signal amplitude is read on a front-of-panel meter which measures the current in V_{123B}. When the current is transferred to V_{123A} for 1 μsec, a positive output pulse is produced which is followed by a negative reflection from the pulse-forming line.

Construction is in progress on two of the MC5 analyzers (120 channels, 120 at a time). The register reset mechanisms have been built, and contracts have been made for the construction of the double-channel units – the bakelite boards which contain the discriminators, interrogate tubes, and register amplifiers – and the scaler boxes. From the cost of these major components, an estimate of the cost of the analyzers may be made at $15,000 to $18,000 each.

The scaler boxes in the MC4 now have been operating about 5000 hr, with only one failure. A tube developed a "whisker" which shorted its supressor to its plate.

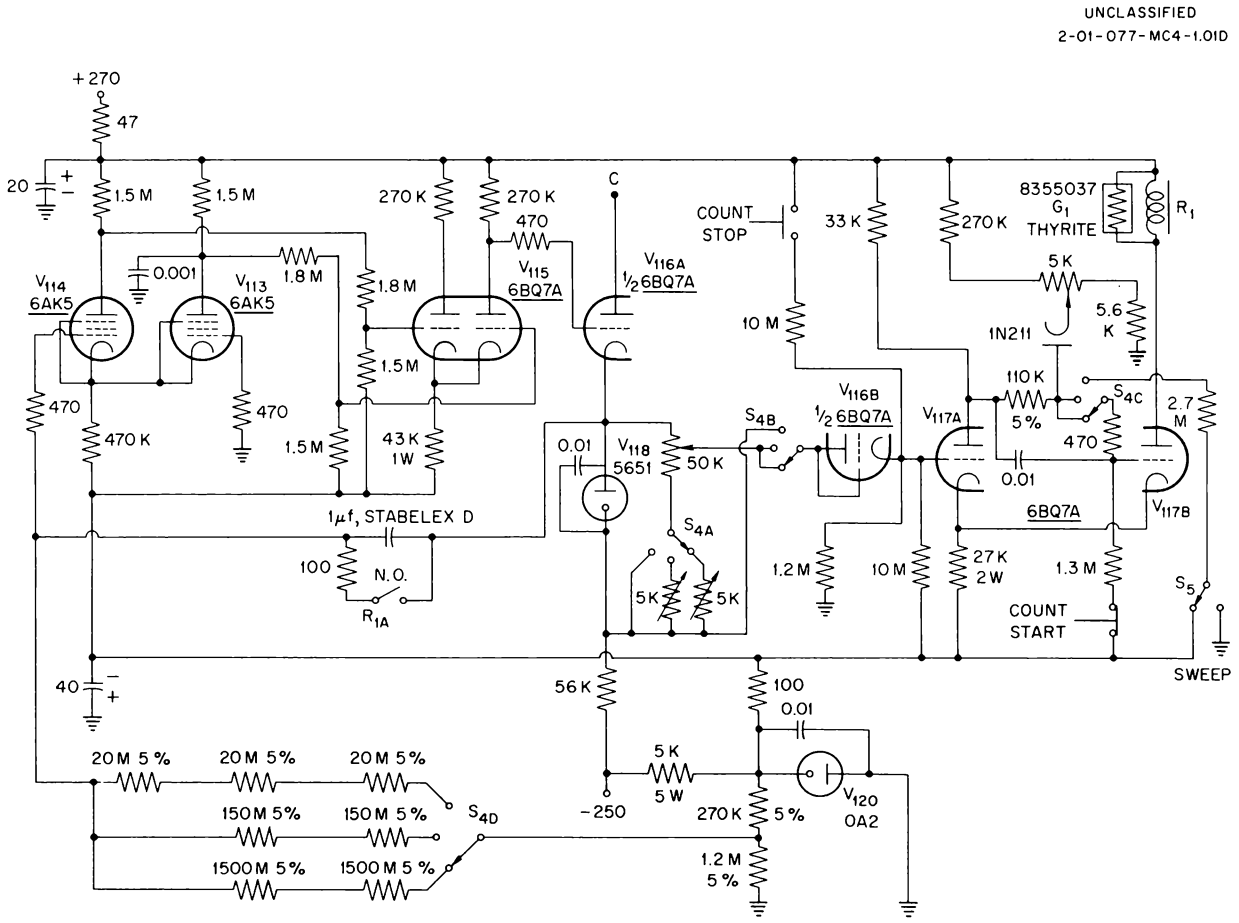

Fig. 3. Integrator Timer for MC4 Analyzer Control Unit.

LIFE TESTS OF FILAMENTARY SUBMINIATURE TUBES

C. C. Harris P. R. Bell G. G. Kelley

There has been some evidence that the life of filamentary tubes can be optimized by operating them at the "proper" filament voltage. In order to determine this proper voltage and in order to learn something of the life of these tubes, we have a life-test program in operation.

Fifty tubes of the type used in the MC4 scalers (CK5854) are on test, continuously conducting at scaler conditions. Twenty-five of these tubes are being operated at the nominal filament voltage of 1.25 v, and the other 25 are being run at 1.38 v. Each group is tested at its operating filament voltage and with the filament voltage reduced by 20%. The test has been in operation slightly over 10,000 hr, and there have been no failures. The margin shown under reduced-filament-voltage conditions indicates that the tubes will begin to show serious reduction in performance around 12,000 hr. Although the lower voltage group shows less margin, it is not known yet how the two groups will compare at the same filament voltage. This test will be made in the near future.

One hundred twenty tubes of the type to be used in the MC5 scalers (1AG4) are on test under scaler conditions, with the filaments on continuously but with plate current cut off half the time. There are three groups of 40 operating with filament voltages of 1.3, 1.1, and 0.9. The tubes are tested at normal and at 20% reduced voltages. These tubes have operated around 5000 hr with no failures. The group at 0.9 v shows that this filament voltage is insufficient for life greater than 4500 hr, but the tubes operate properly at 1.1 v. Comparative checks at the same filament voltages are in progress now.

In all tests and experimentation with these tubes we have had no filament failures due to turning the filaments on and off, nor do we have any evidence that it harms the tube in any way. Therefore, tube life in calendar days will be extended by turning the filaments on only when the tubes are actually being used.

GATED AMPLIFIER

J. Schenck

In connection with a proposed 128-channel pulse-amplitude spectrometer using magnetic core storage, an analog-to-digital converter is being developed in order to transform pulse amplitude into a storage address. This converter, having a conversion time approximately equal to the storage cycling time (5 to 10 μsec), requires for its operation a gated amplifier, or electronic switch, having specifications not met by any known circuits. What is required is a gain-of-two amplifier having two inputs capable of being switched alternately without transients and within 10^{-7} sec to a common output, where the input vs output functions are identical and stable with respect to both inputs over a frequency range extending from dc to over 10 Mc.

The gated amplifier consists of two identical degenerative amplifier sections whose outputs are connected (Fig. 1). Either one amplifier section or the other is operative, depending upon the polarity of the gate signal. Square-wave gate signals of opposite polarity are applied respectively to the grids of the gate tubes V_4 and V_7. The gate signals are of such a level and amplitude that when one is more positive it makes that gate tube conducting, raising the potential of the common cathodes and cutting off the output tube in the corresponding amplifier section. When the gate signal is more negative, the gate tube is cut off and essentially out of the circuit, so that the signal from the input in that amplifier section is then coupled to the cathode of the output tube. Output signal components introduced by the gate signals tend to cancel because they are applied in opposite phase to similar points in a circuit which is symmetrical with respect to the common output.

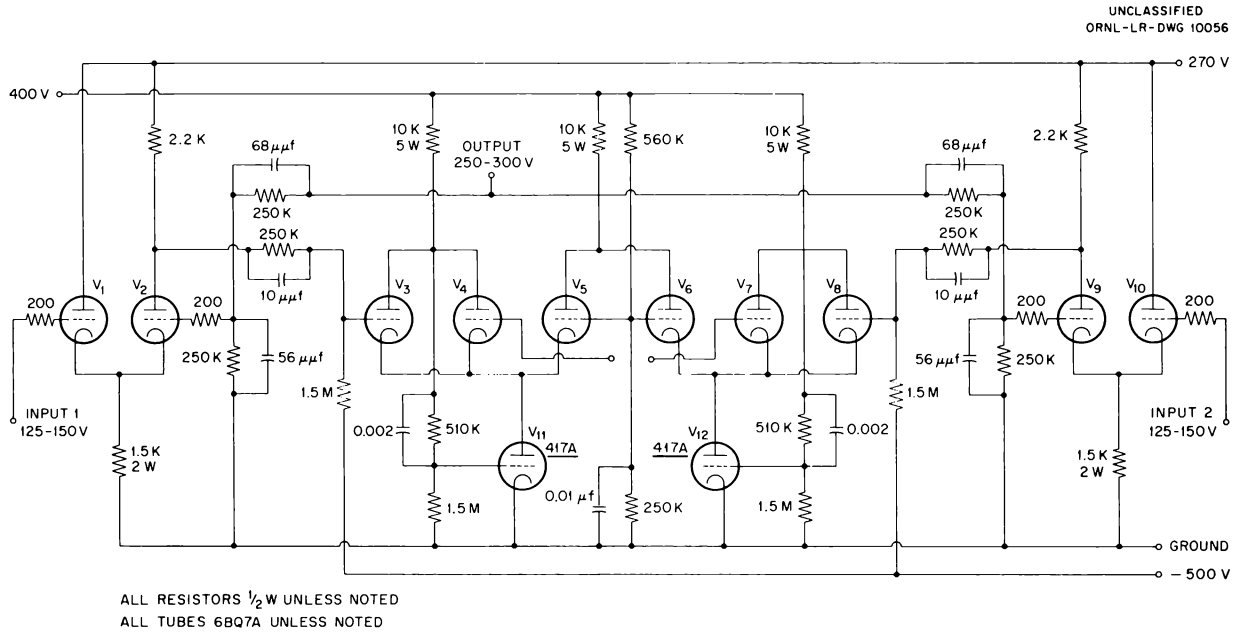

Fig. 1. Circuit Diagram for Stable Gated Amplifier.

The network containing the tubes V_3, V_4, and V_{11} is itself a degenerative unity-gain wide-band amplifier stage having inputs at the grids of V_3 and V_4 and the output at the common cathodes. The output will correspond to whichever input is the more positive, since a more positive signal on the grid of one tube tends to cut off the other. Because of the high loop gain and 100% negative feedback of this stage, the output impedance at the common cathode is consequently very low and therefore provides an effective cathode drive for the output tube. The same description applies to the network of the other amplifier section containing tubes V_7, V_8, and V_{12}.

Cathode-coupled stages are employed at the input for both amplifier sections. A negative feedback voltage equal to one-half the output voltage is returned to the free grids of the cathode-coupled pairs. The output of these stages is therefore a measure of the amount of unbalance of the potential at the grids. This potential unbalance is further amplified by the output tubes. The substantial loop gain and large amount of degeneration result in good linearity, stability, wide bandwidth, and further cancellation of residual unbalanced switching transients.